THÈSE DE DOCTORAT
DE L'UNIVERSITÉ DE LILLE

LABORATOIRE DE MÉCANIQUE, MULTIPHYSIQUE ET MULTIECHELLE (FRE 2016, CNRS)

Présentée par

Yue SUN

pour obtenir le grade de

DOCTEUR DE L'UNIVERSITÉ DE LILLE

Domaine

GÉNIE CIVIL

Sujet de la thèse

Finite Element Modeling of the cyclic behavior of concrete: mesoscopic approaches

(Modélisation du comportement cyclique des bétons : approches mésoscopiques)

Soutenance le 13 novembre 2019

Y. MALECOT, Professeur	Université Grenoble Alpes,	*Rapporteur*
F. BENBOUDJEMA, Professeur	ENS Cachan	*Rapporteur*
T. MASSART, Professeur	Université Libre de Bruxelles	*Invité*
J.M. TORRENTI, Professeur	IFSTTAR	*Membre*
C. DE SA, Professeur	ENS Paris-Saclay	*Membre*
E. ROUBIN, MCF	Université Grenoble Alpes	*Membre*
Y. JIA, MCF	Université de Lille	*Membre*
J.B. COLLIAT, Professeur	Université de Lille	*Directeur de thèse*
J.F. SHAO, Professeur	Université de Lille	*Co-directeur de thèse*

LaMcube - UNIVERSITÉ LILLE

Abstract

We present in this work a Finite Element based model, which is devoted to describing failure mechanics of quasi-brittle materials and identifying the minimum necessary ingredients for the fatigue behaviors with low number of cycles. The material will be studied at meso-scale, and be considered as heterogeneous media. The model is formulated in a sound framework of the Enhanced Finite Element Method (EFEM). As internal enhancements, two kinds of discontinuities are performed. On the one hand, strong discontinuities aim to illustrate cracks and fractures. On the other hand, weak discontinuities are used to describe heterogeneities. In addition to the initiations and propagations of cracks, the closure of cracks is also taken into account.

As a first step of validation, the proposed model is applied to reproduce the mechanical responses of heterogeneous material by adding the closure mechanism to the mode-I and mode-II strong discontinuity. We show the ability of the model to simulate some of the main characteristics of such materials, for instance, the emerged asymmetric traction/compression behavior, the stiffness recovery, the plastic deformation, and the hysteresis phenomenon.

Further, we compare the simulation results to experimental ones. The studied concrete material is composed of a matrix of cement and aggregates. By applying the same formulations and loadings, the proposed model succeeds in reproducing the macroscopic responses for monotonic and cyclic compression tests. Finally, the model is also tested by comparing with the experimental data in triaxial loadings.

Résumé

Nous présentons dans ce travail un modèle basé sur les éléments finis, qui est consacré à la description des mécanismes de ruptures des matériaux quasi fragiles et à l'identification des ingrédients minimum nécessaires pour les comportements à la fatigue avec petit numbre de cycles. Le matériel sera étudié à méso-échelle, et sera considéré comme un milieu hétérogène. Le modèle est développé dans un cadre de la méthode EFEM (Enhanced Finite Element Method). En tant qu'enrichissements internes, deux types de discontinuités sont effectués. D'une part, les discontinuités fortes visent à illustrer les fissures et les fractures. D'autre part, les discontinuités faibles sont utilisées pour décrire les hétérogénéités. En plus de l'initiation et de la propagation des fissures, la recherche de la refermeture des fissures est également prise en compte.

Dans une première étape de validation, le modèle proposé est appliqué pour reproduire les réponses mécaniques de matériaux hétérogènes, en ajoutant le mécanisme de fermeture aux discontinuités fortes du mode-I et du mode-II. Nous montrons la capacité du modèle à simuler certaines des caractéristiques principales de ces matériaux, par exemple, l'émergence du comportement asymétrique de traction/compression, la récupération de rigidité, la déformation plastique, et le phénomène de l'hystérésis.

De plus, nous comparons les résultats de simulation aux résultats expérimentaux. Le béton étudié est composé d'une matrice de ciment et de granulats. En appliquant les mêmes formulations et charges, le modèle proposé réussit à reproduire les réponses macroscopiques pour les essais de compression monotone et cyclique. Enfin, le modèle est également testé en comparant avec les données expérimentales dans les charges triaxiales.

Remerciements

Je tiens, en premier lieu, à remercier Professeurs Malécot et Benboudjema, d'avoir accepté la lourde tâche de rapporteurs et consacrer du temps à lire ma thèse. Je souhaiterais aussi remercier Madame Jia, Madame De sa, Mosieur Torrenti, Monsieur Massart, Monsieur Roubin de s'être joints au jury, et d'avoir partager votre vision de la recherche.

Je tiens à remercier très sincèrement mes directeurs de thèse, le Professeur Jean-Baptiste Colliat et Jianfu SHAO, de m'avoir proposé ce sujet de thèse et de partager ses brillantes visions de la recherche. Je tiens à remercier tout particulièrement le Professeur Jean-Baptiste Colliat, pour m'avoir aidé, guidé, et répondu à mes innombrable questions depuis mon stage de Master 2 à la finalisation de cette thèse. Merci pour votre gentillesse et votre patience tout le temps.

Je tiens également à remercier Emmanuel Roubin d'avoir partagé ses idées avec moi et d'avoir accepté de se joindre au jury. Merci à lui pour ses conseils et sa visite à Lille. C'est un grand honneur pour moi d'avoir pu échanger et discuter avec lui à Grenoble. Son travail est un point de départ important pour ma thèse.

Enfin, je ne vais jamais finir ma thèse toute seule. J'ai eu le plaisir de rencontrer beaucoup de gens magnifiques pendant ces trois ans de thèse. Un grand merci à notre rencontre, Monsieur Shen, Madame Jia, Lunyang, Jin, Bei, Yajun, Meng, Yulong, Xiaodan, Jianjian, Yue, Hailing, Dongmei, Xi, Siyu, Jueliang, Wang, Xiaolong, Jinzhou, Chuangen, Susheng... J'adresse au final mes remerciements à mes familles et mon ami Zhan pour les soutients et encouragement.

List of symbols

σ	stress tensor
ε	strain tensor
d	displacement vector
$\boldsymbol{T}$	traction vector
T_n	projection of the traction vector on the normal vector
T_t	projection of the traction vector on the discontinuity surface
$\mathcal{S}$	discontinuity interface within the finite element
$\mathcal{S}_u$	strong discontinuity interface within the finite element
$\mathcal{S}_\varepsilon$	weak discontinuity interface within the finite element
$\tilde{\bullet}/\hat{\bullet}$	weak/strong discontinuity
$\bullet^+/\bullet^-$	upper/lower part of the sub-volume of the finite element
$[\lvert\boldsymbol{\varepsilon}\rvert]$	jump of the weak discontinuity (strain field)
$[\lvert\boldsymbol{u}\rvert]$	jump of the strong discontinuity (displacement field)
$[u]_{\max}$	maximum value of the crack
E	Young's module
ν	Poisson's coefficient
$\mathbf{C}$	Hooke tensor
$\mathcal{H}$	Heaviside function
σ_{y}	critical tensile stress

φ	friction angle
$\mathcal{G}_{\text{op}}$	fracture energy, the necessary energy for a total opening/sliding
$\mathcal{G}_{\text{cl}}$	closing energy, the necessary energy for a total closing
C	cohesion of the material
$\boldsymbol{n}_p$	the sliding direction of the mode-II discontinuity, corresponding to the "position"
$\boldsymbol{n}_t$	the shear stress direction of the mode-II discontinuity, corresponding to the "tendency"

Contents

Chapter I

Introduction

Background

Concrete is one of the most commonly used artificial materials around the world and plays a significant role in structures. For example the recently built Daxing airport in Beijing, see Fig. I .1, more than one million cubic meter of concrete is used for the main building. Despite the low cost and widespread usage of concrete for a long history, it is a complex material in many respects and is worthy of further research.

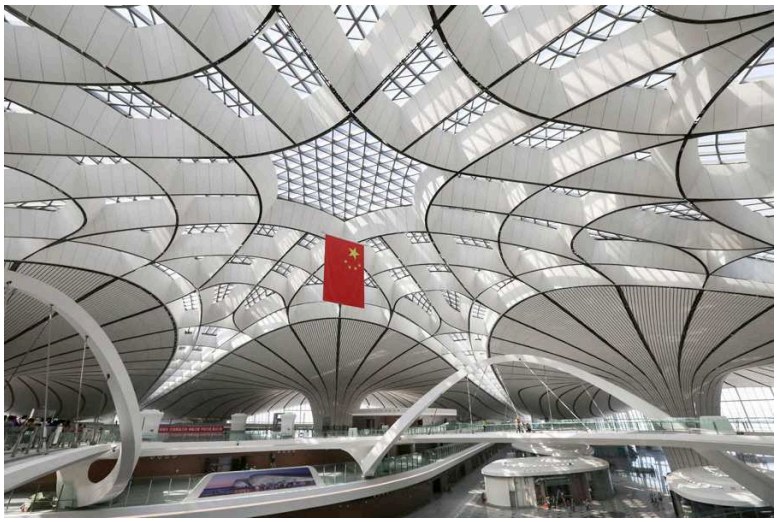

Figure I .1: Recently built Daxing airport in Beijing.

On the one hand, concrete is a sort of time-dependent material, which involves the effects of creep, shrinkage, and aging. The intrinsic nature of concrete and the influences of

the environment induce variations of properties for concrete over its lifetime. On the other hand, concrete is a material showing a complex structure. Beginning at the mesoscopic scale, concrete exhibits aggregate pieces and macro-pores, and complexity of its structure increases when increasingly finer scales are considered. At the microscopic scale, the mixed chemical reactions give rise to Calcium silicate hydrates (CSH), portlandite (CH), ettringite (Aft), and a great number of porosity in the cement paste. In addition, as a quasi-brittle material, concrete shows complicated mechanical behaviors, such as the non-symmetric responses in traction and compression as well as the hysteresis phenomenon in cyclic loadings, see Fig. I .2. **From a general point of view, the main assumption made in this thesis is that those two complexities are strongly linked.**

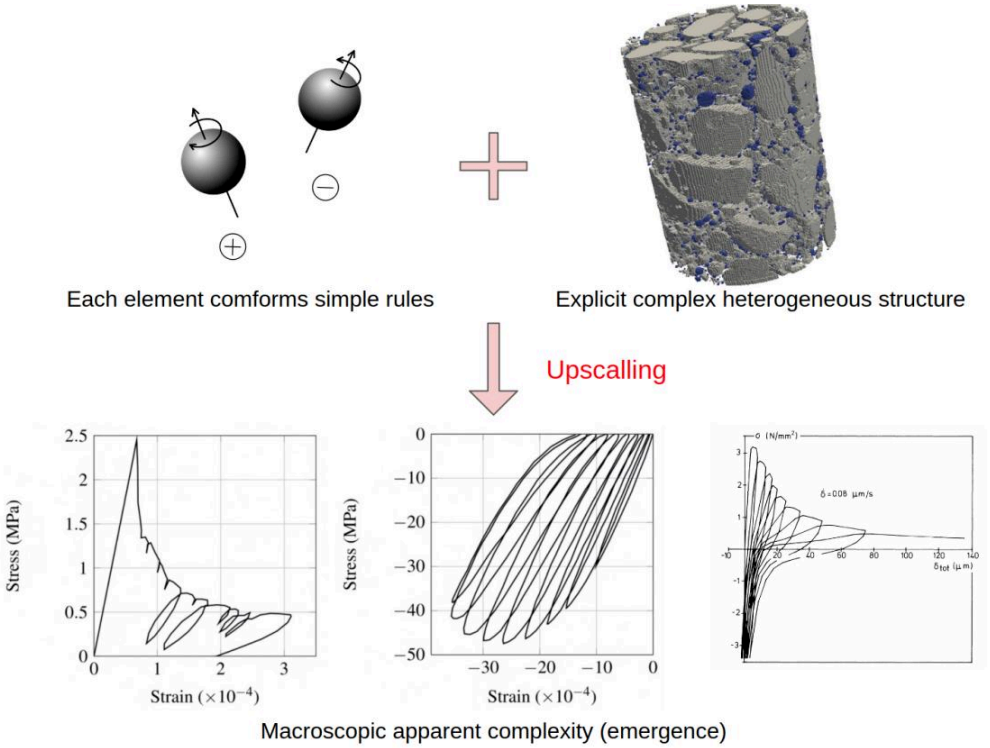

Figure I .2: Main hypothesis of this dissertation that complex mechanical behaviors of concrete (Mazars et al., 1990; Reinhardt, 1984; Terrien, 1980) can emerge from the up-scaling of elements with simple behaviors and explicit heterogeneous structure of concrete (Stamati et al., 2018a).

The hypothesis stems from the non-linear complex adaptive system (Ahmed et al., 2005). The essence of the complex system is that each individual constituent conforms to (very) simple rules. However, when the system is studied as a whole, emergent responses can be observed after upscaling which are not exist at the single element. Besides, by

understanding the behaviors of each element, it may be beneficial for us to understand the entire system.

Naturally, the macroscopic mechanical behaviors of concrete are known a priori from experimental tests, see Fig. I .2. The complex heterogeneous structure of concrete is thus defined as the explicit heterogeneous geometry of the material. At the mesoscopic scale, the heterogeneities are referred to as the aggregates and macro-pores, see Fig. I .2. It can be constructed within the framework of the finite element method, with a large number of elements and explicit representation of heterogeneities. Moreover, a newly developed technique, namely X-ray tomography, makes it possible to establish a morphological structure of concrete based on real tomographic images (Stamati et al., 2018a). Therefore, it is interesting to look backward to clarify the simple rules of each element.

Based on the previous assumption, attempts to solve the simple mechanical behaviors of each element have been made by former studies. One of the studies is documented by Roubin (2013), in which each element is governed by two mechanisms: localization and traction-separation. It has been demonstrated that even though only "opening" mechanism is applied to elements, the model is capable of performing failure behaviors of concrete in traction as well as in compression. Moreover, non-symmetric behaviors can also be observed. Another study is documented by Hauseux (2015); Vallade (2016), that each element is also piloted by two mechanisms: localization and sliding-opening. In this case, only "frictional sliding" mechanism is proposed to each element. Also, non-symmetric failure responses in traction and compression are obtained.

However, with the focus placed on the cyclic loading, neither of these models is capable of producing all of the constituents of fatigue behaviors, which involves the progressive loss of stiffness, the growing permanent strain, the hysteresis loops, etc.. **Therefore, the objective of this study is to clarify the key mechanisms of each element to perform the behaviors of concrete in cyclic loadings.**

It is widely known that the fracture is one of the most encountered failure modes for concretes. At present, the computational failure mechanism is regarded as a study of significant value. Based on the mechanical behaviors as observed in experimental tests, many computational models have been proposed over the last decades with regard to the macroscopic models, or the phenomenological models. The degradation of the material is caused by the governing laws which are defined over the global specimen, such as the damage model (Comi and Perego, 2001; Mazars, 1984; Ragueneau, 2007; Richard and Ragueneau, 2013), and the coupled plastic-damage model (Grassl and Jirásek, 2006;

Lubliner et al., 1989a), just to mention a few. A lot of them achieved at reproducing many typical mechanical behaviors of concrete, such as the unilateral effect (Comi and Perego, 2001), the fatigue behaviors (Alliche, 2004), and the hysteresis phenomenon (Richard and Ragueneau, 2013).

The benefit of the macroscopic models is that they can perform simulations of various structures, such as bridge, radioactive storage, and petroleum extraction. However, describing the complex behaviors of the material requires growing complicated governing laws and more specific parameters. Moreover, the physical resources of fractures and plastic strains may not be explained in an explicit way. In general, it seems that many typical behaviors of concrete (unilateral effect, hysteresis loops, shrinkage) are associated with the development of cracks, such as the closure of cracks and the friction between the lips of cracks. Therefore, it is sensible to infer that most of these mechanical behaviors may take their origin at smaller scales. Taking into consideration of local properties appears to be a significant step in making an accurate and robust description of concrete's behaviors. Based on this hypothesis, a set of models have been proposed as the micro-mechanical models.

The micro-mechanical model relies on the assumption if an equivalent continuum over the specimen, that is, the Representative Volume Elements (RVE). Regarding the size of voids and cracks at the microscopic scale, micro-mechanical models attempt to establish a relationship between the micro-structure of the material and its macroscopic mechanical behaviors. Many models of this category have been introduced over the years to describe the mechanical behaviors performed by various engineering materials, such as porous ductile material (Tvergaard, 1982), rocks (Kachanov, 1982a,b), and latter initially anisotropic materials (Qi, 2016), etc.. The frictional sliding and the closure mechanism of micro-cracks are also taken into account. However, the micro-mechanical models fail to give the consideration to the underlying structural effect of the heterogeneous material, and the fractures are described in an implicit way. Therefore, another set of approaches have been developed in parallel, which are referred to as the discontinuous approach.

The discontinuous approach is addressed within the multi-scale framework (Zaitsev, 1985). The main idea is to consider constitutive behaviors at the local scale for each phase while defining an explicit geometry of the heterogeneous morphological structure. Therefore, the effect of heterogeneities is taken into account. Moreover, in combination with the X-ray tomography technique, it makes it possible to provide simulation with real morphological structures (Stamati et al., 2018b).

This study falls into the latter category. Aiming at providing a discontinuous approach

to simulate the fatigue behaviors of concrete, the establishment of the model consists of two parts, which are the construction of the morphological model and the construction of the mechanical model.

On the one hand, the used method for providing explicit representations on the morphological structures is referred to as the non-adapted mesh strategy. In regards to the concrete, the investigation scale is defined as the mesoscopic scale, specifically in millimeters and centimeters. At this scale, the concrete is a highly heterogeneous material, which exhibits aggregates, cement matrix, and macro-pores. The morphological structure is projected to a uniformed and unstructured mesh. In a case of a two-phase material (matrix and aggregates), the projection produces two types of elements: i) the elements that are entirely included in one phase, and ii) the elements that are crossed by the interfaces of aggregates. The latter type of elements carries a discontinuity in the strain field. This jump in the strain field is called the weak discontinuity.

On the other hand, the used method to represent cracks is referred to as the strong discontinuity, i.e., jump in the displacement field. Many models have been introduced over the years which use the strong discontinuity. The governing law usually consists of a localization criterion, which decides the appearance of the cracks; and a softening law, which describes the degradation of the material. Aiming to produce the fatigue behaviors of concrete, a closure mechanism is considered in the model.

With the fatigue behaviors of concrete concerned, there are a variety of possible explanations. For instance, the friction between the cracks, the additional dissipated energy, the irreversible crushed pores, and the release of the stresses that already exist during production. The benefit of the studied model is that the proposed mechanical behaviors at the local scale can be fairly simple and singular. Therefore, we attempt to develop a robust and efficient approach while revealing:

- What are the **minimum necessary ingredients** for performing fatigue behaviors, which involves loss of stiffness, increasing permanent strain, hysteresis loops, etc..
- What are the effects of each of these ingredients in the aspect of macroscopic responses as well as mesoscopic crack patterns.

This thesis consists of three chapters. In **Chapter 1**, a brief overview of the experimental facts and recent computational models is presented. Then the construction of the morphological model and mechanical model is detailed in **Chapter 2**. Referring to

the "simple rules" of each element, see Fig. I .2, the mechanical behaviors of elements are defined upon a strong discontinuity of the mode-I. The element is split by the micro-crack, and the crack carries a vertical opening. A closure mechanism is then applied to the element representing a decreasing value of this separate. In this case, the closure of crack leads to additional dissipated energy. However, from the perspective of physical meaning, no friction is considered. Therefore, it is interesting to know if some of the fatigue behaviors can be observed if only the additional dissipated energy is considered, or if frictional sliding is one of the essential constituents of fatigue behaviors. Next, in **Chapter 3**, a closure mechanism is performed in the strong discontinuity of the mode-II. The micro-cracks of this type is comparable to a frictional sliding. The so-called closure represents a process that the crack slides back or even continues propagating in the opposite direction. In the case of the mode-II strong discontinuity, the friction between the lips of cracks is taken into consideration. Therefore, it is interesting to ascertain if more fatigue behaviors can be observed with the consideration of friction. For both types of strong discontinuity, mode-I and mode-II, the model is then examined by comparison with experimental tests, in which the experiment data is provided by Piotrowska (2013). The evaluation of the models is conducted in both axial loading and triaxial loading.

Major contributions

The overall originality of this thesis is that several ingredients of the fatigue behaviors of concrete are discussed separately. Several major contributions of this study are mainly concentrated on the following points:

- Based on former studies of the strong discontinuity of the type mode-I, the closure mechanism is formulated to the model. The closure mechanism enables the additional dissipated energy while the friction between the cracks is not involved. Therefore, we can clarify that the additional dissipated energy along with the localization and traction-separation mechanism can be the minimum necessary ingredients for many main features of fatigue behaviors, such as the hysteresis loops and the stiffness recovery. In addition, the unilateral effect is also observed.

- The closure mechanism is then formulated to mode-II strong discontinuities, which includes the additional dissipated energy as well as the frictional sliding. Compared with the previous assumption, we can deduce that the friction between the lips of crack plays a significant rule in fatigue behaviors. This model performs some main

features of fatigue behaviors that the previous model does not achieve, such as the increasing permanent deformation.

- Besides the macroscopic mechanical responses, the approaches of this thesis also shown some interesting evaluations of crack patterns. The morphological model exhibits a large number of finite elements and explicit representation of heterogeneities, the crack pattern is tortuous with branching and may be stopped by inclusions. Also, the crack closures may exist even in monotonic loadings.

Chapter II

State of art

Contents

1 Introduction

As one of the most widely used artificial materials, concrete is an important component in civil engineering structures. As it is presented in the general introduction, we made the assumption that the apparent complexity of the mechanical behaviors of concrete is strongly linked with its complex heterogeneous structure. In this chapter, we will begin by providing a literature review on characteristics of concrete which are observed in experimental tests. Then the second part of this chapter presents an overview of two advanced discretization techniques. Finally, we shall introduce a brief bibliographic review of numerical models, which allow us to reproduce concrete behaviors.

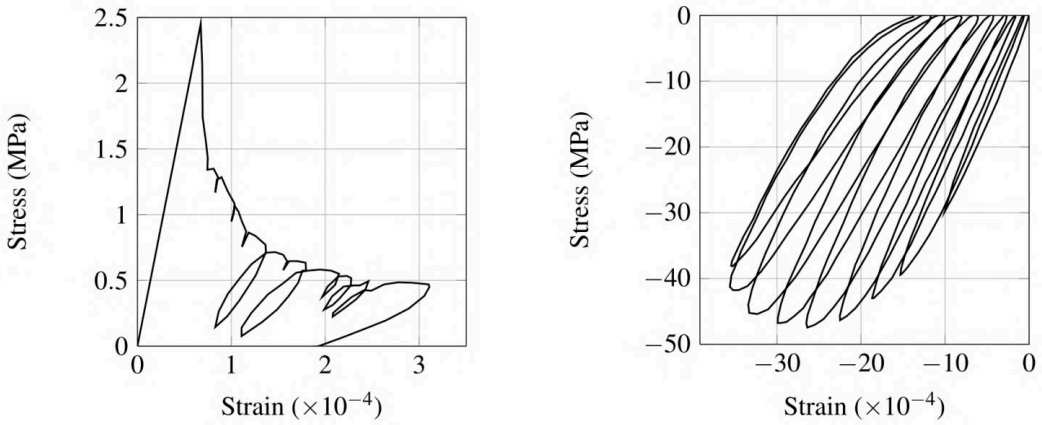

(a) Traction (b) Compression

Figure II .1: Concrete behaviors under uniaxial traction (Terrien, 1980) and compression (Ramtani, 1990) loadings.

2 Experimental facts

Concrete is a material with complex behaviors. This section attempts to show experimental observations of concrete. The first part of this section presents some typical mechanical properties of concrete observed in experimental tests. The mechanical properties of concretes are discussed separately in uniaxial tests, i.e., without confining pressure, and in triaxial tests. Recent research has suggested that multiple mechanical behaviors of the concrete at the macroscopic scale are strongly influenced by the morphological structures of the material and the properties of the material components in smaller scales (Stamati et al., 2018a). Thus the second part of this section goes on to present a widely used technique that allows us to capture the characteristics of the material inside the concrete.

2.1 Concrete behaviors under uniaxial and triaxial loadings

It is generally agreed that the failure behaviors of concrete under mechanical loadings are accompanied by the development of cracks. In the case of uniaxial loadings, the typical macroscopic responses of concrete are plotted in Fig. II .1. As shown in the figure, concrete is asymmetric under traction/compression loadings. It has brittle tensile behavior and is more ductile in compression.

Fig. II .1 shows that in the first stage of the tensile loads, a linear response is ob-

served before the peak. According to recent research (Kishta, 2016), some micro-cracks will appear and diffuse throughout the material, particularly around the stress concentration area, for example, near the aggregates. These micro-cracks preferably develop in the direction perpendicular to the maximum extension. When the micro-cracks begin to coalesce and turn into macroscopic cracks, the material reaches its peak and turns to the post-peak stage. At this stage, the material rapidly loses its stiffness and strength. If cyclic loadings are applied, hysteresis loops and plastic deformations can be noticed.

The behavior of concrete in compression is rather ductile. The material has a much higher compressive strength than the tensile material, see Fig. II .1. Compression cracks are parallel to the loading direction due to the lateral expansion and induce the volume dilatation (Yazdani and Schreyer, 1988). At the post-peak stage, the material progressively loses its stiffness, hysteresis loops and plastic deformations can also be observed in cyclic compression loadings. The hysteresis phenomenon has several explanations. On the one hand, experimental observations reveal that micro-pores, micro-cracks, and residual stresses exist in virgin concrete due to the chemical hydration reaction. As degradation develops, residual stresses are released and disappear, resulting in permanent strain (Ramtani et al., 1992). On the other hand, plastic deformation and hysteresis loop are part of the consequence of friction between the lips of the cracks, i.e., the closure of cracks. As the imposed loading decreases, a few cracks remain open while others close, even for a state of zero stress.

Regarding the closure of cracks, it leads to another behavior of the concrete that can be observed in experimental tests, the unilateral effect (Mazars et al., 1990; Papa, 1996). The observed behavior of concrete is that when the applied loading switches from tension to compression, the damaged material in traction regains its stiffness in compression. Even though the material has been severely damaged in tension, the initial stiffness and strength remain unchanged in compression.

In addition to the behaviors of concrete under uniaxial loadings, many civil engineering applications are performed under triaxial conditions with different confining pressure, such as dams, bridge pillars, structural impacts, and radioactive waste treatment. It is therefore also essential to determine the mechanical behaviors under confining pressures.

Many researches are available in the literature which present concrete behavior under

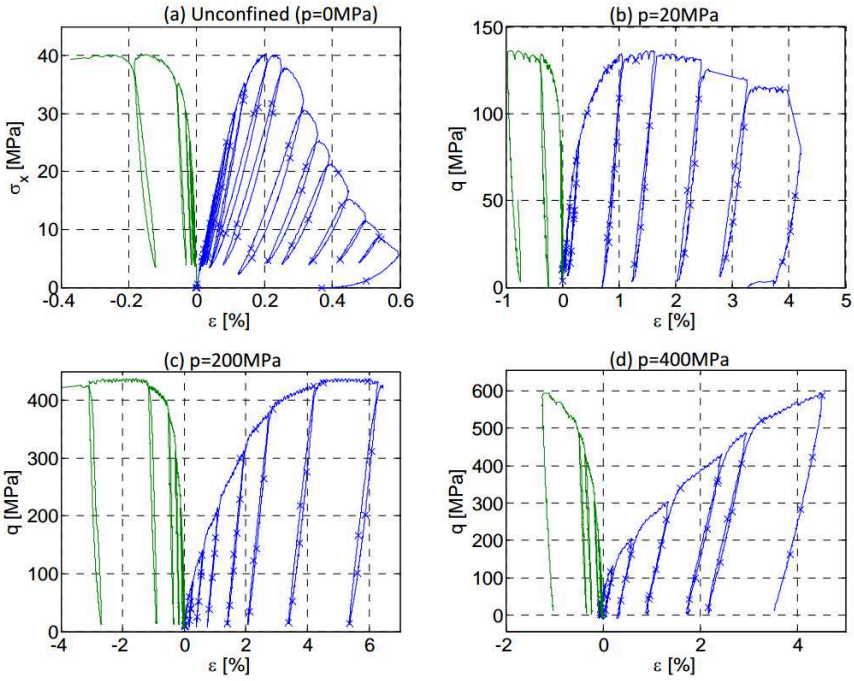

Figure II .2: Responses of concrete in terms of axial stress and deviatoric strain under different confining pressures (Malecot et al., 2010).

moderate confining pressure (Chuan-Zhi et al., 1987; Imran and Pantazopoulou, 1996; Kupfer et al., 1969a; Linhua et al., 1991; Pugh, 1973; Sfer et al., 2002) and high confining pressure (Gabet et al., 2008; Taliercio et al., 1999; Vu et al., 2009). A typical response of concrete under different level of confining pressure is shown in Fig. II .2.

The results of the triaxial tests shown in Fig. II .2 depicts a transition from quasi-brittle to ductile behaviors. Concerning the hydrostatic pressure, an increase in confining pressure leads to an increase in material capacity, and a gradual stiffening is observed in the confining phase. More extremely, under very high confinement, concrete behaves like a non-cohesive granular stacking (Malecot et al., 2010; Piotrowska, 2013). The characteristics of cracks under different containment pressures also present different patterns. As plotted in Fig. II .3, the cracks are quasi-vertical under a relatively low confining pressure. And as the hydrostatic pressure increases to a very high level ($> 100MPa$), the cracks tend to be perpendicular to the loading direction. In between, inclined cracks are observed in a damaged concrete.

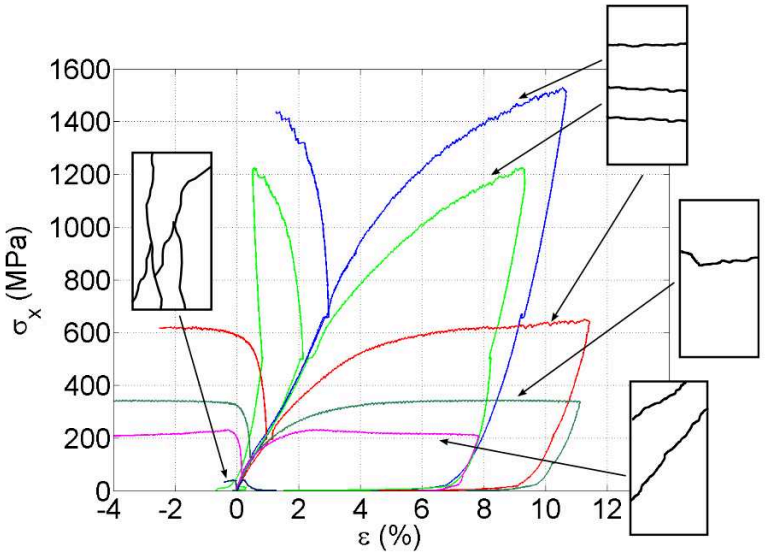

Figure II .3: Observed failure patterns of the concrete in different confining pressures (Piotrowska, 2013).

2.2 X-ray tomographic investigations of concrete

As a heterogeneous material, concrete presents complex heterogeneities natures over a wide range of scales. These characteristics pose many challenges to experimental tests and numerical simulations because the properties of the constituents have significant influences on the macroscopic response of quasi-brittle materials. Several techniques are used to investigate the heterogeneous microstructure of the materials, such as the backscattered electron imaging of polished surface, and the X-ray micro-tomography (Piotrowska, 2013; Ren et al., 2015; Stamati et al., 2018a). X-ray micro-tomography is a non-destructive technique. Combined with image analysis technique, it could provide reliable representations of concrete heterogeneities at the mesoscopic scale in 3D (Hashemi et al., 2014; Lu et al., 2006; Poinard et al., 2011; Stamati et al., 2018a), and can access the damage mechanisms under loadings (Elaqra et al., 2007; Landis et al., 2003; Poinard et al., 2012; Wong and Chau, 2005). Recent researches provide a way to reproduce the material response by explicitly representing the heterogeneities of the meso-scale with the help of this technique (Stamati et al., 2018b), see Fig. II .4.

In this manuscript, the material behaviors that we want to reproduce by numerical modeling focus mainly on:

1. The progressive failure of the material due to the initiation and propagation of cracks;

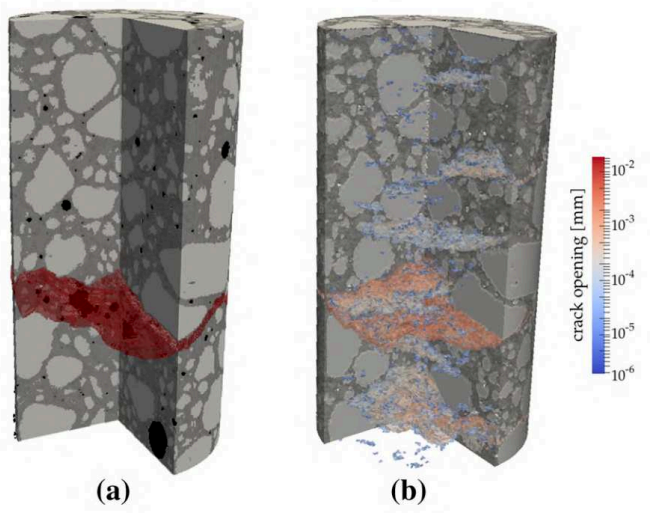

Figure II .4: Comparison of crack patterns at post-peak stage between: (a) segmented 3D image of experimental scan and (b) numerical crack pattern Stamati et al. (2018b).

2. The effect of heterogeneities at the mesoscopic scale, which leads to stress concentration and tortuous crack paths;

3. The fatigue behaviors of the material, including the hysteresis phenomena and stiffness recovery, which are associated with crack closures;

4. The triaxial behaviors of the material under confined pressures.

In order to verify the performances of the numerical simulation, it is interesting to compare it with an experiential result. Therefore, the experimental results that we used in this manuscript are provided by Piotrowska (2013), in which, experimental characterizations of concrete behaviors are well detailed. To establish the effect of the granular skeleton, three types of aggregates are used: the crushed aggregate, the rolled aggregate, and the glass balls, see Fig. II .5. The concretes are then applied to cyclic compressional loadings under different confining pressure (0, 50, 100, 200, 650 MPa). The comparison of the material responses between the numerical simulation and those of experimental results will be presented in the following chapters.

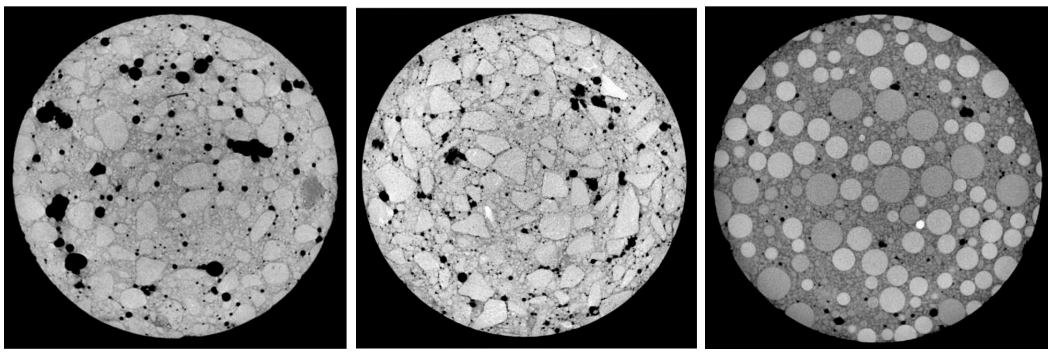

(a) Rolled aggregate concrete (b) Crushed aggregate concrete (c) Glass ball concrete

Figure II .5: Tomographic cross-sectional view of three concretes which exhibit different coarse aggregates (Piotrowska, 2013).

3 Advanced discretization techniques for image-based modeling

The broadly used civil engineering materials are found as heterogeneous materials at the mesoscopic/microscopic scale, for example, the rocks, soils, shales, and concretes, etc.. Obviously, the overall characteristics of the material are strongly influenced by the size, shape, and distribution of the inclusion compositions or porous phases. Thus, a large amount of research has been devoted to investigating the relationships between the macroscopic responses of the material and its microstructural characteristics.

X-ray tomography techniques allow us to obtain the geometrical information inside the heterogeneous material. In an attempt to combine the mechanical behaviors of the material with its compositions while considering the complex microstructure, discretization tools are needed to enable numerical simulations. Two categories of discretization techniques are discussed here: the non-conforming mesh generations and the conforming mesh generations.

Based on raw implicit 3D images, different components of the material can be distinguished by image analysis, i.e., phase segmentation. Some efficient tools can be used such as thresholding from gray-scale images (Stamati et al., 2018a), or the level-set functions (Kamel et al., 2019b). Referring to the non-conforming strategy, it projects the implicit geometry onto an unstructured mesh. The geometrical information is inherited and taken into account by kinematic enhancement, namely the weak discontinuity. This strategy al-

lows efficient automatic simulations without pre-processing. However, the non-conforming mesh method presents difficulties when attempting to capture all geometrical details with a uniformed mesh size. This limitation is visible in the case where the size of the finite element is larger than the narrowness between inclusions. Obviously, some geometrical information will be lost. On the contrary, the conforming strategy is very suitable for capturing microstructure details with refined finite elements.

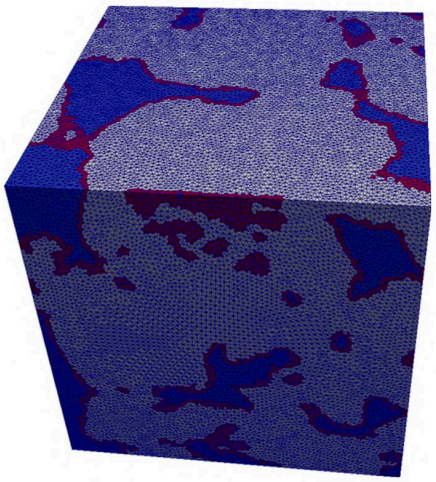

Figure II .6: Illustration of the embedded weak discontinuity model for porous rocks using non-conforming mesh strategy, with solid phase colored in gray, pore phase in blue, and the enriched elements in red (Kamel et al., 2019a).

The conforming discretization strategy allows producing high-quality meshes with automatic selective refinement. The use of uniform mesh elements to handle complex geometries may require a large number of elements. Thus the strategy of the conforming mesh method is to apply a size function to manage the geometrical features of micro-structure. Therefore, the narrowness between inclusions and the interface curvatures can be well described with refined finite elements.

As it can be seen in Fig. II .6 and Fig. II .7, both discretization strategies are capable of automatically constructing models based on implicating 3D images. Compared with the non-conforming mesh strategy, the conforming mesh technique is adapted to capture more geometric details of the microstructure. And the porous phase can be treated naturally, as shown in Fig. II .7, which is not directly in the case of kinematic enrichment. The pore phase of a non-conforming model can only be approximately represented by low material

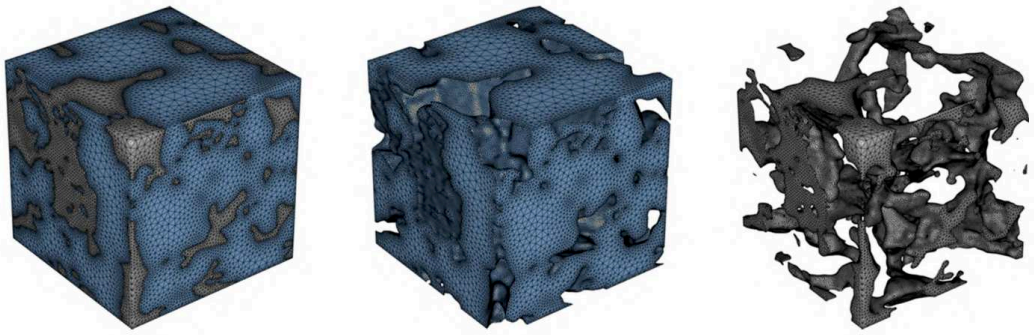

Figure II .7: Illustration of the optimized conform mesh for porous rocks, with in the left: the global mesh for solid phase and pore phase; in the centre: the mesh of solid phase only; in the right: the mesh of pore phase only (Kamel et al., 2019a).

stiffness parameters.

4 Modeling for the quasi-brittle materials

It is a common sense that the fracture is one of the most encountered failure modes for engineering materials. Therefore, the prediction of material fractures plays a significant role in the context of civil engineering. Over the past two decades, many computational models have been proposed. These models provide tools to prevent structure failures, and also to understand and analyses the failure processes inside the material.

In this section, we present an overview of computational models, including their main ideas as well as their advantages and limitations. And we classify these models into two categories:

1. Numerical models using continuous approach, i.e., the cracking description is implicit,

2. Numerical models using discontinuous approach, i.e., the cracking description is explicit.

4.1 Continuous approach with implicit cracks

Aiming at describing the failure of brittle or quasi-brittle materials, the continuous approach is a kind of strategy that represents fractures as a process of strain localization and damage growth. It usually considers a hypothesis which assumes an equivalent

homogeneous continuum over the representative volume. For instance, the averaged stress.

$$\sigma^{\mathrm{M}} = \frac{1}{V}\int_{V} \sigma(\boldsymbol{x}) d\ \boldsymbol{x}. \tag{4.1}$$

This hypothesis is named as Representative Volume Element (RVE). Under this assumption, the proposed model behaves as homogeneous material at the RVE scale:

$$\sigma^{\mathrm{M}} = f(\varepsilon^{\mathrm{M}}). \tag{4.2}$$

Consequently, the representative volume only makes sense if the cross-section is much bigger than the size of cracks and heterogeneities. The displacement field is considered as continuous and without any explicit cracks. We present several models in the following part that belong to this category, and their main characters are also discussed.

4.1.1 Theory of plasticity

The main idea of the theory of plasticity is to decompose the strain filed into two separate parts,

$$\varepsilon = \varepsilon_e + \varepsilon_p, \tag{4.3}$$

where the elastic strain ε^e represents the elastic and undamaged material, and the plastic strain ε^p links with the cracked material which is irreversible. The stress filed is obtained by Hooke's law:

$$\sigma = \mathbb{C} : \varepsilon_e = \mathbb{C} : (\varepsilon - \varepsilon_p), \tag{4.4}$$

with $\mathbb{C}$ represents the stiffness of the material. The typical strain-stress relationship can be expressed in Fig. II .8. For the model exhibits only the plastic mechanisms, i.e., irreversible dissipated energies, the unloading path has exactly the same slope as the initial one.

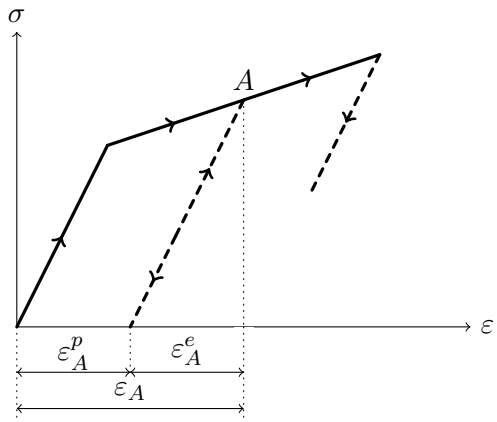

Figure II .8: Illustration of the basic idea of the theory of plasticity in a cyclic occasion.

Applying the theory of plasticity to concrete-like materials (Chen and Chen, 1975; Dragon and Mroz, 1979; Etse and Willam, 1994; Grassl et al., 2002; Hofstetter and Mang, 1995; Menetrey and Willam, 1995), a basic constitutive plasticity model always consist of a yield function, a flow rule, a hardening law and/or softening law. A considerable amount of literature has proposed several classical and widely used yield functions, such as the Rankine principal stress criterion, which limits the tensile strength, and Drucker-Prager yield function, which adapts to compressional descriptions. The flow rule determines the evolution of the plastic strain rate. And the equipment of the hardening/softening law makes the plasticity models very suitable to describe failure conditions and development of permanent strain, and also material behaviors under biaxial/triaxial loadings.

However, plasticity models along, lack the description of stiffness degradation due to the growth of micro-cracks, and other related behaviors such as the stiffness recovery and unilateral effect under cyclic or fatigue loadings. Thus the theory of plasticity is usually used by combining with other models, such as the damage model. .

4.1.2 Damage theory

The main idea of the damage theory is to introduce a damage variable D to describe the degradation of the material. The equation relating the stress-strain relationship in terms of the damage variable gives as:

$$\sigma = (1 - D)\mathbb{C}_0 : \varepsilon \tag{4.5}$$

where $\mathbb{C}_0$ represents the original stiffness.

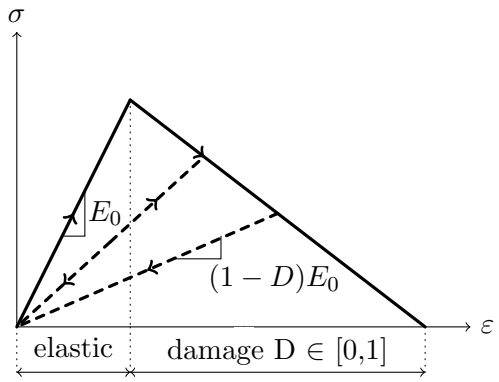

Figure II .9: Illustration of the basic idea of the damage theory in a cyclic occasion.

Depending on the damage describing is isotropic or anisotropic, the damage variable can be a scalar D (for isotropic damage), or a tensor $\bar{\bar{\mathbf{D}}}$ (for anisotropic damage). Referring to isotropic damage, the damage variable D varies from 0 to 1, where 0 represents a virgin state, and 1 represents a fully cracked state. In Fig. II .9 we propose a simple example where the assumption of the damage is elastic for stiffness degradation. It can be seen that the unloading path leads to the initial zero-zero strain-stress point, i.e., the model carries perfect reversible crack closures.

The very first damage model applying to concrete failure was proposed in 1984 (Mazars, 1984). He proposed two separate damage variables D_t and D_c, for pure tension and pure compression case. And the damage variable D for general stress state is obtained by a linear combination described as:

$$D = \alpha_t D_t + \alpha_c D_c. \tag{4.6}$$

The Mazars model constructs independent control for uniaxial tension and compression loadings, and also shows a good approximation for biaxial tests. However, some of the main features of the cyclic loadings are not taken into accounts, such as the unilateral effect and the plastic strain.

Based on the Mazars model, Comi and Perego (2001) proposed a damage model where the two damage variables have their separate activation criteria. And the unilateral effect with bulk stiffness recovery is included in the model thanks to the closure of micro-cracks. Even though still lack of plastic strain and volumetric dilatation, thus not adapted to describe failure behaviors under cyclic loading, the model provides accurate approximations to the biaxial data (Kupfer et al., 1969b).

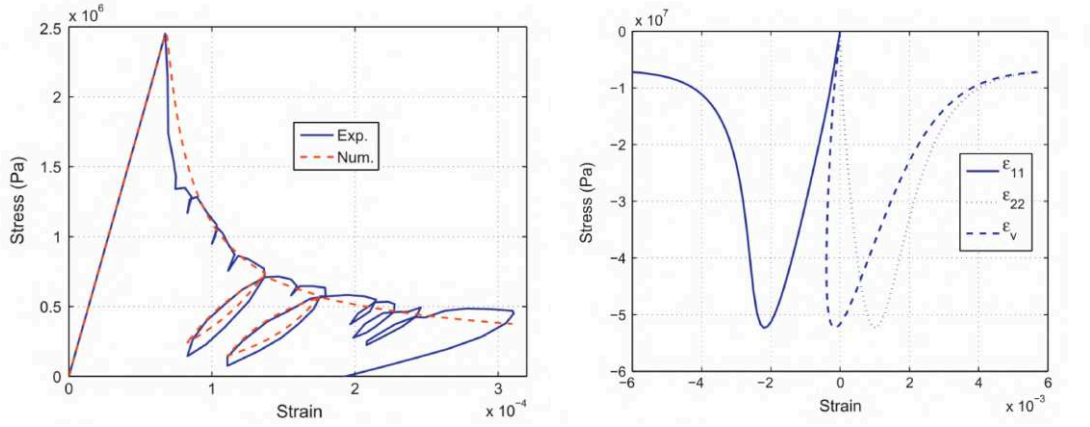

(a) Comparison between numerical and experimental stress-strain relations for tensile loadings

(b) Uniaxial compression test and its multi-axial numerical responses

Figure II .10: Responses of the damage model (Richard and Ragueneau, 2013) in traction and in compression.

Referring to the description of behaviors of the material under cyclic loadings, many recent researches of damage mechanics provide reliable solutions. Several models describe the fatigue behaviors by associating the damage with the number of cycle, which leads to the loss of stiffness and the decreasing of resistance of the material (Ramakrishnan and Malhotra, 1993; T.C. Hsu, 1981; Tepfers and Kutti, 1979). However, they have difficulties when extend to 3D problems and multiaxial problems (Ragueneau, 2007). And some approaches are only concerned in cyclic loadings with increasing amplitude, because the elastic strain does not exceed the previous maximum value. Thus they are not applicable for cyclic loadings with constant or variable amplitude.

Subjected to cyclic loadings, several damage mechanics models have been proposed which based on the thermodynamics with irreversible processes (Alliche, 2004; Ragueneau, 2007), or couple the damage with the friction or the plasticity (Desmorat et al., 2007a). The proposed model of Desmorat et al. (2007b) coupled the internal sliding and friction with the damage, which allows damage growths and structural failures in fatigue loadings. The asymmetric traction/compression behavior and stiffness recovery are addressed by applying micro-defects closure. And the model proposed by Richard and Ragueneau (2013) split the tension/compression behavior into two distinct parts, where the tensile behaviors are generated by isotropic damage, and the compressional behaviors are driven by non-

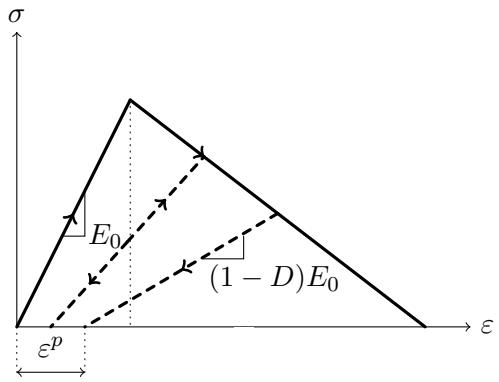

Figure II .11: Illustration of the basic idea of the plastic-damage theory in a cyclic occasion.

associative plasticity mechanism with hardening effect. With the consideration of frictional sliding and closure function, permanent strain, dilatation, and a full and linear unilateral effect are taken into accounts. Complex uniaxial behavior can be obtained, see Fig. II .10.

4.1.3 Plastic-damage theory

It has been discussed in the previous part that plasticity theory and damage theory alone, each of them has its advantages and limitations. The combination of the plasticity theory and the damage theory gave birth to the plastic-damage theory. The stress-strain relationship for a classical plastic-damage theory writes as:

$$\sigma = (1 - D)\ \bar{\sigma} = (1 - D)\mathbb{C}_0(\varepsilon - \varepsilon_p), \tag{4.7}$$

with $\bar{\sigma}$ is the effective stress and σ is the nominal stress.

By considering a linear softening relationship and an elastic-damage assumption for stiffness degradation, a simple example of the plastic-damage theory is depicted in Fig. II .11.

Referring to the damage part, the isotropic damage in more widely used (Bourgeois et al., 2003; Gatuingt and Pijaudier-Cabot, 2002; Krätzig and Pölling, 2004; Salari et al., 2004) since the anisotropic damage itself is complex. The combination with the plasticity makes it rather more difficult to implement (Carol et al., 2001; Chaboche, 1992; Hansen et al., 2001; Krajcinovic, 1985).

The selection of damage criteria is one of the critical issue related to the plastic-damage model. Denoted as the damage variable D, it can be driven by plastic stress/strain (Chow and Wang, 1987; Grassl and Jirásek, 2006; Mazars, 1984; Ortiz, 1985), or based on the release of fracture/damage energy (Lubliner et al., 1989b; Mazars and Lemaitre, 1985; Simo and Ju, 1987). As for the combined plasticity part, two main groups are developed: one of them combines plasticity based on the effective stress $\bar{\sigma}$ (undamaged space) (Grassl and Jirásek, 2006); another group comprises plasticity based on the nominal stress σ (damaged space) (Lubliner et al., 1989b).

A classical plasticity theory has three essential parts: the yield criterion, the flow rule, and the hardening/softening law. The yield criterion, Mohr-Coulomb or Drucker-Prager or other criterion, usually have the form

$$F(\sigma) = c, \text{ or } F(\bar{\sigma}) = c, \tag{4.8}$$

where c denotes the cohesion and/or other associative constant. The main idea of the combination of plasticity and damage theory is to evaluate c through a plastic-damage variable. In the model of Lubliner et al. (1989a), for instance, the isotropic hardening law is represented by the increase of c, it will never decrease until it reaches a critical value. The vanish of the plastic-damage variable describes a strain-softening behavior.

4.1.4 Crack band theory

The crack band theory is firstly proposed by Bazant and Oh (1983). The main idea of the crack band theory is to consider a fracture process zone with its width w_c, the non-linear behaviors of the material are described in this zone, i.e., the crack band. The material remains an elastic behavior outside the band. The two parts of the material are linked with each other through a continuous strain field.

As it is depicted in Fig. II .12(a), an actual crack morphology within a heterogeneous material is rather complex. The cracks tend to pass around the hard aggregates which leads to highly tortuous crack paths. The crack band of width w_c in the model can be considered as a homogenization of the micro heterogeneities and micro-cracks. Hence the researched volume must be much bigger than the size of heterogeneities.

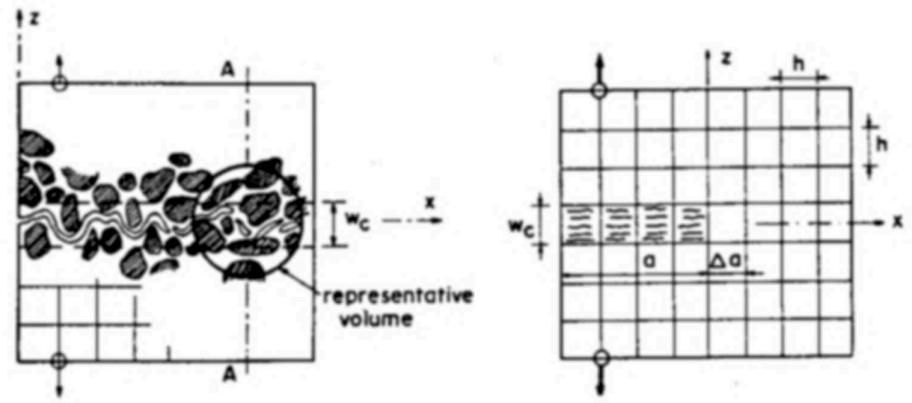

(a) The actual crack morphology (b) The equivalent crack band

Figure II .12: Illustration of the hypothesis of the crack band theory (Bazant and Oh, 1983).

The model of Bazant and Oh (1983) uses three parameters to describe the fracture of the material: the fracture energy, the width of the crack band w_c and the strength limit. And the model is capable of reproducing many features of the materials in different scales. However, the bandwidth dependency of the crack is not yet resolved.

4.1.5 Smeared crack theory

The first smeared crack theory that has been put into literation is the model proposed by Rashid (1968). Similar to the theory of plasticity that have been presented in the previous part, the smeared crack theory also decompose the strain field into two parts, an elastic part, and an inelastic part, which is called the crack strain in this theory,

$$\varepsilon = \varepsilon^e + \varepsilon^c. \tag{4.9}$$

And the stress field is obtained by applying the Hooke's law,

$$\sigma = \mathbb{C}\varepsilon^e. \tag{4.10}$$

The illustration of the decomposition gives in Fig. II .13. Unlike the plasticity theory, that the development of the plasticity relies on yield criteria and flow rule, the crack strain is related directly to the traction transmitted across the crack plane (Jirásek, 2011). A crack will be initiated when the traction attains the strength of the material.

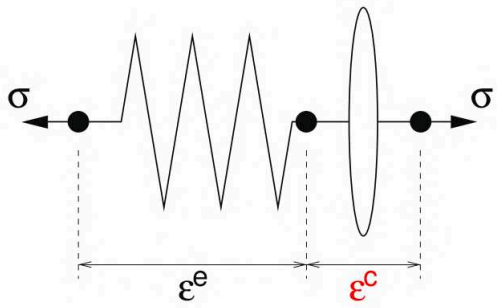

Figure II .13: Representation of the basic idea of the smeared crack theory (Jirásek, 2011).

Initially, the direction of the crack is assumed to be fixed. And the shear stress is formulated using the so-called retention factor (Suidan and Schnobrich, 1973). This assumption leads to drawbacks of stress-locking (Jirasek and Zimmermann, 1998a; Rots et al., 1985), which overestimate the remaining strength after the material comes to failure procedure, and the loss of objectivity upon mesh alignment (Rots et al., 1985). To the above ends, the use of classical smeared crack theory should remain cautious. Herein, a smeared theory with rotation crack direction was proposed by (Jirasek and Zimmermann, 1998a). However, the rotating model suffers from mesh-induced direction bias, which might lead to unstable simulations. These difficulties were finally overcome by (Jirasek and Zimmermann, 1998b). The model applies a standard rotating crack model at the early stage of the loading. Then turns to a damage-type description after the crack opening reaches the critical value.

4.1.6 Phase-field Method

The main idea of phase-field method is that the crack propagates along the energy minimization trajectory. This idea is firstly proposed by Francfort and Marigo (G. A. Francfort and J. J. Marigo, 1998) (it is not called phase-filed then). The classical Griffith's theory provides a criterion for crack propagation, but it has its limitations under these grounds:

1. Crack initiation,
2. Determinations of curvilinear or kinking crack paths, and branching angles,
3. Crack jumps along the crack path.

These limitations are overcome by proposing variational methods based on energy minimization. Thus gave birth to a variational model for brittle fracture evaluations (Bourdin et al., 2008; Buliga, 1998; Dal Maso and Toader, 2002).

After that, a Γ-convergence approximation is proposed in Bourdin et al. (2000), which is a numerical approximation of the variational approach to fracture. This approximation regularizes and diffuses a sharp crack surface into a diffused crack surface which is governed by a scalar auxiliary variable. The variable links the broken and unbroken material, and the equivalent crack surface is associated with the energy. Fig. II .14 illustrates this regularization. In the literature of Miehe et al. (2010a), a thermodynamically consistent phase-field model is proposed. It overcomes many difficulties for non-thermodynamically consistent models that, they are only reliable in particular situations such as monotonous loadings.

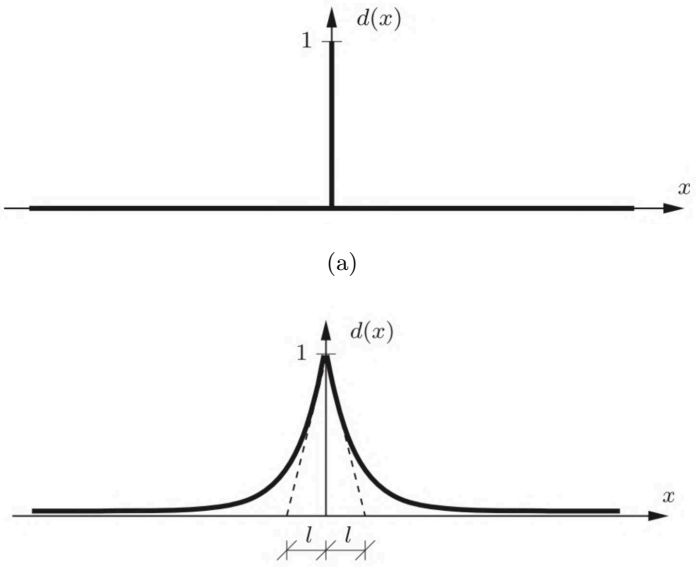

Figure II .14: Sharp and regularized diffuse crack topology in phase-field method with: (a) Sharp crack at $x = 0$, (b) Diffusive crack at $x = 0$ with length scale l (Miehe et al., 2010a).

We show here a numerical example in Fig. II .15. A traction loading is applied to a cube which has a rigid sphere in it. We have a similar numerical example which will be detailed in a later section 8.1.

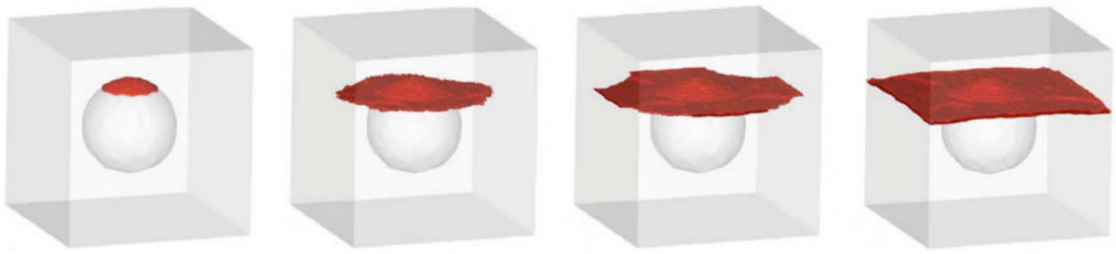

(a) (b) (c) (d)

Figure II .15: Evolution of the crack topology for a tensile test by using a phase-field method; the test is applied to a cube which exhibits a rigid sphere in the center (Miehe et al., 2010b).

There are many advantages of the phase-field method that first, the model doesn't require predefined cracks, and the propagations are also automatic. Second, it's possible to have merging and branching cracks. For instance, in recent researches dealing with dynamic brittle fractures (Borden et al., 2012; Hofacker and Miehe, 2012; Li et al., 2016), some numerical applications show complex crack paths. And finally, it may couple with multi-physics. Some investigations have been put into literature, for example, the coupling of thermo-mechanical (Kuhn and Müller, 2010) and the coupling of hydro-mechanical (Miehe et al., 2015).

However, it also has some limitations:

1. The computational cost is expensive related to mesh size requirement,

2. The location of the crack tip may not reliable.

4.2 Discontinuous approach with explicit cracks

In the previous section, it has been presented with several models that belong to the category of continuous approach. This section follows moves on to consider another group of models, which belong to the category of discontinuous approaches. Unlike the continuum approach, which is based on the hypothesis RVE, the discontinuous approach introduces displacement discontinuities in the displacement field or kinematic enrichment in the model. Both of them allow explicit representations of the cracks.

4.2.1 Linear Elastic Fracture Mechanics (LEFM)

The Linear Elastic Fracture Mechanics (LEFM) is based on the framework of explicit discontinuities, which is firstly proposed by Griffith (1921). It establishes a theory according to which the strength of a quasi-brittle material actually depends on the size of defects and flaws. This method is therefore suitable for simulating materials with defects or micro-cracks. However, it does not describe the initiation and propagation of cracks. And it is only applied correctly if the mathematical discontinuity is fine enough in the fracture zone of the crack tip (Bazant and Planas, 1997).

The Cohesive Zone Model (CZM) is developed based on LEFM. It is firstly proposed by Dugdale (1960) Barenblatt (1962), and then Hillerborg et al. (1976) enriched the model with the use of fracture energy, i.e., the fictitious crack model. Applied to concrete-like materials, this model consists of several traction displacement relationships. Discretization techniques were then developed for cohesive models. Regarding the modeling of cohesive cracks within the finite element framework, two main strategies can be presented from a general point of view (Bazant and Jirásek, 2002). Depending on the occurred position of displacement discontinuity is only between adjacent elements or arbitrary across the finite-element, two categories give as:

1. Discrete inter-element cracks
   In this approach, the displacement discontinuity occurs only between adjacent elements. If the crack path is not known in advance, a remeshing technique is required, and the cracks extend between elements. In the work of Xu and Needleman (1994) and Camacho and Ortiz (1996), a cohesive zone is inserted between the pairs of elements as an inter-element. And if the crack path is known a priori, the mesh can be constructed by tracing the trajectory of the discontinuity. Hence the crack path could coincide with the boundaries (Allix and Ladevèze, 1992; Rots, 1991). This type of approach has been used for modeling quasi-brittle material such as concrete (Carpinteri, 1989) and ductile materials (Gullerud et al., 2000).

2. Discrete intra-element cracks
   In this approach, the displacement discontinuity is incorporated within the finite element at the element level, and the crack could pass through the mesh along an arbitrary trajectory. The model could consist of embedded discontinuities based on the assumed strain method (Armero and Linder, 2009; Belytschko et al., 1988; Dvorkin et al., 1990) , or extended finite element method which belongs to the family

of partition unity method (Moës et al., 1999; Wells, 2001).

The cohesive zone model can be treated using the extended finite element method or embedded finite element method, which could make the model more flexible and robust.

4.2.2 Enriched kinematic based models

It is a common sense that the failure response of the material is always associated with the strain localization. Thus many models based on kinematic enhancement have been developed to capture the strain localization. In this part, two kinds of enhancements are considered:

- The weak discontinuity enhancement, representing a strain discontinuity, is applied to the model explicit heterogeneities in the material (Belytschko et al., 1988; Roubin et al., 2015; Sukumar et al., 2001),
- The strong discontinuity enhancement, representing a displacement discontinuity (Dvorkin and Assanelli, 1991; Simo et al., 1993), is applied to the model for cracks and fractures in the material.

These enhancements have been widely used in different models. For instance, the weak discontinuity enhancement proposes a methodology to model interfaces of material's inclusions without meshing the internal boundaries (no-adapt meshing method) (Roubin et al., 2015; Sukumar et al., 2001). It has been improved by Belytschko et al. (1988), that two weak discontinuities are developed in the element to represent a localization band Fig. II .16.

Referring to the strong discontinuity enhancement, the associated displacement field can be decomposed into two parts, i.e., a continuous field that exists on a coarse scale and has a standard continuum stress-strain relationship, and a discontinuous one that exists on a fine scale across the discontinuity interface. Many fundamental differences between enriched kinematic models are mainly associated with the treatment of the fine-scale kinematics and statics.

In the following literature, we are going to discuss different families of enriched kinematic models according to their: 1. fine-scale enhancement strategies; 2. strong discontinuity approach kinematics (SDA); 3. support for additional displacement models.

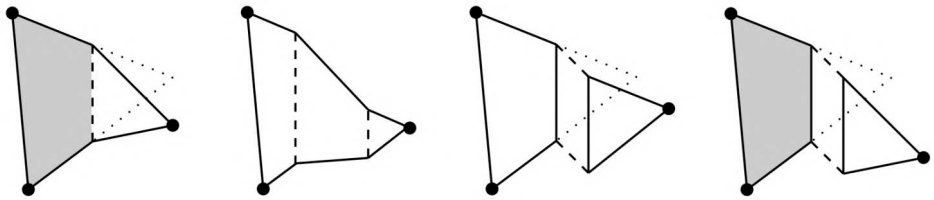

Figure II .16: Element with strong and/or weak discontinuity with: (a) one weak discontinuity, (b) two weak discontinuities, (c) one strong discontinuity, (d) one weak and one strong discontinuity (Roubin et al., 2015).

Enhancement of the standard finite element interpolation

In general, the fracture of quasi-brittle material contains highly localized deformation, and the failure zone is relatively concentrated and converged regarding the size of the material. For this reason, it is suitable to use the enriched kinematic based models, which can embed strong discontinuities in the displacement field. We can decompose the displacement field into two parts: a continuous part at a coarse-scale and a discontinuous part at a fine-scale. Depending on the strategies which deal with fine-scale enhancement, we can separate them into three families: Statically Optimal Symmetric Formulation (SOS), Kinematically Optimal Symmetric Formulation (KOS) and Statically and Kinematically Optimal Non-symmetric Formulation (SKON).

Within the framework of embedded finite element method (EFEM), a comparison between these gropes has been detailed put into the literature (Jirásek, 2000). And the kinematics and statics enhancements employed to both EFEM and extended finite element method (XFEM) have been discussed in (Wu, 2011), in which four groups of enriched finite elements with non-uniform discontinuity modes are investigated.

The three basic types of enhancement at the discontinuity are given as follows.

1. Statically Optimal Symmetric Formulation (SOS)
   This formulation is developed by many authors (Armero and Garikipati, 1996; Belytschko et al., 1988; Larsson et al., 1996; Sluys and Berends, 1998). The primary assumption of this formulation is that we do not introduce any displacement enhancement terms, hence all terms that associated with the displacement enhance-

ment disappear. The interpolation matrix of the enhanced part of the strain field is chosen to satisfy the so-called zero mean condition (patch test), leading to a continuous stress field in the formulation.
Under this assumption, it directly links the bulk stresses and tractions at the discontinuity, which gives a "natural" stress continuity condition. However, it doesn't represent the kinematics of an opening crack. And this may lead to a drawback of spurious stress locking. It is worth noting that this formulation seems like never have been used in XFEM.

2. Kinematically Optimal Symmetric Formulation (KOS)
Dealing with the problem of lacking accurate representations of strong discontinuity kinematics at a fine-scale in SOS enhancement, KOS reproduces one with meaningful description (Lotfi and Shing, 1995). The enhanced strain interpolation matrix is obtained by the symmetrical kinematics operator ∇^s. However, unlike SOS, KOS enhancement has a poor solution to the stress field around the failure surface, especially for a coarse mesh. And this may lead to pathological stress field that the bulk stresses lying outside the discontinuity interface before failure occurs (Wu et al., 2015).

3. Statically and Kinematically Optimal Non-symmetric Formulation (SKON)
The combination of advantages of the two previous approaches gives birth to the SKON enhancement. It takes the optimal static and kinematic equations and provides a better numerical simulation. It was outlined in Dvorkin et al. (1990) Simo and Rifai (1990) and then fully detailed in Oliver (1996a). The actual and the virtual strain field are handled in different assumption, that the prior is under the KOS consideration and the latter satisfies the zero mean condition of SOS enhancement. As a result of this combination, though it losses the symmetric description of the stiffness matrix, the SKON method has "natural" traction continuity across the discontinuity, and a reasonable stress field around the failure surface even for a coarse mesh. The problem of spurious stress locking effect is also fixed. Another benefit of the SKON approach is that it demands no specific characteristic length of the localization (Jirásek, 2000).

The later two enhancement, KOS and SKON, have been used in both EFEM and XFEM. As it is presented in the literature Jirásek (2000) and Wu (2011), the SKON approach is always suggested due to its better element performance in providing robust and reliable results, no matter in the framework of EFEM or XFEM. In the following part

of the redaction, this is also the chosen strategy in our numerical simulations.

Strong discontinuity approach (SDA)

The SDA has been firstly proposed by Simo et al. (1993) and then in Armero and Garikipati (1996), and has been widely organized and developed within the framework of enriched kinematics based models. It is applied to the simulation of the failures behaviors of quasi-brittle materials over last years (Armero and Garikipati, 1996; Oliver, 1996b, 2000; Simo et al., 1993). The three main features of SDA (Kishta, 2016; Oliver et al., 2001) are listed in the followings:

- The use of local continuum constitutive laws which is equipped with strain softening,
- The consideration of strong discontinuity kinematics, i.e., the appearance of displacement jumps in the continuum kinematics,
- The strong discontinuity analysis.

Within the framework of mathematics and mechanics, the main objective of SDA is to develop a compatible relationship between the strong discontinuity kinematics and the continuum constitutive equations. It should respect the following requirements (Roubin, 2013):

- The stress field should remain bounded over the domain Ω_e,
- The continuity of the traction vector across the discontinuity interface should be guaranteed.

In this part, two main groups of the strong discontinuity analysis are discussed:

1. Continuum Strong Discontinuity Approach (CSDA)
   The main idea of this approach is to use a continuum constitutive model (isotropic scalar continuum damage models, plasticity models, etc.) over the finite element. This approach proceeds a constitutive model that returns bounded stresses when the unbounded strain field is introduced. A parameter κ is used to regularize the Dirac's delta function, whose objective is to ensure the interpolation functions smooth enough. This approach has been well detailed in Oliver (1996b) and Oliver et al. (2002).

2. Discrete Strong Discontinuity Approach (DSDA)
   In this approach, a continuum constitutive law is applied over the bulk volume while a

discontinuity behavior is defined only on the internal surface. A discrete constitutive law (so-called the traction-separation law) is proposed to link the traction vector to the crack opening. It has some characteristics, namely:

- different material laws are adopted to the bulk material and the discontinuity,
- a localization criterion is needed to describe the initiation of the strong discontinuity, which could be stress-based (which is used in our work) or energy-based,
- the interface element and the continuum finite element are numerically integrated in the same way, leading to less spurious stress effect than the continuum formulations (Dias-da Costa et al., 2009a).

Under this assumption, Oliver (2000) and Brancherie (2003) present that this approach derives from a continuum constitutive model a discrete constitutive equation, and also a corresponding complete discrete constitutive model. This method has also been developed in Wells (2001), Dias-da Costa et al. (2009a), and Dias-da Costa et al. (2009b) etc..

These two families of approaches, CSDA and DSDA, are usually developed in different research frameworks. Under the consideration of zero dissipation before localization, they are equivalent approaches (Brancherie, 2003). And some authors have tried to link them to each other (Planas et al., 1993). Recently, more strategies have been proposed such as the proportional strong discontinuity approach (PSDA) and generalized discrete strong discontinuity approach (GSDA) (Dias-da Costa et al., 2009a). We are not going to detail them here. The chosen approach used this dissertation is the DSDA.

Supports of additional displacement mode

We have presented in previous parts two ways to classify the enriched kinematic base models into different groups. Another common and important manner to distinguish these models is based on their supports of additional displacement mode, i.e., additional degrees of freedom. Two kinds of supports are discussed here: nodal enrichment (Belytschko et al., 1988; Duarte and Oden, 1996; Moës et al., 1999) which is based on the local or global Partition of Unity Methode (PUM) (Babuška and Melenk, 1997; Melenk and Babuška, 1996), and element-based enrichment (Armero and Garikipati, 1996; Needleman and Xu, 1994; Oliver, 1996a; Ortiz et al., 1987; Simo et al., 1993) which is based on the concept of Assumed Enhanced Strain (AES) (Simo and Rifai, 1990).

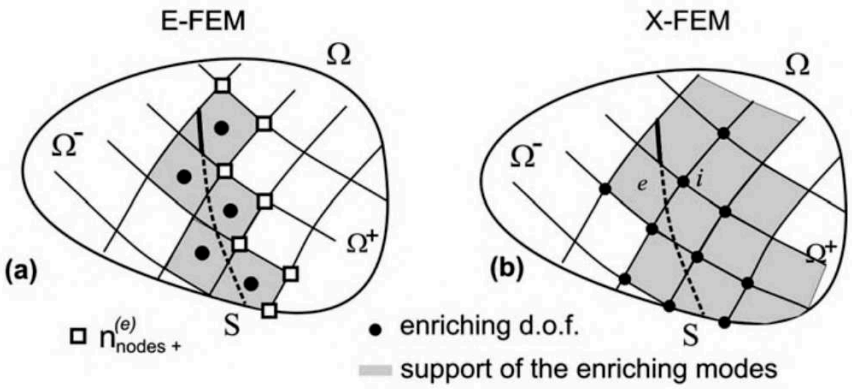

Figure II .17: Representation of a element-based enrichment (left) and a nodal enrichment (right) (Oliver et al., 2006).

The most extensively used methods within the nodal and element enrichment methods are the Extended Finite Element Method(XFEM) and the Embedded Finite Element Method (EFEM). Just for notice that this kind of classification is parallel and separate from the previously introduced distinguish ways. There are different models, EFEM or XFEM, that could have SOS/KOS/SKON enhancements and CSDA/DSDA approaches.

As it is depicted in Fig. II .17, the additional degree of freedom is attached on the node for XFEM and inside the element for EFEM. The consequence of this difference is that EFEM has fixed global unknowns no matter how many cracks begin to initiate in the solid, while XFEM has an increasing global unknowns. This effect could be negligible for a small number of enhanced elements (such as at the beginning of the material's failure). However, it may lead to severe consequence afterward.

1. Embedded Finite Element Method (EFEM)

   The embedded finite element method (EFEM) allows an explicit discontinuity pass across the finite element with an arbitrary trajectory. This basic idea was firstly inspired by Ortiz (1985) and Needleman and Xu (1994), which enriched the standard finite element by introducing one weak discontinuity (see Fig. II .16(a)). Then Belytschko et al. (1988) proposed a model that could embed two weak discontinuities which forms a softening band. Soon the models with strong discontinuities were proposed (Dvorkin et al., 1990; Simo et al., 1993).

Unlike diffused cracking descriptions, which "smears" the effect of crack over the whole finite element and represents this effect by an equivalent inelastic strain, EFEM separates the displacement field into a continuous part and a discontinuous part. The discontinuous part, which is an additional degree of freedom and also an additional unknown, can be solved at the element level. This characteristic of EFEM brings an advantage that the global equilibrium equations can be solved in terms of the standard nodal displacement.

As it has been presented in the previous part, the stress field always remains bounded over the finite element Ω_e within the framework of EFEM. A suitable traction-separation law governs the constitutive behavior across the discontinuity surface. This allows the traction transmits across the crack and links to the crack opening value, which provides a quite nature physical consideration. In a computational modeling process, the displacement jump is a static variable. Thus the traction and the stress field are constant in each element. Therefore, the nodal forces can be evaluated from the standard form within the framework of the finite element method. It worth reminding that the global nodal displacements have a constant size too. This provides a significant convenience that the required memory for calculation remains constant.

2. Extended Finite Element Method (XFEM)

Unlike EFEM which condensate the additional degree of freedom at the finite element level, XFEM is a kind of model which considers the displacement discontinuity as global unknowns. Similar to nodal displacement, the displacement discontinuities give additional degrees of freedom to each node. This idea is realized with the help of Partition of Unity Method (PUM). Actually, XFEM can be considered as a particular case of PUM. The main feature of the PUM is that it offers a feasible approach to include a priori knowledge about the problem being solved in the finite element space. This knowledge may come from analytical solutions or simplify assumptions.

The XFEM overcomes some difficulties and limitations that EFEM meets that first, the stiffness matrix of finite element is non-symmetric due to the applying of SKON,

XFEM could have symmetric stiffness matrix. And second, the EFEM enrichment is non-conforming, and the strain field is compatible in a weak sense. XFEM has conforming displacement. The displacement field of XFEM is only discontinuous at the crack, and continuous everywhere else.

In numerous researches about finite element enrichments that have been put into literature, the models' names are sometimes different and confusing. The XFEM that we present here is named General Finite Element Method (GFEM) in some researches. There have been investigations (Borja, 2008; Dias-Da-Costa et al., 2010; Jirasek and Zimmermann, 1998a; Oliver et al., 2006) that offer a comparison between these techniques and their common features within a unified framework.

5 Conclusion

In many engineering applications, it is necessary to predict the failure of the material and understand the failure process inside the materials. To this purpose, numerical modeling is an indispensable tool to provide reliable analysis about the behaviors of the materials. In this work, our attention is focused on the quasi-brittle materials, in particular, the concrete. Nowadays, we can say that it is one of the most widely used artificial material in civil engineerings. Numerous characters of the concrete have been observed in engineering applications or experiments: the softening behavior, the progressive loss of stiffness, the asymmetric traction/compression response, the contraction and dilatation of volume, the hysteresis behaviors under cyclic loadings, and ductile behaviors in triaxial loadings, etc..

In the scope of numerical modeling of brittle or quasi-brittle materials, we have presented an overview of several methods in this chapter. Considering the advantages and limitations among these methods, the choice is made here to use EFEM to reproduce these observed failure behaviors. Compared to other methods, we chose EFEM under these considerations:

1. EFEM permits complicate crack patterns that the crack path is explicit and traces an arbitrary trajectory, free to have multi-cracks which may branch and conjoint.

2. Under the choosing scale of mesoscopic, concrete is a highly heterogeneous material. EFEM allows explicit representations of heterogeneities through kinematic enrichment without requiring an adapted-meshing strategy.

3. The computational cost is relatively fewer. Since the global equilibrium equations remain a constant size, the needed memory for the global system won't increase, even for a high ratio of cracking elements to total elements in the mesh. This brings significant conveniences during numerical simulation, especially when the mesh is 3D, and the model contains complex crack paths and heterogeneities.

4. Emergent phenomena are observed with a high number of finite elements. Employing simple and meaningful criteria at local scale, complex behaviors can be obtained in the macroscopic scale. For instance, the asymmetric traction/compression response, this behavior is an emergence from the structural effect.

Chapter III

EFEM simulation of concrete fatigue, use of mode-I strong discontinuity

Contents

1 Introduction

The growth and propagation of micro-cracks is a leading cause of fatigue and damage for brittle/quasi-brittle materials, such as shale, concrete-like materials, and rocks. At present, the computational failure mechanics is a study of significant value, for example, the underground storage of radioactive wastes. How to predict and quantify the structure for its durability is one of the major challenges facing such a site. Besides, the mineral exploration from oil shale, the development of fractures is significant to petrol or gas production. At the mesoscopic scale, one of the characteristics of the materials referred to above is that they are very heterogeneous materials. As for concrete, aggregates are embedded in the mortar matrix. As for argillite, it may contain varies inclusions depending on its resources, such as quartz, silicalite, and clay minerals. These heterogeneities can cause localization and initiation of cracks. Another characteristic of these kinds of materials is that they show complex mechanical behaviors, some of which are observed in loading-unloading charges, such as the hysteresis loops, the unilateral effect, the stiffness recovery, etc.. There are a number of potential reasons for these phenomena. Among these explanations, an important one is related to the closure of cracks.

Over the most recent decades, plenty of numerical models have been proposed and well documented to describe the fatigue behaviors of the quasi-brittle material. As it is conducted in the first chapter, there is a set of solutions that are proposed as the macroscopic

models. Among numerous studies, several models have achieved the fatigue behaviors of materials by applying damage models along or coupled with friction sliding and plasticity. In the previous case, the damage model involves two internal damage variables (Mazars and Pijaudier-Cabot, 1989; Pijaudier-Cabot and Bazant, 1987; Wu et al., 2006) (namely d^t and d^c, corresponding to traction and compression). Depending on the specific status, loading or unloading, the crack closure or micro-cracks closure reopening (MCR) effects can be achieved by activating/deactivating (partially) the corresponding damage parameters. In the latter case, the damage evolutions are coupled with internal sliding (Desmorat et al., 2007b) or plasticity mechanism with the hardening effect (Richard and Ragueneau, 2013).

The method used in this dissertation is based on the strong discontinuity approach, namely the Embedded Finite Element Method (EFEM) (Ortiz et al., 1987; Simo et al., 1993). EFEM is an element-based enhancement model, with additional degree of freedom attached inside the element as internal variables. It is capable of yielding the mesh dependence without adding special artificial numerical parameters. As the energy is dissipated over a two-dimension discontinuity interface, by applying a specific kinematic enhancement to the element, the total dissipated energy becomes independent of the mesh size (Simo et al., 1993). Besides, as the additional interval variable is an element-based enhancement, the increasing number of cracked elements will not affect the size of the assembled stiffness matrix for the total system. Therefore, the model is capable of simulating a system with a large number of elements that carry strong discontinuities. The ratio of the fractured elements to the total elements can be very high. Another benefit of Embedded Finite Element method is that the strong discontinuities can pass through the element in an arbitrary trajectory. Therefore, it is capable of performing simulation of complex and accurate cracks, such as cracks with several branches, cracks stopped by heterogeneities, and a crack that meets another crack.

Moreover, individual to strong discontinuity, the weak discontinuity (Ortiz et al., 1987) can be alternatively included in the model to represent heterogeneities, even for complex geometry (Roubin, 2013). Due to the non-adapted meshing method, the heterogeneities can be taken into consideration in an explicit way (Moës et al., 2003). The main idea is that the original mesh will homogeneously place nodes in the field, and will be independent of the morphology of the material, i.e., independent from the interface of the heterogeneities. Therefore, there will be a set of elements split into two sub-domains by the interface of heterogeneity. The orientation of the interface will be noted in the element

as normal vectors, and the volumes next to the interface are also taken into consideration, carrying corresponding parameters of materials. One benefit of the weak discontinuity is that the complexity and number of the heterogeneities will not affect the size of the assembled stiffness matrix for the total system either.

The study performed in this chapter is closely related to the previous work undertaken by (Roubin, 2013). In this work, only the strong discontinuity of the type mode-I (traction separation openings) was applied to the model, with complex behaviors of the material observed. For example, the non-symmetric responses in simple traction and compression, the progressive loss of stiffness and plasticity in compressional cyclic loadings. However, to the author's knowledge, the behavior performed by crack closure in Embedded Finite Element has yet to be taken into consideration. Therefore, based on the prior studies, the objective of this chapter is to apply a closure mechanism to the model.

Regarding the fatigue behaviors of quasi-brittle materials, such as the hysteresis loops, there are many possible explanations for the cause of this phenomenon, such as the additional dissipated energies, the irreversible crushed pores, the friction between the cracks, etc. In this chapter, the effect of the pores is excluded from consideration. And physically, the friction between cracks can not be modeled by the traction-separation opening, i.e., mode-I strong discontinuity. Thus, in this chapter, we expect to confirm if fatigue behaviors can be observed if only supplementary dissipated energies are concerned.

This chapter consists of three parts. In the first part of this chapter, we give the mathematical representation of the two kinds of discontinuities and their governing equations under the framework of the Finite Element Method. Then, a few representative examples are presented in the second part to demonstrate the performance of the model. The model is tested first with a simple morphology model, and then with a more complex morphological model. Finally, a comparison between the numerical simulation and the experimental one is performed. The experimental results are given by Piotrowska (2013).

2 Kinematics of discontinuity in solids

Let us consider the reference domain $\Omega \subset \mathbb{R}^{n_{dim}}$ of a solid exhibiting heterogeneities and cracks, see Fig. III .1. It is surrounded by a closed boundary $\Gamma \subset \mathbb{R}^{n_{dim}-1}$, which can

be divided into two disjointed boundaries: the displacement boundary Γ_u and the traction boundary Γ_t, which satisfy the following two conditions: $\Gamma_u \cup \Gamma_t = \Gamma$, and $\Gamma_u \cap \Gamma_t = \varnothing$.

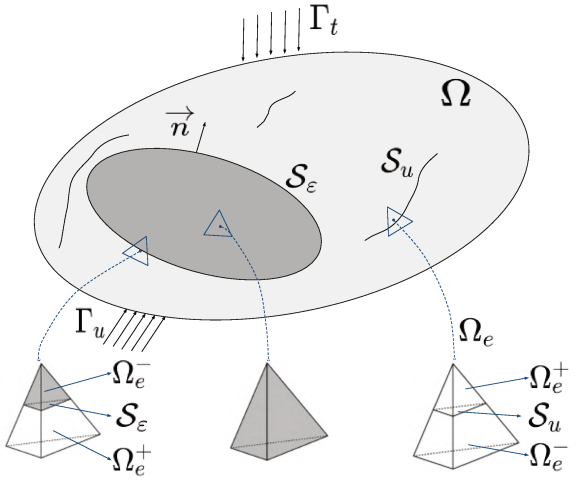

Figure III .1: Reference body exhibiting heterogeneities and cracks and their corresponding enhanced elements.

At the inner of the dealing body, the solid brings two kinds of discontinuities: the weak discontinuity representing the heterogeneity interface, and the strong discontinuity representing the displacement discontinuities in the material, such as fractures, cracks, and slip lines.

Considering the framework of Finite Element Method, the domain can be discretized by a set of elements Ω_e, with $\Omega = \cup_{e=1}^{n_e} \Omega_e$. Since the material is heterogeneous and the mesh method is non-adapted, there will be a set of elements crossed by the interface of heterogeneity $\mathcal{S}_\varepsilon$, dividing the elements into two parts Ω_e^+ and Ω_e^- with a unit vector $\boldsymbol{n}$ pointing from Ω_e^- to Ω^+. We group these element into a set $\mathscr{E}_\varepsilon$.

Another set of elements are divided into two parts by the failure path $\mathcal{S}_u$. Naturally, the discontinuity surface $\mathcal{S}_\varepsilon$ is defined by the geometry of material, whereas the discontinuity surface $\mathcal{S}_u$ cannot be determined prior; its path and orientation usually depend on particular criteria. We group these elements into a set $\mathscr{E}_u$. It's not difficult to see that the size of $\mathscr{E}_u$ will grow bigger while the failures develop, whereas the size of $\mathscr{E}_\varepsilon$ will remain the same since it depends on the geometry of solid.

It is assumed that an element has one single discontinuity surface splitting the element

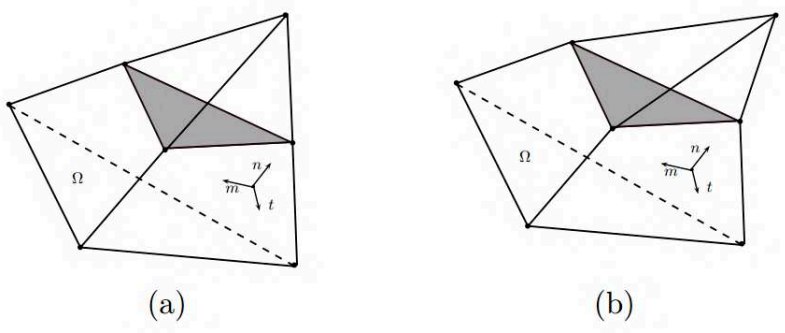

Figure III .2: Representation of the strain discontinuity in a tetrahedral element. (Vallade, 2016)

into two parts. Hence, we consider that the kinematics failure will take place in the heterogeneity interface if the element is "close" enough to the heterogeneity. Upon this consideration, there will be a set of intersection $\mathscr{E} = \mathscr{E}_\varepsilon \cap \mathscr{E}_u$, representing elements who carry two kinds of discontinuities. Furthermore, it is assumed that the bulk part has a purely elastic kinematics relationship, and the kinematic behavior of the strong/weak discontinuity are independent. Hence, the strain field admits an additive form

$$\boldsymbol{\varepsilon}(\boldsymbol{x}) := \nabla^{\mathrm{sym}}\overline{\boldsymbol{u}}(\boldsymbol{x}) + \tilde{\boldsymbol{\varepsilon}}(\boldsymbol{x}) + \hat{\boldsymbol{\varepsilon}}(\boldsymbol{x}), \tag{2.1}$$

where $\nabla^{\mathrm{sym}} := \frac{1}{2}[\nabla(\bullet) + \nabla^T(\bullet)]$ denotes the symmetric gradient operator. Notation $\tilde{\bullet}$ / $\hat{\bullet}$ represents the weak / strong discontinuity.

2.1 Kinematics and governing equations of weak discontinuity

In this section, the attention is focused on the elements which are divided into two parts by the heterogeneity interface. They carry different elastic parameters: Young's Modules and Poisson's ratios. A strain discontinuity is emerged from this difference, as it shows in Figure III .2. The upper part of the element has a weaker Young's module than the lower part; thus, the upper part carries a higher strain deformation. There is a jump of strain field between the two sub-domains. As it represents in the figure, $\boldsymbol{n}$ is the direction vector of the discontinuity interface, pointing from Ω_e^- to Ω_e^+. An orthonormal basis $(\boldsymbol{n}, \boldsymbol{m}, \boldsymbol{t})$ attached to the interface is constructed. In order to respect the continuity of displacement field, we have:

$$\boldsymbol{u}^+(\boldsymbol{x}) = \boldsymbol{u}^-(\boldsymbol{x}), \forall \boldsymbol{x} \in \mathcal{S}_\varepsilon, \tag{2.2}$$

The strain jump of the weak discontinuity $[|\boldsymbol{\varepsilon}|] := \varepsilon^+(\boldsymbol{x}) - \varepsilon^-(\boldsymbol{x})$ can be calculated by the symmetrical gradient of the corresponding displacement field

$$\nabla^{\mathrm{sym}}\boldsymbol{u}|_{\mathcal{S}_\varepsilon} = \frac{1}{2}(\nabla\boldsymbol{u} + \nabla^T\boldsymbol{u})|_{\mathcal{S}_\varepsilon} \text{ with } \nabla\boldsymbol{u} = \begin{pmatrix} \partial u_{1,n} & \partial u_{1,m} & \partial u_{1,t} \\ \partial u_{2,n} & \partial u_{2,m} & \partial u_{2,t} \\ \partial u_{3,n} & \partial u_{3,m} & \partial u_{3,t} \end{pmatrix}_{(\boldsymbol{n},\boldsymbol{m},\boldsymbol{t})} \tag{2.3}$$

Physically, the derivative of the displacement field has a discontinuity along the direction perpendicular to the interface surface but no discontinuity in the direction along the interface. Accordingly, $\nabla(\tilde{\boldsymbol{u}}^+)\cdot\boldsymbol{m} = \nabla(\tilde{\boldsymbol{u}}^-)\cdot\boldsymbol{m}$ and $\nabla(\tilde{\boldsymbol{u}}^+)\cdot\boldsymbol{t} = \nabla(\tilde{\boldsymbol{u}}^-)\cdot\boldsymbol{t}$. Bring into Eq. (2.3), the last two colons of the matrix $\nabla\boldsymbol{u}$ have the same value at Ω^+ and Ω^-. Hence, the jump in the strain field can be defined entirely by three unknown values: $[|\boldsymbol{\varepsilon}|] = \{[\varepsilon]_n[\varepsilon]_m[\varepsilon]_m\}^T$ (Roubin et al., 2015). We can take the displacement field $\tilde{\boldsymbol{u}}$ in a first order form (Ibrahimbegovic et al., 2005):

$$\tilde{\boldsymbol{u}}(\boldsymbol{x}) = \Theta\boldsymbol{n}\cdot(\boldsymbol{x}-\boldsymbol{\xi})([\varepsilon]_n\boldsymbol{n} + [\varepsilon]_m\boldsymbol{m} + [\varepsilon]_t\boldsymbol{t}) \text{ with } \Theta = \begin{cases} \Theta^+ & \forall x \in \Omega_e^+ \\ \Theta^- & \forall x \in \Omega_e^- \end{cases} \tag{2.4}$$

where $\boldsymbol{\xi}$ represents the position of interface surface $\mathcal{S}_\varepsilon$ and $\boldsymbol{n}\cdot(\boldsymbol{x}-\boldsymbol{\xi})$ can be seen as a signed distance to the discontinuity surface. Θ is a still undefined function of Ω_e, the explicit expression will be given latter with the help of variational formulations. We can obtain the weak shape of the enhanced strain field by taking the symmetrical gradient of $\tilde{u}$ (Benkemoun et al., 2015):

$$\tilde{\boldsymbol{\varepsilon}} = \nabla^{\mathrm{sym}}(\tilde{\boldsymbol{u}}) = \Theta([\varepsilon]_n\boldsymbol{n}\otimes\boldsymbol{n} + \frac{[\varepsilon]_m}{2}(\boldsymbol{n}\otimes\boldsymbol{m})^{\mathrm{sym}} + \frac{[\varepsilon]_t}{2}(\boldsymbol{n}\otimes\boldsymbol{t})^{\mathrm{sym}}) \tag{2.5}$$

In a more straightforward way, we can write the equation (2.5) into another form (Wells, 2001) as:

$$\tilde{\boldsymbol{\varepsilon}} = \zeta(\boldsymbol{s}\otimes\boldsymbol{n})^{\mathrm{sym}}, \tag{2.6}$$

where ζ is the magnitude of the strain jump, and $\boldsymbol{s}$ represent the orientation of the jump, which can be decomposed into three direction $\boldsymbol{s} = a\boldsymbol{n} + b\boldsymbol{m} + c\boldsymbol{t}$. Hence, Eq. (2.6) can be written into the following formula:

$$\tilde{\boldsymbol{\varepsilon}} = \zeta a(\boldsymbol{n}\otimes\boldsymbol{n})^{\mathrm{sym}} + \zeta b(\boldsymbol{n}\otimes\boldsymbol{m})^{\mathrm{sym}} + \zeta c(\boldsymbol{n}\otimes\boldsymbol{t})^{\mathrm{sym}}. \tag{2.7}$$

Naturally, if the orientation $\boldsymbol{s}$ is parallel to the normal vector $\boldsymbol{n}$, $[\varepsilon]_n$ will be the only variable non null, representing the direction of strain jump is perpendicular to the weak

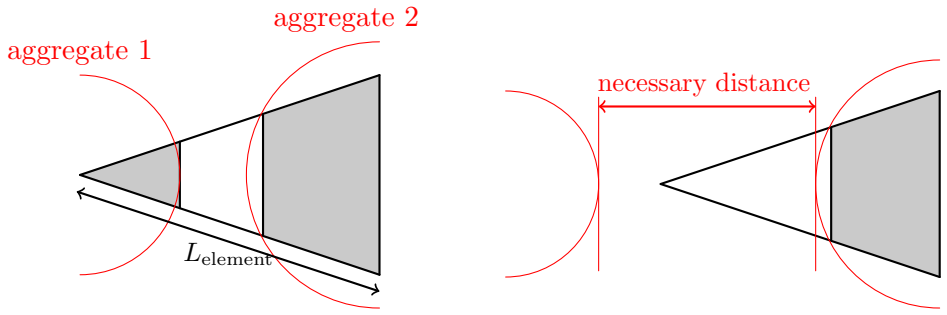

(a) In case of a triangle element cut by two heterogeneity

(b) In case of a triangle element cut by one heterogeneity

Figure III .3: Representation of the necessary distance between aggregates to ensure single discontinuity interface in an element.

discontinuity interface; and if $\boldsymbol{s}$ is perpendicular to $\boldsymbol{n}$ ($a = 0$), $[\varepsilon]_n$ will equal to zero, representing the direction of strain jump is parallel to the weak discontinuity interface.

In this dissertation, the choice is made to have only one weak discontinuity developed in one finite element. Hence, a necessary distance between two heterogeneity has to be ensured, or the size of the element should be limited. Normally the minimal distance between two inclusions in the excursion field should be superior to the maximal size of the element. For example, in the figure III .3(a), the tetrahedral element is cut by two heterogeneity; as a consequence, the morphological model can't be represented correctly. Hence, if the heterogeneous structure of the material carries narrow distances between aggregates or complex curvature of the interface, thinner finite element mesh is required to capture more geometric details.

2.2 Kinematics and governing equations of strong discontinuity

In this section, we are going to explain the strong discontinuity, which is independent of the weak discontinuity. On the subject of the weak discontinuity, the interface is decided by the heterogeneity interface which is purely geometrical, whereas the interface of a strong discontinuity representing a crack or a slip line, is determined by particular criteria.

Let us consider an element Ω_e exhibits a strong discontinuity dividing itself into two sub-domains Ω_e^+ and Ω_e^- with the discontinuity surface $\mathcal{S}_u$. The discontinuity of the displacement field can be expressed with Heaviside function $\mathcal{H}_{\mathcal{S}_u}$, which centered at $\mathcal{S}_u$.

The displacement field can be written as

$$\boldsymbol{u} = \bar{\boldsymbol{u}} + \mathcal{H}_{\mathcal{S}_u}[|\boldsymbol{u}|], \tag{2.8}$$

with $\bar{\boldsymbol{u}}$ is the regular part of the displacement field, and $[|\boldsymbol{u}|]$ is a continuous function representing the displacement jump. For the sake of simplicity, $[|\boldsymbol{u}|]$ is considered as a unity function over the finite element. As we can see in Fig. III .4, the boundary condition cannot be done on just one of the filed $\bar{\boldsymbol{u}}$ or $[|\boldsymbol{u}|]$ (Oliver, 1996a), which might lead to ill formulation problem (Roubin, 2013). In order to overcome this difficulty, an arbitrary function φ_e is introduced. It is a continuous function and should respect the following conditions

$$\begin{cases} \varphi_e = 0, \text{ for all nodes in } \Omega_e^-, \\ \varphi_e = 0, \text{ for all nodes in } \Omega_e^+. \end{cases} \tag{2.9}$$

Hence, an arbitrary displacement function $\hat{\boldsymbol{u}}$ writes as

$$\hat{\boldsymbol{u}} = \bar{\boldsymbol{u}} + \varphi_e[|\boldsymbol{u}|]. \tag{2.10}$$

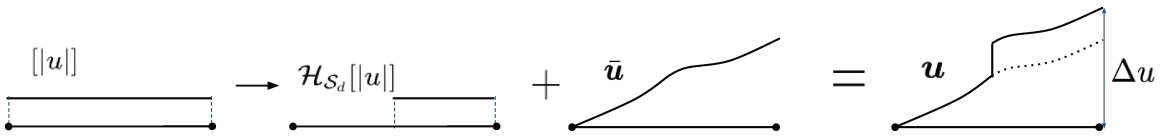

Figure III .4: An one-dimension decomposition of the displacement field satisfying the boundary condition $\Delta\boldsymbol{u}$.

It is worth noting that the function φ_e is arbitrary with the only requirement of satisfying the conditions in Eq. (2.9). In our case, it is chosen as a linear function. Thus the arbitrary displacement function $\hat{\boldsymbol{u}}$ can also be expressed as shown in Fig. III .5.

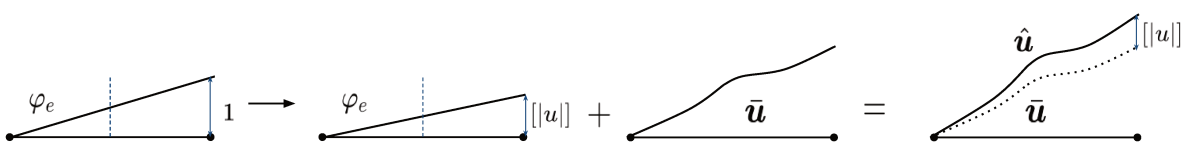

Figure III .5: An one-dimension decomposition of the arbitrary displacement function.

Incorporation the two equations, Eq. (2.8) and Eq. (2.10), the theoretical displacement field can be expressed as

$$\boldsymbol{u} = \hat{\boldsymbol{u}} + (\mathcal{H}_{\mathcal{S}_u} - \varphi_e)[|\boldsymbol{u}|]. \tag{2.11}$$

The displacement field defined by Eq. (2.8) and Eq. (2.11) are completely equivalent. Considering a one-dimension example, the displacement field can be expressed in Fig. III .6.

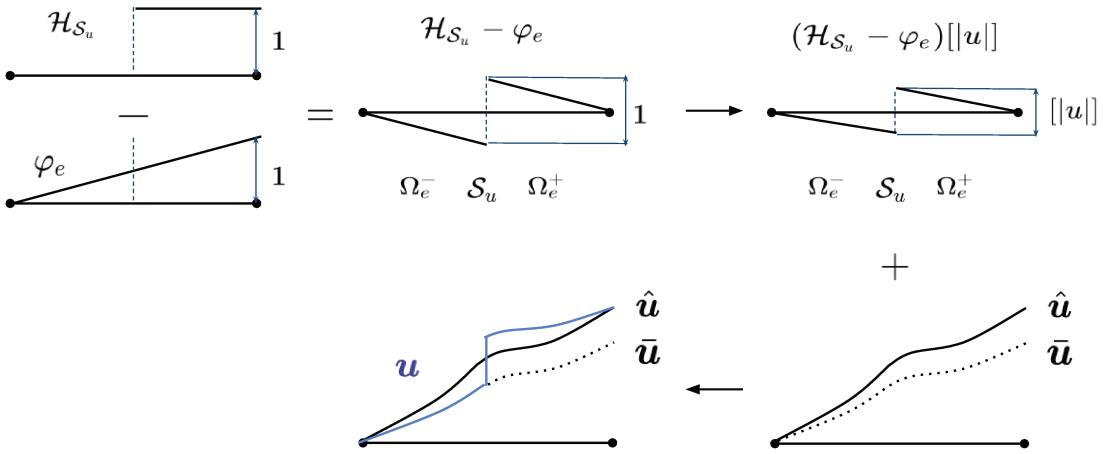

Figure III .6: An one-dimension decomposition of the displacement field.

The corresponding strain field can be obtained by taking the symmetric gradient of the displacement field shown as Eq (2.11). It admits an additive form too:

$$\boldsymbol{\varepsilon} = \nabla^{\mathrm{sym}}\boldsymbol{u} = \underbrace{\nabla^{\mathrm{sym}}\hat{\boldsymbol{u}}}_{\text{regular}} + \underbrace{(\mathcal{H}_{\mathcal{S}_u} - \varphi_e)\nabla^{\mathrm{sym}}([|\boldsymbol{u}|]) - ([|\boldsymbol{u}|] \otimes \nabla\varphi_e)^{\mathrm{sym}}}_{\text{bounded enhancement}} + \underbrace{\delta_{\Gamma_d}([|\boldsymbol{u}|] \otimes n)}_{\text{unbounded enhancement}} \quad . \tag{2.12}$$

We can use the standard stress-strain constitutive equation for the regular displacement field. The unbounded character $\hat{\varepsilon}_u$ carries the Dirac-delta distribution δ, which emerges from the gradient of the Heaviside function. It is a discontinuous function which is centered at the discontinuity interface $\mathcal{S}_u$ (infinite value at the interface and null value otherwise).

The bounded enhancement, note as $\hat{\varepsilon}_b$, can be simplified by assuming $[|\boldsymbol{u}|]$ as a constant function, referred as Kinematically Enhanced Strain (KES). It leads to a null value of $(\mathcal{H}_{\Gamma_d} - \varphi_e)\nabla^{\mathrm{sym}}([|u|])$, and Eq. (2.12) can be wrote as

$$\hat{\boldsymbol{\varepsilon}} = \hat{\boldsymbol{\varepsilon}}_b + \hat{\boldsymbol{\varepsilon}}_u = -([|\boldsymbol{u}|] \otimes \nabla\varphi_e)^{\mathrm{sym}} + \delta_{\mathcal{S}}([|\boldsymbol{u}|] \otimes \boldsymbol{n}) \tag{2.13}$$

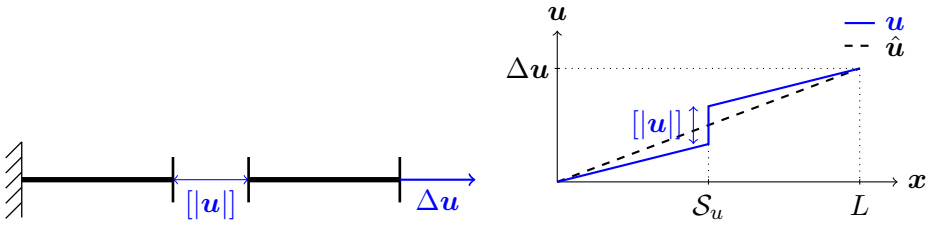

(a) One-dimension bar exhibiting strong discontinuity

(b) The displacement field

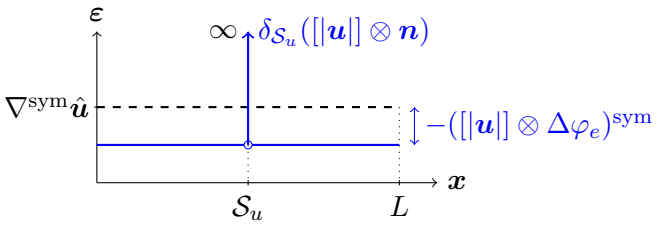

(c) The strain field

Figure III .7: One-dimension representation of the decomposition of the displacement field

Let us consider a one-dimension example. Supposing as a homogeneous bar exhibiting a strong discontinuity with the jump of displacement $[|\boldsymbol{u}|]$, length of the bar is L and a displacement $\Delta\boldsymbol{u}$ is imposed in its right extreme. As shown in Eq. (2.11), the displacement field consists of a regular part $\hat{\boldsymbol{u}}$ and an enhancement part $(\mathcal{H}_{\mathcal{S}_u} - \varphi_e)([|\boldsymbol{u}|])$. The displacement field can be expressed in Fig. III .7(b). The one-dimension bar is homogeneous, and the regular displacement field (black dashed line) is linear. The displacement jump $[|\boldsymbol{u}|]$ is centered at the discontinuity interface $\mathcal{S}_u$ with additive enhanced displacement. Considering the strain field, an unbounded enhancement is centered at the interface with its value equals to infinity, thus "unbounded", which is represented by the Dirac-delta distribution δ. Moreover, in this case, the regular displacement field $\hat{\boldsymbol{u}}$ is more "steep" than the displacement field outside the discontinuity. As consequence, this difference can be expressed in the strain field as the bounded enhancement $-([|\boldsymbol{u}|]\otimes\Delta\varphi_e)^{sym}$, see Fig. III .7(c).

Unlike the strain enhancement, it should be noticed that the stress field is always bounded among the elements $\forall\boldsymbol{x} \in \Omega$. Beyond the discontinuity, the bulk $\Omega\backslash\mathcal{S}$ remains an elastic behavior, which can be describes by Hooke's law

$$\boldsymbol{\sigma} = \mathbf{C} : \boldsymbol{\varepsilon}, \tag{2.14}$$

with matrix $\boldsymbol{C}$ denote

$$\mathbf{C} = \frac{E}{1+\nu}\begin{bmatrix} \frac{1-\nu}{1-2\nu} & \frac{\nu}{1-2\nu} & \frac{\nu}{1-2\nu} & 0 & 0 & 0 \\ \frac{\nu}{1-2\nu} & \frac{1-\nu}{1-2\nu} & \frac{\nu}{1-2\nu} & 0 & 0 & 0 \\ \frac{\nu}{1-2\nu} & \frac{\nu}{1-2\nu} & \frac{1-\nu}{1-2\nu} & 0 & 0 & 0 \\ 0 & 0 & 0 & \frac{1}{2} & 0 & 0 \\ 0 & 0 & 0 & 0 & \frac{1}{2} & 0 \\ 0 & 0 & 0 & 0 & 0 & \frac{1}{2} \end{bmatrix} \tag{2.15}$$

In the case of a weak discontinuity, the two sub-domains are isotropic, the operator $\boldsymbol{C}^{+|-}$ is calculated in terms of the Young's modulus $E^{+|-}$ and Porcine ration $\nu^{+|-}$.

In the case of exhibiting a weak discontinuity, a strong discontinuity, or both of them, we can obtain the stress field $\boldsymbol{\sigma}_{\mathcal{S}}^{+|-}(\boldsymbol{x}), \forall \boldsymbol{x} \in \Omega^{+|-} \cap \mathcal{S}$ representing the stress "in this side of" and "in another side of" the discontinuity interface $\mathcal{S}$. However, the stress field should always satisfy the traction continuity condition, i.e.,

$$\boldsymbol{\sigma}^{+}(\boldsymbol{x}) \cdot \boldsymbol{n} = \boldsymbol{\sigma}^{-}(\boldsymbol{x}) \cdot \boldsymbol{n} = \boldsymbol{T}, \ \forall \boldsymbol{x} \in \mathcal{S}, \tag{2.16}$$

where the vector $\boldsymbol{T}$ represents the traction vector transfer across the interface and links the two sub-domains, it should be continuous itself along with the analysis. In the following section, we are going to introduce a discrete model at the discontinuity defining the local mechanism through traction vector $\boldsymbol{T}$ with an additional internal variable $[|\boldsymbol{u}|]$.

3 Admissible discontinuity model with closure of cracks at fine-scale

In this section, the attention is focused on the strong discontinuity. As mentioned in the previous part, the element is divided into two sub-domains by the discontinuity surface $\mathcal{S}$. Supposing that the interface is flat and has a single constant normal vector pointing from Ω^{-} to Ω^{+}, a traction vector $\boldsymbol{T}$ is proposed linking the stress field at the discontinuity surface. In existing EFEMs, many enriched discontinuity modes have been proposed to describe variable behaviors. For example the traction fracture (Roubin et al.,

2015), the shear fracture (Hauseux, 2015), or coupling with hydraulic problem (Vallade, 2016), etc., the used criteria usually contain a localization law, traction or shear, defining the localization of the cracks and their orientations; and the separation law, providing the material a cohesive behavior after failure emerges. Based on these previous works, an admissible discontinuity model with the closure of cracks is proposed in this section as a further try.

The discrete model is formulated based on the relationship between the traction vector $\boldsymbol{T}$ and the crack opening $[|\boldsymbol{u}|]$ at the discontinuity surface. First of all, the continuum part $\Omega \backslash \mathcal{S}_u$ remains elastic itself rather the strong discontinuity is present or not. Then at the discontinuity interface $\mathcal{S}$, the traction vector, defined as $\boldsymbol{T} = \boldsymbol{\sigma}|_{\mathcal{S}} \cdot \boldsymbol{n}$, has a kinematic relationships in terms of the crack opening $[|\boldsymbol{u}|]$. These kinematic relationships are what we are going to discuss in the following part.

A one-dimension bar is proposed as a simple example for each procedure, see Fig. III .8. To illustrate the elastic behavior of the sub-volumes, the bar is represented as a spring. The length of the bar is L, and we apply a displacement $\Delta \boldsymbol{u}$ to the right extreme of the bar. It is worth noting that in the following parts, even though a "crack" might be placed between two sub-domains of the bar to represent the "opening", our discontinuity model won't bring a "physical" separation in the element. The one-dimensional example is proposed to describe the physical meaning of the model. And it should also be noticed that all following works are within the small deformation setting. In the following parts, the governing laws at different stages is described.

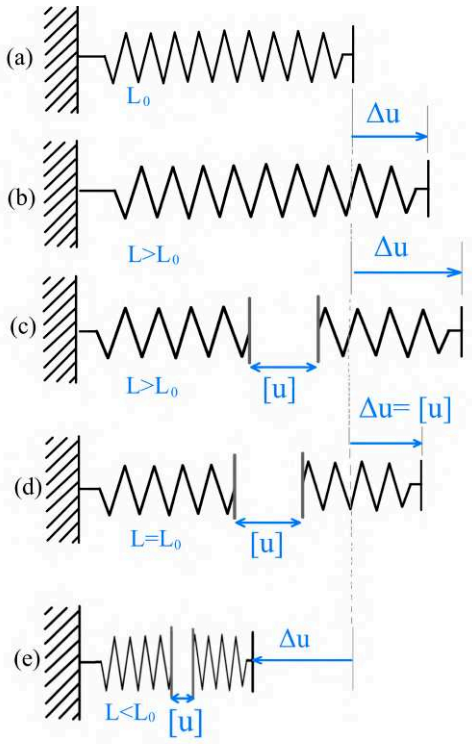

Figure III .8: Representative graphic for the crack opening and closing of the mode-I strong discontinuity.

3.1 Failure criterion and discontinuity orientation

At the beginning of loading, the element has an elastic behavior. The inelastic behavior of the element occurs after the stress field, or the strain field reaches a specific value, which is determined by the localization criterion. Our localization criterion is stress-based. The critical value of the stress is called the yield stress, note σ_{y}. It is considered as a local parameter of the material. The localization criterion wrote as:

$$\Phi_{\mathrm{l}} = \sigma_{\mathrm{eq}} - \sigma_{\mathrm{y}}, \tag{3.1}$$

where a negative value of Φ_{l} means an elastic behavior while a positive value leads to the localization and the cracks appear.

As we can see in the equation (3.1), the equivalent stress σ_{eq} is a constant value. In the case of a matrix element (no weak discontinuity is present), the equivalent stress is determined by the major principal stress which is the first eigenvalue of the stress matrix, $\sigma_{\mathrm{eq}} = \sigma_{\mathrm{I}}$. The orientation of the discontinuity interface $\boldsymbol{n}$ is simply the eigenvector

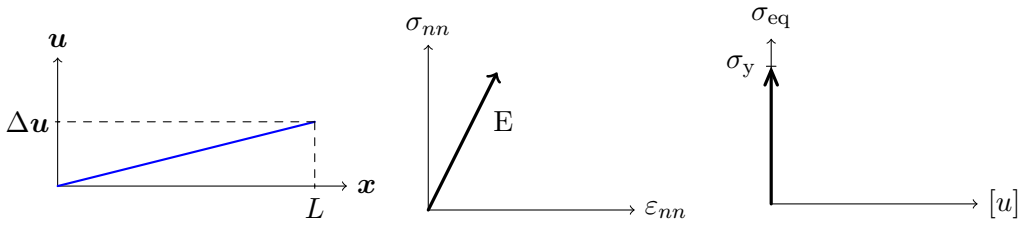

(a) The displacement field (b) Behavior outside the discontinuity interface (c) Behavior at the discontinuity interface

Figure III .9: Local constitutive model at the continuous part and at the discontinuity interface at the moment of localization.

corresponding the first eigenvalue σ_{I}, $\boldsymbol{n} = \boldsymbol{n}_I$. The localization criterion writes:

$$\Phi_{\mathrm{l}}^{\mathrm{strong}} = \sigma_{\mathrm{I}} - \sigma_{\mathrm{y}}. \tag{3.2}$$

This criterion is firstly been proposed by William John Macquorn Rankine. Rankine's criterion is a maximum-normal stress criterion and is wildly used for brittle materials.

In another case where a heterogeneity interface traverses through an element, it is assumed that the localization will occur at this interface because the crack is "close" enough to the material discontinuity. Thus the normal vector $\boldsymbol{n}$ is defined purely by the geometric of the material but the stress field. The equivalent stress is calculated by the projection of the traction vector $\boldsymbol{T}$ on the normal vector $\boldsymbol{n}$, the localization criterion writes:

$$\Phi_{\mathrm{l}}^{\mathrm{weak}} = \boldsymbol{n} \cdot \boldsymbol{T} - \sigma_{\mathrm{y}} \tag{3.3}$$

Applying to a one-dimension example, the sound material is elastic, expressed in Fig. III .8(a) is a spring. In Fig. III .8(b) the material is stretched under an imposed displacement Δu. The localization takes place once the stress reaches the critical tensile strength. The displacement field and local constitutive behavior are shown in Fig. III .9. The element has a pure elastic behavior, the Young's module E and the Poisson's ratio ν are two elastic parameters of the material.

3.2 Traction separation law for strong discontinuity

The traction-separation law is brought into use after the failure occurs. As it is mentioned in the previous section, it mainly describes the equivalent stress at the discontinuity

interface. Recalling that the discontinuity surface is considered flat, bring a constant normal vector $\boldsymbol{n}$ pointing from Ω^- to Ω^+. Since the vector $\boldsymbol{n}$ has already determined by localization law or the geometry of the material, we can separate the opening value of $[u]$ from $[|\boldsymbol{u}|]$ and use it as a constant variable which is embedded in the element. The equivalent stress and the opening value of the crack are linked through a hardening function $q_{\mathrm{o}}([u])$ at the discontinuity interface

$$\Phi_{\mathrm{o}} = \sigma_{\mathrm{eq}} - (\ \sigma_{\mathrm{y}} - q_{\mathrm{o}}([u])\ ), \text{ with } [|\boldsymbol{u}|] = [u] \cdot \boldsymbol{n}. \tag{3.4}$$

A positive value of the opening criterion Φ_{o} means an in-equilibrium state of the element and the crack needs to go further until it reaches an equilibrium state, i.e., Φ_{o} equals to zero. A negative value leads to an elastic loading or unloading, or closure of cracks, which we will discuss later.

Regarding the harden function $q_{\mathrm{o}}([u])$ for quasi-brittle materials like concrete, it should follow two conditions: First, it should be a simple decreasing function. Second, it has a magnitude value of $[u] = 0$, which equals to σ_{y}, like the one at the localization state. Upon satisfaction, the function proposed here gives as

$$q_{\mathrm{o}}([u]) = \sigma_{\mathrm{y}} \left(1 - \exp\left(-\frac{\sigma_{\mathrm{y}}}{\mathcal{G}_{\mathrm{op}}}[u]\right)\right). \tag{3.5}$$

The harden function Eq (3.5) is an exponentially decreasing function in terms of the opening value $[u]$. The partial derivative equation of the hardening function is continuous, which is important to solve the non-linear problem. It will approximate to zero value as the crack opening increase. The fracture energy $\mathcal{G}_{\mathrm{op}}$ is considered as a local material parameter, which represents the necessary energy to create a fully opened fracture. Physically, a bigger value of the fracture energy represents a more ductile material.

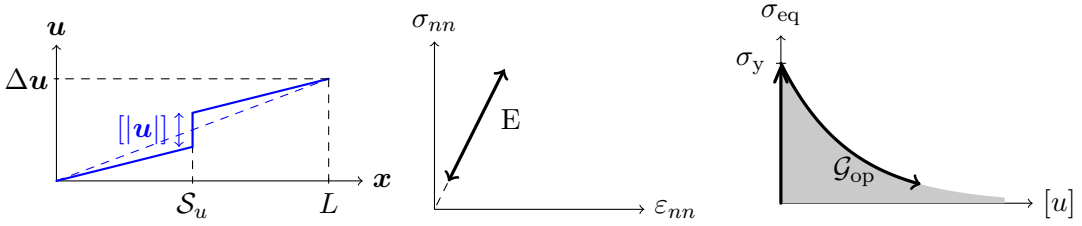

(a) The displacement field (b) Behavior outside the discontinuity interface (c) Behavior at the discontinuity interface

Figure III .10: Local constitutive model at the continuous part and at the discontinuity interface at the traction separation stage.

Assuming a strong discontinuity to the one-dimension example as shown in Fig. III .9, the local constitutive model is depicted in Fig. III .10. Naturally, as the imposed displacement Δu increases, the crack continues propagates at the traction separation phase. The traction separation law respects the equation Eq. 3.5. And the bulk volumes $\Omega_e \backslash \mathcal{S}$ always remain elastic, see Fig. III .8(b).

3.3 Closure law for mode I separation

Based on the previous admissible discontinuity model, a closure law is proposed in this section. It occurs after the normal stress turns to negative. Several conditions are always respected: Firstly, the bulk parts $\Omega_e \backslash \mathcal{S}$ remains elastic itself, verified the Hooke's law; Secondly, the traction continuous condition is always respected, it is a criterion which links the two sub-domains Ω^- and Ω^+ through the equivalent stress at the discontinuity; Finally, it is a function in terms of the opening value $[u]$ which is an internal variable, and can never be negative. In addition, we want it to be constructed as clean as possible, in other words, little additional parameters.

The applied crack closure mechanism is defined on three hypotheses. The objective is to encompass the proposed criteria in a physically meaningful context. Unlike most phenomenological models that are built at the microscopic scale or macroscopic scale, and the interests are mainly focused on the stress-strain relationships, our hypothesis is made at the mesoscopic scale, and the complexity consists mainly in associating the mechanical behaviors of the material with the opening and closing of cracks.

- **Hypothesis 1.** The required energy for a total closing equals to the energy dissipated at the opening phase.

  This hypothesis is based on the consideration of energy. We consider that the energy required to completely close a crack equals to the energy that has dissipated during the opening phase. This assumption allows the model to be rather simple and clean. In latter numerical tests, if we encounter problems with the results, it is also possible to impose the energy required for closing equals to twice, or half of the dissipated energy in opening. In addition, no additional parameters are demanded in the closing mechanism.

- **Hypothesis 2.** The critical tensile strength will partially recover depends on the degree of closing, and it will not fully recover, see Fig. III .11.

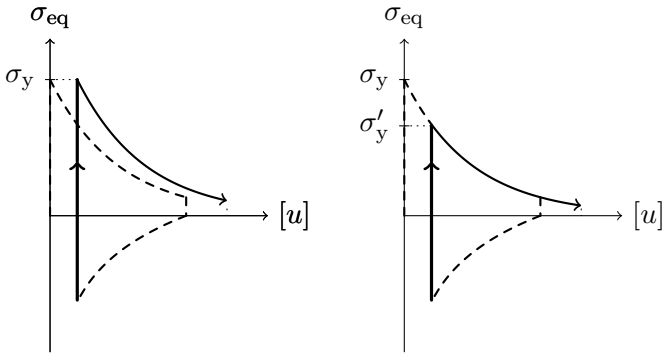

(a) Phenomenological model with recovered tensile strength (b) Phenomenological model with damaged tensile strength

Figure III .11: Two hypothesis for local constitutive models with recovered and non-recovered tensile strength.

This third hypothesis is associated with the reloading phase to an already damaged material. The localization of a sound material takes place when the maximum tensile stress reaches the critical strength σ_y. Upon physical consideration, for an already localized material, even the crack is partially closed, the tensile strength should not fully be recovered as sound material. Hence, we define the tensile strength $\sigma'_y = \sigma_y \exp\left(-\frac{\sigma_y}{\mathcal{G}_{op}}[u]\right)$ with $[u]$ the current crack opening value after crack closures. The material will recover more strength if the crack is massively closed. And if the crack is still in a very opening position, the tensile strength of the material limited because the material is already in a weakened state.

- **Hypothesis 3.** The closing mechanism is non-linear and exponential, the crack opening value tends to zero for an infinite compression but the crack will never totally close, see Fig. III .12.

  Regarding this hypothesis, the closing mechanism is assumed to be exponential, which leads to an increasing value of the required compressional stress for closing the crack. One of the reasons for proposing this hypothesis is that, a linear closing mechanism is not continuous. What's more, there will be a critical equivalent stress value, which corresponds to the utterly closing of the crack. Then, it worth deliberating the behaviors of the material after it reaches this critical stress and the crack close to zero: is it physical to consider the material to recover to a sound state after the crack has closed. As a result, we choose a non-linear closing mechanism. It can be regarded as the closing of the crack is getting harder and harder as the imposed

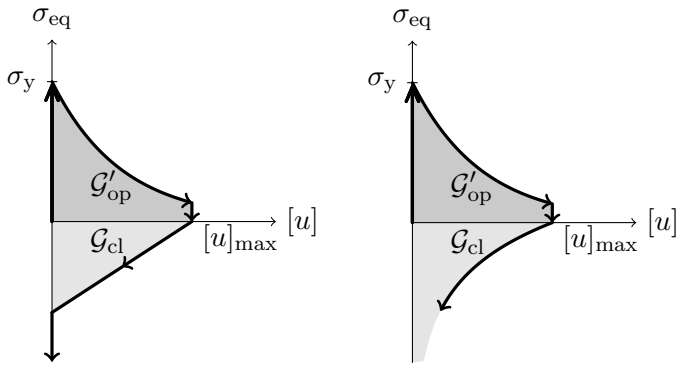

(a) Phenomenological model with linear closing law

(b) Phenomenological model with exponential closing law

Figure III .12: Two hypothesis for local constitutive models with linear and non-linear closing laws at the discontinuity interface.

displacement decreases. Thus the crack will never wholly closed because the needed stress is infinite. This assumption also verifies sort of the spirit of "symmetric", that the material will become more and more fragile in the opening procedure, and will become more and more difficult to continue closing in the closing phase. Also, an analytical resolution is available for the exponential closing law at the local scale.

3.3.1 Unloading procedure

First, let us now consider an unloading procedure to the element which has already a crack opening. Physically, the bulk part (the volume outside the discontinuity interface) will obey an elastic unloading behavior, while the opening value $[u]$ remain the same. This is because the tensile energy is still stored in the bulk volumes, and the discontinuity interface is under traction before a total release of the elastic energy. It is worth noting that the elastic unloading procedure will end before the imposed displacement $\Delta \boldsymbol{u}$ decrease to 0. More specifically, the elastic unloading procedure will finish when $\Delta \boldsymbol{u} = [u]$, with $[u]$ is the opening value during the opening procedure, see Fig. III .13.

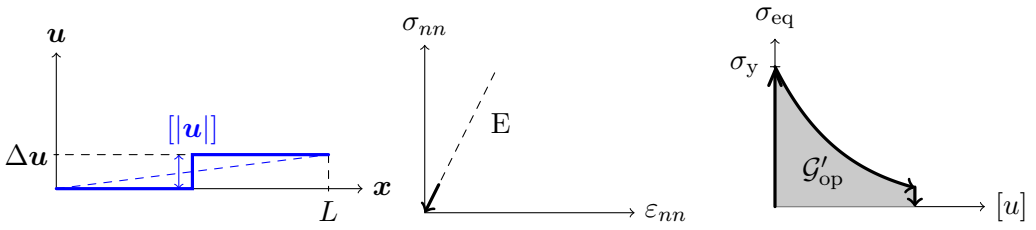

(a) The displacement field (b) Behavior outside the discontinuity interface (c) Behavior at the discontinuity interface

Figure III .13: Local constitutive model at the continuous part and at the discontinuity interface as the imposed displacement decrease.

The corresponding one-dimensional example is plotted in Fig. III .8(d). At the state of null stress, the elastic parts have recovered their original length while the crack opening value remains constant. At this moment, the gradient of displacement field equals to zero (related to the deformation field), the bulk volume has completely released the elastic energy stored in itself. At the point of Fig.III .13(a), the volume outside the discontinuity interface has a null gradient of the displacement field, leads to null value for normal deformation and stress. Hence, the unloading procedure carries a pure elastic mechanism, which corresponds to the release of the stored energy in the bulk volumes.

3.3.2 Closure of cracks

Following the unloading procedure, the opening crack will obey a closure procedure if the equivalent stress decrease to a negative value, which means that compressional stress is applied to the crack.

During the closure procedure, it worth some particular attention at the point of $\Delta \boldsymbol{u} = 0$. The imposed displacement equals to zero. However, the opening crack still has a positive value. It is assumed that the closure of cracks occurs after the equivalent stress turns to negative in a non-linear way. With the decreasing of the opening value $[u]$, the necessary compressional normal stress increases, and the opening crack will never completely close because the required normal stress will be infinitive big.

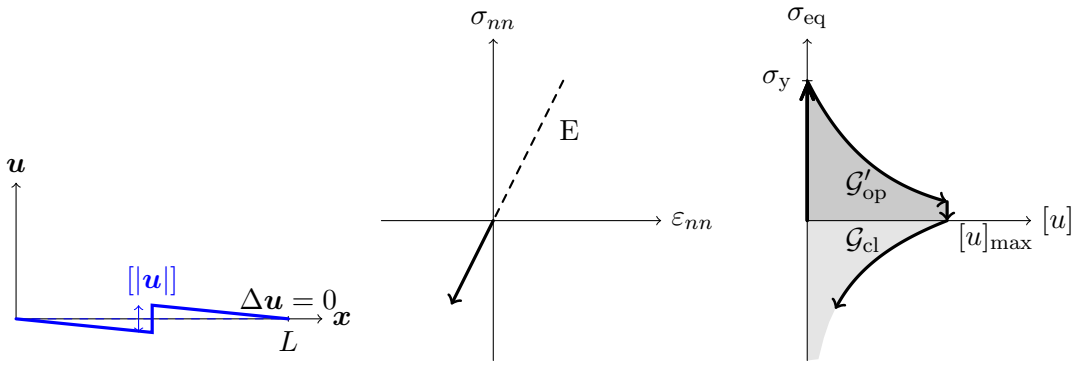

(a) The displacement field (b) Behavior at the continuous part (c) Behavior at the discontinuity interface

Figure III .14: Local constitutive model at the continuous part and at the discontinuity interface at the crack closing phase.

As shown in Fig. III .14, a non-linear function is proposed to simulate the closure of cracks. It is assumed that the dissipate energy during the opening $\mathcal{G}'_{\text{op}}$ equals to the required energy to completely close the crack $\mathcal{G}_{\text{cl}}$. As this point, we have the imposed displacement $\Delta u = 0$, and the crack opening value $[u] < [u]_{\max}$.

3.3.3 Reloading procedure

Let us now apply a reloading displacement to the element. As the normal stress rides up from negative to positive, firstly the elastic bulk part (outside the discontinuity interface) will obey a linear unloading behavior, then followed by linear reloading, until the equivalent stress reaches the failure strength σ'_{y}. Physically, it means that the crack opening always exhibits in the element. Naturally, the corresponding failure parameters are weaker than the unbroken element. The following procedures, such as opening, unloading, closing, will be the same as shown in previous parts, see Fig. III .15.

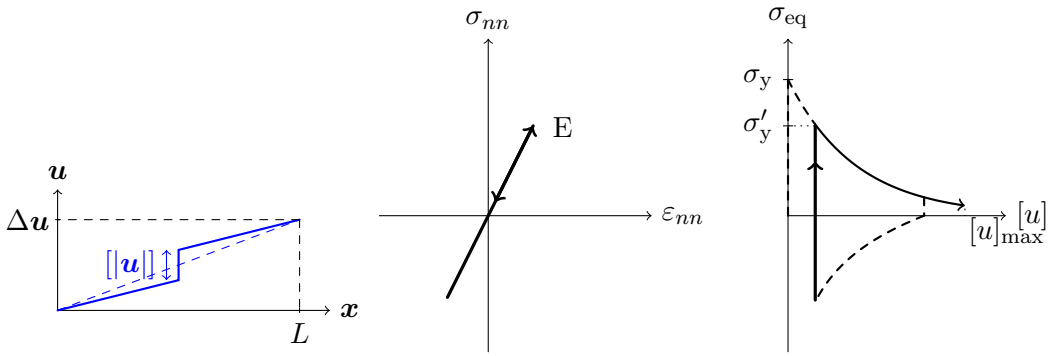

(a) The displacement field (b) Behavior at the continuous part (c) Behavior at the discontinuity interface

Figure III .15: Local constitutive model at the continuous part and at the discontinuity interface as the imposed displacement reloads.

3.3.4 Governing equations

The admissible model's behaviors at the fine-scale have been decomposed into different procedures, as introduced in previous parts. Remark that: first, the volume outside the discontinuity interface has a linear and elastic behavior. Next, the normal stress or the equivalent stress, which links the discontinuity surface and the continuous volume is described in terms of the opening value $[u]$. Then, $[u]_{\max}$ is always the maximum opening value that the discontinuity has ever reached. It is an essential parameter for calculating the dissipated energy during the opening procedure.

Upon the consideration of constructing the model in a terse way, it is assumed that the dissipated energy (the gray part in Figure III .14(b)) during the opening process equals to the necessary energy for the complete closure of the crack (the light gray part in Figure III .14(b)). The dissipated energy is calculated as

$$E_{\text{op}} = \int_0^{[u]_{\max}} \sigma_{\text{eq}}([u])\ d[u] = \mathcal{G}_{\text{op}}(1 - \exp(-\frac{\sigma_{\text{y}}\ [u]_{\max}}{\mathcal{G}_{\text{op}}})) = \mathcal{G}_{\text{cl}}. \tag{3.6}$$

Hence the dissipate energy can be completely defined by known parameters $\mathcal{G}_{\text{op}}$, σ_{y}, and the maxim opening value, note $[u]_{\max}$, no additional parameters are required.

Regarding the closure law, it should respect the following equation:

$$E_{\text{cl}} = \int_{[u]_{\max}}^{0} \sigma_{\text{eq}}([u])\ d[u] = E_{\text{op}} = \mathcal{G}_{\text{cl}}. \tag{3.7}$$

The choice made here is :

$$\Phi_c = -\sigma_{eq} + \underbrace{\frac{\mathcal{G}_{cl}}{[u]_{max}} \ln\left(\frac{[u]}{[u]_{max}}\right)}_{q_c}, \tag{3.8}$$

where $[u]$ is always inferior to $[u]_{max}$, and a positive value of Φ_c means the crack should continue closing to a further position while a null value represents a plastically admissible stress state. The latter part of the criterion can also be regarded as a harden function q_c. A negative value of Φ_c means an elastic loading or reloading. Since a condition is always respected that $[u]$ inferiors or equals to $[u]_{max}$, it is impossible to have positive values for Φ_o and Φ_c at the same time.

4 Finite Element approximations

4.1 Variational methods in discontinuity enhancement [Hu-Washizu]

The main idea of the Hu-Washizu is to have three independent fields $(\hat{\boldsymbol{u}}, \boldsymbol{\varepsilon}, \boldsymbol{\sigma})$, representing the displacement field, the strain field, and the stress field, respectively. Then three corresponding virtual field are proposed, note $(\hat{\boldsymbol{\eta}}, \boldsymbol{\tau}, \boldsymbol{\gamma})$, also mutually independent. The variational formulations (Roubin et al., 2015; Vallade, 2016; Washizu, 1968) gives as

$$HW_{\hat{u}}(\hat{\boldsymbol{u}}, \boldsymbol{\varepsilon}, \boldsymbol{\sigma}; \hat{\boldsymbol{\eta}}) = \int_\Omega \nabla^{sym}\hat{\boldsymbol{\eta}} : \boldsymbol{\sigma} d\Omega - \int_\Omega \hat{\boldsymbol{\eta}} \cdot \rho\bar{\boldsymbol{b}} d\Omega - \int_\Gamma \hat{\boldsymbol{\eta}} \cdot \bar{\boldsymbol{t}} d\partial\Omega = 0, \tag{4.1a}$$

$$HW_{\boldsymbol{\sigma}}(\hat{\boldsymbol{u}}, \boldsymbol{\varepsilon}, \boldsymbol{\sigma}; \boldsymbol{\tau}) = \int_\Omega \boldsymbol{\tau} : (\nabla^{sym}\hat{\boldsymbol{u}} - \boldsymbol{\varepsilon}) = 0, \tag{4.1b}$$

$$HW_{\boldsymbol{\varepsilon}}(\hat{\boldsymbol{u}}, \boldsymbol{\varepsilon}, \boldsymbol{\sigma}; \boldsymbol{\gamma}) = \int_\Omega \boldsymbol{\gamma} : (\check{\boldsymbol{\sigma}}(\boldsymbol{\varepsilon}) - \boldsymbol{\sigma}) d\Omega = 0, \tag{4.1c}$$

Within the studied domain Ω where these fields are defined, the two boundaries Γ_u and Γ_t, prescribed as displacement boundary and traction boundary (see Figure III .1), are disjoint boundaries. Naturally, two boundary conditions should be respected

$$\boldsymbol{u}(\boldsymbol{x}) = \bar{\boldsymbol{u}}(\boldsymbol{x}), \ \forall \boldsymbol{x} \in \Gamma_u, \tag{4.2a}$$

$$\boldsymbol{\sigma}(\boldsymbol{x}) \cdot \boldsymbol{n}^*(\boldsymbol{x}) = \bar{\boldsymbol{t}}(\boldsymbol{x}), \ \forall \boldsymbol{x} \in \Gamma_t, \tag{4.2b}$$

where $\boldsymbol{n}^*$ is the outward unit normal vector at the boundary.

The first variational formulation states the equilibrium equation with $\rho\bar{\boldsymbol{b}}$ and $\bar{\boldsymbol{t}}$ prescribed, respectively, the body force and the surface force. Also, we can derive from Eq. (4.1) the kinematic equation, which defines the strains in terms of the displacement field $\varepsilon = \nabla^{\text{sym}} u$; and the constitutive model, which defines the stress in terms of the strain field $\sigma = \check{\sigma}(\varepsilon)$. These two classic formulation makes Eq (4.1b) Eq (4.1c) irrelevant.

4.2 Incompatible modes

A three-field variational formulation in terms of the independent displacement field, the strain field, and the stress field is presented in the previous section. Within the framework of the finite element method, a classic method of incompatible modes is introduced in this section. The central idea is assuming that both actual and virtual fields are enhanced in an additional way, making them divided into three parts, the standard part, the enhanced weak discontinuity and the enhanced strong discontinuity as Eq (4.3):

$$\boldsymbol{\varepsilon} = \underbrace{\boldsymbol{\nabla}^{\text{sym}}\hat{\boldsymbol{u}}}_{\text{compatible}} + \underbrace{\underbrace{\tilde{\boldsymbol{\varepsilon}}}_{\text{weak}} + \underbrace{\hat{\boldsymbol{\varepsilon}}}_{\text{strong}}}_{\text{incompatible}} \quad \text{and} \quad \boldsymbol{\gamma} = \underbrace{\boldsymbol{\nabla}^{\text{sym}}\hat{\boldsymbol{\eta}}}_{\text{compatible}} + \underbrace{\underbrace{\tilde{\boldsymbol{\gamma}}}_{\text{weak}} + \underbrace{\hat{\boldsymbol{\gamma}}}_{\text{strong}}}_{\text{incompatible}} \tag{4.3}$$

By taking into consideration of the orthogonal relationship between the enhanced and the virtual part of the strain and stress field (Roubin et al., 2015), we arrive at the following simplified formulation:

$$\int_\Omega \nabla^{\text{sym}}\hat{\boldsymbol{\eta}} : \check{\boldsymbol{\sigma}}(\nabla^{\text{sym}}\hat{\boldsymbol{u}} + \tilde{\boldsymbol{\varepsilon}} + \hat{\boldsymbol{\varepsilon}})d\Omega - \int_\Omega \hat{\boldsymbol{\eta}} \cdot \rho\bar{\boldsymbol{b}}d\Omega - \int_{\Gamma_t} \hat{\boldsymbol{\eta}} \cdot \bar{\boldsymbol{t}}d\partial\Omega = 0, \tag{4.4a}$$

$$\int_\Omega \tilde{\boldsymbol{\gamma}} : \check{\boldsymbol{\sigma}}(\nabla^{\text{sym}}\hat{\boldsymbol{u}} + \tilde{\boldsymbol{\varepsilon}} + \hat{\boldsymbol{\varepsilon}})d\Omega = 0, \tag{4.4b}$$

$$\int_\Omega \hat{\boldsymbol{\gamma}} : \check{\boldsymbol{\sigma}}(\nabla^{\text{sym}}\hat{\boldsymbol{u}} + \tilde{\boldsymbol{\varepsilon}} + \hat{\boldsymbol{\varepsilon}})d\Omega = 0, \tag{4.4c}$$

To ensure the convergence of the method, the patch test should be respected after imposing the orthogonal condition. By assuming that the discontinuity interface is flat, which means making the normal vector of the interface $\boldsymbol{n}$ a constant over each element, we will take the Θ as a function only depending on the volume of sub-domains (Roubin, 2013):

$$\Theta^+ = \frac{V^-}{V} \quad \text{and} \quad \Theta^- = -\frac{V^+}{V}. \tag{4.5}$$

Afterwards, the strong enhanced strain field consists of two parts: the bounded part $\hat{\boldsymbol{\gamma}}_b$ and the unbounded part $\delta_{\Gamma_d}([|u|] \otimes \boldsymbol{n})^s$. Take into the consideration of zero mean condition, the bounded part of the strong enhanced strain field can be explicitly defined.

Following the Enhanced Assumed Strain(EAS) method, the complete form of the strong enhancement of the strain field is obtained by

$$\hat{\boldsymbol{\gamma}} = \underbrace{\delta_{\Gamma_d}([|\boldsymbol{\eta}|] \otimes \boldsymbol{n})^{\mathrm{sym}}}_{\text{unbounded}} \underbrace{-\frac{A}{V}([|\boldsymbol{\eta}|] \otimes \boldsymbol{n})^{\mathrm{sym}}}_{\text{bounded}} \tag{4.6}$$

4.3 Finite Element interpolation

In this section, the three-field variational formulation Eq. (4.4) is solved within the finite element method framework. Depending on whether the strain field is actual or virtual, they are not discretized in the same way. The actual strain field is enhanced using KES in a kinematics point of view, whereas the virtual strain field is enhanced using the EAS (refers as $\bullet^*$ in the following part) in a statical point of view. Based on DSDA, the actual discretization of the strain field is defined by keeping only the bounded enhanced part, while the virtual discretization has the full enhancement. Hence, the discretization is written as follows:

$$\boldsymbol{\varepsilon} = \boldsymbol{\nabla}^{\mathrm{sym}}\hat{\boldsymbol{u}} + \tilde{\boldsymbol{\varepsilon}} + \hat{\boldsymbol{\varepsilon}} = \mathbf{B}\ \boldsymbol{d} + \mathbf{G}_{\mathrm{w}}\ [|\boldsymbol{\varepsilon}|] + \mathbf{G}_{\mathrm{s}}\ [|\boldsymbol{u}|], \tag{4.7a}$$

$$\boldsymbol{\gamma} = \boldsymbol{\nabla}^{\mathrm{sym}}\hat{\boldsymbol{\eta}} + \tilde{\boldsymbol{\gamma}} + \hat{\boldsymbol{\gamma}} = \mathbf{B}\ \boldsymbol{d} + \mathbf{G}_{\mathrm{w}}\ [|\boldsymbol{\gamma}|] + (\mathbf{G}^*_{\mathrm{s,b}} + \mathbf{G}^*_{\mathrm{s,u}})\ [|\boldsymbol{\eta}|], \tag{4.7b}$$

where several introduced interpolation matrices are: $\boldsymbol{B}(=\partial \boldsymbol{N})$ the standard strain interpolation matrix, $\mathbf{G}_{\mathrm{w}}$ the actual and virtual field corresponding to the weak discontinuity, $\mathbf{G}_{\mathrm{s}}$ the bounded part of the actual field corresponding to the strong discontinuity, $\mathbf{G}^*_{\mathrm{s}} := \mathbf{G}^*_{\mathrm{s,b}} + \mathbf{G}^*_{\mathrm{s,u}}$ the full enhancement of the virtual field corresponding to the strong discontinuity, $\boldsymbol{d}$ the nodal displacement field, and $[|\boldsymbol{\varepsilon}|]$ (resp.$[|\boldsymbol{u}|]$) corresponds to the supplement unknown variables brought by weak (resp. strong) discontinuity. Note that the strain fields are all expressed in Voigt notation.

Considering the discretization of the system, we can write the global equilibrium equation in a residual form

$$\bar{\mathcal{R}} := \mathop{\mathbb{A}}_{e=1}^{n_{\mathrm{e}}} \bar{\mathcal{R}}_e = \bar{\boldsymbol{f}}_{\mathrm{ext}} - \mathop{\mathbb{A}}_{e=1}^{n_{\mathrm{e}}} \left(\int_{\Omega_e} \boldsymbol{B}^T \boldsymbol{\sigma} d\Omega \right) = \bar{0}, \tag{4.8}$$

where $\mathop{\mathbb{A}}_{e=1}^{n_e}$ represents the standard assembly operator which group all n_{e} elements into the computational domain Ω. The vector $\bar{\boldsymbol{f}}_{\mathrm{ext}}$ denote the external force, which consists of the

body force and the surface force

$$\bar{\boldsymbol{f}}_{\text{ext}} = \mathop{\mathbb{A}}_{e=1}^{n_{\text{e}}} \left(\int_{\Omega_e} \boldsymbol{N}^T \boldsymbol{b} \; d\Omega + \int_{\Gamma_t^e} \boldsymbol{N}^T \boldsymbol{t} \; d\Gamma \right). \tag{4.9}$$

By replacing parameters in Eq. (4.4) with Eq. (4.7), we can obtain the following equations

$$\int_{\Omega} \mathbf{G}_{\text{w}}^T \check{\boldsymbol{\sigma}}(\boldsymbol{d}, [|\boldsymbol{\varepsilon}|], [|\boldsymbol{u}|]) \; d\Omega = 0 \tag{4.10a}$$

$$\int_{\Omega} (\mathbf{G}_{\text{s,b}}^{*,T} + \mathbf{G}_{\text{s,u}}^{*,T}) \check{\boldsymbol{\sigma}}(\boldsymbol{d}, [|\boldsymbol{\varepsilon}|], [|\boldsymbol{u}|]) d\Omega = 0. \tag{4.10b}$$

Then take into consideration of Eq. (4.6), it's easy to see that

$$\hat{\boldsymbol{\gamma}} = (\mathbf{G}_{\text{s,b}}^* + \mathbf{G}_{\text{s,u}}^*) \; [|\boldsymbol{\eta}|] = -\frac{A}{V} ([|\boldsymbol{\eta}|] \otimes \boldsymbol{n})^{\text{sym}} + \delta_{\mathcal{S}} ([|\boldsymbol{\eta}|] \otimes \boldsymbol{n})^{\text{sym}}, \tag{4.11}$$

where $(\bullet \times \boldsymbol{n})^{\text{sym}}$ is noted as a operator $\boldsymbol{H}_{\text{s}}^*$ for the rest part, leads to an equivalent Voigt notation for the traction vector

$$\boldsymbol{T} = \underbrace{\check{\boldsymbol{\sigma}} \cdot \boldsymbol{n}}_{\text{matrix notation}} = \underbrace{\boldsymbol{H}_{\text{s}}^{*,T} \check{\boldsymbol{\sigma}}}_{\text{Voigt notation}} . \tag{4.12}$$

One of the proprieties of the Dirac-delta distribution $\delta_{\mathcal{S}}$ is that $\int f(\boldsymbol{x}) \delta_{\mathcal{S}} d\boldsymbol{x} = \int f(\boldsymbol{x} = \mathcal{S}) d\boldsymbol{x}$. Thus the unbounded part of the virtual strain field can be further simplified into the form

$$\int_{\Omega} \mathbf{G}_{\text{s,u}}^{*,T} \check{\boldsymbol{\sigma}}(\boldsymbol{d}, [|\boldsymbol{\varepsilon}|], [|\boldsymbol{u}|]) d\Omega = \int_{\mathcal{S}} \boldsymbol{T}(\boldsymbol{d}, [|\boldsymbol{\varepsilon}|], [|\boldsymbol{u}|]) d\partial\Omega. \tag{4.13}$$

As for the interpolation matrix corresponding to weak discontinuity, $\mathbf{G}_{\text{w}}$ is defined separately in two parts $\Theta^{+|-}$ as:

$$\mathbf{G}_{\text{w}} = \begin{cases} \mathbf{G}_{\text{w}}^+ = \Theta^+ \boldsymbol{H}_{\text{w}} = \frac{V^-}{V} \boldsymbol{H}_{\text{w}} & \text{in } \Omega_e^+ \\ \mathbf{G}_{\text{w}}^- = \Theta^- \boldsymbol{H}_{\text{w}} = -\frac{V^+}{V} \boldsymbol{H}_{\text{w}} & \text{in } \Omega_e^-, \end{cases} \tag{4.14}$$

where the constant matrix $\boldsymbol{H}_{\text{w}}$ carries only the information on the normal vector $\boldsymbol{n}$.

Recording to the equation Eq. (2.13), we can see that the bounded part of the strong enhancement of the actual strain field writes as $([|\boldsymbol{u}|] \otimes \nabla \varphi_e)^s$. Hence $\mathbf{G}_{\text{s}}$ is the equivalent symmetric operator $(\bullet \otimes \nabla \varphi_e)^s$ in Voigt notation, with φ_e is a explicitly defined arbitrary function to separate nodes at Ω_e^+ from Ω_e^- by setting unit value to nodes at Ω_e^+ and null

at other part. The arbitrary function is defined as follows:

$$\varphi_e(\boldsymbol{x}) = \sum_{a=1}^{n_e} \boldsymbol{N}_a p_a \text{ with } p_a = \begin{cases} 1 & \text{if node number } a \in \Omega_e^+ \\ 0 & \text{if node number } a \in \Omega_e^-. \end{cases} \tag{4.15}$$

In summary, the discretized system gives as (Roubin et al., 2015)

$$\bar{\mathcal{R}} := \mathop{\mathbb{A}}_{e=1}^{n_e} \left(\bar{\boldsymbol{f}}_{\text{int}} - \bar{\boldsymbol{f}}_{\text{ext}}\right) = \mathop{\mathbb{A}}_{e=1}^{n_e} \left(\bar{\boldsymbol{f}}_{\text{ext}}^e - \int_{\Omega_e} \boldsymbol{B}^T \check{\boldsymbol{\sigma}}(\boldsymbol{d}, [|\boldsymbol{\varepsilon}|], [|\boldsymbol{u}|]) d\Omega\right) = \bar{0}, \tag{4.16a}$$

$$\bar{\mathcal{R}}^e_{[|\boldsymbol{\varepsilon}|]} = \int_{\Omega_e} \mathbf{G}_{\text{w}}^T \check{\boldsymbol{\sigma}}(\boldsymbol{d}, [|\boldsymbol{\varepsilon}|], [|\boldsymbol{u}|])\ d\Omega = \bar{0}\ , \tag{4.16b}$$

$$\bar{\mathcal{R}}^e_{[|\boldsymbol{u}|]} = \int_{\Omega_e} \boldsymbol{G}_{\text{s}}^{*,T} \check{\boldsymbol{\sigma}}(\boldsymbol{d}, [|\boldsymbol{\varepsilon}|], [|\boldsymbol{u}|])\ d\Omega = \int_{\Omega_e \backslash \mathcal{S}} \mathbf{G}_{\text{s,b}}^{*,T} \check{\boldsymbol{\sigma}}(\boldsymbol{d}, [|\boldsymbol{\varepsilon}|], [|\boldsymbol{u}|]) d\Omega + \int_{\mathcal{S}} \boldsymbol{T} d\partial\Omega = \bar{0}. \tag{4.16c}$$

The first discretized equation Eq. (4.16a) represents the equilibrium of the global system, while Eq.(4.16b) and Eq. (4.16c) are local equations for each element. It is recalled that the latter two equations corresponding to the weak enhancement and strong enhancement $[|\boldsymbol{\varepsilon}|]$ and $[|\boldsymbol{u}|]$ are considered as the internal variables, and are solved at the element level. Hence, the global equilibrium equation Eq. (4.16a) always has the same size no matter how many heterogeneities exist in the system or how many elements begin to crack.

5 Numerical resolution with Finite Element Method

In this section, the focus is made on the resolution of the system, the equation Eq. (4.16), by using explicit interpolation functions. Within the framework of the numerical implementation, the approximate solution of a non-linear system usually needs to solve a set of simultaneous iterative algorithms, like Newton's method been used here. The main idea is to discrete the load step $[0, T]$ into (k) iteration steps.

Without loss of generality, let us consider an equation $\Psi(x_i)$ depending on m variables. Within a specific time increment $[T_n, T_{n+1}]$, the solution will start from the known variables at step T_n. The variables at step T_{n+1} can be solved by the approximate equation written as

$$\Psi(x_i)\Big|_{n+1}^{k+1} \cong \Psi(x_i)\Big|_{n+1}^{k} + \sum_i^m \frac{\partial \Psi}{\partial x_i}\Big|_{n+1}^{k} dx_i\Big|_{n+1}^{k} = 0, \tag{5.1}$$

and $\boldsymbol{K}$ is note as a tangent matrix which can be calculated as

$$\boldsymbol{K} = -\frac{\partial \Psi}{\partial x_i}. \tag{5.2}$$

5.1 Linearisation of equations

The resolution of the system in our case (Eq. (4.16)) carries several considered variables $\{x_i\} = \{\boldsymbol{d}, [|\boldsymbol{\varepsilon}|], [|\boldsymbol{u}|]\}$, and non-linear equations refer to as $\bar{\mathcal{R}}$, $\bar{\mathcal{R}}^e_{[|\boldsymbol{\varepsilon}|]}$, and $\bar{\mathcal{R}}^e_{[|\boldsymbol{u}|]}$. Within the framework of the Finite Element Method, the equation of global equilibrium and the weak discontinuity can be written as the following equations

$$\begin{aligned}
\boldsymbol{f}^e_{\text{int}} &= \int_{\Omega_e} \boldsymbol{B}^T \check{\boldsymbol{\sigma}}(\boldsymbol{d}, [|\boldsymbol{\varepsilon}|], [|\boldsymbol{u}|]) d\Omega = \boldsymbol{K}_{\text{bb}}\boldsymbol{d} + \boldsymbol{K}_{\text{bw}}[|\boldsymbol{\varepsilon}|] + \boldsymbol{K}_{\text{bs}}[u], \\
\bar{\mathcal{R}}^e_{[|\boldsymbol{\varepsilon}|]} &= \int_{\Omega_e} \mathbf{G}^T_{\text{w}} \check{\boldsymbol{\sigma}}(\boldsymbol{d}, [|\boldsymbol{\varepsilon}|], [|\boldsymbol{u}|])\ d\Omega = \boldsymbol{K}_{\text{wb}}\boldsymbol{d} + \boldsymbol{K}_{\text{ww}}[|\boldsymbol{\varepsilon}|] + \boldsymbol{K}_{\text{ws}}[u],
\end{aligned}$$

with

$$\begin{aligned}
\boldsymbol{K}_{\text{bb}} &= \boldsymbol{B}^T \left(V^+\boldsymbol{C}^+ + V^-\boldsymbol{C}^-\right)\boldsymbol{B} \\
\boldsymbol{K}_{\text{bw}} &= \frac{V^+V^-}{V}\boldsymbol{B}^T(\boldsymbol{C}^+ - \boldsymbol{C}^-)\boldsymbol{H}_{\text{w}} \\
\boldsymbol{K}_{\text{bs}} &= \boldsymbol{B}^T(V^+\boldsymbol{C}^+ + V^-\boldsymbol{C}^-)\mathbf{G}_{\text{s}}\boldsymbol{n}_p \\
\boldsymbol{K}_{\text{wb}} &= \frac{V^+V^-}{V}\boldsymbol{H}^T_{\text{w}}(\boldsymbol{C}^+ - \boldsymbol{C}^-)\boldsymbol{B} \\
\boldsymbol{K}_{\text{ww}} &= \frac{V^+V^-}{V}\boldsymbol{H}^T_{\text{w}}(V^-\boldsymbol{C}^+ + V^+\boldsymbol{C}^-)\boldsymbol{H}_{\text{w}} \\
\boldsymbol{K}_{\text{ws}} &= \frac{V^+V^-}{V}\boldsymbol{H}_{\text{w}}(\boldsymbol{C}^+ - \boldsymbol{C}^-)\mathbf{G}_{\text{s}}\boldsymbol{n}_p.
\end{aligned}$$

Based on the Newton's method, their linearisation formulation gives as (Roubin et al., 2015)

$$\begin{aligned}
&\mathop{\mathbb{A}}_{e=1}^{n_{\text{e}}} \left(\boldsymbol{K}_{\text{bb}}\Delta\boldsymbol{d}\Big|_{n+1}^{(k+1)} + \boldsymbol{K}_{\text{bw}}\Delta[|\boldsymbol{\varepsilon}|]\Big|_{n+1}^{(k+1)} + \boldsymbol{K}_{\text{bs}}\Delta[u]\Big|_{n+1}^{(k+1)} \right) = -\mathop{\mathbb{A}}_{e=1}^{n_{\text{e}}} \left(\boldsymbol{f}^e_{\text{int}}\Big|_{n+1}^{(k)} - \boldsymbol{f}^e_{\text{ext}} \right), \\
&K_{\text{wb}}\Delta\boldsymbol{d}\Big|_{n+1}^{(k+1)} + \boldsymbol{K}_{\text{ww}}\Delta[|\boldsymbol{\varepsilon}|]\Big|_{n+1}^{(k+1)} + \boldsymbol{K}_{\text{ws}}\Delta[u]\Big|_{n+1}^{(k+1)} = -\bar{\mathcal{R}}^e_{[|\boldsymbol{\varepsilon}|]}\Big|_{n+1}^{(k)}.
\end{aligned}$$

And the linearisation of the traction-separation law writes:

$$\boldsymbol{K}_{\text{s}^*\text{b}}\Big|_{n+1}^{(k)}\Delta\boldsymbol{d}\Big|_{n+1}^{(k+1)} + \boldsymbol{K}_{\text{s}^*\text{w}}\Big|_{n+1}^{(k)}\Delta[|\boldsymbol{\varepsilon}|]\Big|_{n+1}^{(k+1)} + (\boldsymbol{K}_{\text{s}^*\text{s}} + K_{\text{qo}})\Big|_{n+1}^{(k)}\Delta[u]\Big|_{n+1}^{(k+1)} = -\Phi_{\text{o}}\Big|_{n+1}^{(k)} \tag{5.3}$$

with

$$\begin{aligned}
\boldsymbol{K}_{\mathrm{s^*b}} &= \frac{\partial \sigma_{\mathrm{eq}}}{\partial \boldsymbol{T}} \frac{1}{V} \boldsymbol{H}_{\mathrm{s}}^{*,T} (V^+ \boldsymbol{C}^+ + V^- \boldsymbol{C}^-) \boldsymbol{B} \\
\boldsymbol{K}_{\mathrm{s^*w}} &= \frac{\partial \sigma_{\mathrm{eq}}}{\partial \boldsymbol{T}} \frac{V^+ V^-}{V} \boldsymbol{H}_{\mathrm{s}}^{*,T} (\boldsymbol{C}^+ - \boldsymbol{C}^-) \boldsymbol{H}_{\mathrm{w}} \\
\boldsymbol{K}_{\mathrm{s^*s}} &= \frac{\partial \sigma_{\mathrm{eq}}}{\partial \boldsymbol{T}} \frac{1}{V} \boldsymbol{H}_{\mathrm{s}}^{*,T} (V^+ \boldsymbol{C}^+ + V^- \boldsymbol{C}^-) \mathbf{G}_{\mathrm{s}} \boldsymbol{n}_p \\
K_{\mathrm{qo}} &= \frac{\sigma_y^2}{\mathcal{G}_{\mathrm{op}}} e^{-\sigma_{\mathrm{y}}[u]/\mathcal{G}_{\mathrm{op}}}
\end{aligned}$$

Since the cracks are considered as internal variables, the linearisation of the closure procedure should be calculated at the element scale. The behavior at the volume outside the discontinuity interface is linear and elastic, and at the interface, it is described by the cohesive criterion or the closure criterion. The traction vector $\boldsymbol{T}$ is the parameter which links the bulk volume and the discrete discontinuity interface. With the assumptions of plat interface and constant stress, the integration can be calculated based on the average value of weighted volumes of sub-domain $V^{+|-}$:

$$\boldsymbol{T} = \frac{1}{V} \boldsymbol{H}_{\mathrm{s}}^{*,T} (V^+ \check{\boldsymbol{\sigma}}^+ + V^- \check{\boldsymbol{\sigma}}^-) \tag{5.4}$$

It is recalled that the closure criterion writes as $\Phi_c = -\sigma_{\mathrm{eq}} + q_{\mathrm{c}}([u])$. It is a function in terms of two variables: $\{\boldsymbol{T}, [u]\}$, thus the increment of Φ_{c} gives:

$$\Delta \Phi_{\mathrm{c}} = -\frac{\partial \sigma_{\mathrm{eq}}}{\partial \boldsymbol{T}} \Delta \boldsymbol{T} + \frac{\partial q_{\mathrm{c}}}{\partial [u]} \Delta [u], \tag{5.5}$$

$$\Delta \Phi_{\mathrm{c}} = -\boldsymbol{K}_{\mathrm{s^*b}} \Delta \boldsymbol{d} - \boldsymbol{K}_{\mathrm{s^*w}} \Delta [|\boldsymbol{\varepsilon}|] - \boldsymbol{K}_{\mathrm{s^*s}} \Delta [u] + K_{\mathrm{qc}} \Delta [u],$$

with

$$K_{\mathrm{qc}} = \frac{\mathcal{G}_{\mathrm{cl}}}{[u]_{\max} [u]}.$$

Hence, the linearisation of the closure law is like:

$$-\boldsymbol{K}_{\mathrm{s^*b}} \Big|_{n+1}^{(k)} \Delta \boldsymbol{d} \Big|_{n+1}^{(k+1)} - \boldsymbol{K}_{\mathrm{s^*w}} \Big|_{n+1}^{(k)} \Delta [|\boldsymbol{\varepsilon}|] \Big|_{n+1}^{(k+1)} - (\boldsymbol{K}_{\mathrm{s^*s}} - K_{\mathrm{qc}}) \Big|_{n+1}^{(k)} \Delta [u] \Big|_{n+1}^{(k+1)} = -\Phi_{\mathrm{c}} \Big|_{n+1}^{(k)} \tag{5.6}$$

It worth recalling that $\mathcal{G}_{\mathrm{cl}}$ is not an additionally applied parameter. It represents the necessary energy for completely closing the crack, which equals to the dissipate energy during the opening procedure $\mathcal{G}'_{\mathrm{op}}$.

5.2 Solving the system

Once the linearisation of the three equations is done, we can write them into a matrix like :

$$\begin{bmatrix} \boldsymbol{K}_{\mathrm{bb}} & \boldsymbol{K}_{\mathrm{bw}} & \boldsymbol{K}_{\mathrm{bs}} \\ \boldsymbol{K}_{\mathrm{wb}} & \boldsymbol{K}_{\mathrm{ww}} & \boldsymbol{K}_{\mathrm{ws}} \\ \boldsymbol{K}_{\mathrm{s^*b}} & \boldsymbol{K}_{\mathrm{s^*w}} & \boldsymbol{K}_{\mathrm{s^*s}} + K_{\mathrm{qo}} \end{bmatrix}_{n+1}^{(k)} \begin{Bmatrix} \Delta \boldsymbol{d} \\ \Delta[|\varepsilon|] \\ \Delta[u] \end{Bmatrix}_{n+1}^{(k+1)} = \begin{Bmatrix} -(\boldsymbol{f}_{\mathrm{int}}^e - \boldsymbol{f}_{\mathrm{ext}}^e) \\ -\mathcal{R}_{[|\boldsymbol{\varepsilon}|]}^e \\ -\Phi_{\mathrm{o}} \end{Bmatrix}_{n+1}^{(k)}, \tag{5.7}$$

or

$$\begin{bmatrix} \boldsymbol{K}_{\mathrm{bb}} & \boldsymbol{K}_{\mathrm{bw}} & \boldsymbol{K}_{\mathrm{bs}} \\ \boldsymbol{K}_{\mathrm{wb}} & \boldsymbol{K}_{\mathrm{ww}} & \boldsymbol{K}_{\mathrm{ws}} \\ -\boldsymbol{K}_{\mathrm{s^*b}} & -\boldsymbol{K}_{\mathrm{s^*w}} & -\boldsymbol{K}_{\mathrm{s^*s}} + K_{\mathrm{qc}} \end{bmatrix}_{n+1}^{(k)} \begin{Bmatrix} \Delta \boldsymbol{d} \\ \Delta[|\varepsilon|] \\ \Delta[u] \end{Bmatrix}_{n+1}^{(k+1)} = \begin{Bmatrix} -(\boldsymbol{f}_{\mathrm{int}}^e - \boldsymbol{f}_{\mathrm{ext}}^e) \\ -\mathcal{R}_{[|\boldsymbol{\varepsilon}|]}^e \\ -\Phi_{\mathrm{c}} \end{Bmatrix}_{n+1}^{(k)}, \tag{5.8}$$

depending on the status of the element is opening or closing. It worth reminding that the opening process and the closing process will never happen at the same time, i.e., $\Phi_{\mathrm{o}} \cdot \Phi_{\mathrm{c}} < 0$.

The matrix is solved at two levels, a global one and a local one. Since the traction-separation law and the closure criterion are both non-linear equations, Newton's method is used at the element level for the resolution of the internal variables $[|\boldsymbol{\varepsilon}|]$ and $[|\boldsymbol{u}|]$. It is assumed that the displacement field $\boldsymbol{d}$ remain constant during the resolution of the local system. So we have :

$$\mathcal{R}_{[|\boldsymbol{\varepsilon}|]}^e = \mathbf{0}, \tag{5.9a}$$

$$\Phi_{\mathrm{o}} = 0 \text{ or } \Phi_{\mathrm{c}} = 0. \tag{5.9b}$$

Once the equation (5.9) is solved at the element level, the following step is to resolve the global system. This procedure is based on a static condensation. The global equilibrium equation is calculated using an assembled stiffness matrix $\mathbb{K}_{\mathrm{sc}}$. Assuming that the equation (5.9) is now solved, we can get the modified stiffness matrix $\boldsymbol{K}_{\mathrm{sc}}$ for the element

in the opening procedure (Roubin et al., 2015):

$$\boldsymbol{K}_{\mathrm{sc}}\Big|_{n+1}^{(k)} = \boldsymbol{K}_{\mathrm{bb}} - \begin{bmatrix} \boldsymbol{K}_{\mathrm{bw}} & \boldsymbol{K}_{\mathrm{bs}} \end{bmatrix} \left(\begin{bmatrix} \boldsymbol{K}_{\mathrm{ww}} & \boldsymbol{K}_{\mathrm{ws}} \\ \boldsymbol{K}_{\mathrm{s^*w}} & \boldsymbol{K}_{\mathrm{s^*s}} + K_{\mathrm{qo}} \end{bmatrix}_{n+1}^{(k)} \right)^{-1} \begin{bmatrix} \boldsymbol{K}_{\mathrm{wb}} \\ \boldsymbol{K}_{\mathrm{s^*b}} \end{bmatrix}_{n+1}^{(k)} . \tag{5.10}$$

As we can see, the linearized system during the closure procedure Eq. (5.8) writes differently Eq. (5.7). Their main difference falls to the third row, which represents the strong discontinuity within each element. Assuming the local equation has been solved, i.e., $\Phi_{\mathrm{c}} = 0$, we have

$$\boldsymbol{K}_{\mathrm{bb}}\Delta\boldsymbol{d}\Big|_{n+1}^{(k+1)} + \begin{bmatrix} \boldsymbol{K}_{\mathrm{bw}} & \boldsymbol{K}_{\mathrm{bs}} \end{bmatrix} \begin{Bmatrix} \Delta[|\boldsymbol{\varepsilon}|] \\ \Delta[u] \end{Bmatrix}_{n+1}^{(k+1)} = -(\boldsymbol{f}_{\mathrm{int}}^{e} - \boldsymbol{f}_{\mathrm{ext}}^{e})\Big|_{n+1}^{(k)}. \tag{5.11}$$

Then the internal variables can be written in terms of the displacement:

$$\begin{bmatrix} \boldsymbol{K}_{\mathrm{ww}} & \boldsymbol{K}_{\mathrm{ws}} \\ -\boldsymbol{K}_{\mathrm{s^*w}} & -\boldsymbol{K}_{\mathrm{s^*s}} + K_{\mathrm{qo}} \end{bmatrix}_{n+1}^{(k)} \begin{Bmatrix} \Delta[|\boldsymbol{\varepsilon}|] \\ \Delta[u] \end{Bmatrix}_{n+1}^{(k+1)} = - \begin{bmatrix} \boldsymbol{K}_{\mathrm{wb}} \\ -\boldsymbol{K}_{\mathrm{s^*b}} \end{bmatrix}_{n+1}^{(k)} \Delta\boldsymbol{d}\Big|_{n+1}^{(k+1)}. \tag{5.12}$$

By removing the first matrix in this equation, we get :

$$\begin{Bmatrix} \Delta[|\boldsymbol{\varepsilon}|] \\ \Delta[u] \end{Bmatrix}_{n+1}^{(k+1)} = - \left(\begin{bmatrix} \boldsymbol{K}_{\mathrm{ww}} & \boldsymbol{K}_{\mathrm{ws}} \\ -\boldsymbol{K}_{\mathrm{s^*w}} & -\boldsymbol{K}_{\mathrm{s^*s}} + K_{\mathrm{qc}} \end{bmatrix}_{n+1}^{(k)} \right)^{-1} \begin{bmatrix} \boldsymbol{K}_{\mathrm{wb}} \\ -\boldsymbol{K}_{\mathrm{s^*b}} \end{bmatrix}_{n+1}^{(k)} \Delta\boldsymbol{d}\Big|_{n+1}^{(k+1)} \tag{5.13}$$

And combining the Eq. (5.11) and Eq. (5.13), the stiffness matrix $\boldsymbol{K}_{\mathrm{sc}}$ for the element in closure procedure writes as:

$$\boldsymbol{K}_{\mathrm{sc}}\Big|_{n+1}^{(k)} = \boldsymbol{K}_{\mathrm{bb}} - \begin{bmatrix} \boldsymbol{K}_{\mathrm{bw}} & \boldsymbol{K}_{\mathrm{bs}} \end{bmatrix} \left(\begin{bmatrix} \boldsymbol{K}_{\mathrm{ww}} & \boldsymbol{K}_{\mathrm{ws}} \\ -\boldsymbol{K}_{\mathrm{s^*w}} & -\boldsymbol{K}_{\mathrm{s^*s}} + K_{\mathrm{qc}} \end{bmatrix}_{n+1}^{(k)} \right)^{-1} \begin{bmatrix} \boldsymbol{K}_{\mathrm{wb}} \\ -\boldsymbol{K}_{\mathrm{s^*b}} \end{bmatrix}_{n+1}^{(k)} . \tag{5.14}$$

In summery, the global system is solved using the assembled matrix $\mathbb{K}_{\mathrm{sc}}$, with

$$\mathbb{K}_{\mathrm{sc}}\Big|_{n+1}^{(k)} = \mathop{\mathbb{A}}_{e=1}^{n_{\mathrm{e}}} \boldsymbol{K}_{\mathrm{sc}}\Big|_{n+1}^{(k)}, \tag{5.15}$$

similar assemblage also applied to the matrix $\mathbb{K}_{\mathrm{bb}}$.

In the assembled matrix, the modified stiffness matrix at the element level $\boldsymbol{K}_{\text{sc}}$ might be calculated by Eq. (5.10) or Eq. (5.14), depending on the element is in opening procedure or closing procedure. And using the static condensation, the resolving equations at global level writes as

$$\mathbb{K}_{\text{sc}}\Big|_{n+1}^{(k)} \Delta \boldsymbol{d}\Big|_{n+1}^{(k+1)} = -\underset{e=1}{\overset{n_{\text{e}}}{\mathbb{A}}} \{\boldsymbol{f}_{\text{int}}^{e} - \boldsymbol{f}_{\text{ext}}^{e}\}\Big|_{n+1}^{(k)}. \tag{5.16}$$

From Eq. (5.10) and Eq. (5.14), we can see that the stiffness matrix $\mathbb{K}_{\text{sc}}$ has the same size of matrix $\mathbb{K}_{\text{bb}}$, which equals to the size of the global system no matter there is an enhancement or not. Hence the required memory only depends on the number of elements or the number of nodes of the global system. No matter how many heterogeneities presents in the system or how many elements begin to fail, the total degree of freedom remains the same. Therefore, this property allows the modeling of multi-cracking without increasing the to-be-solved size of the system.

It is recalled that at the local level, an element carrying strong discontinuity requires more solving time to resolve the non-linear equation. Therefore, an increasing number of crushed elements leads to an increasing solving time of the global system.

5.3 Resolution of the cohesive criterion

The cracks start opening after the localization occurs. It contains a harden function q_{o} to simulate the failure mechanism for a quasi-brittle material. It is assumed that the normal vector of the interface remains constant over the calculation. Being an equation in terms of the opening value $[u]$, the cohesive criterion can be reformed into (Roubin et al., 2015):

$$T_e + M[u] = \sigma_{\text{y}} \exp(-\frac{\sigma_{\text{y}}}{\mathcal{G}_{\text{op}}}[u]), \tag{5.17}$$

with

$$T_e = \left(\boldsymbol{K}_{\text{s}^*\text{b}} - \boldsymbol{K}_{\text{s}^*\text{w}} \boldsymbol{K}_{\text{ww}}^{-1} \boldsymbol{K}_{\text{wb}}\right) \boldsymbol{d}, \text{and} \tag{5.18}$$

$$M = \left(\boldsymbol{K}_{\text{s}^*\text{s}} - \boldsymbol{K}_{\text{s}^*\text{w}} \boldsymbol{K}_{\text{ww}}^{-1} \boldsymbol{K}_{\text{ws}}\right). \tag{5.19}$$

With the condition that normal vector $\boldsymbol{n}$ is constant, $\boldsymbol{K}_{\text{s}^*\text{b}}, \boldsymbol{K}_{\text{s}^*\text{w}}, \boldsymbol{K}_{\text{ww}}, \boldsymbol{K}_{\text{wb}}$ are constant matrix too. So T_e is a constant depending on d in a linear way. As for M, it is determined by the time traction vector $\boldsymbol{n}$ is defined. A solution can only be solved if $T_e > \sigma_{\text{y}}$ and $M < 0$. With the help of the Lamber W function (Corless et al., 1996) W_0,

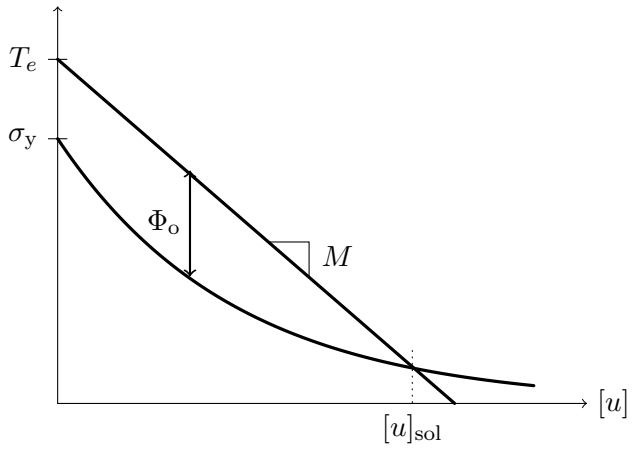

Figure III .16: Resolution of the strong discontinuity equation in the traction-opening procedure.

an analytical solution gives as:

$$[u]_{\text{sol}} = \frac{\mathcal{G}_{\text{op}}}{\sigma_{\text{y}}} \left(W_0 \left(\frac{\sigma_{\text{y}}^2 \exp(\frac{\sigma_{\text{y}} T_e}{\mathcal{G}_{\text{op}} M})}{\mathcal{G}_{\text{op}} M} \right) - \frac{\sigma_{\text{y}} T_e}{\mathcal{G}_{\text{op}} M} \right), \tag{5.20}$$

and the resolution is plotted in Fig. III .16.

5.3.1 Closure law

A closing process in the strong discontinuity of mode-I represents a decreasing value of the crack. The governing law for the closure mechanism is non-linear, and writes as:

$$\Phi_{\text{c}} = -\sigma_{\text{eq}} + q_{\text{c}}, \text{ with } q_{\text{c}} = \frac{\mathcal{G}_{\text{cl}}}{[u]_{\max}} \ln \left(\frac{[u]}{[u]_{\max}} \right). \tag{5.21}$$

In order to solve the equation at local scale (5.9), let us assume that the local system has already been solved, with $\mathcal{R}^e_{[|\boldsymbol{\varepsilon}|]} = 0$ and $\mathcal{R}^e_{[|\boldsymbol{u}|]} = 0$:

$$\boldsymbol{K}_{\text{wb}} \boldsymbol{d} + \boldsymbol{K}_{\text{ww}} [|\boldsymbol{\varepsilon}|] + \boldsymbol{K}_{\text{ws}} [u] = 0, \tag{5.22}$$

and

$$-\boldsymbol{K}_{\text{s*b}} \boldsymbol{d} - \boldsymbol{K}_{\text{s*w}} [|\boldsymbol{\varepsilon}|] - \boldsymbol{K}_{\text{s*s}} [u] + \frac{\mathcal{G}_{\text{cl}}}{[u]_{\max}} \ln \left(\frac{[u]}{[u]_{\max}} \right) = 0. \tag{5.23}$$

By replacing all terms of $[|\boldsymbol{\varepsilon}|]$ by $\boldsymbol{d}$ and $[u]$, we can obtain the following equation:

$$\left(-\boldsymbol{K}_{\text{s*b}} + \boldsymbol{K}_{\text{s*w}} \boldsymbol{K}_{\text{ww}}^{-1} \boldsymbol{K}_{\text{wb}} \right) \boldsymbol{d} + \left(-\boldsymbol{K}_{\text{s*s}} + \boldsymbol{K}_{\text{s*w}} \boldsymbol{K}_{\text{ww}}^{-1} \boldsymbol{K}_{\text{ws}} \right) [u] + \frac{\mathcal{G}_{\text{cl}}}{[u]_{\max}} \ln \left(\frac{[u]}{[u]_{\max}} \right) = 0. \tag{5.24}$$

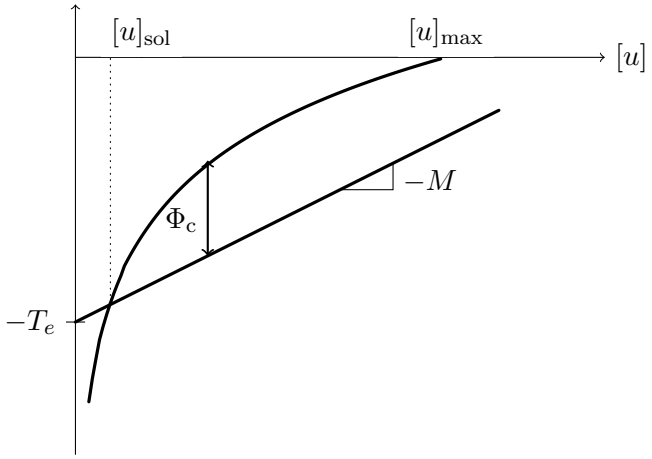

Figure III .17: Resolution of the strong discontinuity equation in the closing procedure.

Hence, we can reform this function into this shape:

$$-T_e - M[u] = \frac{\mathcal{G}_{\text{cl}}}{[u]_{\max}} \ln\left(\frac{[u]}{[u]_{\max}}\right), \tag{5.25}$$

and the analytical solution for $[u]$ can be solved as:

$$[u]_{\text{sol}} = -\mathcal{G}_{\text{cl}} W_0\left(-\frac{M[u]_{\max}^2 \exp(\frac{T_e[u]_{\max}}{\mathcal{G}_{\text{cl}}})}{\mathcal{G}_{\text{cl}}}\right) \Big/ \left(M[u]_{\max}\right), \tag{5.26}$$

and the resolution of the crack opening $[u]_{\text{sol}}$ is plotted in Fig. III .17.

Once the opening value $[u]_{\text{sol}}$ is determined, the value of weak discontinuity $[|\varepsilon|]_{\text{sol}}$ can be analytically calculated as (Roubin, 2013)

$$[|\varepsilon|]_{\text{sol}} = -\boldsymbol{K}_{\text{ww}}^{-1}\left(\boldsymbol{K}_{\text{wb}}\boldsymbol{d} + \boldsymbol{K}_{\text{ws}}[u]_{\text{sol}}\right) \tag{5.27}$$

6 Numerical implementation within the framework of Finite Element Method

In this section, we are going to evaluate and illustrate the performance of our model by applying the model to a finite element framework which uses 4-node tetrahedral elements. The discretization of tetrahedral elements has several superiorities. First of all, it leads to an exact representation of the constant stress problem due to the volume tessellation of the mesh. In addition, a complete kinematics behavior can be represented. Thus, it

carries favorable precision of the geometrical construction and mechanical behavior. In spite of these advantages, this more complex modeling carries some inconveniences which link to the layout of the enhancement.

In the implementation, the strain field and the stress field can be entirely determined by a 3×3 matrix or in its Voigt notation with six constant components. The stress field is generally computed from the displacement field by its symmetric gradient ∇^{sym}. As for the interpolation form, the standard part of the strain field is defined as:

$$\nabla^{\text{sym}}(\hat{\boldsymbol{u}}) = \boldsymbol{B}\boldsymbol{d} \;\rightleftharpoons\; \nabla^{\text{sym}}(\hat{\boldsymbol{u}}) = \sum_{a=1}^{4} \boldsymbol{B}_a \boldsymbol{d}_a, \tag{6.1}$$

where a represents the node at the element, and $\boldsymbol{d}_a$ is the displacement vector at node a. Afterwards, the interpolation matrix of the shape function derivatives wrote as:

$$\mathbf{B}_a = \begin{bmatrix} \frac{\partial N_a}{\partial x} & 0 & 0 \\ 0 & \frac{\partial N_a}{\partial y} & 0 \\ 0 & 0 & \frac{\partial N_a}{\partial z} \\ \frac{\partial N_a}{\partial y} & \frac{\partial N_a}{\partial x} & 0 \\ 0 & \frac{\partial N_a}{\partial z} & \frac{\partial N_a}{\partial y} \\ \frac{\partial N_a}{\partial z} & 0 & \frac{\partial N_a}{\partial x} \end{bmatrix}, \; a = [1..4] \tag{6.2}$$

In case of weak discontinuity, the element is divided into two parts, Ω^+ and Ω^-, by the heterogeneity interface Γ_d which is independent to the stress field. It is assumed that the discontinuity interface is flat and has a constant normal vector $\boldsymbol{n}$. Obviously, depending on the orientation of the interface and de volume of the sub-domain $V^{+|-}$, the shape of sub-domain $\Omega^{+|-}$ is not trivial, it could be polyhedron of 6 and 4, 5 and 5 or 4 and 6 nodes. Whereas the interpolation formulation involves only the volume of the sub-domain, thus the major attention is made on V^+ and V^-. It is recalled that the determination of the volume of sub-domain and the orientation of the interface is an issue purely geometrical regardless of the stress field.

Carrying a unique constant normal vector $\boldsymbol{n}$ of the discontinuity interface, a local orthogonal system can be constructed as shown in the figure III .18. Each component of the

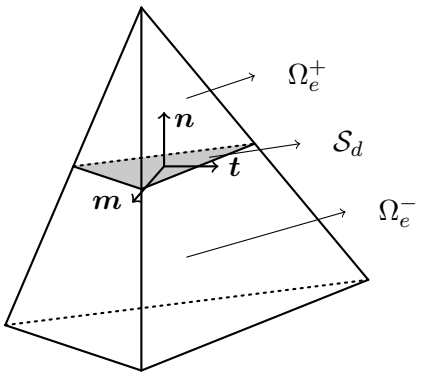

Figure III .18: Local orthogonal coordinate of the discontinuity interface in a tetrahedral element.

local system has its global coordinate system as $\boldsymbol{n} = \{n_x n_y n_z\}^T$.

Using the same Voigt notation, the interpolation matrix for weak discontinuity $\boldsymbol{H}_{\mathrm{w}}$ can be constructed as:

$$\boldsymbol{H}_{\mathrm{w}} = \begin{bmatrix} n_x^2 & n_x m_x & n_x t_x \\ n_y^2 & n_y m_y & n_y t_y \\ n_z^2 & n_z m_z & n_z t_z \\ 2n_x n_y & n_x m_y + n_y m_x & n_x t_y + n_y t_x \\ 2n_y n_z & n_y m_z + n_z m_y & n_y t_z + n_z t_y \\ 2n_x n_z & n_x m_z + n_z m_x & n_x t_z + n_z t_x \end{bmatrix}, \tag{6.3}$$

where the matrix is a constant matrix that only carries information on the interface vector $\boldsymbol{n}$. In case of exhibiting strong discontinuity, the actual strain field is enhanced using KES while the virtual strain field is enhanced using EAS, the corresponding interpolation matrix

are defined as the following equations:

$$\mathbf{G}^*_{\mathrm{s,b}} = -\frac{A}{V}\boldsymbol{H}^*_{\mathrm{s}} \text{ with } \mathbf{H}^*_{\mathrm{s}} = \begin{bmatrix} n_x & 0 & 0 \\ 0 & n_y & 0 \\ 0 & 0 & n_z \\ n_y & n_x & 0 \\ 0 & n_z & n_y \\ n_z & 0 & n_x \end{bmatrix}, \text{ and } \mathbf{G}_{\mathrm{s}} = - \begin{bmatrix} \frac{\partial \varphi_e}{\partial x} & 0 & 0 \\ 0 & \frac{\partial \varphi_e}{\partial y} & 0 \\ 0 & 0 & \frac{\partial \varphi_e}{\partial z} \\ \frac{\partial \varphi_e}{\partial y} & \frac{\partial \varphi_e}{\partial x} & 0 \\ 0 & \frac{\partial \varphi_e}{\partial z} & \frac{\partial \varphi_e}{\partial y} \\ \frac{\partial \varphi_e}{\partial z} & 0 & \frac{\partial \varphi_e}{\partial x} \end{bmatrix} \tag{6.4}$$

It is worth noting that an isotropic damage is applied in the model, i.e., a linear degradation on stress field, writes as:

$$\boldsymbol{\sigma} = \boldsymbol{\sigma} \cdot \exp\left(-\frac{\sigma_{\mathrm{y}} \cdot [u]}{3.0\ \mathcal{G}_{\mathrm{op}}}\right). \tag{6.5}$$

As we know, the increasing value of the crack opening will induce the degradation on the normal traction vector T_n. However, the kinematic mechanical behaviors that impose in the model is rather simple, the growing fracture in the finite element will not induce any failure behaviors on tangent stress. This limitation becomes non-negligible in compression tests, where the tangent stress plays a significant role in macroscopic responses of the material. Therefore, the isotropic damage allows the degradation on tangent stress.

After the explicit definitions of the interpolation matrix as introduced above, the algorithm for resolving the system is presented in algorithm 1. The resolution of the system is calculated on two levels, the element level and the global level. Following Eq. (5.7) and Eq. (5.8), the jump of strain field $[|\varepsilon|]$ and the jump of displacement field $[u]$ are computed as internal variables at the element level. During the resolution at fine-scale, it is assumed that the displacement field remain fixed. Then a modified stiffness matrix $\boldsymbol{K}_{\mathrm{sc}}$ is calculated for each element. The global system is resolved using the assembled matrix $\mathbb{K}_{\mathrm{sc}}$ as Eq. (5.16). A pseudo code for the algorithm is written in algorithm 1. Noting that $\bullet_i$ represents the i^{th} iterate .

Algorithm 1 Implementation for the system exhibits strong and weak discontinuity

$\boldsymbol{\varepsilon}^e = \boldsymbol{B} \cdot \boldsymbol{d}$, $\boldsymbol{\sigma}^e = \boldsymbol{C} \cdot \boldsymbol{\varepsilon}^e$
loop at the element level:
if no strong discontinuity exhibits in the element **then**
    if The element exhibits weak discontinuity **then**
        $\sigma_{\text{eq}} = \boldsymbol{n} \cdot \boldsymbol{\sigma}^e \cdot \boldsymbol{n}$
    else
        Calculate σ_{I} and $\boldsymbol{n}$, $\sigma_{\text{eq}} = \sigma_{\text{I}}$
    end if
    if $\sigma_{\text{eq}} > \sigma_{\text{y}}$ **then**
        The element admits a localization, $\Phi_{\text{l}} > 0$
        Calculate T_e and M (Eq. (5.19))
        Resolution of opening value $[u]_{i+1}$ (Eq. (5.20)) and $[|\boldsymbol{\varepsilon}|]$ (Eq. (5.27))
        goto *putout*.
    else
        The element stay elastic
        goto *putout*.
    end if
else
    Calculate T_e and M (Eq. (5.19))
    $\sigma_{nn} = T_e + M[u]_i$
    if $\Phi_{\text{o}} > 0$ **then**
        Resolution of opening value $[u]_{i+1}$ (Eq. (5.20)) and $[|\boldsymbol{\varepsilon}|]$ (Eq. (5.27))
        goto *putout*.
    end if
    if $\Phi_{\text{c}} > 0$ **then**
        Resolution of opening value $[u]_{i+1}$ (Eq. (5.26)) and $[|\boldsymbol{\varepsilon}|]$ (Eq. (5.27))
        goto *putout*.
    end if
end if
global system:
Calculate modified stiffness matrix $\boldsymbol{K}_{\text{sc}}$ for each element
Resolving the global system with assembled matrix $\mathbb{K}_{\text{sc}}$ (Eq. (5.16))

In order to verify the validation of the proposed model, we consider here an example with one single tetrahedral element with its length equals to 1.0 millimeter, see Fig. III .19. It is a homogeneous element. Thus it can have only the strong discontinuity. Applying an uniaxial tension at the node 2 towards to direction z, a discontinuity interface is obtained at the centroid of the element once the tensile strength of the material is reached, as shown in Fig. III .19(b). The normal vector of the discontinuity surface is determined by the major principal stress, in this case, following the direction of $(0, 0, 1)$.

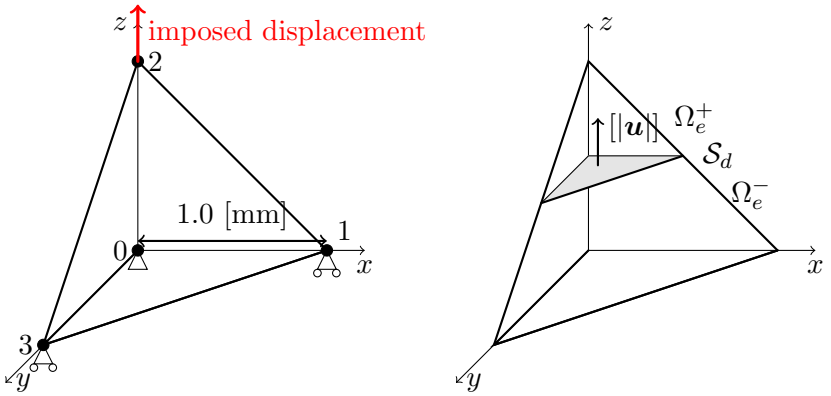

(a) Proposed element and its dimension (b) The discontinuity surface apparents in the element

Figure III .19: Basic geometric information and boundary conditions for the studied single tetrahedral element.

E [GPa]	ν [-]	σ_y [MPa]	$\mathcal{G}_{\text{op}}$ $[J/m^2]$
20.0	0.2	4.0	1.0 or 2.0

Table III .1: Considered material parameters for the single element.

The linear elastic parameters and failure parameters of the element are given in Table. III .1. Two fracture energies are considered to illustrate the effect of this parameter. The responses of the element are determined by the proposed mechanics, which contain the localization, the opening of the cracks and the closing of the cracks. Fig. III .20 represents a comparison between the analytical solutions and the numerical results for the two sets of parameters. As expected, the obtained results show a favorable coincide for

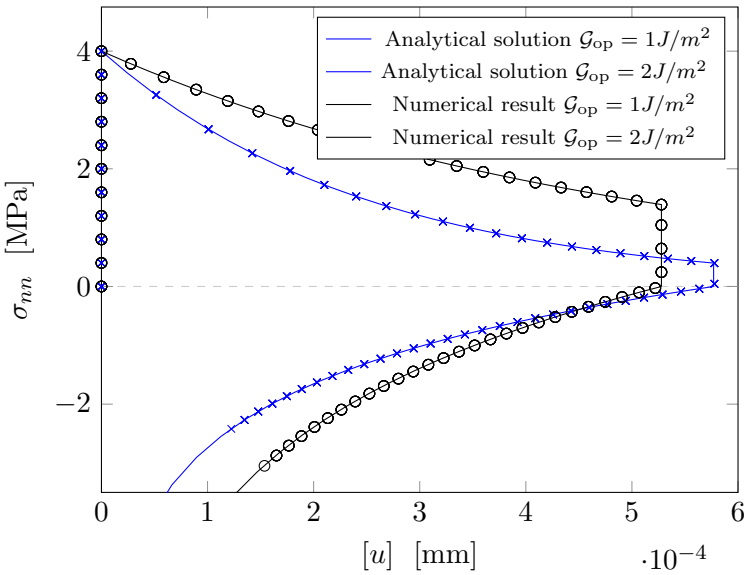

Figure III .20: Comparison between the analytical solution and the numerical result under uniaxial tensile loadings.

different fracture energies. And it can also be observed that, applying the same trajectory of displacement, the element which carries smaller fracture energy is more fragile. The crack opening develops faster than the other element.

Next, in order to investigate the performance of the closure law, let us apply a cyclic tensile loading to the same node to the model with or without closure law. Firstly, it can be seen from Fig. III .21 that for the same loading path, the two models have the same opening value $[u]$ during the opening procedure, which is reasonable, because they have the same traction-separation criteria. Secondly, focus on their most evident difference: the closure procedure. Owing to the closure law, the first model shows an ability to close the crack, and partially recovers the tensile strength. Shown in the figure, the decreased value of $[u]$ does not exist in the second model, which leads to a consequence that the model without closure law carries a much bigger value of the compression stress on the discontinuity interface. This value of the compression stress comes from the response of the bulk part $(\Omega^e \backslash \mathcal{S})$, which is considered as always elastic itself. In this context, the model with closure law will dissipate more energy not only in the closure procedure but also in the opening procedure.

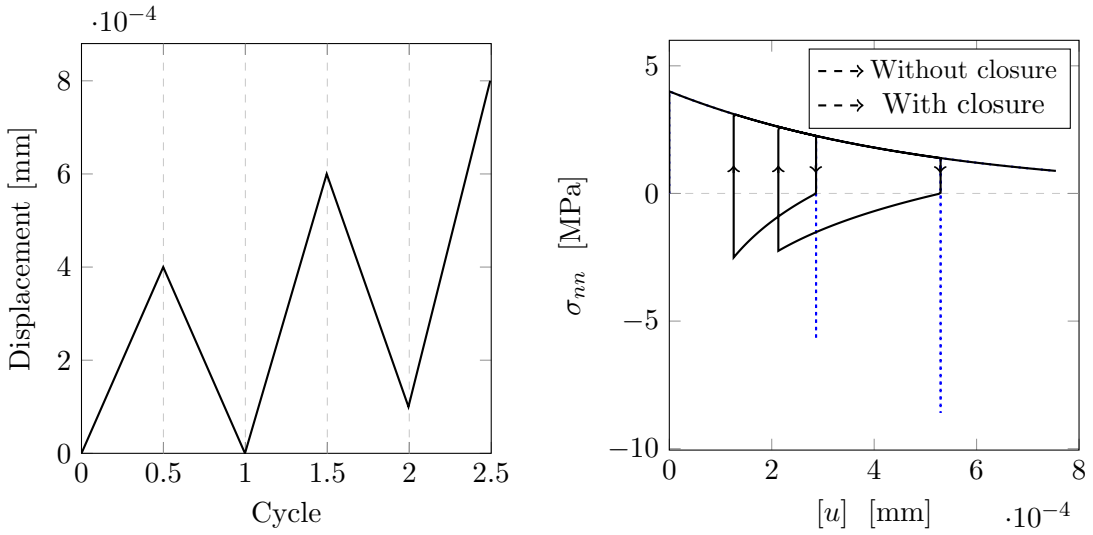

(a) (b)

Figure III .21: Comparison between the model with/without closure law for a single tetrahedral element with (a) the imposed cyclic loading path, the responses at the discontinuity surface are illustrated in (b).

7 Illustration of the performances of the model considering only the strong discontinuities

In this section, the attention is focused on the performance of the EFEM model, which considers only the strong discontinuity. The objective is to illustrate the effect of the proposed physical mechanisms on a homogeneous material. The effect of the exhibiting heterogeneities is not discussed in this part.

The considered specimen is in the shape of a cube, which is formed by five tetrahedral elements with its length equals to 1.0 millimeter. As shown in Fig. III .22, it is a very coarse and morphological simple model. The parameters of the material are written in Table. III .2.

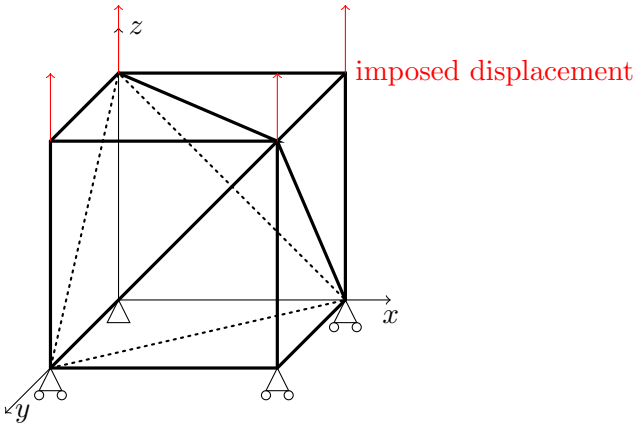

Figure III .22: Basic geometric information and boundary conditions for the cube which is formed by 5 tetrahedral elements.

E [GPa]	ν [-]	σ_y [MPa]	$\mathcal{G}_{\text{op}}$ $[J/m^2]$
20.0	0.2	4.0	2.0

Table III .2: Considered material parameters for each element in the cube.

In this case, a uniaxial cyclic loading is applied to the cube. For sake of simplicity, and comparable to the previous example, the loading path is the same as shown in Fig. III .21(a). The responses of the specimen are displayed in Fig III .23 by macroscopic stress (obtained by dividing the reactive force by the axial surface of the cube) in terms of the deformation (obtained by dividing the applied displacement by the length of the cube). In addition, more interests are made on the differences between the models in aspect of the energy.

First, it's evident that the macroscopic Young's module is the same as we apply to the material because the cube is homogeneous, and the tensile resistance of the sample equals precisely to the proposed failure strength, which is 4 MPa.

Second, the variations of the elastic energy, the dissipated energy, and the total energy are shown in Fig III .23(b) and Fig III .23(d). To associate directly with the responses of the material, which is plotted in stress versus strain, the used unit here for the energy is $[J/mm^3]$. The elastic part of the density of energy is obtained by $\frac{1}{2}\sigma^2/E^M$, corresponding

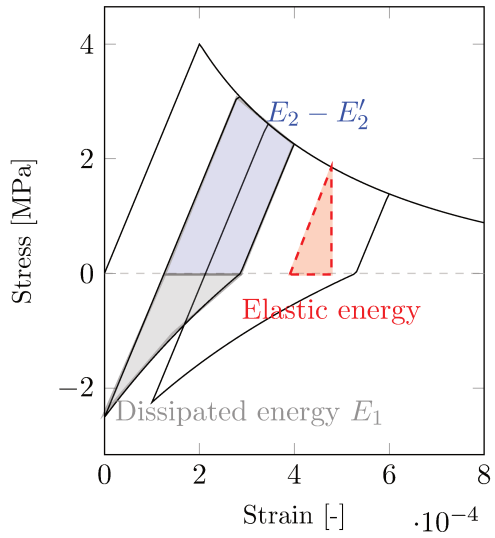

(a) Response of the model with closure mechanism

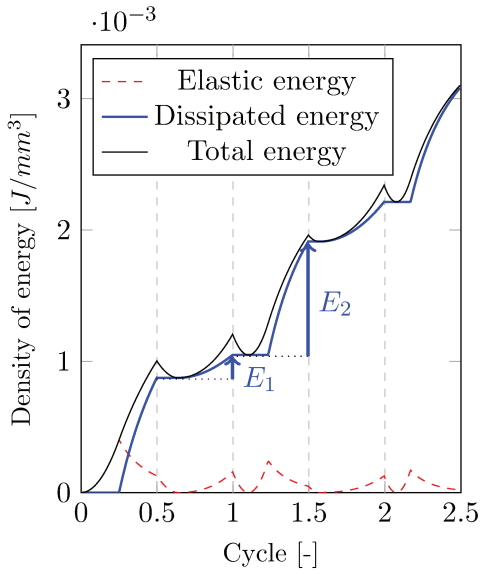

(b) Calculated energy for the model with closure mechanism

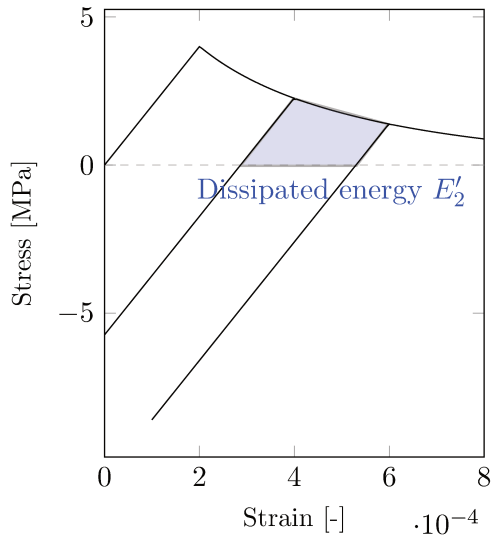

(c) Response of the model without closure mechanism

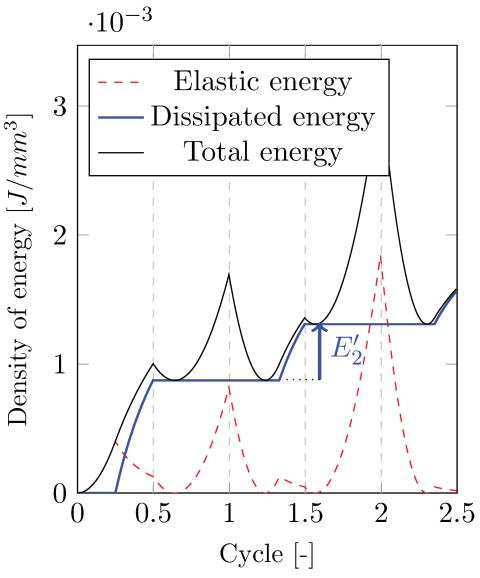

(d) Calculated energy for the model without closure mechanism

Figure III .23: Responses and calculated energies of the homogeneous specimen for the model with and without closure mechanism in tensile cyclic loading.

to the triangle surface in red in Fig III .23(a). It can be seen that for the model without the closure mechanism, there is a lot of elastic energy stored and released in the material. This is because the model carries a higher value of permanent opening, which leads to greater compressional stresses in unloading phases.

Finally, dissipating energy is an irreversible process, and it can be observed that the dissipated energy always remain increasing. And the model with closure law dissipates almost two times more energy compared with the model without adding closure law. Apparently, in the cycle from 0 to 0.5, the two models have exactly the performance in the aspect of the energy. The first difference comes from the unloading phase. As it is marked in Fig III .23(a), the area which notes as E_1 corresponds to the dissipated energy in the closing process for the model with crack closures. This increasing value can also be seen in Fig III .23(b). As for the model without crack closures, there is no energy dissipated in the unloading procedure.

Besides the additional dissipated energy in crack closures, the closure mechanism also induces more dissipated energy in the reopening procedure. As it is plotted in Fig III .23(b) and Fig III .23(d), the dissipated energy for the model with and without closure mechanism in the cycle 1 to 1.5 are marked as E_2 and E_2', respectively. Apparently, E_2 has a bigger value than E_2'. This difference between them comes from the required energy for reopening the crack, which is closed in the previous unloading phase. Drawn in Fig III .23(a), this additional dissipated energy corresponds to the area which is marked in blue.

According to the responses of the homogeneous specimen, we can see that the performances of the model without heterogeneous morphology is rather simple. And the failure behaviors of the specimen can only be observed in traction because the localization criterion is formulated based on the maximum principal stress. In the case of a homogeneous material, the stress field is also homogeneous, and the localization will never be activated.

8 Illustration of the performances of the model considering both the strong and weak discontinuities

It is a common sense that the macroscopic behaviors of concrete are complex. In the previous section, our model is applied to a simple homogeneous specimen. The perfor-

mance of the model is rather simple and unable to reproduce many observed behaviors of concrete. In this section, the effects of the heterogeneities are taken into consideration.

This section begins by applying the model to an example which carries a simple morphological structure. The used morphological model consists of one single spherical heterogeneity in the matrix. The interests are made on the emergent phenomena in the macroscopic scale and the crack patterns observed in the specimen. Then the model is applied to a material which carries a more complex morphological heterogeneous structure.

Note that for the following numerical examples, the uniaxial loadings are displacement-controlled and applied in the z-direction. The lateral faces (normal to x-direction and y-direction) are set as free-stress. For the interface elements between the heterogeneities and the matrix, the critical tensile strength is defined as the same as the matrix. The heterogeneities are considered as purely elastic for the sake of simplicity. Since the elastic parameters are defined differently for matrix and heterogeneities, there will be stress concentrations at the interface. Using the same failure parameter in the matrix and the interface elements will lead to a weaker behavior of the latter.

8.1 Cube with an internal sphere

The heterogeneous morphological structure of the concrete at the mesoscopic scale is complex which exhibits rigid aggregates and macroscopic pores. In this section, a cube with one single internal sphere is proposed, as shown in Fig. III .24. Two cases are considered: the internal sphere is more rigid compared to the matrix, representing the aggregate; or the internal sphere is considered as a macroscopic pore, carrying very weak elastic parameters. The parameters of the material are given in Table. III .3. The field is projected to a Finite Element mesh formed by tetrahedral elements, which has approximately 70 thousand nodes (see Fig. III .24). The used Finite Element mesh method is the non-adapted mesh strategy. In our model, the uniformed mesh is generated by GMSH Geuzaine and Remacle (2009). It will disperse a set of nodes in the field randomly, then links them to FE elements. Then the morphological structure is projected to this unstructured mesh, which produces three types of elements, representing the matrix, the heterogeneous, and the interfaces between them.

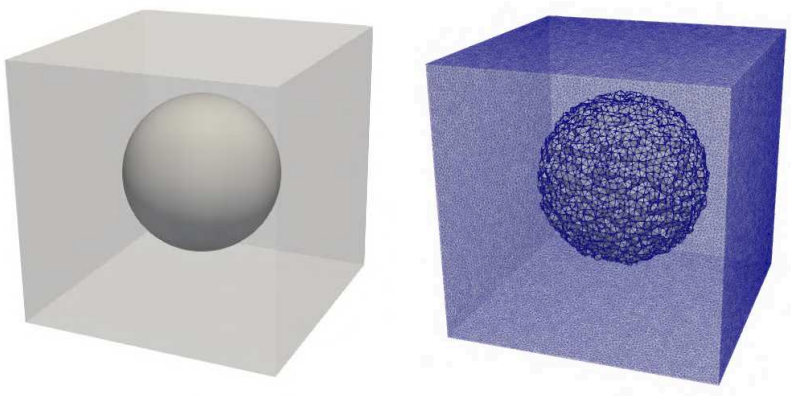

(a) Morphology of the cube with one single internal sphere

(b) Projection of the morphological structure to the finite element mesh

Figure III .24: Morphology of the cube with an internal sphere and its projection to the uniformed mesh.

Phase	E [GPa]	ν [-]	σ_y [MPa]	$\mathcal{G}_{\text{op}}$ $[J/m^2]$
Matrix	20.0	0.2	4.0	0.1
Interface	-	-	4.0	0.1
Aggregate	100.0	0.2	-	-
Pore	1.0×10^{-9}	0.2	-	-

Table III .3: Two sets of considered material parameters for the cube and its internal sphere.

The basic geometry informations of the cube give as:

- Length of cube: 100.0 millimeters
- Radius of the internal sphere: 30.0 millimeters
- Number of nodes and elements in the mesh: 73843 and 375785
- Maximum length of element: 4.5 millimeters
- Minimum length of element: 0.7 millimeters

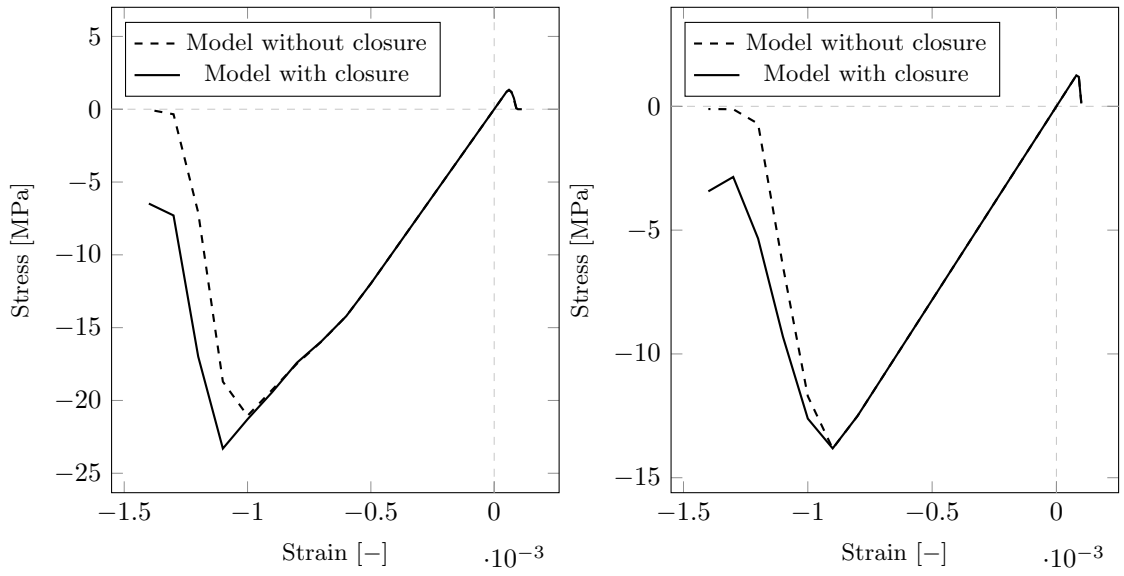

(a) The cube with rigid internal sphere

(b) The cube with an internal hole

Figure III .25: Comparison of the macroscopic responses between the model with/without crack closures for uniaxial loadings.

- Average length of element: 2.3 millimeters

A uniaxial loading is applied to the sample. The reaction of the specimen is plotted by the macroscopic stress versus the strain in Fig.III .25. We can see that first, the tensile and compressional loading have the same macroscopic Young's module, which equals to 24.067 GPa. As expected, this value is between the proposed Young's module of the matrix (20.0 GPa) and aggregate (100.0 GPa), which fits the Hashin-Shtrikman range (Hashin and Shtrikman, 1963)

Second, it is worth noting that for a pure homogeneous material like introduced in the previous section, the simple compression loading won't cause any failure, because the localization criterion at the local scale is based on the maximum principal stress. However, in this case, with a great number of elements and explicit representation of heterogeneity, the macroscopic failures can be observed in both traction and compression. And clearly, an asymmetrical macroscopic response for tensile and compressional loading can be seen, which is a typical propriety for quasi-brittle materials. Also, a reasonable ratio between the compressional strength and tensile strength can be estimated between 12.5 and 16.2.

Then focus is made on the effect of the closure mechanism. The differences between

the model with or without closure law are illustrated in Fig. III .25. In the aspect of the macroscopic responses, there are little differences between the two models in traction. Whereas in compression, it can be observed that the model with closure law behaves a more resistant feature. This phenomenon is related to the appearance of crack closures. To understand the resources of this observation, the crack patterns are analyzed in the following part.

The cube with a rigid internal sphere is applied to a traction loading. Before introducing the evolutions of crack patterns, it worth reminding that the traction-separation law is non-linear and monotonically decreasing. As the value of crack opening increases, the normal stress at the discontinuity surface decreases, which means that the required stress for continuing opening is smaller as the crack develops to a further position. It leads to a consequence that, for the elements at the center of major cracks, they tend to break faster than the element at the sides of the major cracks since they carry bigger values of crack opening. And the rapid development of the fractures at the center of major cracks induces stress releases at the upper and lower sides of the cracks, which activate the crack closures at these domains.

Therefore, in this case, two cracks are apparent on and under the internal sphere, which corresponds to the location of stress concentrations. Before the failure of the specimen, the stress fields adjacent to the two cracks are rather symmetric. Since the elements will become more fragile as the crack opening increases, the symmetric stress field loss balance between them as the softening procedure develops. And one of the macro-crack meets a catastrophic failure, which leads to stress release to another macro-crack. This variation of the macroscopic crack patterns can be easily observed in Fig. III .26.

We can see from Fig. III .27 that outside the two major cracks, there is non micro-cracks diffuse in the cube. The first explanation is that the fracture energy of the material is very small ($\mathcal{G}_{\text{op}} = 0.1 J/m^2$), meaning the material is fragile. And the second reason is that the stress concentration is highly localized. In order to illustrate the degree of closing, we show in Fig. III .27 the percentage of closure and the dissipated closing energy. The percentage of closure is calculated by

$$\#\text{ percentage of crack closure} = \frac{[u]_{\max} - [|\boldsymbol{u}|]}{[u]_{\max}} \times 100\%, \tag{8.1}$$

with $[u]_{\max}$ is the maximum crack opening values, and $[|\boldsymbol{u}|]$ is the value at current loading step. It can be observed that the crack above the sphere is almost totally closed, with the

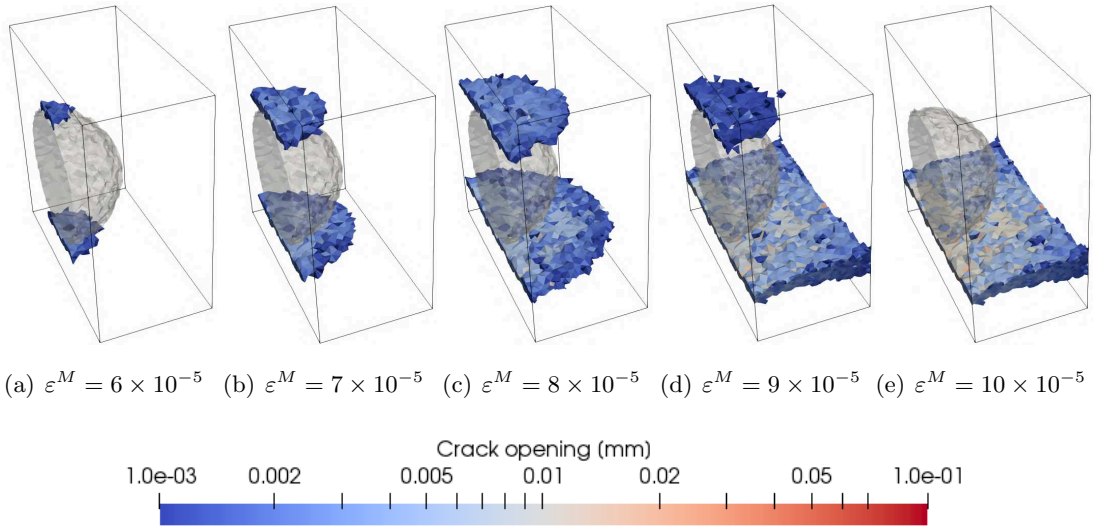

(a) $\varepsilon^M = 6 \times 10^{-5}$ (b) $\varepsilon^M = 7 \times 10^{-5}$ (c) $\varepsilon^M = 8 \times 10^{-5}$ (d) $\varepsilon^M = 9 \times 10^{-5}$ (e) $\varepsilon^M = 10 \times 10^{-5}$

Figure III .26: Variation of the macroscopic crack patterns for simple traction applying to the cube with rigid internal sphere (the cube is split into half in the lateral direction).

closing percentage almost reaches to 100%.

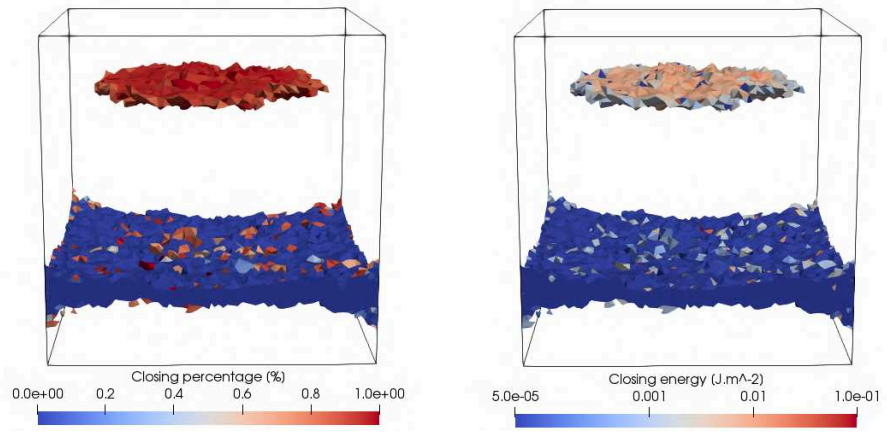

(a) Closing percentages (b) Dissipated energies at crack closures

Figure III .27: Illustration of the degree of closing for all localized elements at the loading step $\varepsilon^M = 10 \times 10^{-5}$.

The crack pattern in compression is more complicated compared to the reactions in traction tests. In Fig. III .28, we can see that the fractured specimen carries more cracks, which traverse the cube in the vertical direction. Since the very damaged elements in

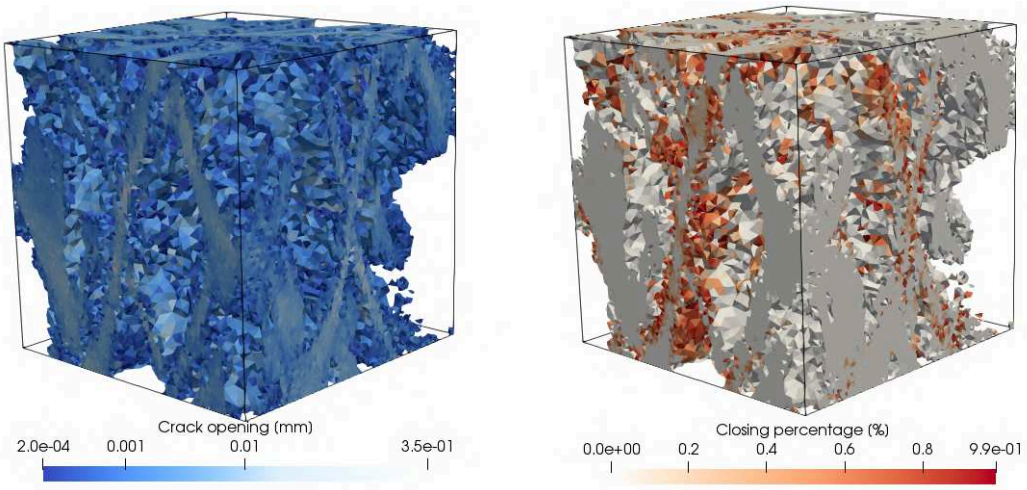

Figure III .28: Observed crack patterns of the cube with rigid internal sphere at the compressional loading of $\varepsilon^M = -1.4 \times 10^{-3}$ for the model with closure mechanism.

the center of major cracks carry higher values of crack opening, they have the priority to propagate faster than the other elements that are less damages. Hence stress releases will occur between two major cracks, leading to crack closures. Similar closing mode can also be observed in traction, see Fig. III .27. Besides the closing elements in the upper macro-crack, there are also several closing elements can be seen in the area which is adjacent to the lower macro-crack.

Next, we apply a negligible Young's module to the internal sphere, representing a macroscopic pore in the matrix. A similar crack pattern can be observed in this case. We can see from Fig. III .29 that only one macro-crack apparent in the middle of the cube. Hence, tiny elements obey a crack closure. These elements are closed because they are adjacent to a major crack, comparable to the closing elements in Fig. III .27 and Fig. III .28.

The above observations lead to a conclusion that the closure of cracks exist in not only cyclic loadings but also in uniaxial simple loadings. As the crack paths growth, the stress concentration between them will be released. Hence, the compression loading test brings a more numerous crack path, and triggers more closure of cracks, leads to a more resistant behavior at the soften part for the macroscopic response.

It has been introduced in the previous chapter that the unilateral effect is one of the

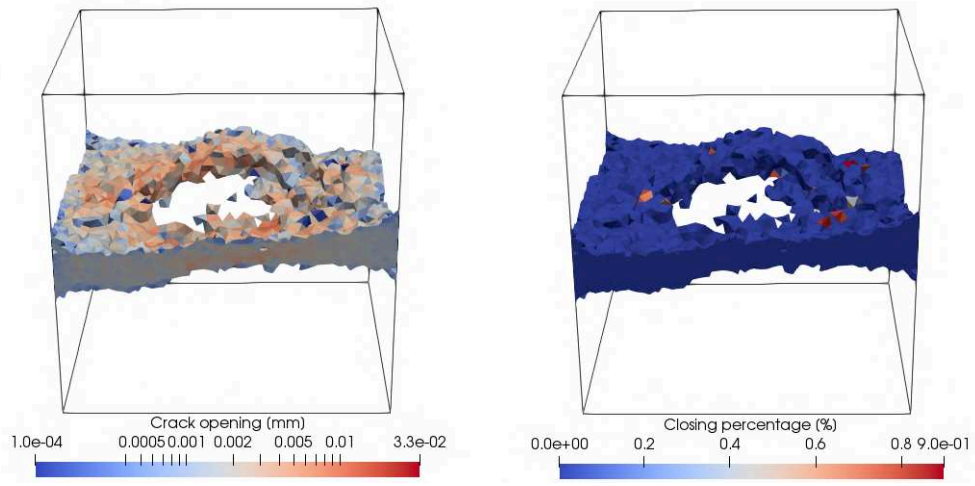

Figure III .29: Observed crack pattern of the cube with internal hole at the tensile loading of $\varepsilon^M = 10 \times 10^{-5}$ for the model with closure law.

typical characteristics of the concrete observed in experimental tests. The unilateral effect represents an effect that when the loading switches from tension to compression, the material has its stiffness recovered after been damaged. The proposed model is now tested in a trajectory that a traction loading switches to compression. We apply a loading-unloading displacement to the cube, which exhibits a rigid sphere. The macroscopic response of the model is plotted in Fig. III .30. To eliminate the influence of the isotropic damage, the model is tested without the isotropic damage.

As it is plotted in Fig. III .30, it can be observed that the model with crack closures has its stiffness recovered after been damaged at the traction loading, i.e., the unilateral effect can be observed. As for the model without crack closures, the elastic stiffness of the material seems has never been damaged by the development of cracks. This is because, for the EFEM model with strong discontinuities, damages and cracks take place at discontinuity interfaces, while the sub-domains always carry a pure elastic behavior. At the unloading phases, it can be seen that the stiffness of the material for the model with crack closures progressively recovers, and leads to a small plastic strain at the point (2). This plastic strain corresponds to the residual crack openings remain in the material at the stage of null stress. And for the model without crack closures, the fractured elements have their crack opening values remain constant. Thus the unloading phase is purely elastic, and higher residual openings lead to more significant plastic strain.

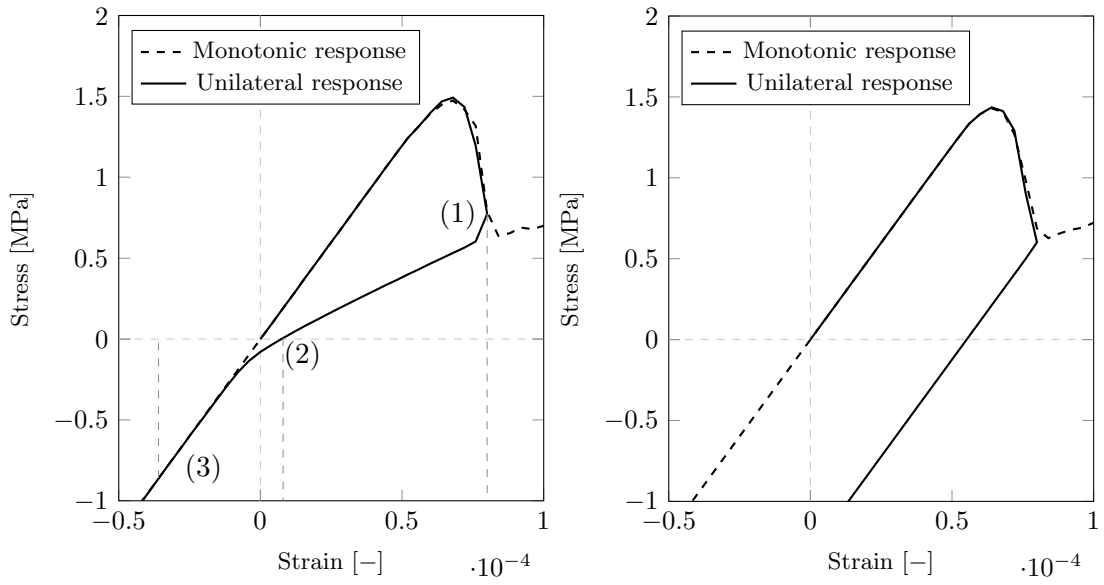

(a) Model with crack closures

(b) Model without crack closures

Figure III .30: Macroscopic responses of the cube with a rigid internal sphere under unilateral loadings for the model with/without crack closures.

We present the crack patterns of the material of three different loading steps in Fig. III .31. In order to illustrate the effect of crack closure mechanism, we put the material which exhibits a model with crack closures in the left and the model without closures in the right for comparing the differences between them. The chosen three loading steps are marked in Fig. III .30, with the macroscopic strain equals to 0.8×10^{-4}, 0.08×10^{-4}, and -0.36×10^{-4}.

It can be seen from Fig. III .31(a) that at the end of the traction loading, the material is heavily damaged with a major macroscopic crack traverses the cube. The crack patterns of the model with or without crack closures are quite similar. And in Fig. III .31(b), it can be seen that for the model with crack closures, there are a group of localized elements have closed while another still opening when the unloading phase arrives at the null stress stage. The plastic strain at the state of unloading is the consequence of these still opening elements. And in Fig. III .31(c), the fractured elements are completely closed as the loading switches to compression, the axial stresses are also turned into compression.

Unlike the model with crack closure mechanism, the model without crack closures produces the crack patterns that barely changed during the unloading and compression

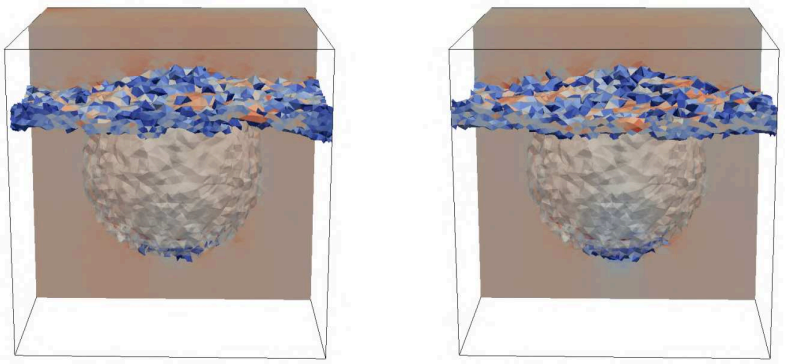

(a) At the stage of end of the traction loading corresponds to the point (1), where $\varepsilon^M = 8 \times 10^{-5}$

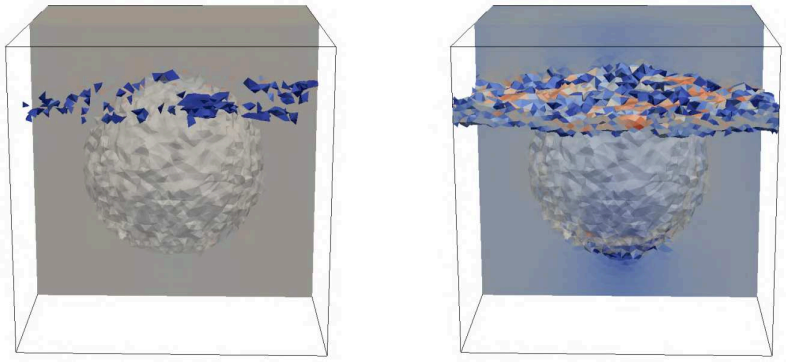

(b) At the state of null stress corresponds to the point (2), where $\varepsilon^M = 0.8 \times 10^{-5}$

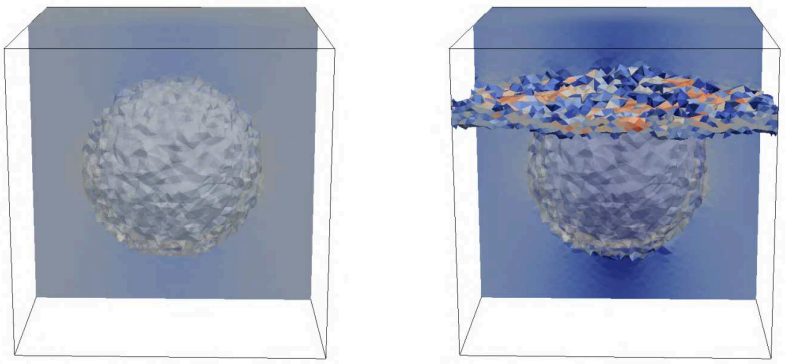

(c) At the state of compression loading corresponds to the point (3), where $\varepsilon^M = -3.6 \times 10^{-5}$

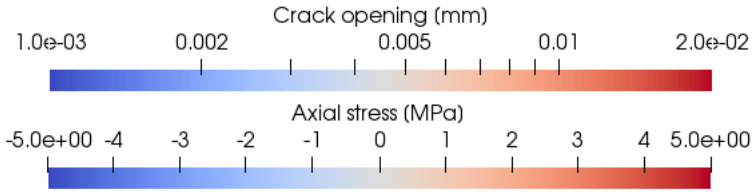

Figure III .31: Illustration of the crack and the axial stresses (shown in the demi-cube) of the cube with a rigid internal sphere at three different stages of unilateral loading, with the model with crack closures in the left and the model without closures in the right.

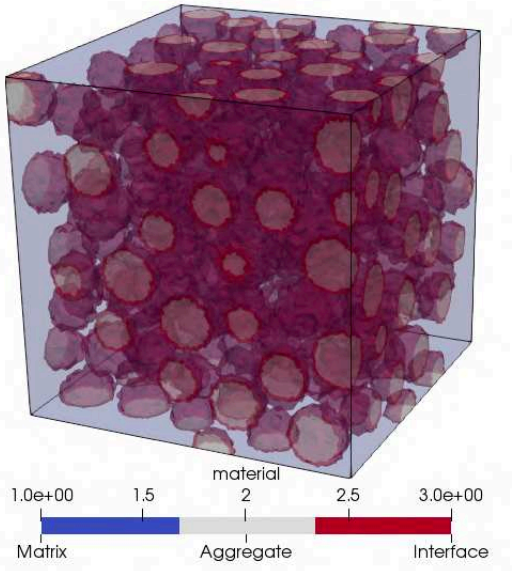

Figure III .32: Represent of the projection of the cube to mesh with aggregate disperse in the matrix and weakly enhanced elements between them.

loading. The already created cracks will not decrease. Speculated in the macroscopic response, as shown in Fig. III .30, the plastic strain always remain constant. And it induces to higher compressional stresses compared to another model.

8.2 Cube with structural morphological heterogeneities

Let us now consider a morphological more complex sample. It is proposed in this section a cube with its length equals to 100 millimeters. The heterogeneous morphological structure is represented by numerous spherical aggregates dispersed randomly in the cube and maybe touch the boundaries, as shown in Fig.III .32. The main idea of the used method (Vallade, 2016) is to generate N spheres of different radius and place them in the field while guaranteeing a minimum distance between each sphere.

The basic geometry informations of the cube give in the following list. It is worth noting that the maximum and average length of element is 3.3 and 1.5 [mm], et the minimum distance between each spheres is 4.0 [mm]. This ensures the correct representation of the weak discontinuity.

- Length of cube: 100.0 millimeters

Phase	E [GPa]	ν [-]	σ_y [MPa]	$\mathcal{G}_{\text{op}}$ $[J/m^2]$
Matrix	20.0	0.2	4.0	1.0
Interface	-	-	4.0	1.0
Aggregate	100.0	0.2	-	-

Table III .4: Considered material parameters for the cube and its rigid inclusions.

- Radius of the spheres: 5.0 to 8.0 millimeters
- Fraction volume: 20%
- Minimum distance between each two sphere: 4.0 millimeters
- Number of nodes and elements in the mesh: 203143 and 1031746
- Maximum length of element: 3.3 millimeters
- Minimum length of element: 0.4 millimeters
- Average length of element: 1.5 millimeters

The material's parameters are listed in Table. III .4. The aggregates are more rigid compared to the matrix, and always remain elastic themselves.

Applying uniaxial loadings to the cube, the responses of the specimen are displayed by the macroscopic stress in terms of the strain, see Fig. III .33. The model with and without closure mechanism are compared in this figure to illustrate the effect of crack closures. It can be observed that the macroscopic Young's module of this sample (approximately 2.6×10^4 Pa), which is bigger than the previous example. This is caused by a higher volume fracture of the aggregate, which carries more rigid elastic parameters.

In the previous example of the cube with an internal sphere, several typical behaviors of concrete can be observed. These behaviors can also be seen in this case of the cube which exhibits a more complex heterogeneous morphology. The asymmetric failure responses in traction and compression loadings can be observed in Fig. III .33. The differences between the model with or without crack closures are very slight for traction, and relatively more obvious for compression. To analysis the effect of the heterogeneous morphology, we

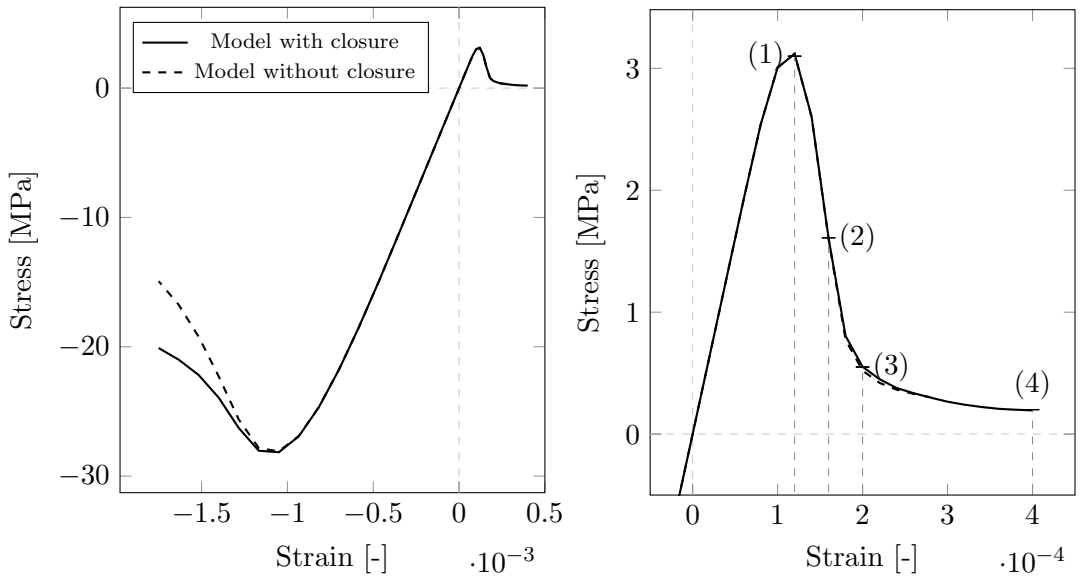

(a) The macroscopic response

(b) Zoom at the tensile responses

Figure III .33: The comparison between the model with/without closure law for the cube under monotonic loading.

choose here four loading stages along with the traction loading, which corresponds to the phase before failure, the phase after failure, relatively damaged phase and very damaged phase. The cracks at these four stages are shown in Fig. III .34.

Fig. III .34(a) plots the crack patterns at the loading stage number (1). It can be seen in Fig. III .33 that the macroscopic response at the stage (1) represents the maximum resistance of the material. A number of micro-cracks can be observed dispersed over the cube, especially beside the inclusions because of the stress concentration. There are no crack closure exhibits in the cube at this phase.

The cracks at the post-failure stage are shown in Fig. III .34(b), which corresponds to the stage (2). The failure behaviors of the specimen are closely related to the development of the macro-cracks. It can be seen that the number of cracks heavily increases, and the micro-cracks link with each other and form some macroscopic cracks and a very small number of crack closures apparent inside the material.

From the stage (3) to stage (4), the macroscopic response of the damaged material tends to steady, and the crack closures broadly develop inside the material. For the sake

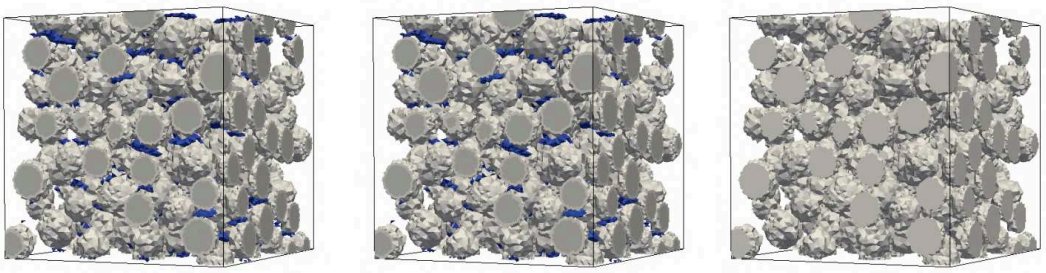

(a) $\epsilon^M = 1.2 \times 10^{-4}$ (point (1) in Fig. III .33)

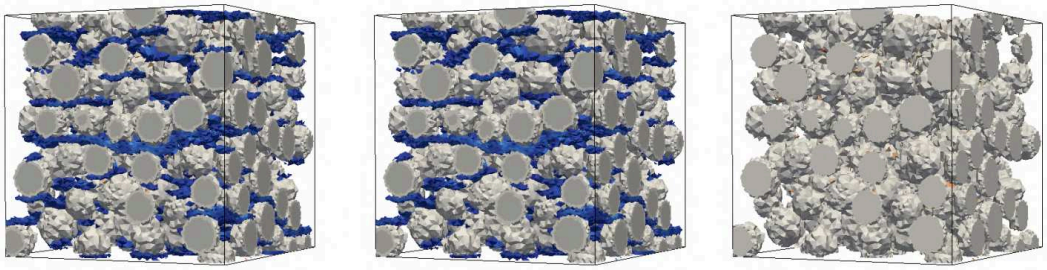

(b) $\epsilon^M = 1.6 \times 10^{-4}$ (point (2) in Fig. III .33)

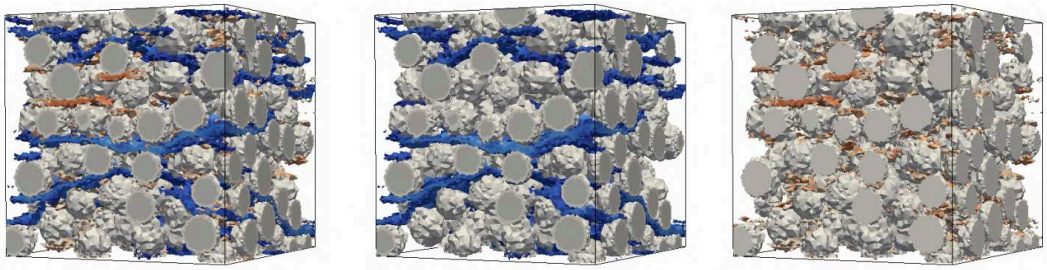

(c) $\epsilon^M = 2.0 \times 10^{-4}$ (point (3) in Fig. III .33)

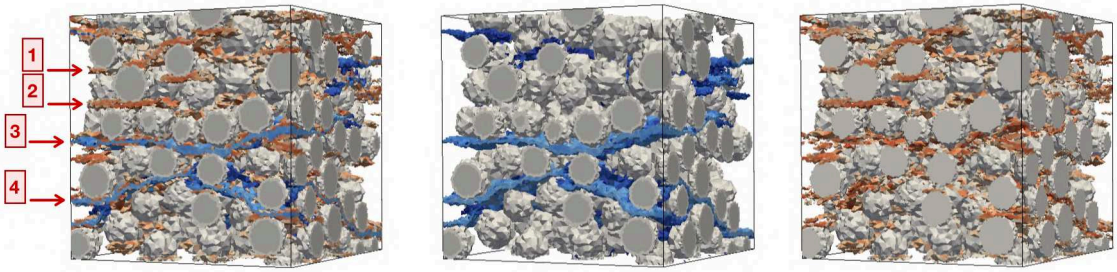

(d) $\epsilon^M = 4.0 \times 10^{-4}$ (point (4) in Fig. III .33)

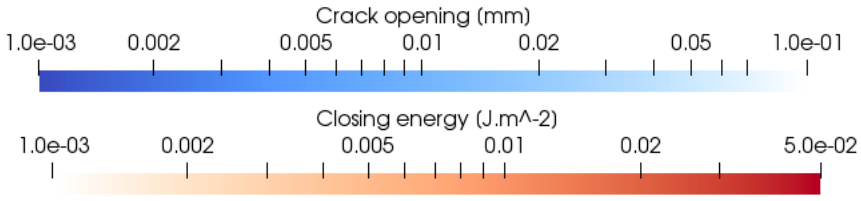

Figure III .34: Cracks (in the middle) and dissipated energy at crack closures (in the right) at four different loading stages for simple traction, they are overlaid in the left, and the rigid inclusions are marked in gray.

of clarity, we label four major cracks, see Fig. III .34(d). It has been introduced in the previous part that the crack closures are triggered by stress releases, and the stress releases are closely related to the development of the heavily fractured elements in the major cracks. Depending on the evolutions of major cracks, we can roughly classify the closing elements into two main categories.

The first crack closing patterns can be represented by crack 1 and 2, as shown in Fig. III .34(c). The crack 1 and 2 are situated in the upper or lower parts of other major cracks but not adjacent to them. The stress releases caused by the developments of other major cracks may lead to the crack closures of cracks. From Fig. III .34(b) to Fig. III .34(d), it can be seen that crack 1 and 2 are almost entirely closed. As for the model without closure law, the stress releases will not produce any crack closures. However, the consequences of the variations of the stress field can also be observed in Fig. III .35. We draw in this figure the increasing value of the crack opening from the stage (3) to the stage (4) (axial macroscopic strain from $\epsilon^M = 2.0 \times 10^{-4}$ to $\epsilon^M = 4.0 \times 10^{-4}$). It can be seen that crack 1 and 2 do not continue propagating as the loading increases.

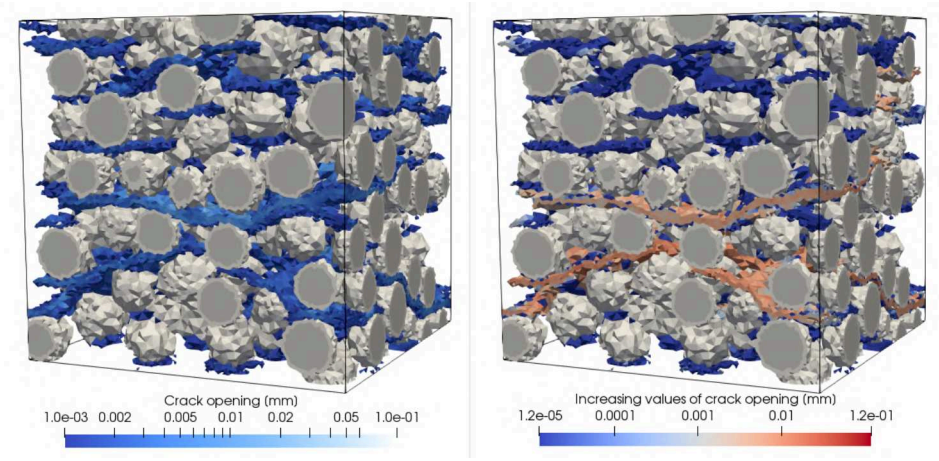

Figure III .35: Cracks for the model without closure law at the stage (4), and the increasing values of crack opening from the stage (3) to the stage (4).

The major cracks number 3 and 4 belong to another category of the closing pattern. Since elements at the center of cracks tend to develop faster than the others, the stress release will induce the crack closures for the elements adjacent to these cracks, see Fig. III .34(d). As for the model without closure law, it can be seen from Fig. III .35 that the increasing fractures are centered in the middle of the cracks 3 and 4. At the sides of these

major cracks, the crack opening values are barely enlarged. And compared with the model with closure mechanism, the cracks at the end of the loadings seem like more dispersed over the material, while the cracks for the model with crack closures are more centered.

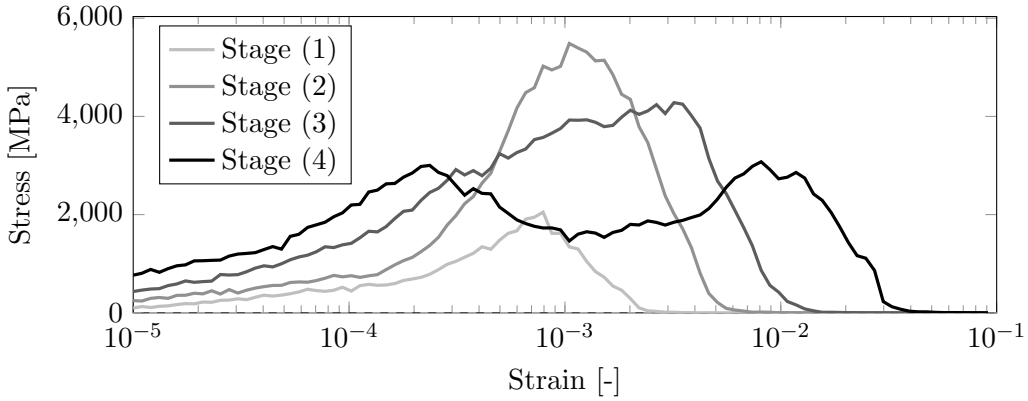

(a) Model with closure mechanism

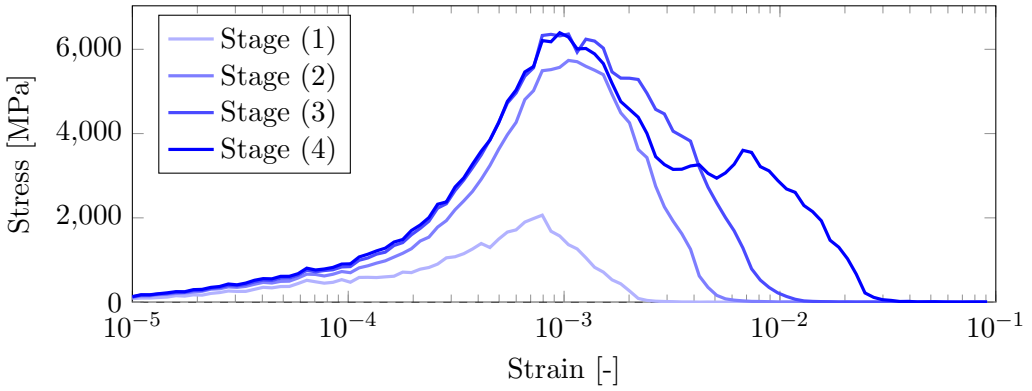

(b) Model without closure mechanism

Figure III .36: Distributions of crack opening values for the model with and without closure mechanism in traction.

We plot the variations of cracks for the model with and without closure law in two histograms of crack opening values, see Fig. III .36. For the model with crack closures, it can be seen that after the crack closures apparent in the material, i.e., after the stage (2), the number of the element which carries a bigger value of crack opening increases, and so does the element which carries a smaller value of crack opening. The former corresponds to the elements which exhibit already a relatively higher level of fracture, which are located at the center of major cracks, for example, the major cracks 3 and 4 in Fig. III .34(c). And the latter corresponds to the crack closures induced by stress releases, for example, the major crack 1 and 2 in Fig. III .34(d). As for the model without closure law,

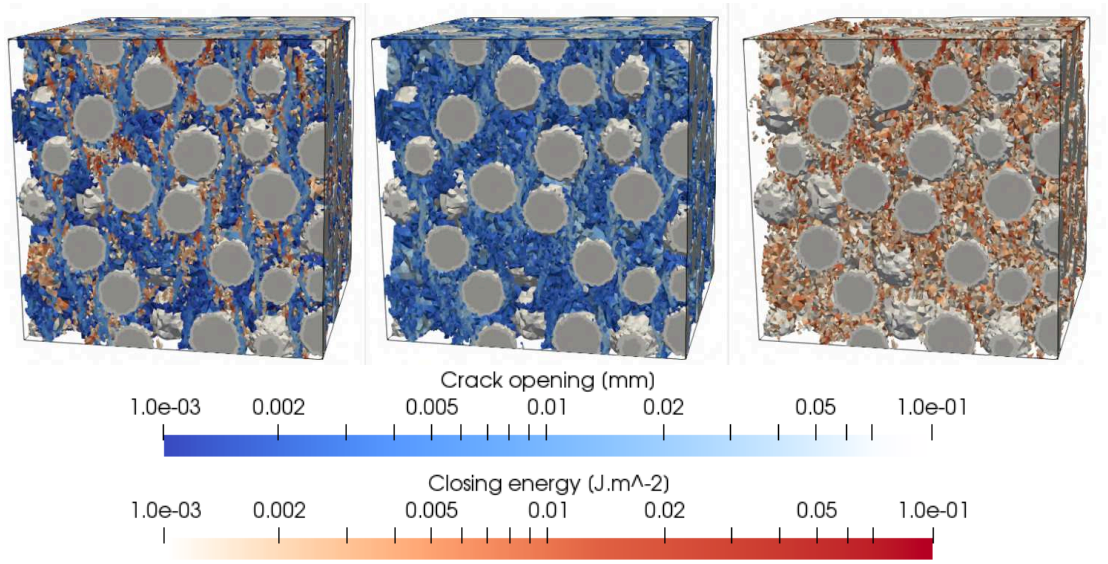

Figure III .37: Crack patterns in compression (in the middle) at the strain equals to -1.5×10^{-3}, the dissipated energy at crack closures (in the right) and the overlaid figure in the left, the rigid inclusions are marked in gray.

we can see from Fig. III .36(b) that it only carries an increasing number of the element which exhibits bigger crack opening value, and the number of the element which carries a relatively smaller crack almost remain constant.

As for the performance of the model in compression, we can see from Fig. III .37 that the crack patterns in compression is rather different. In compression, the cracks are generally parallel to the loading direction. And unlike in traction that the cracks are localized in failure area, the compressional crack pattern is more like distributed all over the specimen. The crack closures are observed located beside the major cracks.

Next, we apply a loading-unloading displacement to the specimen, to illustrate the ability of the model in the aspect of the unilateral effect. In the previous section, the unilateral effect has been examined in a cube which exhibits one single rigid aggregate. We present in this part, the performance of a morphological more complex material under a unilateral loading. The macroscopic responses of the model with crack closures is plotted in Fig. III .38(a). It is worth noting that the isotropic damage is eliminated in this case.

It can be seen in Fig. III .38(a) that, though the material is very damaged in traction, the elastic stiffness under compression is fully recovered after unloading. These observed

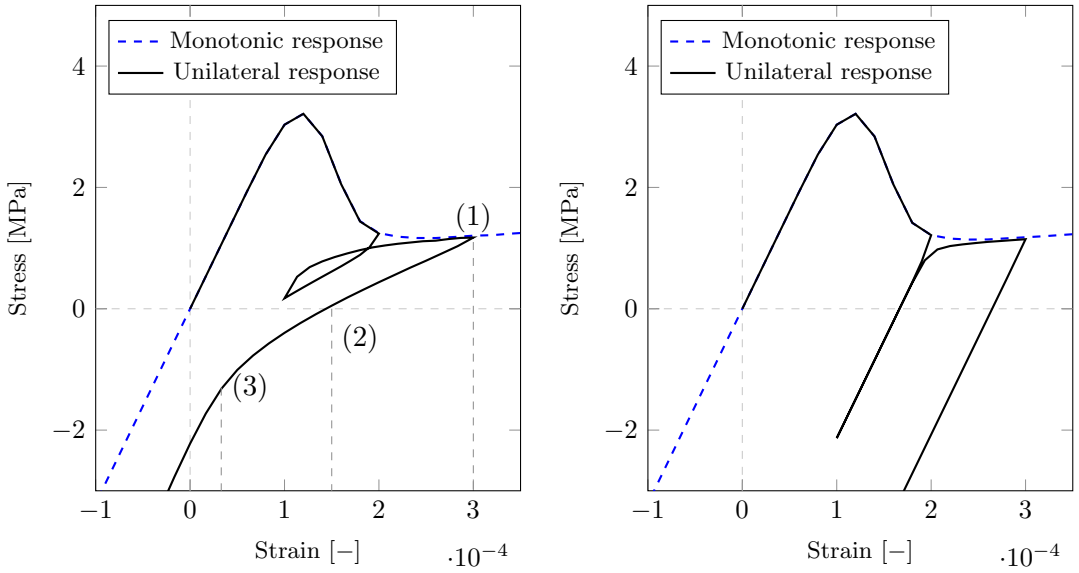

(a) Numerical simulation results of the model with closure mechanism

(b) Numerical simulation results of the model without closure mechanism

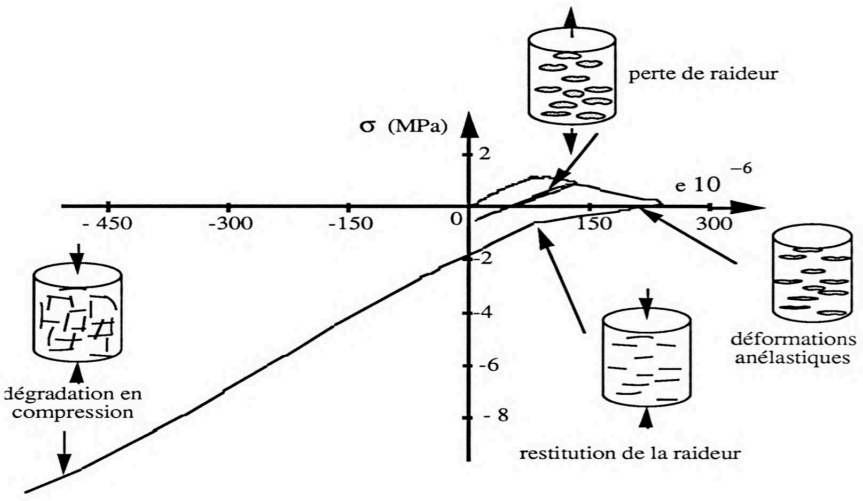

(c) Behavior of a concrete beam under low cycle bending Mazars et al. (1990)

Figure III .38: Illustration of the unilateral behaviors of concrete.

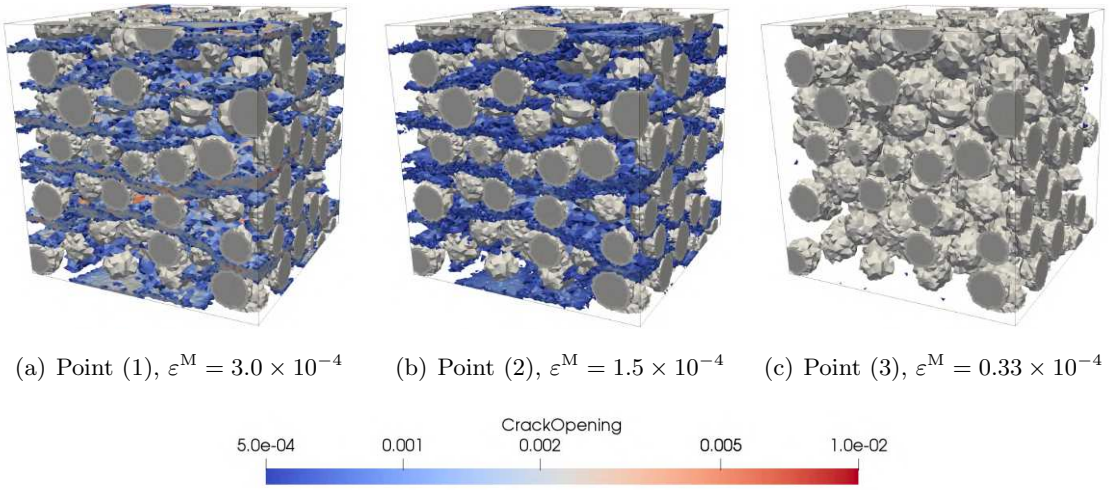

(a) Point (1), $\varepsilon^{\mathrm{M}} = 3.0 \times 10^{-4}$ (b) Point (2), $\varepsilon^{\mathrm{M}} = 1.5 \times 10^{-4}$ (c) Point (3), $\varepsilon^{\mathrm{M}} = 0.33 \times 10^{-4}$

Figure III .39: Variation of the cracks of the material during the unloading process in a unilateral test, the points are marked in Fig. III .38(a).

behaviors are linked with the closure of cracks, see the diagram in Fig. III .38(b). It is worth noting that the curve in Fig. III .38(c) illustrates the response of a concrete beam under cyclic bending, thus the curve itself is not comparable with our simulation results. The resources of the stiffness recovery and the plastic deformation, though, should be the same. It can be observed in Fig. III .38(a) that the stiffness of the material progressively recovered as the imposed tensile displacement reduces and changes to compressional displacement. Also, at the state of null stress, the material carries an amount of permanent opening. Compared with the model exhibits only one sphere that we presented in the previous section, the plastic strain is much more significant. This is because the fracture energy of the material ($\mathcal{G}_{\mathrm{op}} = 1.0 J/m^2$) is bigger than the fracture energy of the cube with an internal sphere ($\mathcal{G}_{\mathrm{op}} = 0.1 J/m^2$) in the previous section. Therefore, the material is more ductile and requires more energy to close the cracks. Besides the stiffness recovery and the plastic deformation, a hysteresis loop can also be seen in Fig. III .38(a), which is also consistent with experimental observations. This is related to the additional dissipated energy which is produced during the crack closures.

Interested in the crack patterns of the model with closure mechanism along with the unilateral loadings, we present the cracks of the material at different states in Fig. III .39. It can be noticed that the evolution of the crack patterns in Fig. III .39 shows a good consistent to the behaviors of concrete in Fig. III .38(c), that:

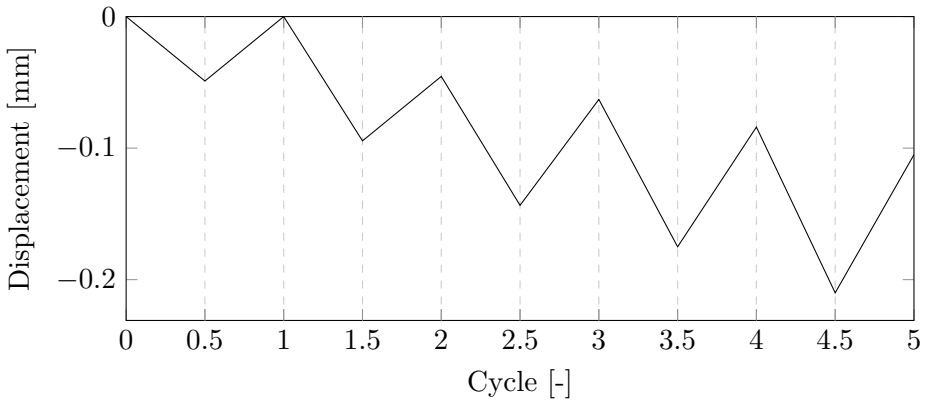

Figure III .40: Proposed displacement path for the cyclic loading.

- At the point (1), a large amount of crack openings apparent in the specimen, accompanied with the loss of stiffness of the material.
- At the point (2), the state of null stress, the cracks are partially closed while leading to an amount of plastic strain, the resource of which is the residual openings.
- At the point (3), the cracks are almost entirely closed, leading to the recovery of the stiffness of the specimen.

Now let us move our attention to the performance of the model under compressional cyclic loadings. The model is displacement-controlled, and the trajectory of displacement gives in Fig. III .40. It is a cyclic loading with increasing amplitude. The macroscopic response shows in Fig. III .41. It is worth noting that an isotropic damage is essential for compressional loading.

We can see from Fig. III .41 that both models, with and without adding closure law, allow the emergence of complex behaviors at the macroscopic scale, such as the volumetric dilatation and progressive loss of stiffness. It can be seen that the first unloading occurs in the elastic phase. Hence the material remains linear and elastic. Also, the curves of the responses under cyclic loadings are enveloped in the curves of monotonic loadings.

The effect of the closure mechanism can be illustrated by comparing the responses of the two models in Fig. III .41 and Fig. III .42. Among several differences between them, the most remarkable observation is the hysteresis phenomenon. The emergence of the hysteresis loops at the macroscopic scale takes its origin from several constituents on the

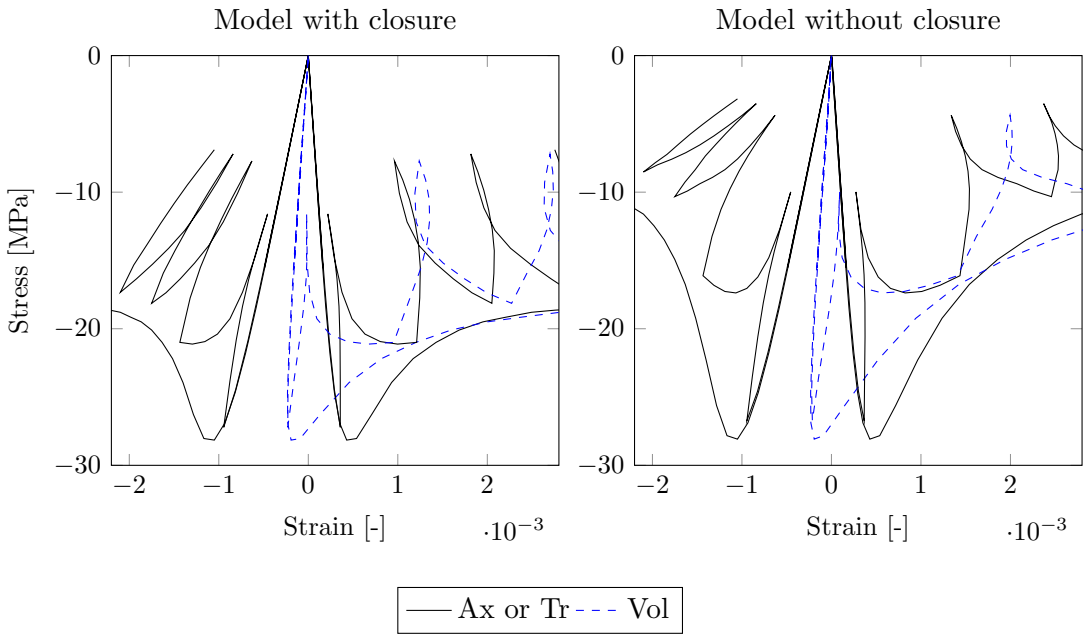

Figure III .41: Macroscopic response of monotonic/cyclic tests for model with/without adding closure law, in terms of axial (note Ax) transversal (note Tr) and volumetric strain (note Vol).

mesoscopic scale.

First, it can be seen that the model adding the closure law is more resistant after the first several cycles. The resource of this phenomenon is the partial recovery of the strength due to the crack closures, see the constitutive model at the fine-scale in Fig. III .15. Thus at the unloading phase, the model with closure law is capable of decreasing the value of crack opening, which leads to a part of stiffness recovery and a higher failure strength at the succeeding reloading phase.

Second, we can see from Fig. III .42 that the model with closure law loss less the stiffness of material compared with the model without closure. Displayed in the curves of response force shown in the figure, the model with closure law has 36% of the initial stiffness at the end of the loading, while the model without crack closure has 15.8% of the initial stiffness. This phenomenon is directly associated with the reducing values of crack openings. As it is mentioned in the previous part, an isotropic damage is obligatory, which links the degradation of Young's module with the crack opening value. Hence the model with crack closure has its stiffness of the material partially recovered after being applied

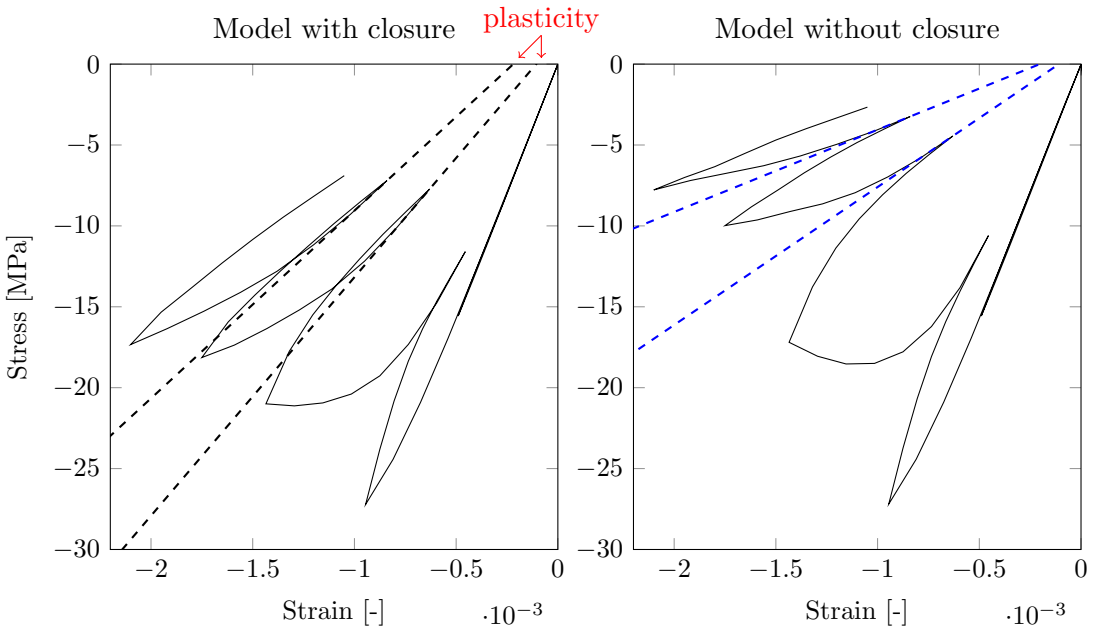

Figure III .42: Illustration of the loss of stiffness and the plastic deformation in cyclic loading for model with/without crack closures.

an unloading displacement.

Third, it can also be observed recording to Fig. III .41 that, the model with closure law has less dilatation effect. This observation is also linked with the reducing value of crack opening. The expansion of the material during failure is induced by the strong discontinuity of the type "opening" at local, and its leading emergence at macroscopic scale. The closure of the cracks can restrict the expansion.

Finally, the plasticity effects can be observed in the specimens during the degradation of the specimen. The model with crack closure carries slightly bigger plasticity at the end of the fourth cycle, which equals to $\varepsilon^p_{\text{with closure}} = 2.2 \times 10^{-4}$, while the value for the model without closure mechanism is $\varepsilon^p_{\text{without closure}} = 2.0 \times 10^{-4}$. It is worth noting that no plastic deformation is formulated in the constitutive model at the local scale. The observed plasticity is a result of the emergence from the meso-scale to macro-scale since the closing procedure brings additional dissipated energy.

In summary, the emergence of the hysteresis phenomenon has several resources, among which the most important ones are the partial recovery of the stiffness of the material and

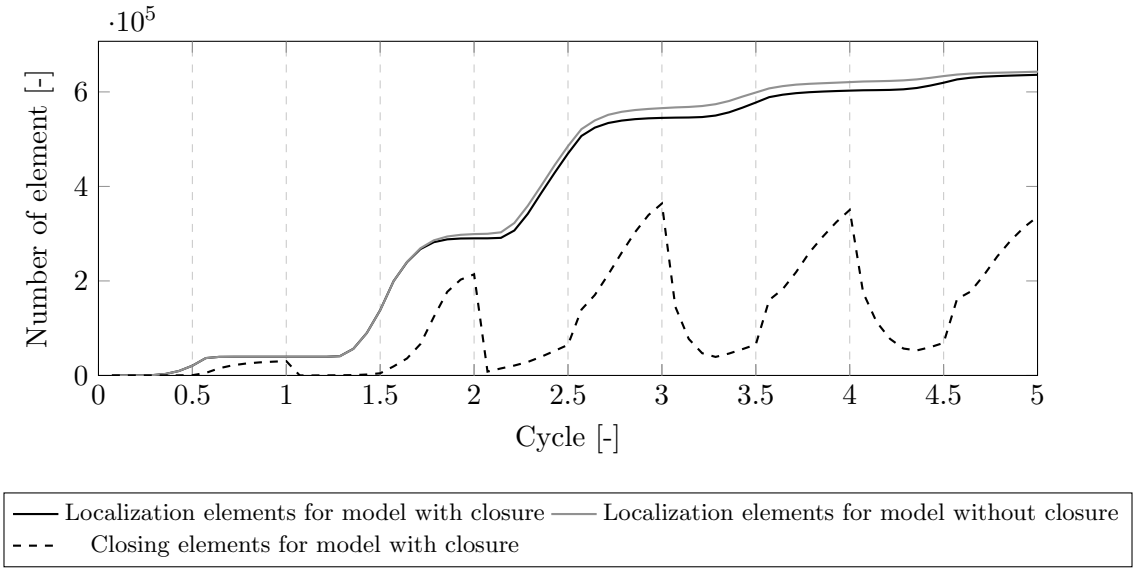

Figure III .43: Accumulate percentage of localized elements and closing elements along the 5 cycles for model with/without crack closure mechanism.

the additional dissipated energy. Also, both of them are part of the effects of the closure mechanism.

Next, we draw the variation of the number of localized elements and closing elements in Fig. III .43. First, as we can see from the figure, the model with and without crack closures both have an amount of fractured element at the first cycle, even the loading stays at the elastic phase. This is because, at this stage, there are micro-cracks scattered over the specimen, but not coalescent and form macroscopic cracks. Second, the figure shows a similar increasing tendency in the number of localized elements during the cyclic loading for both models. Such curves are observed because the localization criterion, which decides the appearance of the cracks, is formulated as the same for both models. Finally, it can also be observed that the number of closing elements for the model with crack closures increases and decreases during the cyclic loading, while the number of localized elements stay constant at the several last cycles. This declares that not all of the localized elements will turn to close state when unloading displacement is applied, the closing and reopening elements are the same groups of elements.

Thus far, this section has argued that, by applying simple mechanisms at the local scale (mesoscopic scale), intricate crack patterns can be seen at the macroscopic scale, and the propagations of cracks may influence each other. The existence of the explicit

heterogeneities induces stress concentrations, thus leads to different levels of damage for finite elements. The very damaged elements are weaker and more damageable. Hence the propagations of cracks are mainly gathered in the most damaged area. Moreover, the rapid development of fractures causes stress releases. Therefore, the crack closures can be observed even in monotonic loadings, which may take place at the sides of a major crack, or between other major cracks. Furthermore, in cyclic loading, the closure mechanism induces additional dissipated energy and stiffness recovery, which leads to the hysteresis phenomenon. Even the friction between the lips of cracks is not taken into concern, the fatigue behaviors of concrete can be observed by adding a closure mechanism at the local scale.

9 Numerical modeling and comparison with experimental results

We present in this section a reasonable comparison between the numerical simulation results and the experimental one, the performances of the developed model are tested by comparing it with experimental results. The experimental data is provided by Piotrowska (2013), which presents experimental results of concrete behavior under cyclic compressional loadings with different confinement levels. Also, three types of coarse aggregates are employed.

It is worth noting that in the following section, several simplifications are applied to the numerical simulations, regarding some limitations of our numerical model. On the one hand, the resolution of the EFEM model is static. Thus the rate of loading is not going to be taken into consideration. On the other hand, the using boundary conditions in numerical simulations are not the same as in experimental tests. In experimental tests, the axial loadings are performed by applying a constant displacement rate of 20 $\mu m/s$ to the specimens (Piotrowska, 2013). Indeed, there will be frictions between the concrete sample and the cap contacting the sample. In the following numerical simulations, for the sake of simplification, it is considered that no friction is taken into consideration. Besides these two points, the influences of the temperature, the humidity, and the maturity of the concrete, are also simplified and considered as negligible.

This section contains three parts. First, several morphological models are constructed regarding the formulations of samples and the type of aggregates. Second, it is presented

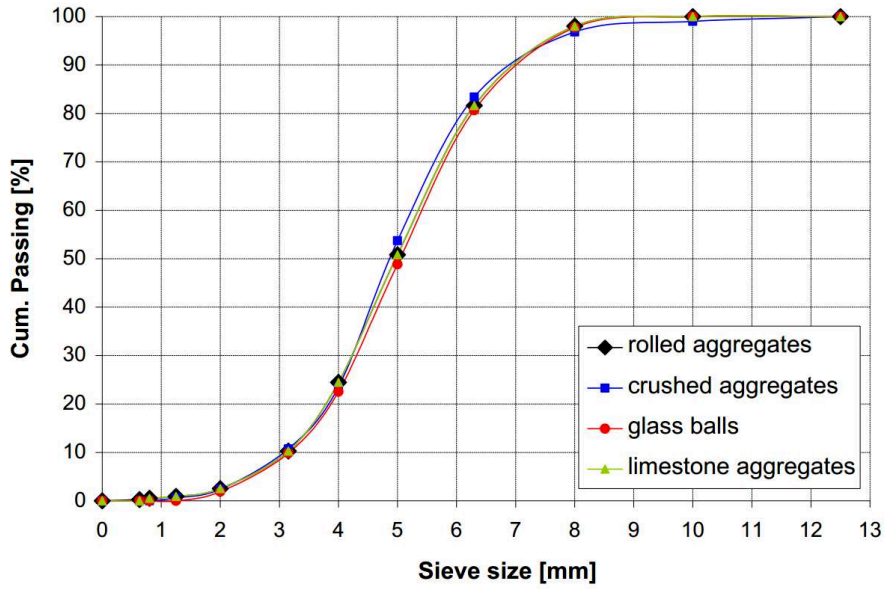

Figure III .44: Granulometry curves of coarse aggregates used in the studied concretes.

in this part the identification of material parameters. Then in the third part, the constructed models are applied to monotonic/cyclic compression tests and are compared to experimental results. Some details and analysis of the numerical simulation results are addressed in this final part.

9.1 Construction of the mesoscopic morphological models

9.1.1 Preparation of the specimens in experiments (Piotrowska, 2013)

The shape of the studied specimen is a cylinder of diameter 7 centimeters and height 14 centimeters. The length/diameter ratio equals to 2, which enables the specimen to be tested under high confinement pressure, and prevents the samples from buckling by limiting the influence of boundary conditions. The study provides investigations on three different concretes, which are distinguished by their type of aggregate:

- rolled aggregate concrete (SR): rolled siliceous aggregates derived from a natural deposit;
- crushed aggregate concrete (SC): crushed aggregates obtained from the siliceous rock;
- glass ball concrete (GB): glass balls.

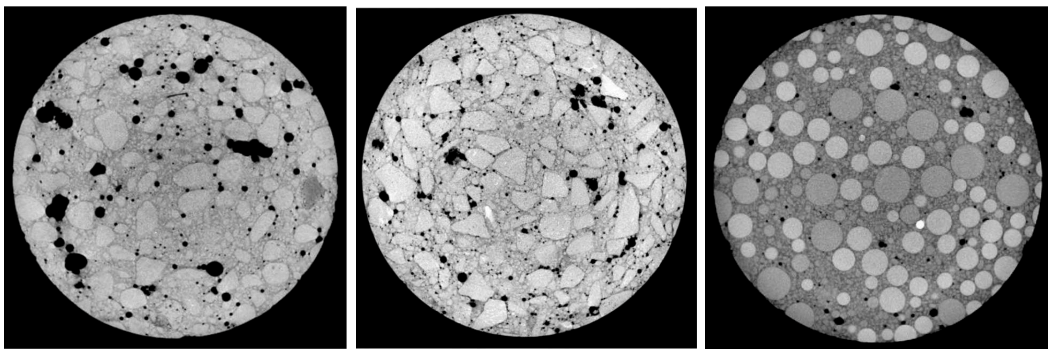

(a) Rolled aggregate concrete (b) Crushed aggregate concrete (c) Glass ball concrete

Figure III .45: Tomographic cross-sectional view of three concrete varying by coarse aggregate shape Piotrowska (2013).

Besides the type of aggregates, the concretes have the same cement matrix and the same volume fraction of aggregates to minimize variables. The distributions of the size of aggregates are arranged as similar as possible, see Fig. III .44.

The fabrication of the specimens is to cast the concrete into a 13.5-liter parallelepiped mold, after 28 days conservation, the block is then being cored and grounded into cylindric shape. Therefore, part of aggregates in the concretes will be cut. It can be seen in the images of X-ray tomographies Fig. III .45.

9.1.2 Construct morphological models using packing spheres

The first step of the numerical construction is to generate the morphological structure. The used method is to arrange N spheres of ranging size and put them randomly in the field (Vallade, 2016). Hence we have a set of spheres $b(r_i, d_i)$, with r_i represents the coordinate of the center of the sphere, and d_i the diameter. In a ranging size of spheres, the distribution of diameters is nearly linear. The next step is to move spheres in order to make sure that there is no overlap between them.

The construction of the numerical model with spheres fits well with the GB (glass ball) concrete. However, we are not able to generate complex shape articles in the field yet. Hence, we are going to construct a morphological model by using spheres for both SR (rolled aggregate) concrete and SC (crushed aggregate) concrete, and different criti-

Category	Diameter ranging [mm]	Relative percentage	Volume fraction
1	$[1.5, 4]$	22%	8.8%
2	$[4, 5]$	28%	11.2%
3	$[5, 6]$	25%	10%
4	$[6, 7]$	15%	6%
5	$[7, 9]$	10%	4%

Table III .5: Five categories that are used to generate morphological heterogeneities in GB concrete to reproduce the size distribution.

cal parameters of the interface are going to be used to represent the differences between coarse aggregates. We take the GB concrete as an example to represent the construction of the morphological model. According to provided information by PIOTROWSKA (Piotrowska, 2013), the volume fraction of the aggregates is 40%, which is chosen to be the same for three concretes. The diameter of glass balls varies from 1.5 millimeters to 9 millimeters, and the size of glass balls respect the granulometry shown in Fig. III .44. The packing spheres method (Vallade, 2016) allows us to generate a set of spheres which respect a linear distribution within the ranging size. Hence, in order to reconstruct the morphological heterogeneities in concrete with the same size distribution, the range of aggregates is divided into five categories, see Table. III .5.

The defined cylindric field is shown in Fig. III .46. Different colors distinguish the different categories' spheres. As it is mentioned in the previous part, we can see that spheres are scattered randomly in the field, and there is no overlap between them. A minimum distance between each aggregate is chosen to be 1.8 millimeters.

We generated three fields in the same setting (Table. III .5). The measured distribution of these generated fields gives in Fig. III .47. It can be seen that there are no obvious differences between these three generations. Also, it can be observed that for each category, the distribution of the size is nearly isotropic. Using five categories of range, we are capable to practically rebuild a similar enough morphological heterogeneities of the concrete shown in Piotrowska (2013).

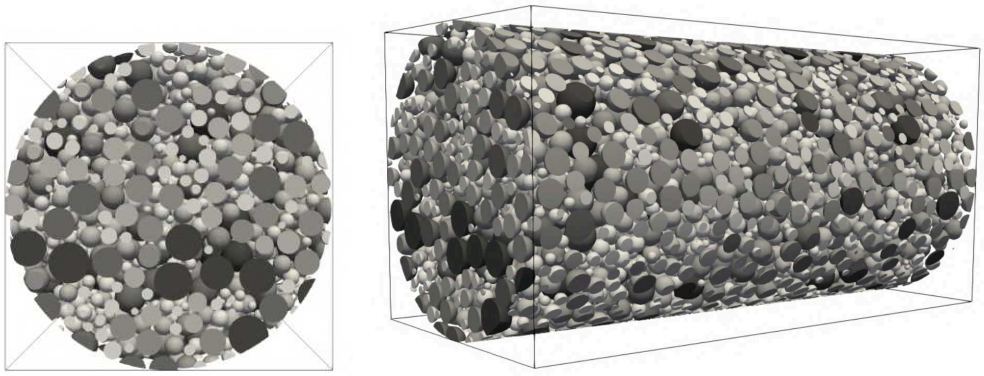

(a) The axial view of the defined field

(b) The 3D view of the defined field

Figure III .46: Generated field which is defined by five categories, aiming at representing the morphological heterogeneities of GB concrete.

Category	Diameter ranging [mm]	Relative percentage	Volume fraction
1	$[4, 5.5]$	52.6%	15.78%
2	$[5.5, 7]$	34.6%	10.38%
3	$[7, 9]$	12.8%	3.84%

Table III .6: Three categories that are used to generate morphological heterogeneities in GB concrete.

However, small diameters of spheres lead to an obligation of thin meshes. They are thus increasing the needed computation time and memory to an incredible level. Hence, in the numerical simulations of the following works, only the spheres of diameter bigger than 4 mm are considered as heterogeneities, see Fig. III .48. In this figure, the fully defined field with all five categories' spheres can be decomposed into two fields: the field containing spheres with a diameter bigger than 4 millimeters, and the field with small spheres (little than 4 millimeters).

As we know, the cracks tend to pass around the hard aggregates, which leads to highly tortuous features. We consider that this effect is less evident and is negligible for small

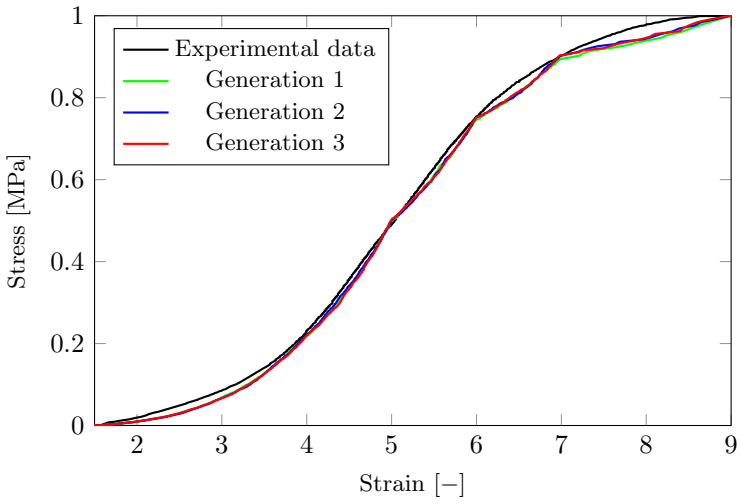

Figure III .47: Comparison of the GB concrete granulometry between the provided experimental data and three generated fields.

inclusions. Therefore, the homogeneous matrix of concrete is considered as a mix of cement paste and small aggregates, which can be considered as an RVE region, see the right figure in Fig. III .48. The modified heterogeneities are then generated using three categories, as shown in Table. III .6. The generated spheres and their distributions of size are given in Fig. III .50 and Fig. III .49.

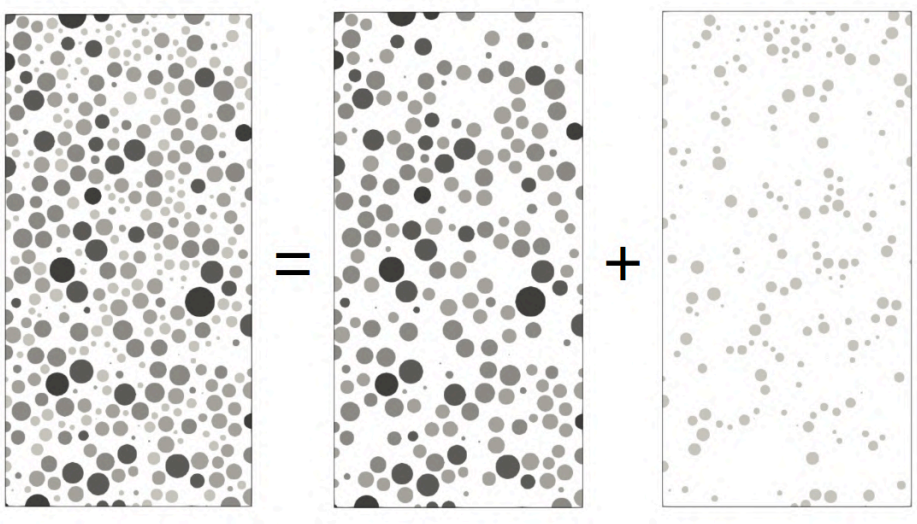

Figure III .48: Decomposition of the fulled defined considering the diameter of spheres is bigger or smaller than 4 millimeters.

In the previous part, we generated the morphological structures which represent the

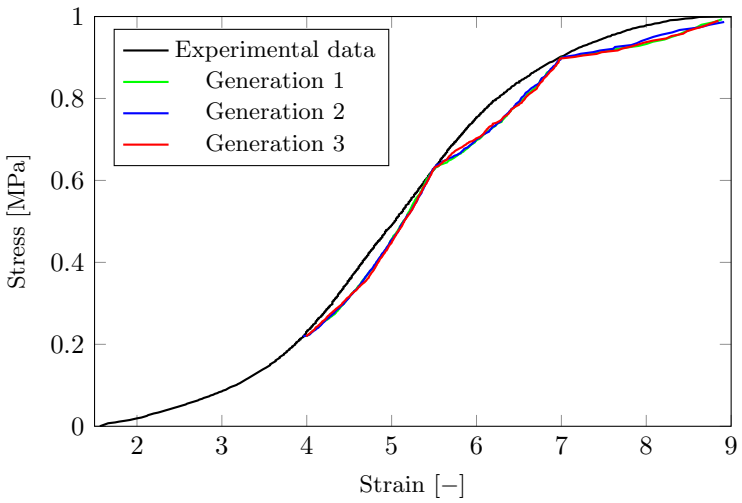

Figure III .49: Comparison of the GB concrete granulometry between the provided data and three generated fields using three categories.

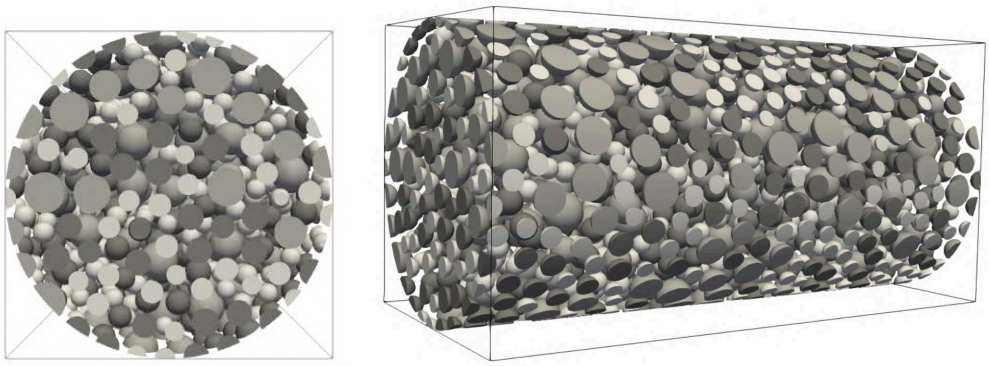

(a) The axial view of the defined field

(b) The 3D view of the defined field

Figure III .50: Defined field with three categories' ranging spheres, aiming at representing the morphological heterogeneities of GB concrete.

heterogeneities of concretes. The next step is to project the defined field onto the Finite Element mesh. The using method here is the GMSH method (Geuzaine and Remacle, 2009). The using mesh is uniformed and unstructured, with an average element size equals to 0.5 millimeters. This is to make sure that there will be maximum one weak discontinuity in a tetrahedral element and is capable of representing geometrical information of the smallest aggregates in the concrete. The used FE mesh carries 1.4 million nodes and 7.5 million elements. The projection is shown in Fig. III .51 and Fig. III .52.

As shown in Fig. III .51, the projection produces three types of inclusions, corresponding to the three categories used to identify size distributions. The concrete matrix is homogeneous and represented in blue. The non-adapted mesh method leads to a group of elements which are crossed by the interface between the matrix and the inclusions. As shown by the zoom in Fig. III .51(b), the interface elements of one inclusion do not overlap with the interface elements of another inclusion, meaning that each interface element contains only one weak discontinuity.

(a) The defined field with random morphology

(b) Projection of a random morphology

Figure III .51: Projection of the defined field for GB concrete onto the Finite Element mesh.

In summary, the construction of the mesoscopic morphological models contains several steps. First, we construct a defined field to represent the morphological heterogeneities of the concrete, which should contain the same volume fraction and granulometry. Second,

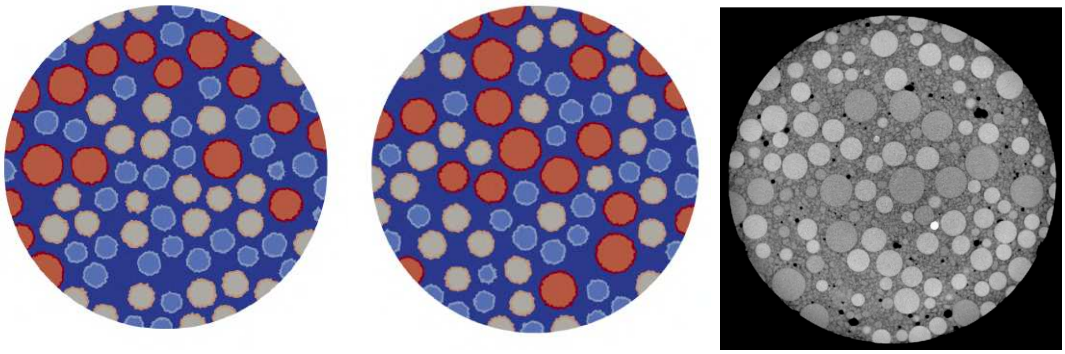

(a) Projection of a random morphology (b) Projection of another random morphology (c) Tomographical X-ray image

Figure III .52: Comparison between two projections and the tomographical X-ray image for GB concrete.

limited by the computational time and memory, it is practicable to only take into account the relatively big aggregates. Thus it is assumed that the homogenized matrix consists of the cement paste and the small aggregates. Last, the defined field is projected to the Finite Element mesh. We can see from Fig. III .52 that the constructed model reproduces similar morphological features as the real GB concrete.

It is worth noting that the concrete of interest has three different kinds of aggregates, GB, SC, and SR. Unlike the GB concrete, the SC and SR concrete have complex shapes for the aggregates, see Fig. III .45. We do not have a reliable method to generate complex shape inclusions for now. Hence, the packing sphere method is applied to construct models for all three kinds of concrete. The differences between inclusions are going to be represented by different critical parameters of the interface elements. Three morphological models are generated for each kind of concrete in order to eliminate the possible "unusual case" since the placement of spheres is random.

9.2 Identification of material parameters

This section aims at finding the correct parameters for the material to reproduce the observed experimental responses of the concrete. In the previous section, we have constructed morphological models for the studied concretes, which contain three different types of aggregates: SC, SR, and GB. The experimental responses of concretes are plotted in Fig. III .53. The macroscopic elastic properties and strengths are given in Table. III .7.

Concrete	SR	SC	GB
Young's modulus E [GPa]	33	33	32
Poisson's ratio ν [-]	0.16	0.16	0.16
Macroscopic compressive strength σ_c^{M}	40	43	33

Table III .7: The identified concrete characteristics in compression tests (Piotrowska, 2013).

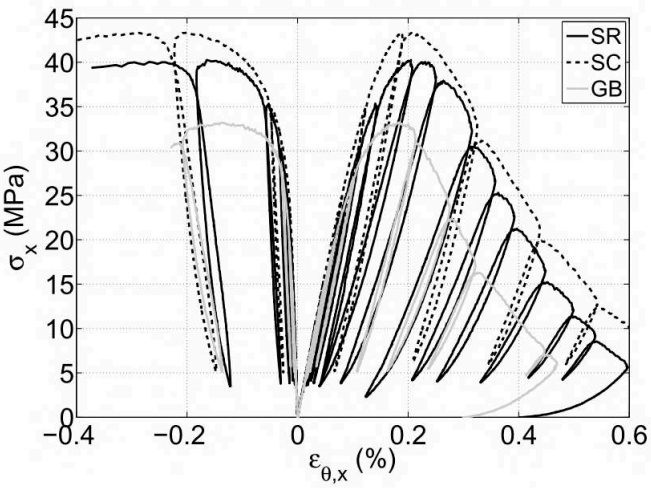

Figure III .53: Macroscopic responses of concrete in simple compression (Piotrowska, 2013).

As it is presented in previous parts, our numerical model consists of two materials: matrix and aggregates. Three different kinds of concrete are considered: the rolled siliceous (SR) concrete, the crushed siliceous (SC) concrete and the glass ball (GB) concrete. Among them, the aggregate of the type siliceous is the same for SR and SC concrete. The properties of the aggregates are summarized in Table. III .8.

For each kind of concrete, the morphological model consists of three types of elements: the matrix element, the aggregate element, and the interface element. As we can see from Table. III .8, the aggregate contains a much higher compressive strength compared with the concrete. Therefore, for the sake of simplification, we consider that the aggregates have a pure elastic behavior. In other words, there will not be any crack initiate in ag-

Aggregate type	Siliceous	Glass
Young's modulus E [GPa]	78	70
Poisson's ratio ν [-]	0.12	0.22
Macroscopic compressive strength σ_c^{M}	330	≈ 1000

Table III .8: The identified material characteristics of inclusions in compression tests (Piotrowska, 2013).

gregate elements. In summary, four unknown parameters are required to be identified to reproduce the observed responses in experiments, see Table. III .9. It is worth noting that, though the closure of cracks is also considered in the numerical model, no additional parameter is required to describe the closure behavior.

Elements type	E [GPa]	ν [-]	σ_{y} [MPa]	$\mathcal{G}_{\mathrm{op}}$ $[J/m^2]$
Matrix	E^1	ν^1	σ_{y}^1	$\mathcal{G}_{\mathrm{op}}^1$
Interface	E^1 & E^2	ν^1 & ν^2	σ_{y}^1	$\mathcal{G}_{\mathrm{op}}^1$
Siliceous aggregate	$E^2 = 78$	$\nu^2 = 0.12$	-	-
Glass aggregate	$E^2 = 70$	$\nu^2 = 0.22$	-	-

Table III .9: The known and unknown parameters of the element, with the unknown parameters are marked in blue color.

The unknown parameters of the material are identified by comparing with the experimental response for simple compressive loading. Among the four unknown parameters, Young's module E^1 and the Poisson's ratio ν^1 are determined in the elastic phase. The macroscopic response of the model should reproduce a good agreement of the concrete, as shown in Table. III .7. The work of Hashin and Shtrikman (1963) allows us to determine an upper and lower bound for the elastic modulus.

One of the important characteristics of the EFEM modeling is that the macroscopic

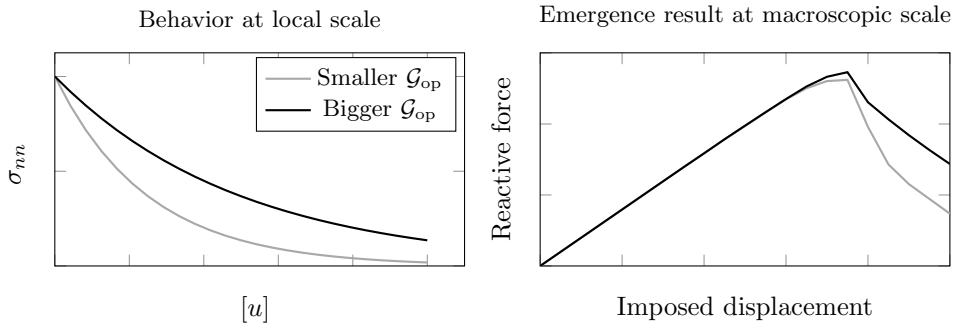

(a) Effect of the fracture energy $\mathcal{G}_{\text{op}}$

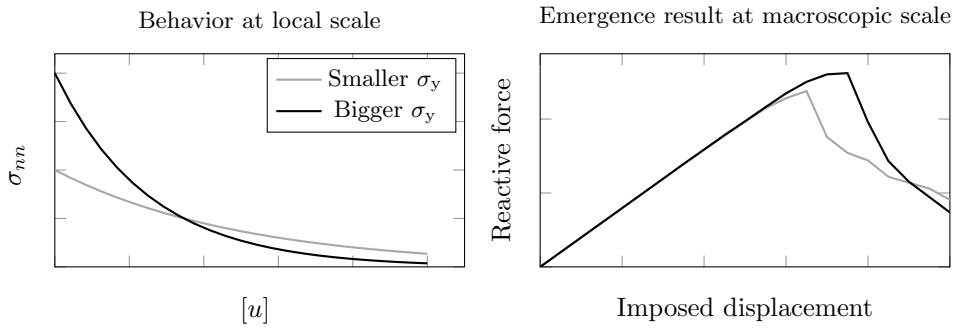

(b) Effect of the tensile strength σ_{y}

Figure III .54: Effect of the fracture energy $\mathcal{G}_{\text{op}}$ and the tensile strength σ_{y} at local scale and its emergent structural effect at the macroscopic scale.

behavior is a result of the structural effect brought by the heterogeneous character and a large number of elements. Thus the non-linear properties of the concrete are associated with both the critical strength σ_{y}^1 and the fracture energy $\mathcal{G}_{\text{op}}^1$ at the local scale.

The effect of the fracture energy $\mathcal{G}_{\text{op}}$ is plotted in Fig. III .54(a). At the local scale, the fracture energy describes the necessary energy to open the crack completely. The phenomenological effect of the fracture energy at macroscopic scale is that bigger $\mathcal{G}_{\text{op}}$ reproduces a slightly higher resistance, and higher reactive force at the softening stage.

The effect of the critical parameter σ_{y} is given in Fig. III .54(b). We can see that a bigger σ_{y} reproduces a higher macroscopic strength of the material. However, since they have the same fracture energy, a bigger σ_{y} brings to the material a more fragile behavior.

In summary, the response of numerical modeling is a result of emergence from the local scale to the macroscopic level. For instance, if we want the material to be less fragile, we can improve the value of the fracture energy $\mathcal{G}_{\text{op}}$ or reduce the critical tensile strength

σ_y. There might be more than one solutions to reproduces a good agreement between the numerical modeling and the experimental one. We are not going to list all of them. After the parameters of the material are identified in monotonic loadings, we are going to apply a cyclic loading to the model to compare its fatigue behaviors with the experimental results.

9.3 Comparison of the fatigue behaviors between the numerical modeling and experimental one

The morphological models have been established in the previous section. In this section, a comparison between the numerical simulations and the experimental results is presented. It worth recalling that the aggregates are considered as having pure elastic behavior; the cracks only initiate and propagate in matrix elements and interface elements. The parameters of the material are established by comparing with the experimental results under monotonic compressional loading. After the parameters of the material are defined, the concrete is applied to cyclic loadings. The identified parameters of the three types of concretes are listed in Table. III .10.

Concrete	E^1 [GPa]	ν^1 [-]	E^2 [GPa]	ν^2 [-]	σ_y [MPa]	$\mathcal{G}_{op}[J/m^2]$
SC	18.0	0.16	78	0.12	3.2	0.9
SR	16.5	0.16	78	0.12	3.0	0.8
GB	18.0	0.16	70	0.22	2.5	0.67

Table III .10: Parameters of the three different types of concrete.

It worth reminding that the matrix in our morphological models consists of the mortar and the small aggregates (diameter inferior to 4 millimeters). Thus the parameters of the matrix are also influenced by the type of inclusions. In view of the fact that the inclusions of SC concrete have the roughest interfaces, we can see from Table. III .10 that the SC concrete has the biggest values of critical strength σ_y and the fracture energy $\mathcal{G}_{op}$ among the three types of concretes. Also, GB concrete has the smallest values. For the same reason, it can explain why SC and SR concrete have the same kind of aggregates but have different matrix parameters.

The comparison between the numerical simulation and the experimental results is plotted in Fig. III .55. In monotonic loading, it can be observed that the numerical simulations are capable of reproducing the failure of the material while guaranteeing a corresponding macroscopic resistance. However, numerical simulations suffer from the stress locking effect. The macroscopic response of the material does not reach zero, even for a large amount of loading. The stress locking phenomena can be explained by: 1. the numerical model exhibits only the mode-I strong discontinuity; 2. the direction of the discontinuity surface is defined a priori by geometric information for interface elements; 3. the volume fractions of the three models are relatively high. As a result, the material carries elastic paths even at the latter stage of the loading.

It can be observed in cyclic loadings, the loss of stiffness and the hysteresis loops. However, compared with the experimental results, the numerical simulation losses more stiffness of the material at the same stage of loading, and the plastic strains are insufficient. In the author's opinion, this is due to the limitations of the pure mode-I strong discontinuity. In compression, the frictions between cracks play an important role during the degradation, and the pure mode-I discontinuity is not capable of reproducing sufficient plasticity and dissipated energy.

10 Conclusion

In this chapter, the aim is to assess a computational model with crack closure mechanism to simulate the behaviors of concrete. The used method is the Embedded Finite Element method. Based on the existing EFEMs, the model incorporates two kinds of enhancement at the mesoscopic scale: the weak enhancement and the strong enhancement. The former enables the model to simulate heterogeneities explicitly. The latter reproduces jumps of the displacement field in the material, representing the cracks. The two kinds of enhancements are independent and additive, making the damage model capable of simulating accurate and complex cracks, such as de-bonding of the interfaces of heterogeneities and the branching of the cracks.

In order to take into consideration the crack closure, a closure criterion is proposed to the model. This criterion is non-linear and requires no additional parameter. The closing criterion is proposed under physical and meaningful considerations. It is assumed

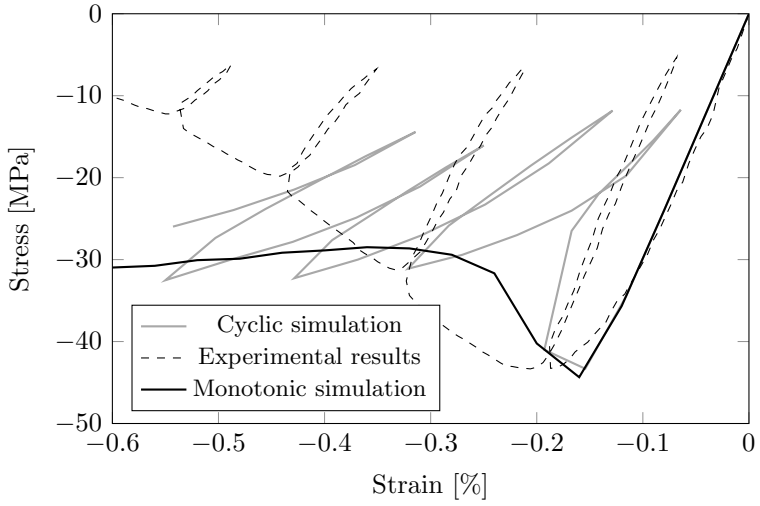

(a) SC

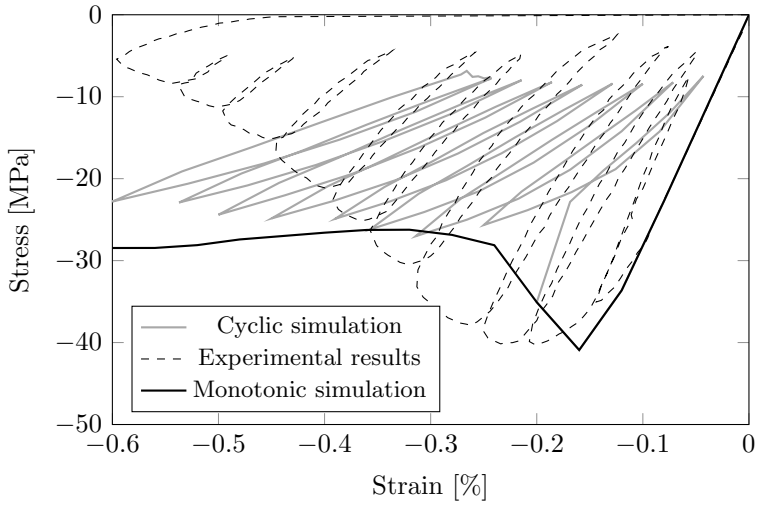

(b) SR

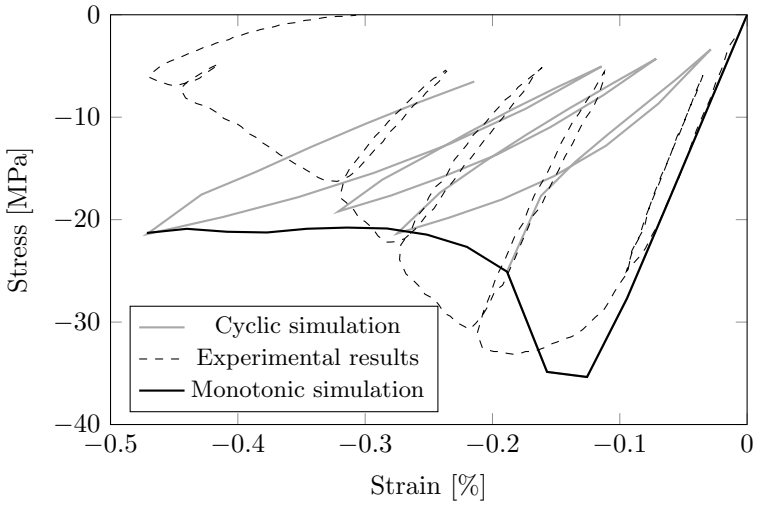

(c) GB

Figure III .55: Comparison of the macroscopic responses between the numerical simulation and the experimental results.

that the energy dissipated in the opening procedure equals the energy required to close the crack completely. A number of representative examples are proposed to demonstrate the performance of the damage model. The attention is primarily paid to the differences between the models adding and without adding the closure criterion.

Firstly, it can be observed that the crack closures exist not only in cyclic loadings but also in monotonic loadings. The crack closures are triggered by stress release. In the case of manifestation of multi-cracks, the closure mechanism has the potential to demonstrate complex but reasonable crack patterns. For example, the simple traction test in 8.1 with the rigid internal sphere, one of the major cracks admits an almost entirely closing during the monotonic loading.

Secondly, the hysteresis phenomenon emerges from crack closures in cyclic loading. This phenomenon stems from the additional dissipated energy released by crack closures and the stiffness recovery of the material.

However, multiple drawbacks are worth noting. At first, the material is incapable of reaching sufficiently softness, especially for compressional loading, namely the stress locking effect. After the macroscopic failure of the material, its macroscopic stress is not equal to zero, even under a substantial amount of loading. One of the reasons is that a set of interface elements cannot meet the failure criterion. This is because the orientation of the discontinuity is pre-defined by the geometry of heterogeneities, and the separation is pure mode-I. Therefore, the stress locking effect will manifest itself when the loading results in shear stress, i.e., the compressional loading, or high volume fraction.

In addition to the stress locking effect, another limitation is observed in the comparison of experimental results. Thought the hysteresis loops could be spotted by applying a closure mechanism to the strong discontinuity of the type mode-I, the simulation result indicates an insufficient plastic deformation. This is due to the friction between the lips of cracks not taken into consideration in the case of a pure mode-I crack opening. Though the crack closure also produces a certain additional dissipated energy, it is relatively not sufficient.

In order to overcome the limitations referred to above, thinner mesh can be applied to reduce the stress locking effect, especially for the target solid with high volume fraction.

However, a thinner mesh means an increase in computation cost, i.e., more necessary memories and calculating time are required. Therefore, it leads to a necessity to factor mode-II separation into the model, or mode-I + mode-II.

Chapter IV

EFEM simulation of concrete fatigue, use of the mode-II strong discontinuity

Contents

1 Introduction

In the previous chapter, we attempted to explore an EFEM model that exhibits 1. a weak discontinuity; 2. a strong discontinuity of the type "opening" (mode I); 3. and crack closures. By applying the model to a quasi-brittle heterogeneous material, many typical behaviors can be observed, such as the asymmetric traction/compression behavior, the volumetric dilatation, the unilateral effect, and the hysteresis phenomena. However, the model was limited by the lack of consideration of friction between micro-cracks. Several differences can be observed during the comparison with the experimental results. Among them, the most important one is insufficient plastic deformation.

In order to take into concern the effect of friction, in this chapter, attention is focused on the strong discontinuity of the type mode-II corresponding to a frictional sliding, see Fig. IV .1(c). In existing works (Hauseux, 2015; Vallade, 2016), two criteria are used to describe mechanical behaviors at the discontinuity interface: the localization criterion, which is chosen to be the Mohr-Coulomb criterion; and a softening failure law, describes the sliding degradation process. Based on these previous studies, we will first apply a weak discontinuity to the model. Then propose here an additive criterion to simulate the "closure" of cracks. Physically, it represents a process by which the crack slides backwards or even continues to propagate in the opposite direction. It is worth emphasizing that in this part, no isotropic damage is used.

This chapter is organized as follows. We formulate in the first part the governing equations for the weak and strong discontinuity of the type mode-II. The closure of the cracks is highlighted. Second, the performance of the model is illustrated with some explicit applications. Finally, the model is tested by comparing it with the experimental results (Piotrowska, 2013).

2 Discontinuity model for mode-II discontinuities

Discontinuities are introduced within the elements to describe the mechanical behavior of the heterogeneous materials at the meso-scale. The weak discontinuities represent the heterogeneities, while the strong discontinuities represent the cracks in the material. As presented in the preceding chapter, the discontinuity interface $\mathcal{S}_u$ divides the element into two sub-domains $\Omega_e = \Omega_e^+ \cup \Omega_e^-$. The bulk part of the element always remains elastic itself, while the failure behavior is described at the discontinuity interface. The governing law

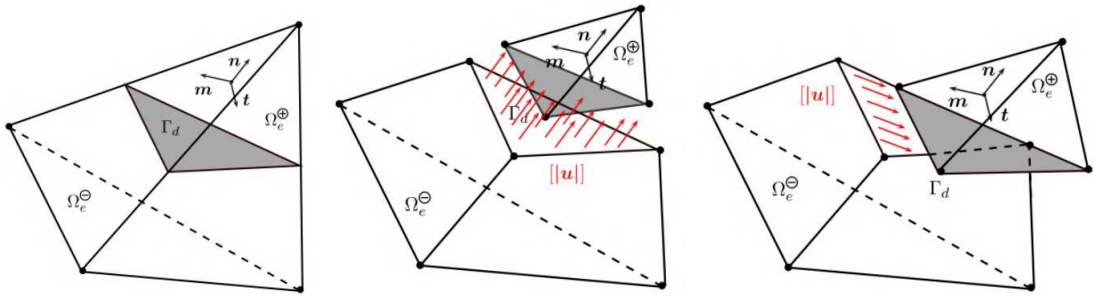

(a) Element (b) Mode I (c) Mode II

Figure IV .1: Representation of the embedded discontinuity of the type mode I and mode II within an finite element (Hauseux, 2015).

links the traction vector $\boldsymbol{T}$ and the crack opening $[|\boldsymbol{u}|]$ to simulate the degradation mechanism. Existing researches have well documented and established the strong discontinuity of the type mode-II. However, previous studies have not dealt with the weak discontinuities. In this section, the mathematical representations of the strong discontinuity and the weak discontinuity are presented.

2.1 Localization criterion - Mohr-Coulomb

There are two main purposes of the localization criterion. On the one hand, the localization law determines the appearance of the localization. On the other hand, it determines the orientation of the discontinuity interface and the sliding direction. Since the target material contains heterogeneities (weak discontinuity), two cases have to be considered.

In the first case, if the crack occurs in a homogeneous element, which means the element carries no geometrical information on the orientation of the discontinuity interface, the Mohr-Coulomb criterion is used. It is a widely used criterion in rocks and relatively brittle solid materials, which contains two critical parameters: the cohesive stress C and the friction angle φ. As a criterion which based on the stress, the localization criterion gives as (Lemaitre et al., 2009; Salençon, 2002)

$$\Phi_{\mathrm{l}} = \operatorname*{Sup}_{n} \left(\|\boldsymbol{T}_{\boldsymbol{t}}\| + T_n \tan\varphi - C \right), \tag{2.1}$$

where $\boldsymbol{T}$ is the traction vector on the discontinuity interface $\boldsymbol{T} = \check{\boldsymbol{\sigma}} \cdot \boldsymbol{n} = \boldsymbol{H}_{\mathrm{s}}^{*,T} \check{\boldsymbol{\sigma}}$, and T_n/T_t is the projection of the traction vector on the normal vector/discontinuity interface.

They have the relationship of $\boldsymbol{T} = \boldsymbol{T}_t + \boldsymbol{T}_n$, with the normal traction vector $\boldsymbol{T}_n = T_n \cdot \boldsymbol{n}$.

In the case of a homogeneous element, no geometric information is provided a priori for the normal vector. The localization criterion can be written with the principal stresses: (assuming that $\sigma_1 > \sigma_2 > \sigma_3$):

$$\Phi_1 = \frac{1}{2\cos\varphi}\left(\sigma_1 - \sigma_3 + (\sigma_1 + \sigma_3)\sin\varphi - 2C\cos\varphi\right). \tag{2.2}$$

Concerning that the friction angle φ and the cohesive stress C are constant parameters of the material, this equation makes it possible to be obtained the coordinates of the normal vector of the discontinuity interface analytically when it equals to zero (Bai and Wierzbicki, 2010). Assuming an arbitrary cutting plan has the unit vector $\boldsymbol{n} = (\nu_1, \nu_2, \nu_2)$, the shear stress and the corresponding normal stress gives as:

$$T_n^2 + T_t^2 = \sigma_1^2\nu_1^2 + \sigma_2^2\nu_2^2 + \sigma_3^2\nu_3^2 \tag{2.3}$$

with

$$T_n = \nu_1^2\sigma_1 + \nu_2^2\sigma_2 + \nu_3^2\sigma_3. \tag{2.4}$$

The components of the unit vector should satisfy $\nu_1^2 + \nu_2^2 + \nu_3^2 = 1$. Thus they can be solved by using the Gauss elimination method:

$$\begin{cases} \nu_1^2 = \dfrac{1}{1 + (\sqrt{1 + c_1^2} - c_1)^2} \\ \nu_2^2 = 0 \\ \nu_3^2 = \dfrac{1}{1 + (\sqrt{1 + c_1^2} + c_1)^2}, \end{cases} \tag{2.5}$$

with $c_1 = \tan\varphi$.

In the second case, if the crack occurs in an element which exhibits a weak discontinuity, it is assumed that the strong discontinuity follows the same interface. Thus the unit vector of the interface is given. Hence, the normal and shear components of the stress vector are calculated as

$$\begin{cases} T_n = \boldsymbol{n} \cdot \boldsymbol{\sigma} \cdot \boldsymbol{n} \\ \|\boldsymbol{T_t}\| = \|\boldsymbol{T} - T_n \cdot \boldsymbol{n}\| = \|\boldsymbol{T} \cdot \boldsymbol{n}_t\|. \end{cases} \tag{2.6}$$

The sliding orientation is determined by the maximum shear stress on the discontinuity interface.

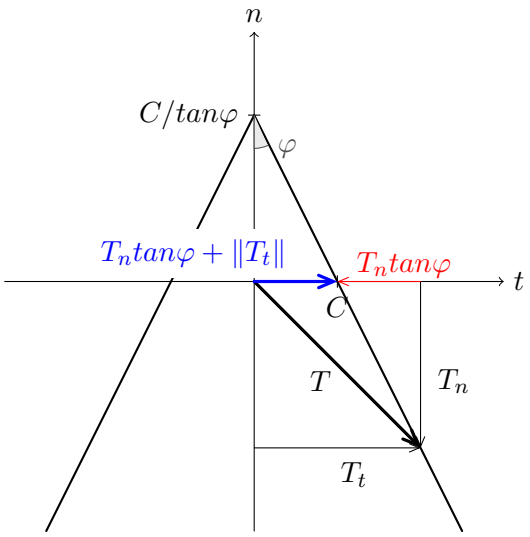

Figure IV .2: Mohr-Coulomb criterion represented on a 2D occasion.

Representing the Mohr-Coulomb criterion in a diagram, as shown in Fig. IV .2, the area below the curves correspond to the elastic mechanism, while at the curve corresponds to the localization criterion Eq. 2.1 equals to zero and the localization occurs in the element. At the moment of localization, we have the relationship: $T_n \tan\varphi + \|\boldsymbol{T_t}\| = C$. We can see from the figure that the traction vector $\boldsymbol{T}$ can be decomposed into the normal stress $\boldsymbol{T}_n$ and the shear stress $\boldsymbol{T}_t$, and the equivalent stress $T_n \tan\varphi + \|\boldsymbol{T_t}\|$ (drawn in blue) equals to the cohesion C. It can be presumed that if the normal stress is positive, which means that the discontinuity interface is in traction, the shear stress T_t would be much smaller at the localization compared with the occasion of normal compressional stress.

2.2 Sliding opening law

The sliding opening procedure occurs after the localization, which describes the failure behaviors of the material. The degradation of the element can be calculated using the equivalent stress at the discontinuity interface Vallade (2016) Hauseux (2015):

$$\Phi_o = \sigma_{eq} - \underbrace{C\exp(-C[u]/\mathcal{G}_{op})}_{\text{residual cohesion } C'}, \text{ with } \sigma_{eq} = \|\boldsymbol{T_t}\| + T_n \tan\varphi. \tag{2.7}$$

In this equation, the fracture energy $\mathcal{G}_{op}$ is a local parameter of the material, representing the necessary dissipate energy for complete sliding-opening. The absolute value of sliding is noted as $[u]$. The relationship between the absolute value of sliding opening and the

oriented sliding vector writes as:

$$[|\boldsymbol{u}|] = [u] \cdot \boldsymbol{n}_p. \tag{2.8}$$

Located at the discontinuity interface, we note:

- $\boldsymbol{n}_p$: the sliding direction (Eq. 2.8), corresponding to the vector which points to the "position" of the crack;
- $\boldsymbol{n}_t$: the direction of shear stress (Eq. 2.6), corresponding to the sliding "tendency" of the sliding.

In the sliding opening procedure, these two vectors are equivalent.

Physically, the projection of the traction vector on the sliding direction $T_t = \boldsymbol{T} \cdot \boldsymbol{n}_t$ can be seen as the friction between two sub-domains Ω^+ and Ω^-. As the sliding procedure goes on, the friction between they becomes weaker. It can be considered as the interface between them has a lower roughness. This procedure of decreasing roughness between the micro-cracks is assumed to be irreversible.

It is proposed here a 2D example of a single cubic element, see Fig. IV .3. It is worth noting that the non-linear mechanism only appears in the discontinuity interface. The bulk volumes have pure elastic behaviors. The two sub-domains are linked by the traction vector $\boldsymbol{T}$ which transfers across the interface. The sliding opening shown in the figure aims at representing the mechanism relationship in the element. The strong discontinuity exists in the element as an internal variable rather than a "physical" separation. In the following parts, the same 2D example is going to be used to represent the local constitutive behaviors at different stages. For the sake of simplify, it is assumed that the normal stress T_n remains constant, and the notation $T_t^{(i)}$ and $C^{(i)}$ represent the corresponding shear stress and the cohesion at status number shown in Fig. IV .4(b).

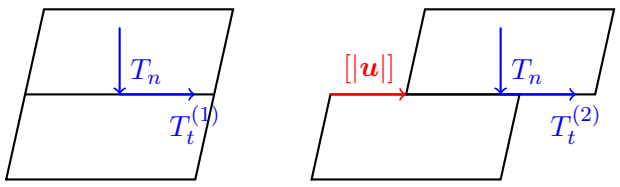

(a) Localization (b) Sliding opening

Figure IV .3: Sliding opening procedure of a 2D element, from (a) the localization to (b) the sliding opening.

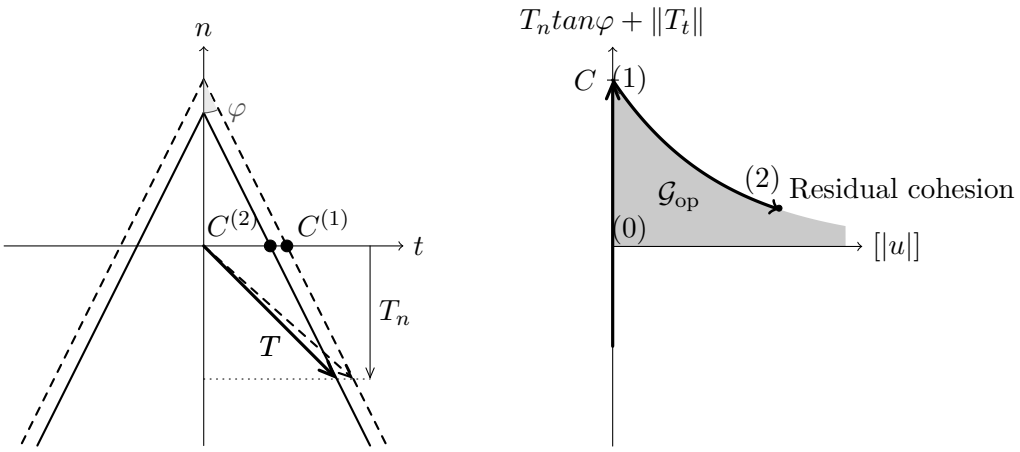

(a) Sliding opening criterion in a Mohr-Coulomb diagram

(b) Kinematic relationship between the equivalent stress and sliding opening value

Figure IV .4: Sliding opening mechanism of the local constitutive model at the discontinuity interface.

The sliding-opening procedure is described by Eq. 2.7, which characterizes a relationship between the equivalent stress σ_{eq} and the residual cohesion C'. As the crack develops, it is considered that the friction between the two sub-domains decreases. Shown in Fig. IV .4(a), it corresponds to a contraction of the elastic region; and shown in Fig. IV .4(b), it corresponds to the decreasing value of the equivalent stress.

For solving the system carrying a strong discontinuity, we have assumed in the previous chapter that the integration is calculated by the average value of weighted volumes of subdomains in the previous chapter. The same consideration is also used for the mode-II resolution:

$$\boldsymbol{T} = \frac{1}{V}\boldsymbol{H}_{\text{s}}^{*,T}(V^{+}\check{\boldsymbol{\sigma}}^{+} + V^{-}\check{\boldsymbol{\sigma}}^{-}). \tag{2.9}$$

And the linearisation of the sliding criterion at the element level should base on the two variables:

$$\Delta\Phi_{\text{o}} = \frac{\partial\sigma_{\text{eq}}}{\partial\boldsymbol{T}}\Delta\boldsymbol{T} + \frac{\partial C'}{\partial[u]}\Delta[u]. \tag{2.10}$$

Reminding that for the strong discontinuity mode-II, the equivalent stress is calculated as $\sigma_{\text{eq}} = \|\boldsymbol{T_t}\| + T_n \tan\varphi$. Thus we have $\partial\sigma_{\text{eq}}/\partial\boldsymbol{T} = \boldsymbol{n}_t + \boldsymbol{n}\tan\varphi$. The linearisation equation of the strong discontinuity mode-II writes as:

$$\begin{aligned}\Delta\Phi_o = &\underbrace{(\boldsymbol{n}_t + \boldsymbol{n}\tan\varphi)\frac{1}{V}\boldsymbol{H}_{\mathrm{s}}^{*,T}(V^{\oplus}\boldsymbol{C}^{+} + V^{\ominus}\boldsymbol{C}^{-})\boldsymbol{B}}_{\boldsymbol{K}'_{\mathrm{s}^*\mathrm{b}}}\Delta\boldsymbol{d}\\ &+\underbrace{(\boldsymbol{n}_t + \boldsymbol{n}\tan\varphi)\frac{V^{+}V^{-}}{V}\boldsymbol{H}_{\mathrm{s}}^{*,T}(\boldsymbol{C}^{+} - \boldsymbol{C}^{-})\boldsymbol{H}_{w}}_{\boldsymbol{K}'_{\mathrm{s}^*\mathrm{w}}}\Delta[|\boldsymbol{\varepsilon}|]\\ &+\underbrace{(\boldsymbol{n}_t + \boldsymbol{n}\tan\varphi)\frac{1}{V}\boldsymbol{H}_{\mathrm{s}}^{*,T}(V^{\oplus}\boldsymbol{C}^{+} + V^{\ominus}\boldsymbol{C}^{-})\boldsymbol{G}_s\boldsymbol{n}_p}_{\boldsymbol{K}'_{\mathrm{s}^*\mathrm{s}}}\Delta[u]\\ &+\underbrace{\frac{C^2}{\mathcal{G}_{\mathrm{op}}}e^{-C[u]/\mathcal{G}_{\mathrm{op}}}}_{K'_{\mathrm{qo}}}\Delta[u],\end{aligned}$$

Assuming that the local system has already been solved, i.e., $\mathcal{R}^e_{[|\boldsymbol{\varepsilon}|]} = 0$ and $\mathcal{R}^e_{[|\boldsymbol{u}|]} = 0$, we have:

$$\boldsymbol{K}_{\mathrm{wb}}\boldsymbol{d} + \boldsymbol{K}_{\mathrm{ww}}[|\boldsymbol{\varepsilon}|] + \boldsymbol{K}_{\mathrm{ws}}[u] = 0, \tag{2.11}$$

and

$$-\boldsymbol{K}'_{\mathrm{s}^*\mathrm{b}}\boldsymbol{d} - \boldsymbol{K}'_{\mathrm{s}^*\mathrm{w}}[|\boldsymbol{\varepsilon}|] - \boldsymbol{K}'_{\mathrm{s}^*\mathrm{s}}[u] + C\exp(-\frac{C}{\mathcal{G}_{\mathrm{op}}}[u]) = 0. \tag{2.12}$$

As given in the previous part, the expression of tangent matrix in Eq. 2.11 give as:

$$\begin{aligned}\boldsymbol{K}_{\mathrm{wb}} &= \frac{V^{+}V^{-}}{V}\boldsymbol{H}_{\mathrm{w}}^{T}(\boldsymbol{C}^{+} - \boldsymbol{C}^{-})\boldsymbol{B}\\ \boldsymbol{K}_{\mathrm{ww}} &= \frac{V^{+}V^{-}}{V}\boldsymbol{H}_{\mathrm{w}}^{T}(V^{-}\boldsymbol{C}^{+} + V^{+}\boldsymbol{C}^{-})\boldsymbol{H}_{\mathrm{w}}\\ \boldsymbol{K}_{\mathrm{ws}} &= \frac{V^{+}V^{-}}{V}\boldsymbol{H}_{\mathrm{w}}(\boldsymbol{C}^{+} - \boldsymbol{C}^{-})\mathbf{G}_{\mathrm{s}}\boldsymbol{n}_p.\end{aligned}$$

Solving the equation Eq. 2.11 and Eq. 2.12, we have:

$$T'_e + M'[u] = C\exp(-\frac{C}{\mathcal{G}_{\mathrm{op}}}[u]), \tag{2.13}$$

with

$$T'_e = \left(\boldsymbol{K}'_{\mathrm{s}^*\mathrm{b}} - \boldsymbol{K}'_{\mathrm{s}^*\mathrm{w}}\boldsymbol{K}_{\mathrm{ww}}^{-1}\boldsymbol{K}_{\mathrm{wb}}\right)\boldsymbol{d} \tag{2.14}$$

$$M' = \left(\boldsymbol{K}'_{\mathrm{s}^*\mathrm{s}} - \boldsymbol{K}'_{\mathrm{s}^*\mathrm{w}}\boldsymbol{K}_{\mathrm{ww}}^{-1}\boldsymbol{K}_{\mathrm{ws}}\right). \tag{2.15}$$

Hence, with the help of the Lamber W function, the analytical solution gives as

$$[u]_{\mathrm{sol}} = \frac{\mathcal{G}_{\mathrm{op}}}{C}\left(W_0\left(\frac{C^2\exp(\frac{CT_e}{\mathcal{G}_{\mathrm{op}}M})}{\mathcal{G}_{\mathrm{op}}M}\right) - \frac{CT_e}{\mathcal{G}_{\mathrm{op}}M}\right), \tag{2.16}$$

and the jump of the strain field gives as

$$[|\varepsilon|]_{\text{sol}} = -\boldsymbol{K}_{\text{ww}}^{-1}\left(\boldsymbol{K}_{\text{wb}}\boldsymbol{d} + \boldsymbol{K}_{\text{ws}}[u]_{\text{sol}}\right). \tag{2.17}$$

2.3 Sliding closing criterion

Based on existing works on the strong discontinuity of mode-II, a closing mechanism is proposed in this section. Due to practical constraints, a simplification on the sliding direction is applied to the model. It is considered that one the sliding direction is determined, the fracture orientation $\boldsymbol{n}_t$ can only remain the same or become opposite to itself. Also, the value of sliding distance $[u]$ is never negative, the sliding between sub-domains is represented by $[|\boldsymbol{u}|]$ which equals to $([u] \cdot \boldsymbol{n}_p)$.

In the following part, we decompose the closing procedure into several different phases. Starting from the opening state, the closing micro-crack will firstly have an unloading phase. Subsequently, as the imposed charge reloads in the opposite direction, and the crack will sliding back to its original position, and then even continue propagating in the opposite direction.

2.3.1 Unloading procedure

Assuming an unloading procedure occurs after the sliding opening, which the loading begins to decrease. Physically, it can be considered as releasing the stored elastic energy in the element.

We show here the same 2D example. An unloading procedure is applied, as shown in Fig. IV .5(a) to Fig. IV .5(b). The element is assumed to compressional stress at the direction perpendicular to the discontinuity interface (the normal stress $T_n < 0$). Also, at the discontinuity interface, the shear stress T_t decreases to zero at the state of completely unloading. As a result, the equivalent stress σ_{eq} equals to $T_n \tan\varphi$ as $T_t = 0$, and it will decrease to negative, see Fig. IV .6(b). In a real numerical test, however, $\sigma_{\text{eq}}^{(3)}$ could be positive, negative or zero, corresponding to tensile, compressional or null loading at the direction perpendicular to the discontinuity surface. The mechanism behavior at the local scale is plotted in Fig. IV .6.

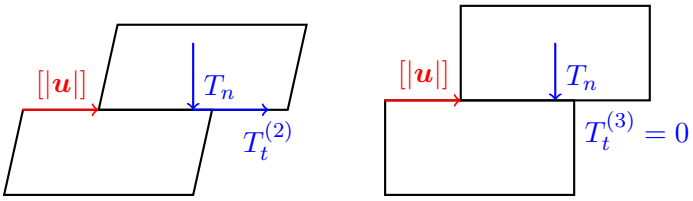

(a) Sliding opening (b) Unloading procedure

Figure IV .5: Unloading procedure of a 2D element, from (a) the sliding opening to (b) the unloading of the elastic volumes.

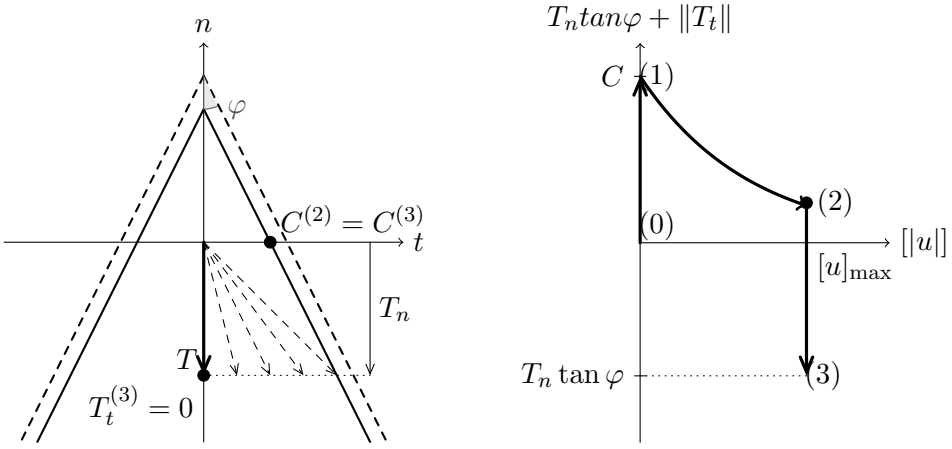

(a) Unloading procedure in a Mohr-Coulomb diagram (b) Kinematic relationship between the equivalent stress and sliding opening value

Figure IV .6: Unloading procedure at the local constitutive model at the discontinuity interface.

As we can see from Fig. IV .6(a), the whole unloading process takes place only in the elastic area. The element has a pure elastic mechanism at this stage. The sliding opening value $[u]$ remains unchanged itself.

2.3.2 Reloading procedure

The closing procedure is triggered after the equivalent stress equals to the residual cohesion, and at this critical point, the shear stress T_t is opposite to its initial direction. The value of sliding opening $[|\boldsymbol{u}|]$ begin to decrease, and physically, it represents a "sliding back" procedure between two sub-domains.

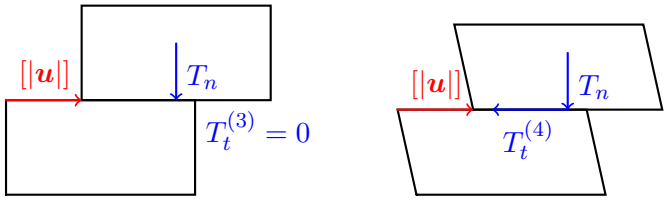

(a) Unloading procedure (b) Reloading procedure

Figure IV .7: Reloading procedure of a 2D element, from (a) the unloading procedure to (b) the elastic reloading of the elastic volumes.

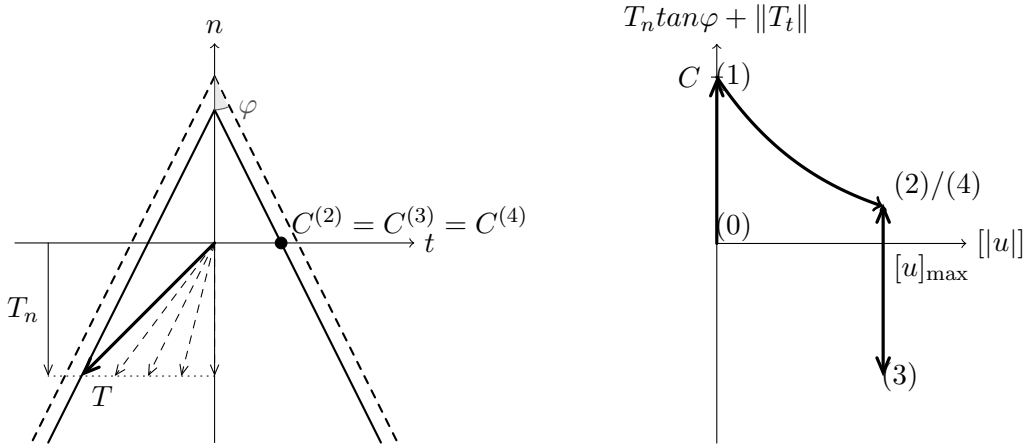

(a) Reloading procedure in a Mohr-Coulomb diagram

(b) Kinematic relationship between the equivalent stress and sliding opening value

Figure IV .8: Reloading procedure of the local constitutive model at the discontinuity interface.

As it is described in the previous section, the unloading procedure carries a pure elastic mechanism which corresponding to a release of energy stored in the bulk volume. The reloading procedure also has a pure elastic behavior which is related to the restoration of elastic energy at the bulk volume. At the discontinuity, the sliding opening value $[u]$ remains unchanged, while the shear stress T_t at the interface increases until reaching the critical value that the equivalent stress equals to the residual cohesion.

In the case of this simple element example, the shear stress increase from zero and follows the direction that is opposite to the initial one, see Fig. IV .7. It can be observed

in Fig. IV .8(a). It is worth noting that the sliding direction $\boldsymbol{n}_p$ remain unchanged since the sliding opening $[|\boldsymbol{u}|]$ is always the same. Also, the direction of the shear stress $\boldsymbol{n}_t$ becomes opposite to itself.

2.3.3 Sliding back - closing and reopening procedure

The sliding back procedure consists of two steps, the so-called "closure" of the micro-crack, and the continue propagating in the opposite direction, which is contrary to its original sliding orientation. Physically, the shear stress T_t represents the friction between two sub-domains, and it is related to the "roughness" at the discontinuity interface. As the sliding-opening procedure develops, it is assumed that the roughness at the interface decreases, written in the functions, it is noted as residual cohesion. Hence, when the fracture "slides back", it follows the same trace as it "slides open". Thus it is considered that the residual cohesion remains constant during this procedure.

In the single element example as shown in Fig. IV .9 and Fig. IV .10, it can be observed that the sliding opening $[|\boldsymbol{u}|]$ decrease from $[u]_{\max}$ to zero (corresponding to Fig. IV .9(a) to Fig. IV .9(b)) and increase from zero to $[|\boldsymbol{u}|]$ but with an opposite direction (corresponding to Fig. IV .9(b) to Fig. IV .9(c)). Plotted in the local constitutive model as in Fig. IV .10(b), this procedure matches to the point 4 to point 5, and point 5 to point 6. It can be seen that the residual cohesion and the traction vector $\boldsymbol{T}$ stay unchanged.

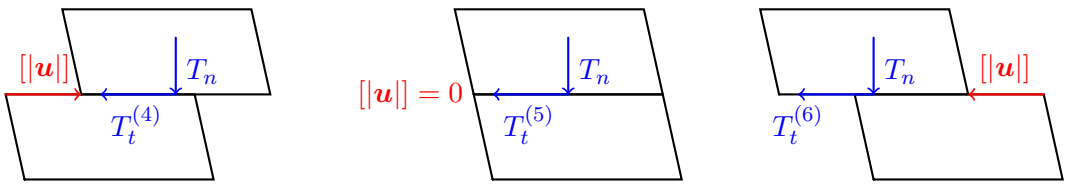

(a) Reloading procedure (b) Closing procedure (c) Reopening procedure

Figure IV .9: Sliding closing procedure of a 2D element, from (a) the reloading of the elastic volumes to (b) the sliding closing of the crack to (c) the reopening of the crack.

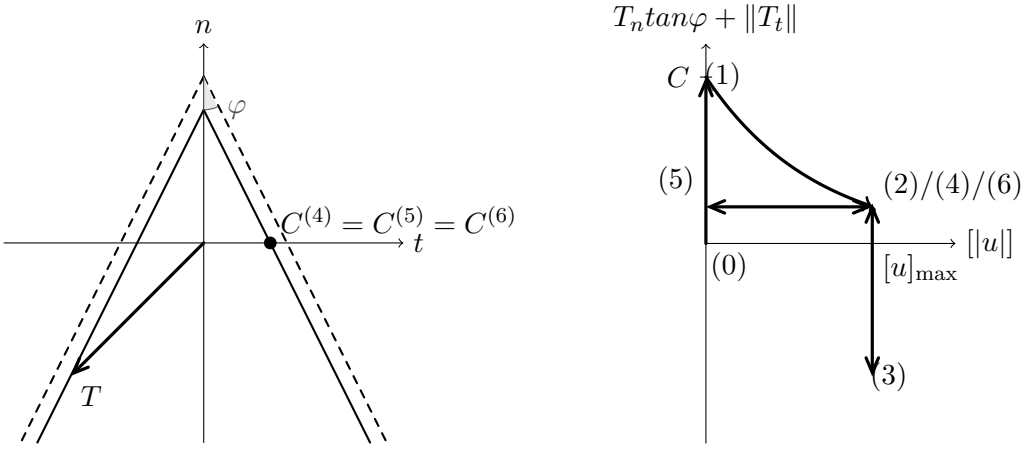

(a) Closing and reopening procedure in a Mohr-Coulomb diagram

(b) Kinematic relationship between the equivalent stress and sliding opening value

Figure IV .10: Sliding closing mechanism of the local constitutive model at the discontinuity interface.

The closing criterion gives as

$$\Phi_{\mathrm{c}} = T_n \tan\varphi + \|\boldsymbol{T_t}\| - C\exp(-\frac{C[u]_{\max}}{\mathcal{G}_{\mathrm{op}}}), \tag{2.18}$$

which equivalents to

$$\Phi_{\mathrm{c}} = T'_e + M'[u] - C\exp(-\frac{C[u]_{\max}}{\mathcal{G}_{\mathrm{op}}}). \tag{2.19}$$

It is a linear equation, hence the analytical solution for the sliding opening value $[u]$ simply gives as:

$$[u] = \left(C\exp(-\frac{C[u]_{\max}}{\mathcal{G}_{\mathrm{op}}}) - T'_e\right)/M'. \tag{2.20}$$

After the sliding opening value reaches the previous maximum opening value $[u]_{\max}$, the equivalent stress equals to the corresponding residual cohesion. Subsequently, the sliding opening procedure is activated. The sliding opening value begins to increase, and the residual cohesion decreases. Physically, it means that the 'roughness' at the discontinuity interface continue decreases as the fracture develops to a further position. It corresponds to the procedure from Fig. IV .11(a) to Fig. IV .11(b), or the point 6 to point 7 in Fig. IV .12.

The reopening procedure follows the same criterion as describes in the previous part, Eq. 2.7. If unloading is applied to the element at this stage, it will follow the same processes as introduced above: unloading, reloading, closing, and reopening, while using the

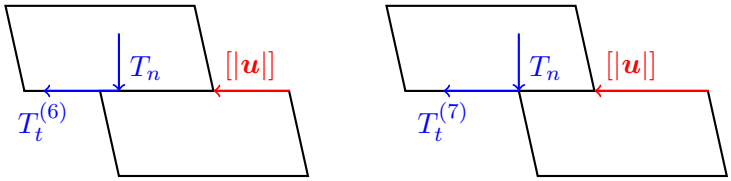

(a) Reopening procedure

(b) Reopening to further positions

Figure IV .11: Opening procedure of a 2D element, from (a) the existent maximum opening position to (b) sliding opening to a further position.

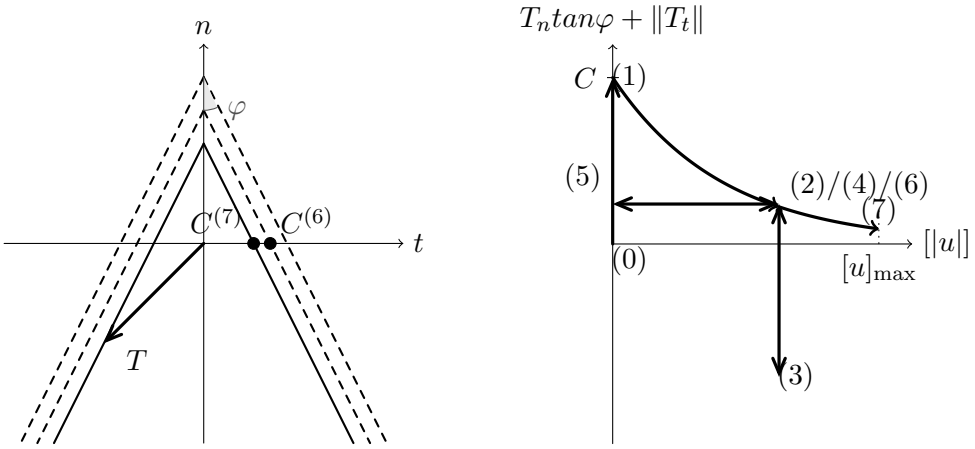

(a) Reopening procedure in a Mohr-Coulomb diagram

(b) Kinematic relationship between the equivalent stress and sliding opening value

Figure IV .12: Opening mechanism of the local constitutive model at the discontinuity interface after crack closures.

new residual cohesion which is calculated with the new $[u]_{\max}$.

In summary, the mechanism behaviors at the discontinuity interface, sliding opening, sliding closing, reopening, etc., are built upon the following considerations:

- The cohesion of the element is associated with the roughness of the discontinuity, which represents the friction between two sub-domains.
- The equivalent stress equals to the residual cohesion, the value of which will decrease when the sliding opening procedure takes place at the discontinuity.
- The sliding closing will not change the residual cohesion of the element since this procedure occurs in the old trace of the $[|\boldsymbol{u}|]$. The roughness of the discontinuity

only decreases when the sliding opening value reaches to a further position which exceeds $[u]_{\max}$.

2.4 Numerical implementation within the framework of Finite Element Method

In this section, the model is applied to a finite element framework with 4-node tetrahedral elements. As it is presented in the previous chapter, the resolution of the system is based on two levels, the element level, and the global level. A modified stiffness matrix $\boldsymbol{K}_{\text{sc}}$ needs to be calculated at the element level, then an assembled matrix $\mathbb{K}_{\text{sc}}$ is built to solve the global system. We present a pseudo-code in algorithm. 2.

Algorithm 2 Implementation for the system exhibits strong and weak discontinuity

$\boldsymbol{\varepsilon}^e = \boldsymbol{B} \cdot \boldsymbol{d}$, $\boldsymbol{\sigma}^e = \boldsymbol{C} \cdot \boldsymbol{\varepsilon}^e$
loop at the element level:
if no strong discontinuity exhibits in the element **then**
  if The element exhibits weak discontinuity **then**
    Normal vector of the interface is determined by the geometric information
    Normal stress $T_n = \boldsymbol{n} \cdot \boldsymbol{\sigma} \cdot \boldsymbol{n}$
    Shear stress $\|\boldsymbol{T_t}\| = \|\boldsymbol{\sigma} \cdot \boldsymbol{n} - T_n \cdot \boldsymbol{n}\|$
    Equivalent stress $\sigma_{\text{eq}} = T_n \tan\varphi + \|\boldsymbol{T_t}\|$
    if $\sigma_{\text{eq}} > C$ **then**
      The element admits a localization, the sliding opening is trigged
      Determin the direction of shear position $\boldsymbol{n}_p$ and shear stress $\boldsymbol{n}_t$ by Eq. 2.6 and Eq. 2.8
      Calculate T_e' and M' (Eq. (2.15)) and resolve the sliding opening value $[u]$
      goto *putout*.
    else
      The element remain elastic
      goto *putout*.
    end if
  else The element exhibits no weak discontinuity
    Calculate equivalent stress σ_{eq} using Eq. 2.2
    if $\sigma_{\text{eq}} > C$ **then**
      The element admits a localization, the sliding opening is trigged
      Determin the direction of shear position $\boldsymbol{n}_p$ and shear stress $\boldsymbol{n}_t$ by Eq. 2.6

and Eq. 2.8

Normal vector is determined by Eq. 2.5, $\boldsymbol{n} = (\nu_1, \nu_2, \nu_3)$

Calculate T_e' and M' (Eq. (2.15)) and resolve the sliding opening value $[u]$

goto *putout*.

else

The element remain elastic

goto *putout*

end if

end if

else Strong discontinuity already exhibits in the element

Calculate the direction of shear stress $\boldsymbol{n}_t^{(i+1)}$

if $\|\boldsymbol{n}_t^{(i+1)} - \boldsymbol{n}_t^{(i)}\| > \sqrt{3}$ **then**

The sliding tendency is changed, $\boldsymbol{n}_t = -\boldsymbol{n}_t$

The element enters into the closing procedure

Calculate opening value $[u]_{i+1}$ (Eq. (2.18)) and $[|\boldsymbol{\varepsilon}|]$ (Eq. (2.20))

if $[|\boldsymbol{u}|] < 0$ **then**

The sliding value has decreased to zero, and will increase in other direction.

$\boldsymbol{n}_p = -\boldsymbol{n}_p$

Calculate new value of M' using the recent $\boldsymbol{n}_p$

Calculate the sliding opening value $[u]$

goto *putout*.

end if

if $[u] > [u]_{\max}$ **then**

The element reaches to the existent maximum opening value, end the closing procedure, begin the sliding opening procedure

Calculate T_e' and M' (Eq. (2.15)) and resolve the sliding opening value $[u]$

goto *putout*.

end if

end if

end if

Putout:

Calculate stress field of the element using $[|\boldsymbol{u}|]$ and $[|\boldsymbol{\varepsilon}|]$

Calculate modified stiffness matrix $\boldsymbol{K}_{\text{sc}}$ for each element

goto *global system*

global system:

56: Resolving the global system with assembled matrix $\mathbb{K}_{sc}$ (Eq. (5.16))

As a first illustration of the validation of the model, we consider here a single tetrahedral element as an example. The element is divided into two sub-domains by the interface between two materials, representing the weak discontinuity. The parameters are given in Table.IV .1, and the basic dimensions and boundary conditions of the elements are shown in Fig. IV .13. Here, we apply a simple occasion to the element that the normal vector of the discontinuity interface to be $\boldsymbol{n} = (0, 0, 1)$, which is parallel to the z axis, see Fig IV .13. The imposed displacement follows the direction of the x axis, which is parallel to the interface. In this case, it is easy to see that the normal vector T_n of the given interface is equal to zero. The sliding-opening $[|\boldsymbol{u}|]$ follows the same direction as the shear vector T_t.

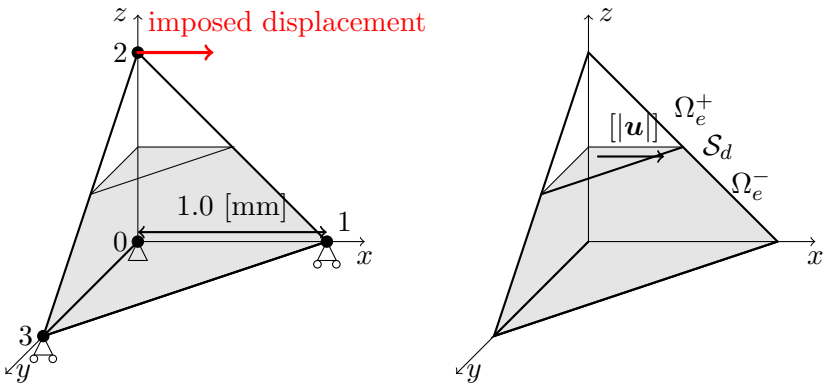

(a) Proposed element and its dimension (b) The discontinuity surface apparents in the element

Figure IV .13: Basic geometric information and boundary conditions for the studied single tetrahedral element.

E [GPa]	ν [-]	C [MPa]	$\tan\varphi$	$\mathcal{G}_{\text{op}}$ $[J/m^2]$
20.0	0.33	6.0	0.5	5.0
70.0	0.33	-	-	-

Table IV .1: Considered material parameters for the single element.

As presented in the previous part, the critical criterion of the model is based on the Mohr-Coulomb criterion. Two critical parameters are considered: the cohesive stress

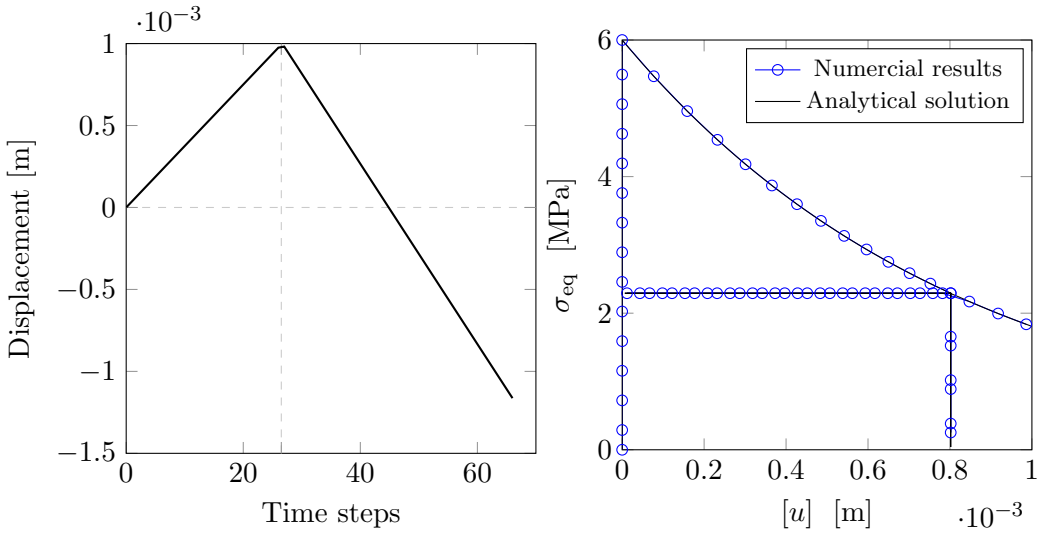

(a) The imposed displacement

(b) Comparison between the numerical result and analytical solution

Figure IV .14: Illustration of the validation of the model on a single tetrahedral element.

C and the friction angle φ. The key point is to compare the equivalent stress $\sigma_{\text{eq}} = T_n \tan\varphi + \|\boldsymbol{T_t}\|$ and the cohesive stress C. Since in this case, the normal traction vector T_n equals to zero, thus the element will reach the critical point when the shear stress T_t equals to C. Once the localization is triggered, the traction vector at the discontinuity interface is manipulated by the sliding-opening law and the closing law. The sliding-opening law carries only one additional parameter, the fracture energy $\mathcal{G}_{\text{op}}$, and the closure mechanism requires no additional material parameter.

As it is plotted in Fig. IV .14, the numerical result shows a good consistent with the analytical solution. If the same displacement trajectory is applied to the model without crack closures, the performance of the element gives in Fig. IV .15. As it is depicted in the figure, we can see that the model with and without closure law have the same sliding-opening performance. Their most evident difference is that the closing of the crack is impossible for the model without closure law, despite a big negative value of equivalent stress. This value of negative equivalent stress comes from the elastic response of the bulk volumes.

Next, we apply two different loadings to an element to illustrate the behaviors of the model in a more damaged occasion and a less damaged occasion. For the sake of clarity,

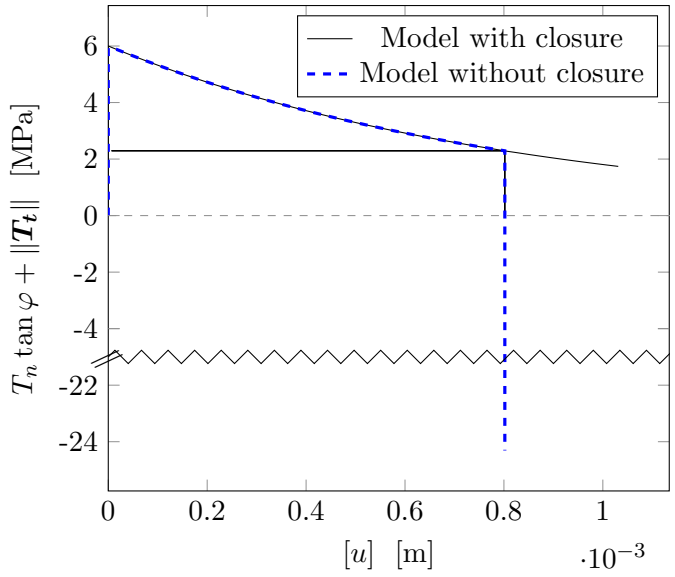

Figure IV .15: Comparison between the model with and without closure mechanism in loading-unloading displacement, the obtained relationship is plotted by the equivalent stress in terms of sliding opening value.

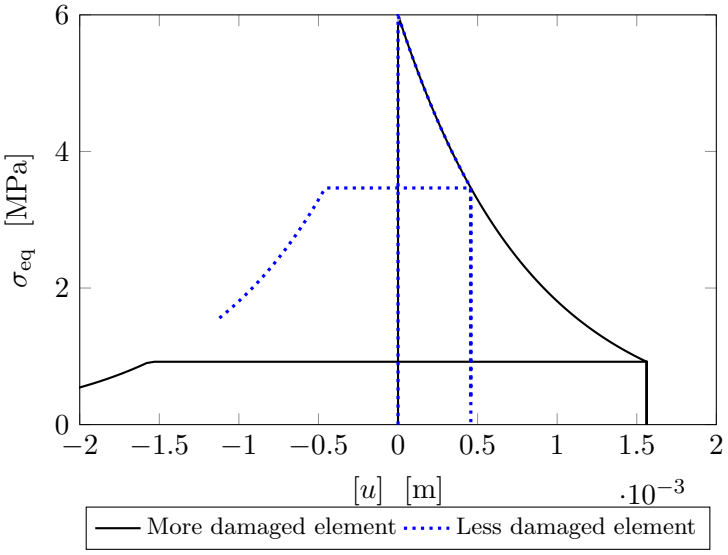

Figure IV .16: Comparison between the behaviors of two elements, which exhibit different levels of damage.

the direction of sliding-opening $\boldsymbol{n}_p$ is taken into concern. Naturally, the sliding-opening orientation $\boldsymbol{n}_p$ depicts a vector in 3D space. Here, it is assumed that the original direction is unit and positive, with $[|\boldsymbol{u}|] = [u]$, while the changed direction when it comes to "closing" is negative, gives as $[|\boldsymbol{u}|] = -[u]$. Clearly, in the phase of sliding-opening, it can be seen from Fig. IV .16 that the required equivalent stress for continuing opening is smaller for the more damaged element. Physically, the needed equivalent stress equals to the residual cohesion of the material, which is related to the roughness at the discontinuity interface. Thus, the already damaged element is more fragile than the sound one. Also, the more damaged it is, the more vulnerable it becomes. Similarly, the required equivalent stress for the subsequent closing phase is also related to the residual cohesion. Therefore, the very damaged element requires less equivalent stress to switch its status from opening to closing and the successive reopening.

3 Representative examples

This section is devoted to present the performances of the mode-II model by applying it to a cube example. Double enhancements are embedded in the element with the strong discontinuity is of the type mode-II. Based on existing EFEM works, a closure law is applied to the model. Without adding any additional numerical parameter, the proposed model makes it possible to take into concern the closing of cracks. Particular attention is focused on a comparison between the model without closing of cracks and the model with crack closure mechanism. From the meso-scale to macro-scale, from element level to global level, we attempt to reproduce several typical behaviors of concrete: i) the macroscopic fatigue of the material for traction and compression; ii) the typical asymmetry of traction/compression responses; iii) with the help of the closure law, the hysteresis loops under cyclic loadings.

Besides the macroscopic performances of the model, crack patterns are also discussed in this section, such as initiations and propagations of cracks. It is assumed that the aggregates have a pure elastic behavior. Thus strong discontinuities only occur in matrix elements and interface elements. The applied parameters are gives in Table. IV .2. It can be seen that the critical parameters for matrix elements and interface elements (cohesion C and friction angle $\tan\varphi$) are set to be the same. The difference in elastic properties will lead to a stress concentration to the interface elements, thus induce a weaker behavior.

Phase	E [GPa]	ν [-]	C [MPa]	$\tan\varphi$ [-]	$\mathcal{G}_{\text{op}}$ $[J/m^2]$
Matrix	20.0	0.2	16.0	0.5	10.0
Interface	-	-	16.0	0.5	10.0
Aggregate	100.0	0.3	-	-	-

Table IV .2: Considered material parameters for the heterogeneous cube.

The basic geometry informations of the cube give as:

- Length of cube: 100.0 millimeters
- Radius of the spheres: 2.0 to 4.0 millimeters
- Volume fraction: 10%
- Number of nodes and elements in the mesh: 298544 and 1529019
- Maximum length of element: 3.0 millimeters
- Minimum length of element: 0.3 millimeters
- Average length of element: 1.4 millimeters

The three types of elements are illustrated in Fig. IV .17 by three different colors. A minimum distance of 4.0 millimeters between each sphere is applied, which is bigger than the biggest length of element (3.0 millimeters). This ensures the correct representation of the weak discontinuities that one element carries at most one weak discontinuity.

3.0.1 Monotonic loadings

In this part, we apply simple traction/compression loadings to the cube. The loading direction follows the z-axis, while the lateral faces of the cube have a boundary condition of stress free. The macroscopic responses in terms of the applied loadings are illustrated in Fig. IV .18.

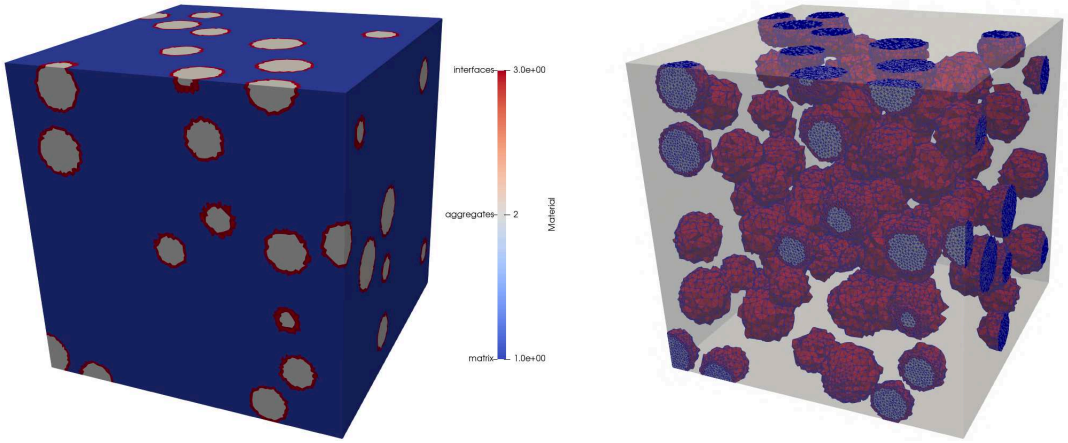

(a) Morphology of the cube with randomly positioned spheres

(b) The rojection to the mesh

Figure IV .17: Morphological structure of the cube and its projection to the uniformed mesh.

First of all, the emergence of asymmetric traction/compression responses can be observed for both models with/without closure of cracks. The ratio between the compressional and tensile resistance is 2.7, which is smaller than the observed ratio for pure mode-I models with the value equals to 8.9. This is because a model which exhibits pure mode-II strong discontinuities has its limitations for describing the failure under traction loadings. Physically, the crack patterns for traction corresponds to an "opening" mechanism. It can be obviously observed in the previous chapter of the mode-I discontinuity simulations. The orientations of the crack should be perpendicular to the loading direction. Since the strong discontinuity of the type mode-II simulates a "sliding" mechanism, it produces a higher tensile resistance under traction loadings. In the following part, our attention is mainly focused on the material behaviors which associate with the compressional loadings.

Second, we draw the transversal and volumetric strain in Fig. IV .19. It is recalled that the loadings are applied on direction Z, and the lateral faces along X-axis and Y-axis are set to be stress-free. Thus the transversal strain is defined as the average value of these faces. The volumetric strain is calculated as the sum of the axial strain and transversal strains:

$$\varepsilon^{\mathrm{M}}_{\mathrm{vol}} = \varepsilon^{\mathrm{M}}_{z} + \varepsilon^{\mathrm{M}}_{\theta_1} + \varepsilon^{\mathrm{M}}_{\theta_2}.$$

It represents the dilatation of the material, which can be expressed as: $\varepsilon^{\mathrm{M}}_{\mathrm{vol}} = \frac{\Delta V}{V}$. It can be seen that the volume of the material begins to expand after it reaches the resistance

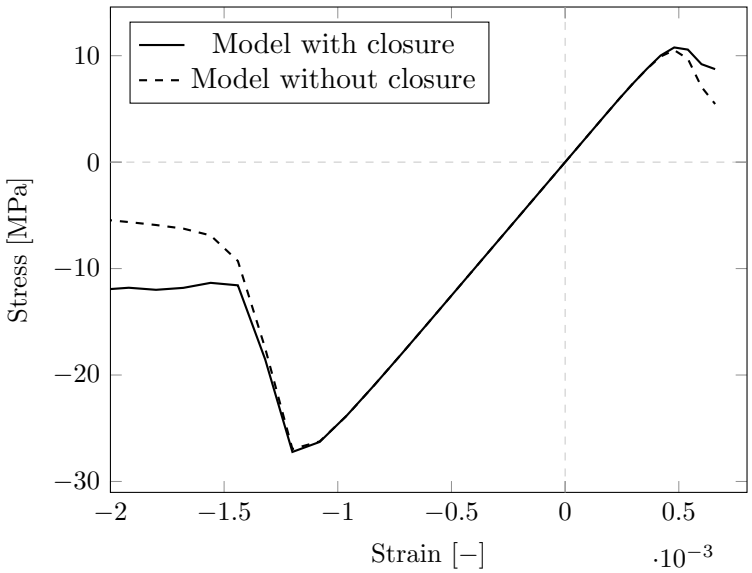

Figure IV .18: Macroscopic responses of the cube under simple traction and compression loadings.

of the material. Compared with the compression behaviors which is obtained by mode-I discontinuity models, the dilatation is much smaller. Subsequently, at the region of an important loading, where the material reaches the residual stress stage, the contraction is observed. This phenomenon is not consistent with the experimental facts. This is because only the mode-II discontinuities are taken into concern. In the case of exhibiting explicit heterogeneities, the "opening" of the cracks should also be taken into consideration. We have presented in the previous chapter that the crack openings of mode-I could induce a big amount of dilatations.

Third, we draw the cracks for the model with/without crack closures at the loading position after the failure of the material, where the strain equals to -2.0×10^{-3}, see Fig. IV .20. The emergence of macroscopic crack paths can be observed in the material. Unlike the crack pattern that we present in the previous chapter with the strong discontinuity of mode-I, the fractures are not parallel to the loading direction. In this case of the mode-II model, the angle between the macroscopic cracks and the loading direction is around 45°. At the strain equals to -2.0×10^{-3}, there are already many closures in the material, see Fig. IV .21. The closing elements are marked in Fig. IV .20. As it is depicted in the figure, the closing behaviors of the material can be observed even in monotonic loadings. The position of the closing elements is located beside the major cracks where the propagations of major fractures reduce stress releases.

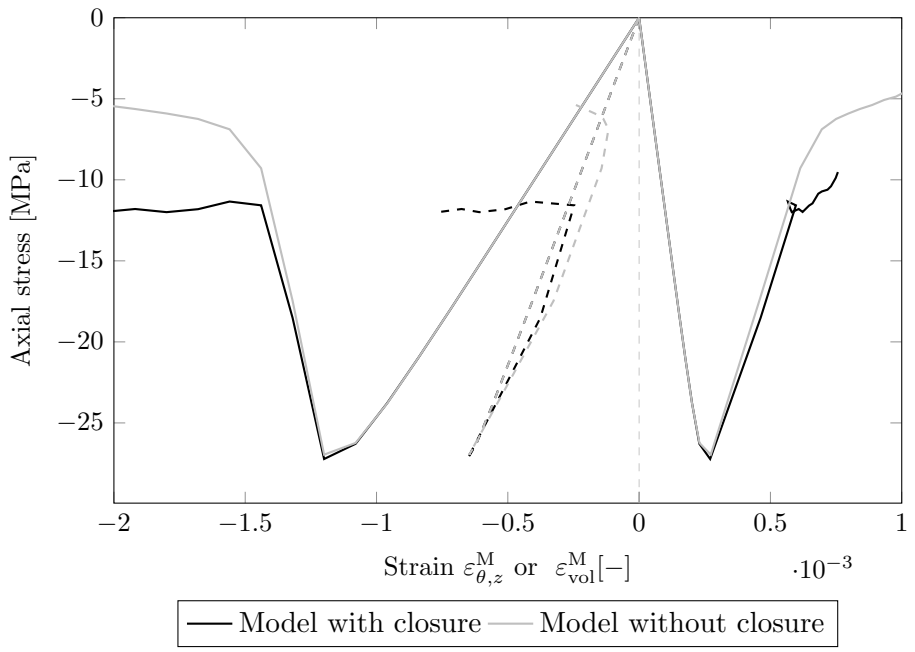

Figure IV .19: Macroscopic responses of the macroscopic stress in terms of the axial, transversal and volumetric strains for compression test.

Last, we draw our attention to Fig. IV .21. Through overlaying the macroscopic response of the material with the number of localized/closing elements, it can be noticed that for the majority of the elements, the localization takes place between the strain $[1.2 \times 10^{-3}, 1.5 \times 10^{-3}]$, and it is also the moment when the failure of the material occurs. The model with and without crack closure mechanism carries almost the same amount of localized elements. This is because these two models have the same localization law, thus at the stage of initiation and propagation of fractures, they have the same crack pattern. Another information that we can obtain from the figure is that the majority part of crack closure is induced after the formulation of localized cracks, which is at the latter part of the loading, and there are rare elements that admit a localization at this stage.

3.0.2 Fatigue loadings

In this section, let us consider fatigue loadings to the heterogeneous cube using the numerical models with mode-II discontinuities. The same morphological model, parameters of the material, and the boundary conditions are used here. The imposed compressional cyclic displacement is plotted in Fig. IV .22. In order to illustrate the effect of the clo-

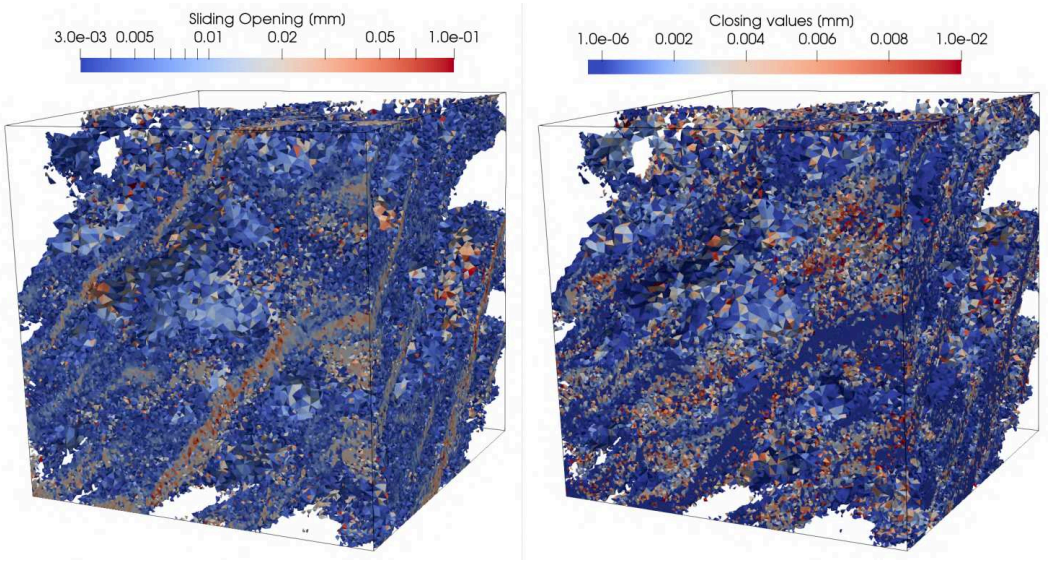

Figure IV .20: Crack pattern of the model with crack closures at the macroscopic strain equals to -2.0×10^{-3}.

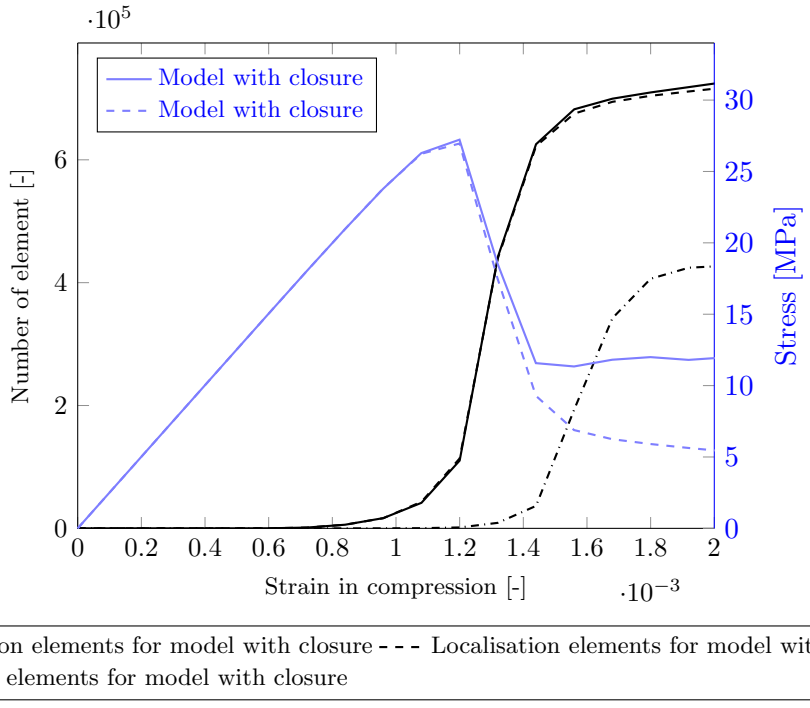

Figure IV .21: Accumulate percentage of elements along the compressional loading and overlaying with the macroscopic compressional response.

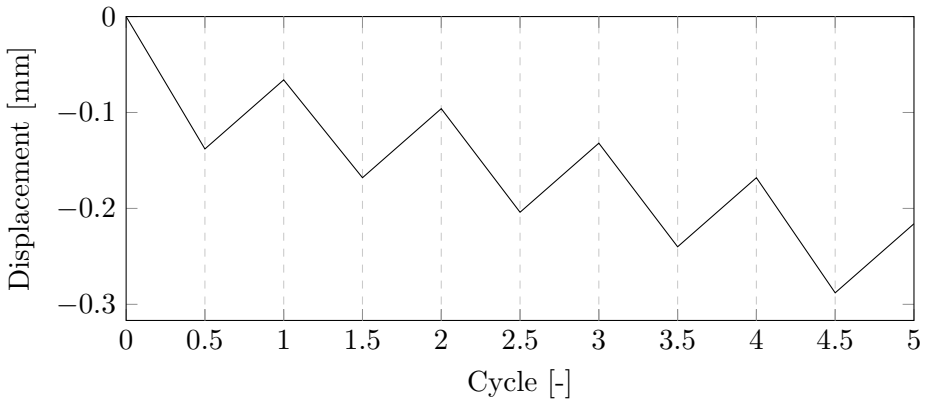

Figure IV .22: Proposed displacement path for the cyclic loading.

sure mechanism, a comparison of the macroscopic responses between the model with and without crack closures are plotted in Fig. IV .23.

It can be seen from the figure that the model with closure mechanism achieves at producing hysteresis loops while the model without does not. The emergence of the hysteresis loops is associated with several constituents, such as the explicit representation of the heterogeneities, the large number of finite elements, the additional dissipated energy, and the plastic deformation. In order to analysis the resources of this phenomenon, we quantified the plasticity and the degree of loss of stiffness, the results are listed in Table. IV .3. In this table, the degree of damage during the cycles is represented by an equivalent variable d_i. The expression gives as (Roubin, 2013):

$$d_i = \frac{E_i^{\mathrm{M}} - E_0^{\mathrm{M}}}{E_0^{\mathrm{M}}}, \tag{3.1}$$

where E_i^{M} represents the macroscopic Young's module at i^{th} cycle and E_0^{M} represents the one at initial stage.

It is worth noting that the plasticity mechanism is not formulated at the mesoscopic scale. The observed plastic deformation is a result of the emergence from the local scale to macro-scale. Comparing the differences between the model with and without crack closure, the former model carries a higher value of increasing plasticity during the cycles. The observed increasing value of plasticity takes its origin from the dissipated energy on the frictional sliding. Also, the hysteresis loops are linked with this supplementary dissipated energy on the crack closures.

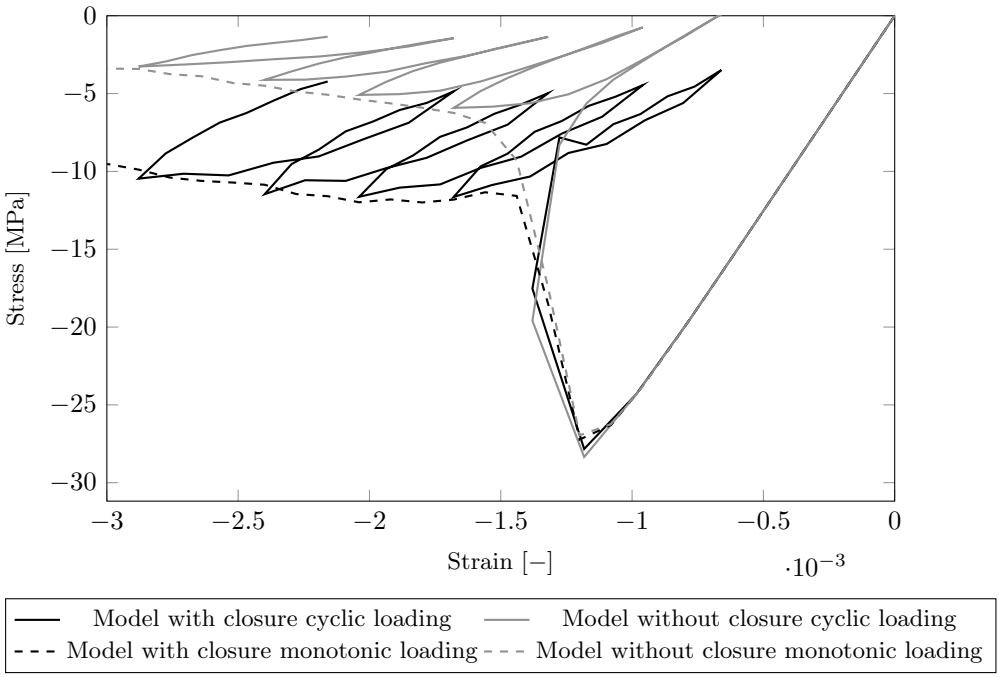

Figure IV .23: Macroscopic responses of the cube under compressional cyclic loadings.

In the previous chapter, the closure mechanism is applied to a model with the mode-I strong discontinuity. The additional dissipated energy is also considered. However, compared with the mode-II discontinuity, the latter allows a larger amount of plasticity. The friction between the lips of micro-cracks plays a significant role in producing plastic deformations.

Then move our attention to the stiffness of the material. The model without crack closures losses a lot more stiffness along with the cyclic loadings, the equivalent damage variable is also more significant than the other model. This is because the model with the closure mechanism has its stiffness partially recovers due to the crack closures.

Last, let us take a look at the number of localized elements and the closing elements, see Fig. IV .25. Referring to the first cycle, the majority of the localization takes place at this stage. It means that during the latter four cycles, the sliding opening/closing behaviors and the re-opening/re-closing behaviors occur mainly in the same groups of elements. Comparing the two models, they have a similar amount of localized element at the end of loading.

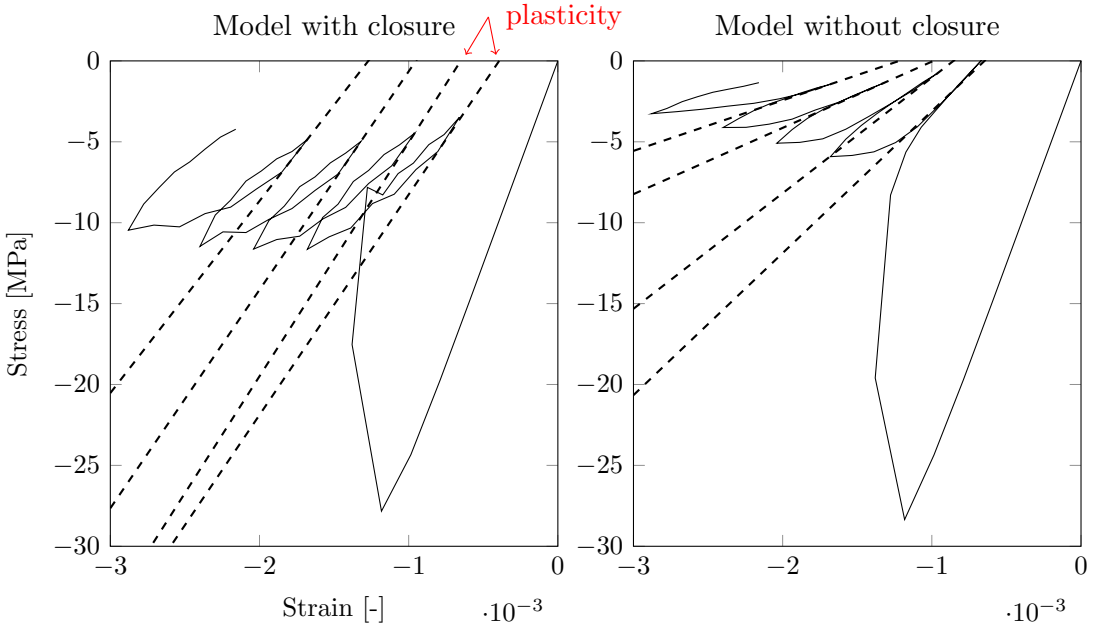

Figure IV .24: Illustration of the loss of stiffness and the macroscopic plasticity in cyclic loading for model with/without crack closures.

Cycle i	Young's Module E_i^M [GPa]		Damage d_i [-]		Plastic deformation ε_i^p [10^{-3}]	
0	25.1	25.1	0	0	0	0
1	14.5	8.8	0.42	0.65	0.39	0.65
2	13.6	7.1	0.46	0.72	0.65	0.86
3	13.5	4.1	0.46	0.84	0.95	0.99
4	11.9	3.1	0.53	0.88	1.27	1.22

Table IV .3: Variation of the damage and plastic deformation along the cyclic loadings, the model exhibits crack closure behavior is marked in gray.

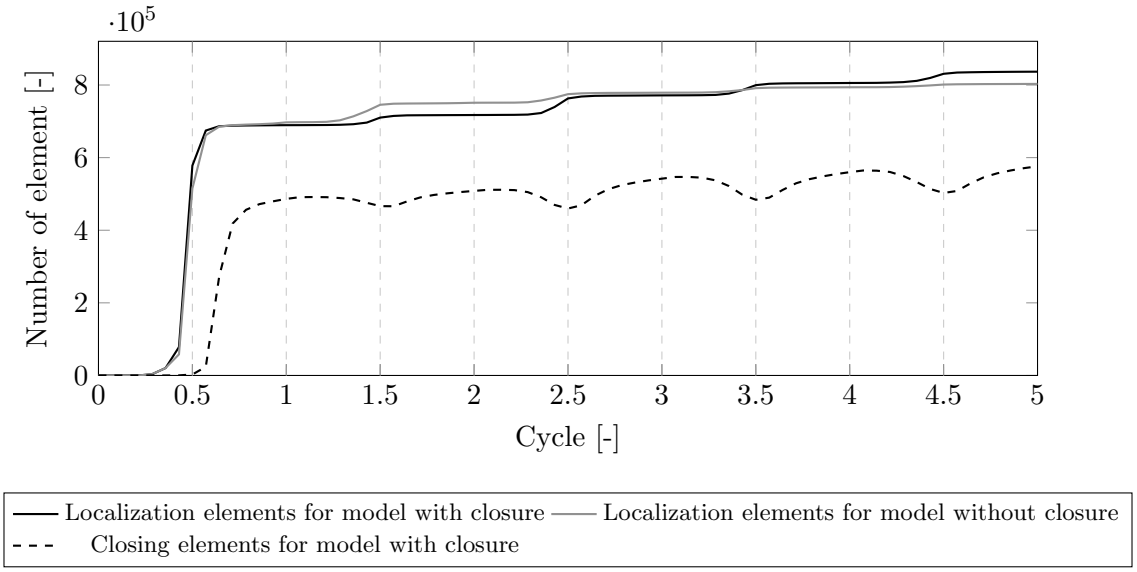

Figure IV .25: Accumulate percentage of localized elements and closing elements along the 5 cycles for model with/without crack closure mechanism.

Before the discussion about the number of closing elements, it is worth noting a priori that we assume the closing elements to be the ones which do not have a sliding-opening value bigger than the already reached maximum opening value. It can be seen that as the displacement trajectory loads and unloads, the number of closing elements also decreases and increases. However, a number of closing elements always remain in the closing status. Among several reasons for this observation, the most important one is that the degrees of damage is different for localized elements, and the most damaged elements are the easiest to trigger the closing process. Thus a number of elements admit a closing process at the first phase of unloading. Then at the subsequent reloading phase, there is only a group of elements arrive at the maximum sliding-opening value and switch to the opening status, while other elements are still in the closing status.

4 Comparison between the numerical simulation and the experimental results

In this section, the proposed model which exhibits mode-II discontinuities and the crack closure mechanism are tested by comparing with the experimental results. The experimental results are provided in Piotrowska (2013). As it is presented in the previous chapter, three kinds of concretes are used, the Crushed aggregate concrete (SC), the Rolled

aggregate concrete (SC) and the Glass ball concrete (GB). In this chapter, the numerical simulations are applied to the same morphological models which have been constructed previously.

This section consists of two parts. We present in the first part the identification of the parameters of the material. The parameters of the material are determined by comparing with the results of monotonic compression loadings. Then the analysis and discussions of the comparison are shown in the second part. The analysis of the results are detailed.

4.1 Identifications of material parameters

This section aims at finding the parameters of the material to reproduce the experimental results. The used morphological model contains two materials, the matrix, and the aggregates. The projection leads to three types of elements, representing the matrix elements, the aggregate elements, and the interface elements. Five parameters are employed in each type of elements: two elastic parameters E and ν; and three parameters which associate with the failure behaviors of the material, the cohesion C, the fracture energy $\mathcal{G}_{\text{op}}$ and the friction angle φ. Among these parameters, the elastic parameters have already been determined in the previous chapter. For the sake of simplicity, the aggregates are considered as pure elastic, and the same critical parameters are used for matrix elements and interface elements. Therefore, three unknown parameters remain to be identified: the cohesion C, the fracture energy $\mathcal{G}_{\text{op}}$, and the friction angle φ for the matrix/interface elements.

The unknown parameters are determined by comparing with the experimental results under monotonic compression loadings. In the previous chapter (mode-I discontinuity model), the behaviors of the material are related to two parameters, the tensile strength, and the fracture energy. The effects of these two parameters have been discussed in chapter 2. In this chapter, similar parameters are also used in the model: a critical stress-based value, the cohesion C; and fracture energy $\mathcal{G}_{\text{op}}$, representing the required energy for completely opening. They have similar effects on the failure behaviors of material. A bigger value of the cohesion reproduces a higher resistance of the material, and also a more fragile behavior at the post-localization region. Also, a bigger value of the fracture energy induces a more ductile behavior, and also a relatively higher resistance. Besides these two parameters, the effect of the friction angle φ is still unclear.

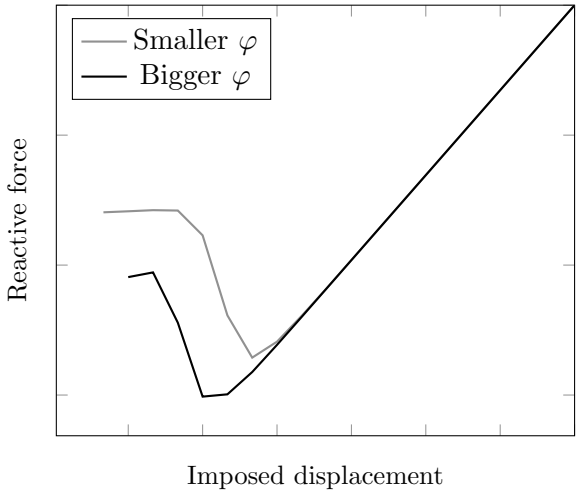

Figure IV .26: Effect of the friction angle φ at emergence macroscopic scale.

Concrete	E^1 [GPa]	ν^1 [-]	E^2 [GPa]	ν^2 [-]	C [MPa]	$\mathcal{G}_{\text{op}}[J/m^2]$	$tan\varphi$ [-]
SC	18.0	0.16	78	0.12	16.0	6.0	0.5
SR	16.5	0.16	78	0.12	14.8	5.0	0.5
GB	18.0	0.16	70	0.22	11.8	3.0	0.5

Table IV .4: Obtained parameters of the material for three different types of concrete.

In order to illustrate the effect of the friction angle φ, we apply here two different values of friction angles at the local scale, their macroscopic responses are plotted in Fig. IV .26. It can be seen that a bigger friction angle induces to more significant resistance of the material for compression. The tendency of the failure behaviors in the post-localization region is quite similar, because the sliding-opening and sliding-closing procedures are only controlled by the cohesion C, and the fracture energy $\mathcal{G}_{\text{op}}$.

After the identification, the obtained parameters for all three types of concretes are listed in Table. IV .4. It can be seen that the SC concrete which exhibits the most coarse aggregates, carries the biggest value of the cohesion and the fracture energy. Also, the GB concrete has the smallest ones. This fact provides a good agreement to the physical defi-

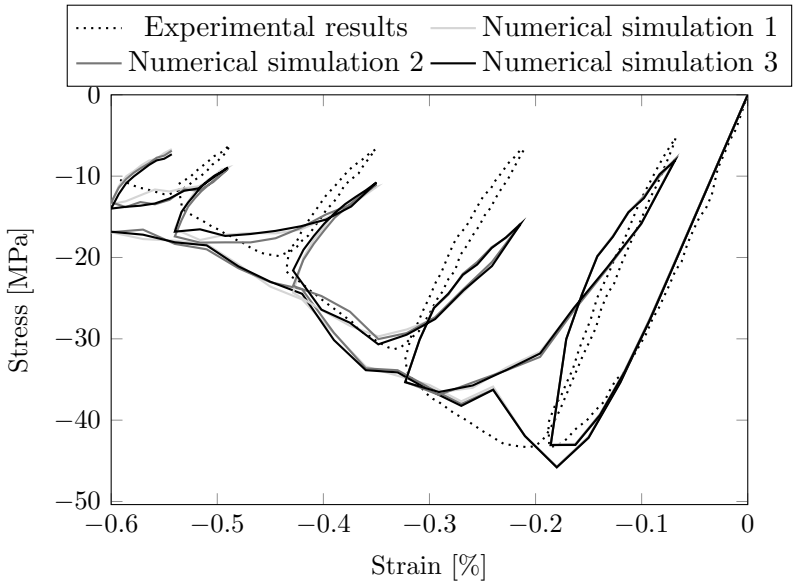

(a) SC

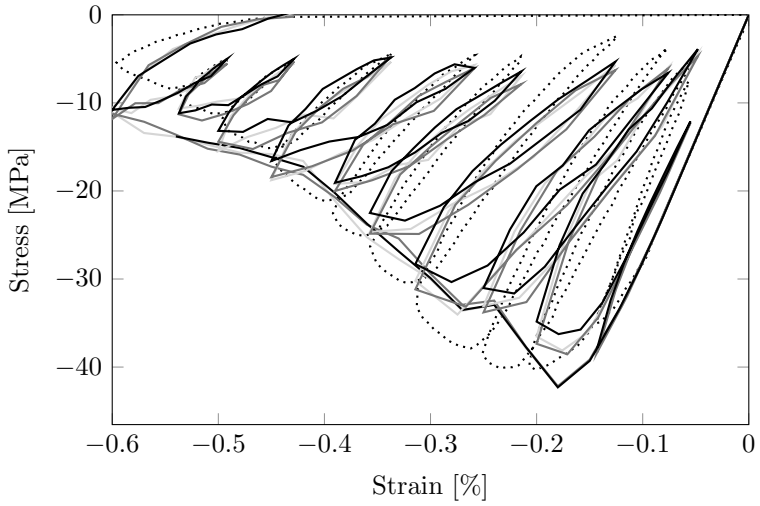

(b) SR

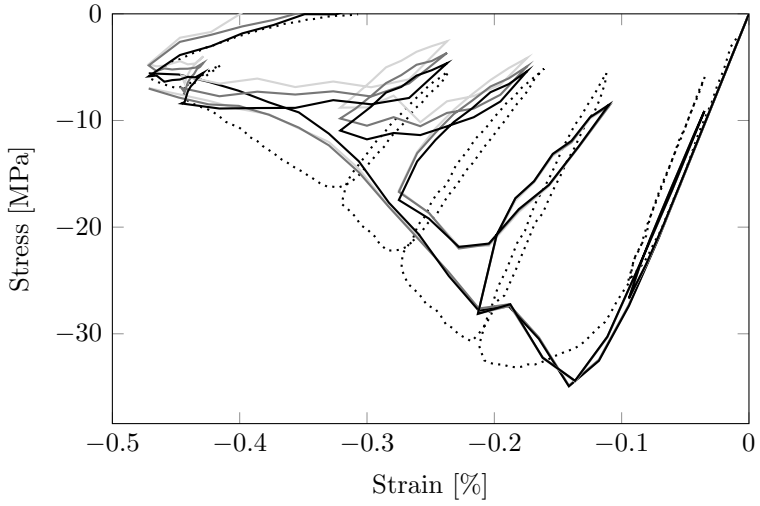

(c) GB

Figure IV .27: Comparison between the experimental results and the numerical simulations for SC, SR and GB concretes.

nitions of these parameters. After the material parameters are identified, fatigue loadings are applied to the material. The comparison between the numerical simulations and the experimental results are plotted in Fig. IV .27.

4.2 Comparison between the simulations and the experimental results

The parameters of the material for three different concretes have been defined in the previous part. The identifications of the parameter are based on the performances of the concrete under simple compressional loadings. In this part, the cyclic loadings are applied to the material with the same parameters. For each kind of the concrete, the trajectory of the imposed displacement is determined by the provided experimental data (the macroscopic deformation multiples the height of the cylinder 140 millimeters).

This section consists of two parts. We present in the first part, the development of the cracks in concretes — especially the influences of the crack closure mechanism. Thus the attention is focused on the differences between the same specimen but in different loading steps. In this part, we take the SC concrete as an example. Then in the second part, our interests are focused on the differences between concretes which exhibit different aggregates, for example, the crushed aggregates and the glass balls.

We illustrate the relationship between the development of cracks and the macroscopic response of the SC concrete in Fig. IV .28. The variations of the number of localized elements and the closing elements are in the same pattern as what we have presented previously, see Fig. IV .21.The number of finite elements which exhibit a localization increases when the failure behaviors of the material take place. At the so-called “post-localization” stage, there are few elements which admit a new localization. It means that the majority of the cracks are initiated when the failure begins. Then the failure behavior of the material is caused by the propagation of the same groups of elements. As the cracks develop and propagate, the crack closures occur in the material.

In order to present what happened inside the material during the compressional loading, we take two loading stages as examples: they are the materials at the macroscopic strain equal to 0.48 and 0.6, corresponding to the stage at the general beginning of crack closures and the end of crack closures. Several figures are drawn in the following part, in Fig. IV .29, showing the development of the crack patterns of the concrete in terms of the

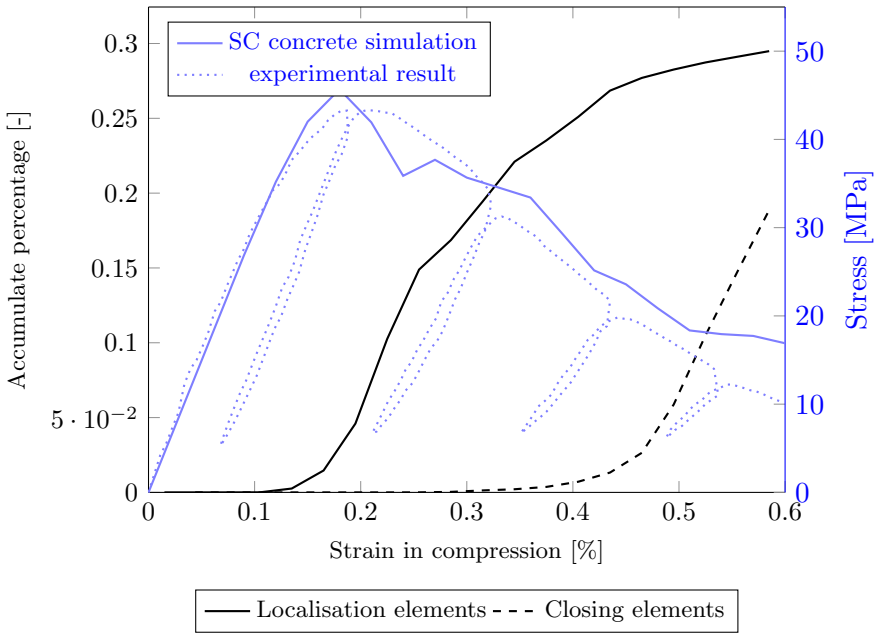

Figure IV .28: Accumulate percentage of elements for SC concrete along the compressional loading and overlaying with the macroscopic compressional response.

sliding-opening values and the closing values.

As we have introduced in the previous parts, that the crack closures are triggered by stress releases. In the case of exhibiting complex multi-cracks, the evaluations of cracks are influenced between each other. As we can see in Fig. IV .29(c) and Fig. IV .29(d), no crack closures are observed in the center of major cracks, while there are a lot of closing cracks between them. The consequences of the crack closures can also be observed in Fig. IV .29(a) and Fig. IV .29(b), that the cracks are less diffused and more concentrated in major cracks.

Next, aiming at finding the influences of the parameters to the material, we present in this part comparison between the SC concrete and the GB concrete. Regarding the parameters of the material for three different types of concrete, it can be seen from Table. IV .4 that the SC concrete has the biggest cohesion and the fracture energy. Thus it should be the most ductile one and carries the biggest resistance. To illustrate the differences between the SC and GB concrete, the same loading step is chosen at the same strain, which equals to 0.48.

The crack patterns for the two concrete are shown in Fig. IV .30. It is worth noting

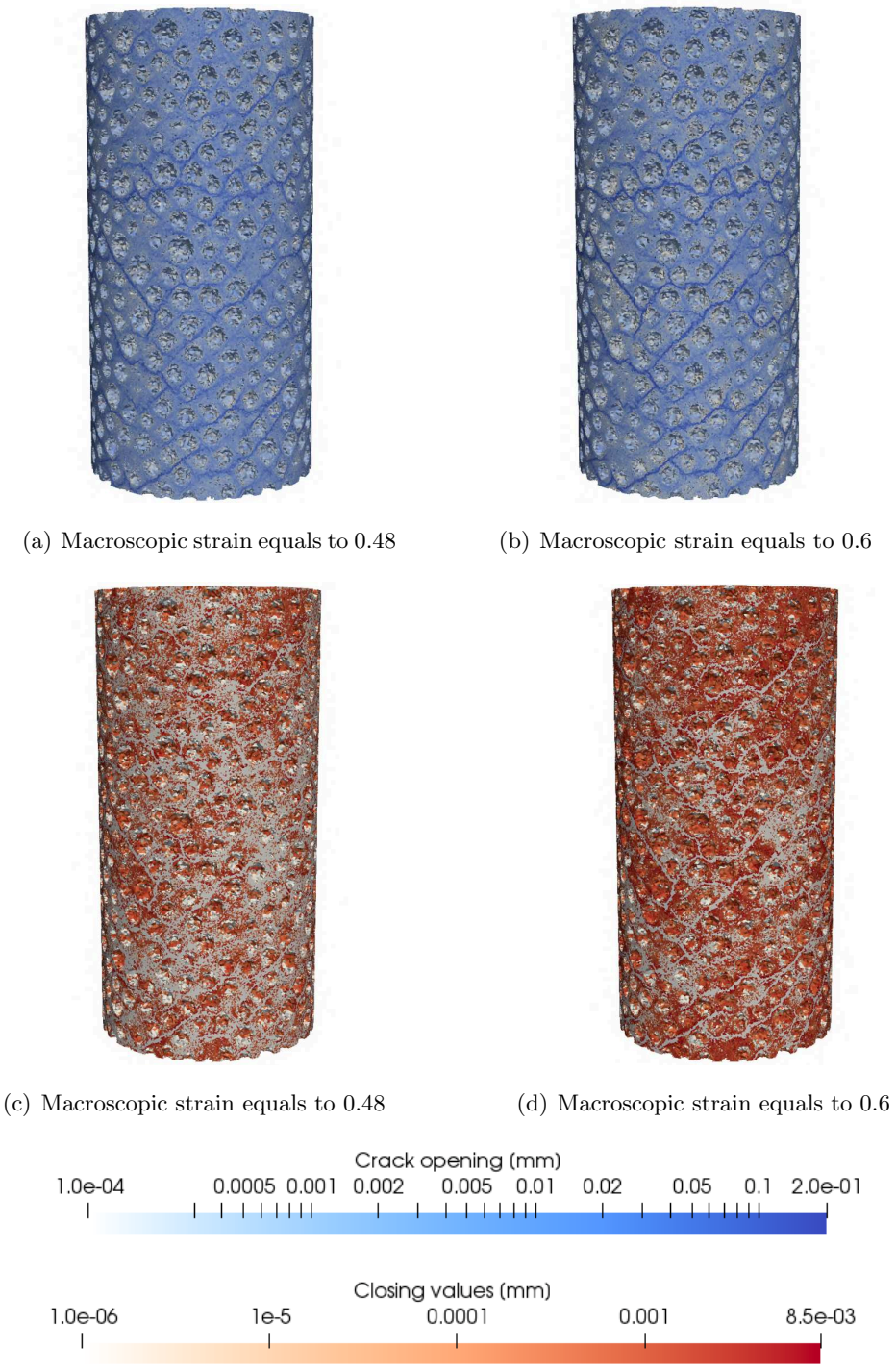

(a) Macroscopic strain equals to 0.48 (b) Macroscopic strain equals to 0.6

(c) Macroscopic strain equals to 0.48 (d) Macroscopic strain equals to 0.6

Figure IV .29: Crack pattern in SC concrete at different loading stage.

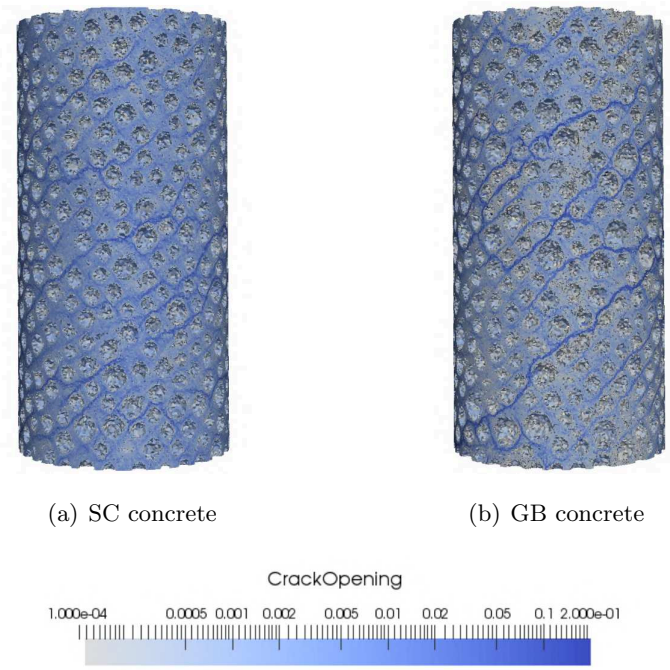

(a) SC concrete (b) GB concrete

Figure IV .30: Crack pattern for SC concrete and GB concrete at the same loading stage with strain equals to 0.48.

that they have different morphological features, thus the cracks will initiate and propagate in different positions. Despite this difference, it can be seen that the multi-cracks for SC concrete has more branches. The GB concrete has less macroscopic cracks, but the cracks are more "localized" and "concentrated". These observations correspond to a more fragile behavior of the GB concrete and verify the physical meanings of our material parameters.

5 Triaxial applications

In the previous section, the focus is made on the performances of the model in uniaxial loadings. Many typical behaviors of a quasi-brittle material have been observed. Also, the comparison between the experimental results shows a good agreement. In this section, our interests are focused on the mechanical behaviors of material under triaxial loadings. The numerical simulations consist of two steps, that first, a triaxial confining pressure is applied to the material, and second, a deviatoric displacement is applied to the material. As a first illustration of the mechanical model's feature, the triaxial loadings are firstly imposed to the specimen that we present in section 3.0.2. Then the comparison between the experimental results under triaxial loadings is also addressed subsequently.

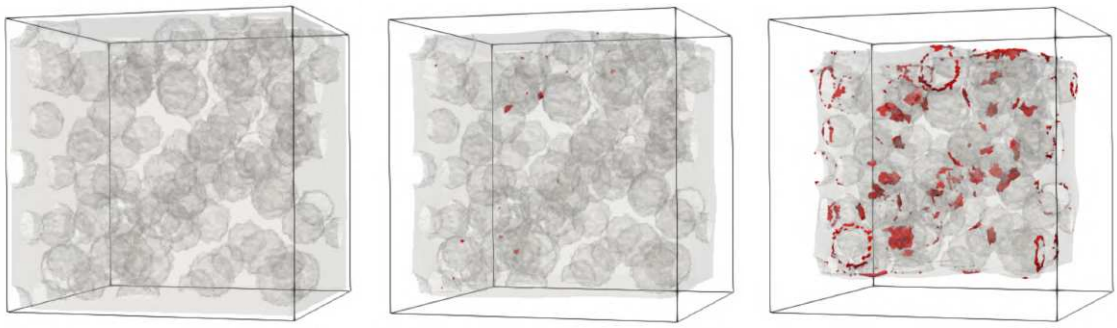

(a) Confining pressure of 10 MPa (b) Confining pressure of 50 MPa (c) Confining pressure of 100 MPa

Figure IV .31: Deformations of the cube under different confining pressures with an amplification factor equals to 100, the localized elements are marked in red.

5.1 Triaxial applications to the cube

In this part, the triaxial loadings are applied to the cube that we present in section 3.0.2. Exactly the same parameters are used here, see Table. IV .2. Three different confining pressures are applied to the cube, 10 MPa, 50 MPa, and 100 MPa. Fig. IV .31 shows the deformation of the material after been applied to different confining pressures. Clearly, higher confining pressure brings bigger deformation and more fractures. It worth reminding that the used localization criterion at the local scale is a Mohr-Coulomb criterion, which, will not activate strong discontinuity for a homogeneous material under confining pressure. The observed fractures in Fig. IV .31 are induced by the stress concentrations caused by explicit heterogeneities. It also can be seen that the cracks are gathered around the rigid inclusions, which indicates the locations of stress concentrations.

We show the macroscopic responses of the material under monotonic triaxial compression in Fig. IV .32. It can be noticed that as the confining pressure increases, the material obtains a higher resistance and becomes more ductile. We draw the responses of the material under triaxial cyclic loadings in Fig. IV .33. We can see from this figure that

- As the confining pressure increases, the surface corresponds to the hysteresis loops decreases. There are almost no hysteresis loops can be observed under a confining pressure of 100 MPa. This mechanical behavior is consistent with experimental observations.

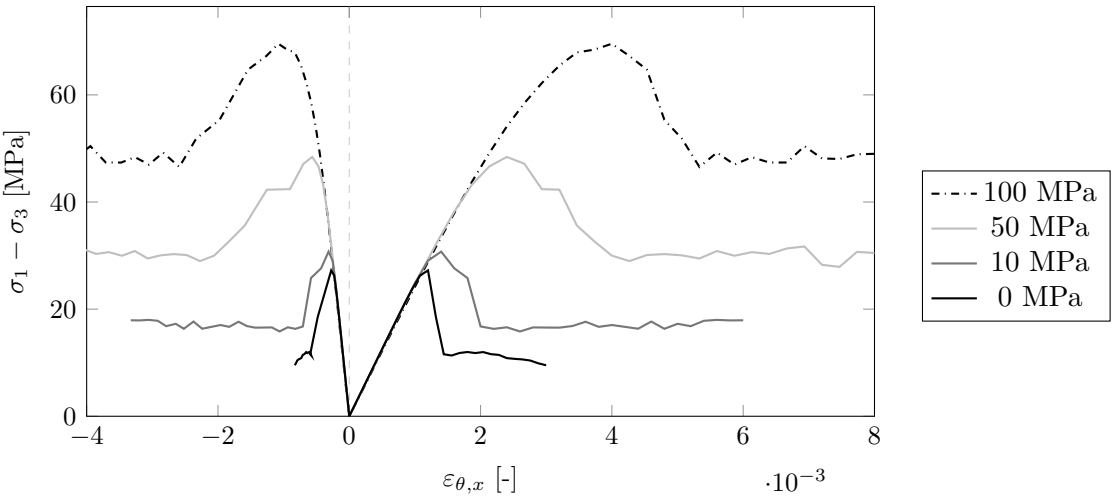

Figure IV .32: Monotonic responses of the material under different confining pressures.

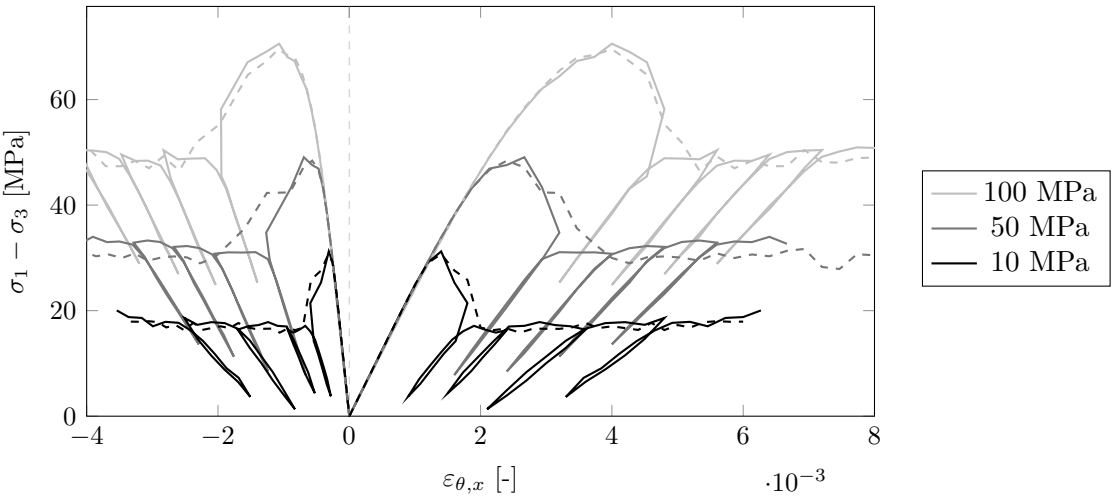

Figure IV .33: Macroscopic responses of the material under three different confining pressures for fatigue loadings.

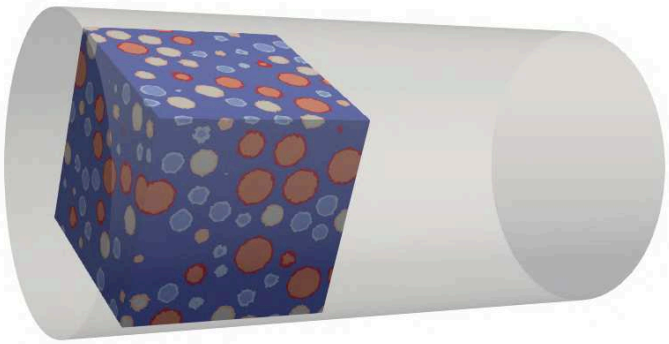

Figure IV .34: Studied specimen for GB concrete for triaxial loading.

- The material loss an amount of stiffness during the fatigue procedure. It can be seen from the figure that as the confining pressure increases, the material losses less of its stiffness.

5.2 Triaxial applications to the experimental specimens

In the previous part, the model is submitted to triaxial loadings. As it is depicted in Fig. IV .33, several typical behaviors of quasi-brittle materials under different levels of confining pressures can be observed. We present in the section 3.0.2 that the simulations of the model show a good agreement with the experimental results. In this part, our interest is focused on a qualitative comparison between experimental and numerical results under triaxial occasions to verify the capacity of the model. The experimental results are provided by Piotrowska (2013).

In doing so, some basic settings regarding this test are mentioned here. The parameters of the material for all three types of concretes remain the same as in uniaxial loading, see Table. IV .4. As it is drawn in Fig. IV .34, the tested morphological model is chosen to be a cube cut from the cylindric specimen.

Fig. IV .35 and Fig. IV .36 plot the comparison of the results for three types of concretes under a confining pressure of 50 MPa and 100 MPa. We can see that in experimental results, peak stress can still be observed under a confining pressure of 50 MPa, while no peak stress occurs under a higher confining pressure of 100 MPa, except the GB concrete. Also, the responses of specimens have a form of a plateau at the post-peak stage, representing that the materials become more ductile under high pressures. As for the numerical results, Fig. IV .35 and Fig. IV .36 illustrate that the simulations also show

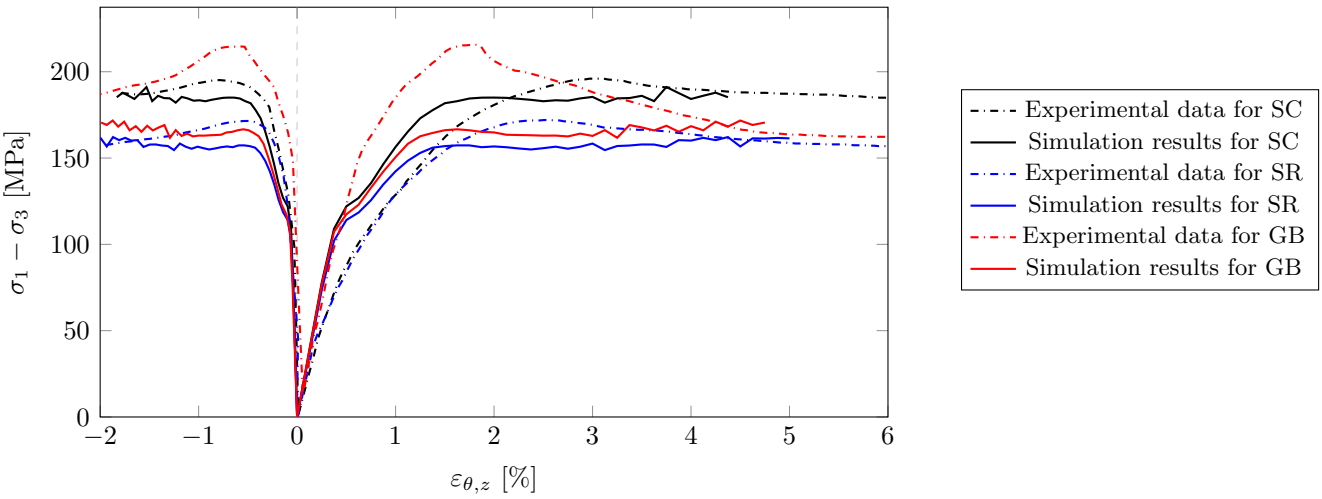

Figure IV .35: Comparison between the experimental and simulation results under a confining pressure of 50 MPa.

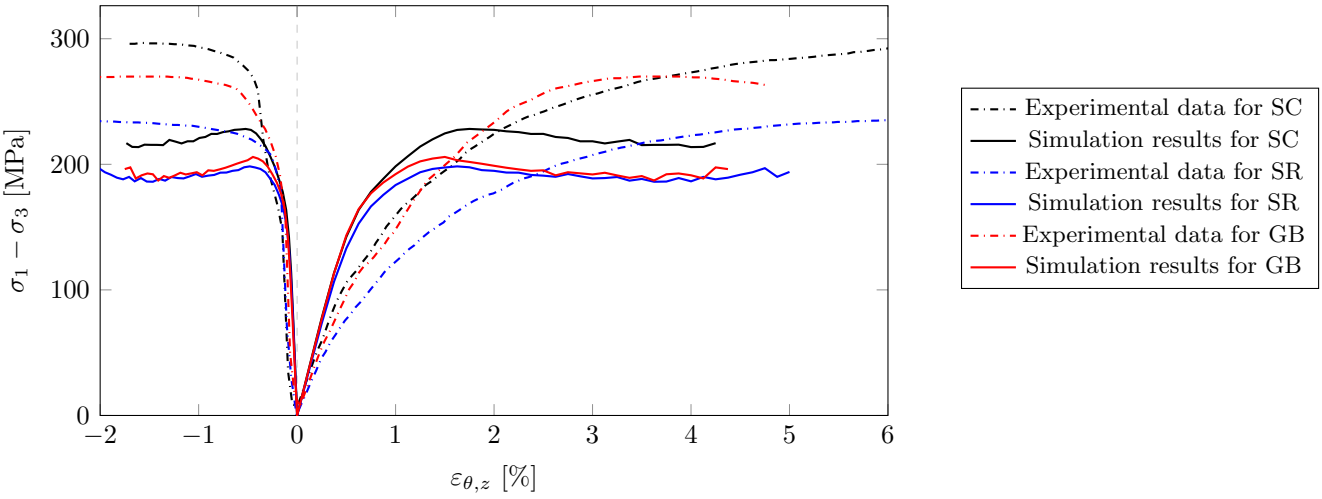

Figure IV .36: Comparison between the experimental and simulation results under a confining pressure of 100 MPa.

plateau stresses, which have similar values for 50 MPa and rather different values for 100 MPa. Among several reasons to explain this inconsistent with the experimental results, the most important one should be related to the hardening behavior of the material. This phenomenon is associated with porosity closure in cement paste under high pressures. As we can see in Fig. III .45, the voids are marked in black in tomographic images, the porosity percentage is essential. In our morphological model, however, the porosity is not taken into consideration. This leads to an underestimating of the plateau stress in triaxial loadings, especially for a high confining pressure.

Another important observation is that in Fig. IV .35, the macroscopic Young's module at the elastic stage for GB concrete is higher than the other two concretes. For SC and SR concretes, decreasing tangential stiffness of material can be observed after short linear phases. In numerical results, however, all three types of concretes have the same elastic Young's module as the GB concrete. This is because the glass balls have much bigger compressive strength than siliceous aggregates (Piotrowska, 2013). Since we assumed a pure elastic behavior for inclusions, the failures of inclusions can not be taken into concern. Thus the simulation results present a macroscopic Young's module of all three types of concretes, which is more similar to the experimental result of GB concrete. At a higher level of confining pressure, as shown in Fig. IV .36, the effect of fractured inclusions is more evident.

In summary, we can improve the performance of the model in triaxial loadings with several modifications. Fist, the fractures of inclusions might be ignorable in uniaxial loadings but is necessary to take into consideration in the case of high pressures. Second, it is also essential to take into account the effects of voids because the porosity closures play an essential role in the material's densification. Moreover, besides these two points, even it is not directly deduced from the figures, the plasticity may also be a significant component to the model because as the confining pressure increases, the quasi-brittle material becomes more ductile.

6 Conclusion

In order to identify the minimum ingredients of concrete fatigue behaviors, we presented in the previous chapter the performances of the model, which exhibits mode-I strong

discontinuity with closure mechanism. The hysteresis phenomenon has been achieved. However, plastic deformation was insufficient. In this chapter, the closure mechanism is applied to a model with mode-II strong discontinuities. Thus, the friction between the lips of micro-cracks is taken into account. In addition to crack closures, the weak discontinuity was also added to the model.

To adapt to the spirit of simple modeling at the local scale, the crack closure mechanism is formulated without requiring additional parameters. To illustrating the emergent effects of the crack closure mechanism, we presented in Sec. 3.0.2 comparisons between the model with crack closures and the model without crack closures. By applying simple traction/compression loadings to the model, the macroscopic responses are strictly symmetric at the elastic stage. Then, asymmetric traction/compression behaviors can be observed after the material reaches the resistances. It can be observed that the crack closure can be triggered even in monotonic loadings. The effects of the closure mechanism were more clearly illustrated in cyclic loadings. As the micro-crack slides forward and backward on the frictional discontinuity, the additional dissipated energy is produced accompanied by the stiffness recovery and the plastic deformation. Thus the hysteresis phenomenon can be observed.

The model was then tested by comparing it with the experimental results. Three types of concrete with different aggregates were simulated. The numerical simulations show a good agreement for monotonic and cyclic loadings. Then the model was applied to triaxial loadings. The results show an essential consideration of the crushed of aggregates and the macro-pores.

Another issue of the pure mode-II discontinuities model is that the volumetric dilatation is not obvious, which is not consistent with experimental facts. In addition, the mode-II discontinuity model is not suitable for describing material behaviors in tractions. This is because the characteristics of the crack under tensile loading are more likely to be an 'opening' than a "sliding". Reviewing these two weak points, it can be noticed that they can be corrected by the spirit of the mode-I discontinuities. In order to overcome these shortcomings and improve the model's performance, it may be interesting to merge the mode-I with mode-II.

Chapter V

Conclusion and perspectives

Summary

In this study, we have made the assumption that the complex mechanical behaviors of concrete can emerge from the upscaling of elements with simple behaviors and explicit heterogeneous structure of concrete, see Fig. I .2. Therefore, with: i) the macroscopic behaviors of concrete are known a priori in experimental tests; ii) the morphological structure is established by large number of elements and explicit representation of heterogeneities; the objective of this study is to clarify the minimum necessary mechanism of each individual element to perform the fatigue behaviors of concrete, and the effects of these ingredients.

For these purposes, the developed numerical model is based on the kinematic enrichment in the context of finite element, two kinds of enhancement are used: the weak discontinuity and the strong discontinuity. By applying the non-adapted mesh strategy, the weak discontinuity allows explicit representations of heterogeneities. The strong discontinuities are implied to represent the cracks in the material in an explicit way. Through combining these two separate enhancements, multiple features of cracks can be observed in the material, such as the explicit tortuous crack paths which pass around rigid aggregates, the merges of cracks, and branches of cracks.

In this work, the numerical model considered two separate discontinuity types: the mode-I discontinuity, representing an "opening" behavior; and the mode-II discontinuity, which produces "frictional sliding". In practice, simple and meaningful criteria are applied at the mesoscopic scale, including the initiation, opening and closing behaviors of

cracks. Physical parameters are used in these criteria. Referring to the mode-I model, the behaviors are linked with the fracture energy and the tensile strength. Referring to mode-II model, the associated parameters are the fracture energy, the cohesion, and the friction angle. It worth emphasizing that no additional parameters are required for the description of the crack closing mechanism. The crack closures are formulated within the physical considerations. From local scale to macroscopic scale, complex mechanical behaviors can be observed, referring to as the emergence phenomena.

Several typical failures and fatigue behaviors of quasi-brittle materials can be observed for the numerical model which exhibits **mode-I discontinuities**:

- The model shows asymmetric responses in traction and compression.
- The crack patterns verifies experimental observations: the cracks are perpendicular to the loading direction for tensile loadings, and are parallel to the loadings for compressional loadings.
- The volumetric dilatation is induced at the post-peak stage.
- Closure of cracks can be observed even in monotonic loadings, which can be considered as a shrinkage of the localization band as the load increases.
- The unilateral effect can be observed.
- The hysteresis phenomena can be seen in cyclic loadings, and also the progressive loss of stiffness and the plastic strains. This observation indicates that without the consideration of frictional sliding, the hysteresis loops can also be seen due the additional dissipated energy.

However, several weak points are worth noticing regarding its macroscopic responses under monotonic and cyclic loadings:

- The model suffers from the stress locking effect, especially in compression. This can be solved by applying mode-II discontinuities to the model.
- The comparison between the numerical simulation and the experimental results is not good enough, because the loss of stiffness in cyclic loadings is too fast, and increasing value of plastic strain is insufficient. This limitation is associated with the lack of consideration of the friction. The friction between the lips of micro-cracks plays an essential role in producing fatigue behaviors of concrete.

Therefore, the mode-II discontinuity is applied to the model. Many features are also observed, such as the asymmetric traction/compression responses. Compared with the former model, the model of **mode-II discontinuity** reveals some different features that:

- The stress locking effect is less severe.
- More plastic deformation can be observed, due to the frictional sliding.
- The model shows a good agreement to the experimental results.

Still, the model contains some limitations:

- The model is not adapted to be applied to traction loadings, the compressive to tensile strength ratio is rather low, and is dependent on one of the material parameters, the friction angle. By the same token, the crack paths for traction are not rigorously perpendicular to the loading direction, which does not correspond to experimental observations.
- The volumetric dilatation is not detected in the softening stage.
- By applying the model to triaxial loadings, the result shows a necessity to take into account the crushed aggregates and macro-pores. However, the crushed aggregates bring other unknown parameters, and increasing the difficulty to identify all of the material's parameters to match the experimental results.

Future works

Regarding the supports and inadequacies of these two models, there is still much work to be done to capture the complex behaviors of quasi-fragile materials and make the model applicable to as many situations as possible. To the author's point of view, describing material behaviors by pure mode-I or mode-II discontinuities is not sufficient. It can be seen in the previous conclusions that the advantages and shortcomings of mode-I and mode-II model are partially complementary to each other. The development of cracks in heterogeneous materials is complex and may exhibit at the same time of cracks that are opening, sliding, and closing. Therefore, formulating "diagonal-opening" discontinuities could usefully improve the performances of the model, referring to as the **mode-mix**.

As a first step of verification, we propose here a simple example, that i) the morphological model is that has been used in Section. 8.1, see Fig. III .24; ii) the mechanical

Phase	E	ν	$\sigma_{\mathrm{y}}^{\mathrm{I}}$	$\mathcal{G}_{\mathrm{op}}^{\mathrm{I}}$	C^{II}	$\tan\varphi^{\mathrm{II}}$	$\mathcal{G}_{\mathrm{op}}^{\mathrm{II}}$
	[GPa]	[-]	[MPa]	$[J/m^2]$	[MPa]	[-]	$[J/m^2]$
Matrix	20.0	0.2	4.0	1.0	10.0	0.6	9.0
Interface	-	-	4.0	1.0	10.0	0.6	9.0
Aggregate	100.0	0.3	-	-	-	-	-

Table V .1: Considered material parameters for the heterogeneous cube.

model may exhibits strong discontinuity of the mode-I or mode-II, which respects several rules:

- Aggregates are more rigid than the matrix. And it is assumed that the aggregate elements have pure elastic behavior, the localization can only take place on interface elements and matrix elements.
- Two mechanisms are proposed to local elements: the localization of mode-I and of mode-II.
- Each element can only have localization of mode-I or mode-II. The localization type is defined by the value of the localization criterion of mode-I/mode-II who arrives first to zero.

It is worth noting that no separation law is applied to the model. Our interests are focused on the portion of localized elements which admits an opening type or sliding type, respectively, in traction and in compression. Normally, after the value of the localization criterion reaches zero, the separation law will be triggered, while the value of the localization criterion should not exceed zero. In this case, the so-called equivalent localization value represents sort of the "dangerous fracture" area. The material's parameters are given in Table. V .1. Then the results are shown in Fig. V .1 and Fig. V .2.

Firstly, let us take a look at the results in traction, see Fig. V .1. We can see that the majority of the localized elements are of the type mode-I, especially for the matrix elements. As for the interface elements, they are preferably localized in mode-II. Then it can be seen that there are a number of elements do not localize. Besides the aggregate

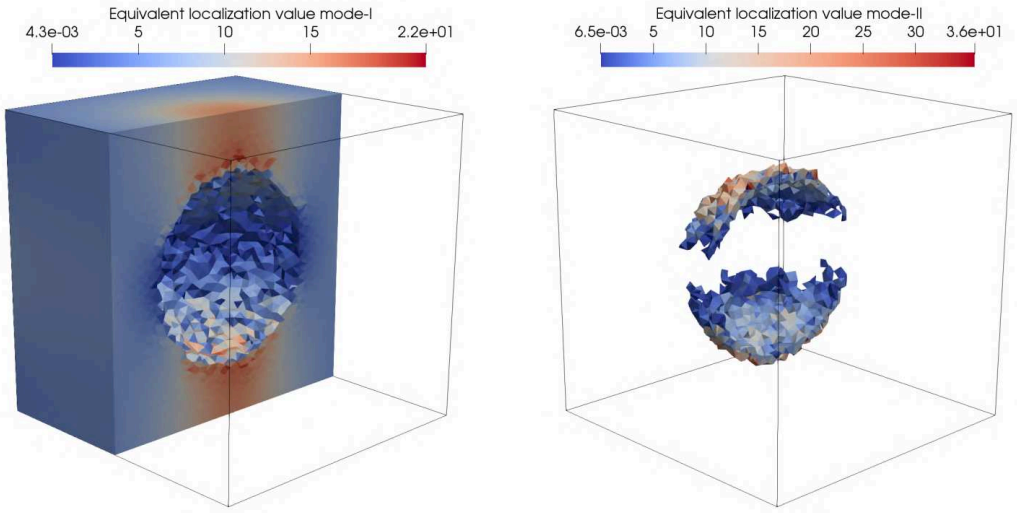

(a) Localized element of mode-I (b) Localized element of mode-II

Figure V .1: Illustration of localized elements of the type mode-I and mode-II.

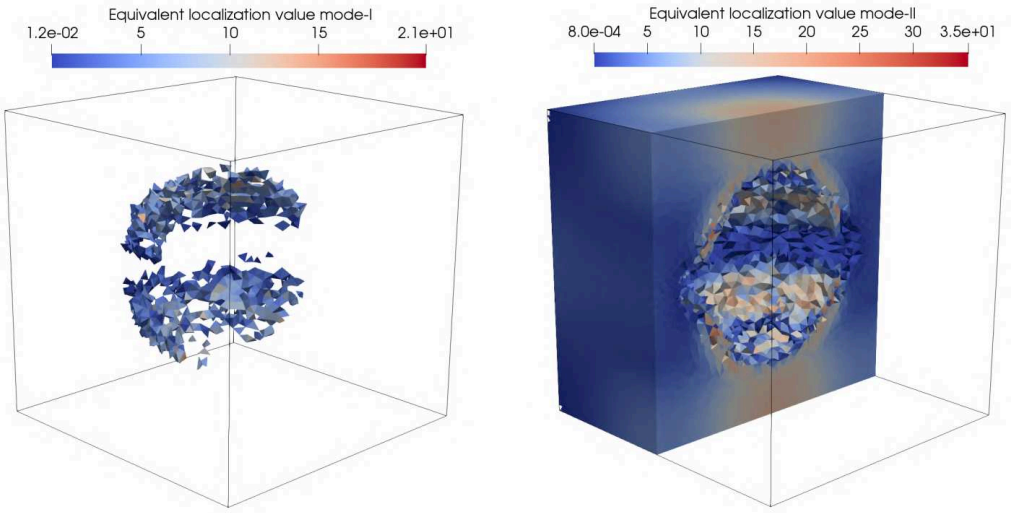

(a) Localized element of mode-I (b) Localized element of mode-II

Figure V .2: Illustration of localized elements of the type mode-I and mode-II in compression.

elements, which are assumed to be purely elastic, interface elements which exhibit a discontinuity interface parallel to the loading direction will also not be localized. Because the normal stress on the discontinuity surface remains relatively low despite a large amount of loadings.

Next, the results of simulation in compression are illustrated in Fig. V .2. It can be seen from the figure that the localized elements are mainly of the type mode-II, while an amount of mode-I localization can also be triggered. It can be deduced that in a case of exhibiting more complex heterogeneous structure, the strong discontinuity of the type mode-I and mode-II will mix and disperse over the specimen.

Upon the previous observations, it is natural to propose a hypothesis that the necessary constituents for performing various mechanical behaviors of concrete should consist of both mechanisms of "opening" and "sliding", the closure mechanism is also essential. In the future, we can improve the performance of our model by proposing a mode-mixed discontinuity, which is to combine the mode-I and mode-II discontinuity.

Moreover, the model is defined to have at most one discontinuity that exhibits in each finite element. Therefore, the model is limited when dealing with a morphological structure with a relatively high volume fraction. Also, if more than one discontinuities are performed in an element, it may improve the capability of the model when capturing the details of microstructure, such as the narrowness between the inclusions.

Bibliography

Ahmed, E., Elgazzar, A. S., and Hegazi, A. S. (2005). An overview of complex adaptive systems. *arXiv preprint nlin/0506059*.

Alliche, A. (2004). Damage model for fatigue loading of concrete. *International Journal of Fatigue*, 26(9):915–921.

Allix, O. and Ladevèze, P. (1992). Interlaminar interface modelling for the prediction of delamination. *Composite Structures*, 22(4):235–242.

Armero, F. and Garikipati, K. (1996). An analysis of strong discontinuities in multiplicative finite strain plasticity and their relation with the numerical simulation of strain localization in solids. Technical Report 20-22.

Armero, F. and Linder, C. (2009). Numerical simulation of dynamic fracture using finite elements with embedded discontinuities. *International Journal of Fracture*, 160(2):119.

Babuŝka, I. and Melenk, J. M. (1997). The partition of unity method. *International journal for numerical methods in engineering*, 40(4):727–758.

Bai, Y. and Wierzbicki, T. (2010). Application of extended mohr–coulomb criterion to ductile fracture. *International Journal of Fracture*, 161(1):1.

Barenblatt, G. I. (1962). The mathematical theory of equilibrium cracks in brittle fracture. In *Advances in applied mechanics*, volume 7, pages 55–129. Elsevier.

Bazant and Oh (1983). Crack band theory for fracture of concrete. *Acta Horticulturae*, 701 II:691–695.

Baz̄ant, Z. P. and Jirásek, M. (2002). Nonlocal integral formulations of plasticity and damage: survey of progress. *Journal of Engineering Mechanics*, 128(11):1119–1149.

Bazant, Z. P. and Planas, J. (1997). *Fracture and size effect in concrete and other quasibrittle materials*, volume 16. CRC press.

Belytschko, T., Fish, J., and Engelmann, B. E. (1988). A finite element with embedded localization zones. Technical Report 1.

Benkemoun, N., Gelet, R., Roubin, E., and Colliat, J.-B. (2015). Poroelastic two-phase material modeling: theoretical formulation and embedded finite element method implementation. *International Journal for Numerical and Analytical Methods in Geomechanics*, 39(12):1255–1275.

Borden, M. J., Verhoosel, C. V., Scott, M. A., Hughes, T. J., and Landis, C. M. (2012). A phase-field description of dynamic brittle fracture. *Computer Methods in Applied Mechanics and Engineering*, 217-220:77–95.

Borja, R. I. (2008). Assumed enhanced strain and the extended finite element methods: A unification of concepts. *Computer Methods in Applied Mechanics and Engineering*, 197(33-40):2789–2803.

Bourdin, B., Francfort, G. A., and Marigo, J. J. (2000). Numerical experiments in revisited brittle fracture. Technical Report 4.

Bourdin, B., Francfort, G. A., and Marigo, J.-J. (2008). The variational approach to fracture. *Journal of elasticity*, 91(1-3):5–148.

Bourgeois, F., Burlion, N., Duveau, G., and Shao, J.-F. (2003). Mise en œuvre d'une modélisation élasto-plastique endommageable du béton: Calculs numériques dans le cadre d'un benchmark edf. *Revue française de génie civil*, 7(5):583–594.

Brancherie, D. (2003). *Modéles continus et" discrets" pour les problémes de localisation et de rupture fragile et/ou ductile*. PhD thesis, École normale supérieure de Cachan-ENS Cachan.

Buliga, M. (1998). Energy minimizing brittle crack propagation. *Journal of Elasticity*, 52(3):201.

Camacho, G. T. and Ortiz, M. (1996). Computational modelling of impact damage in brittle materials. *International Journal of solids and structures*, 33(20-22):2899–2938.

Carol, I., Rizzi, E., and Willam, K. (2001). On the formulation of anisotropic elastic degradation.: Ii. generalized pseudo-rankine model for tensile damage. *International Journal of Solids and Structures*, 38(4):519–546.

Carpinteri, A. (1989). Post-peak and post-bifurcation analysis of cohesive crack propagation. *Engineering Fracture Mechanics*, 32(2):265–278.

Chaboche, J.-L. (1992). Damage induced anisotropy: on the difficulties associated with the active/passive unilateral condition. *International Journal of Damage Mechanics*, 1(2):148–171.

Chen, A. C. and Chen, W.-F. (1975). Constitutive relations for concrete. *Journal of Engineering Mechanics*, 101(ASCE# 11529 Proceeding).

Chow, C. and Wang, J. (1987). An anisotropic theory of continuum damage mechanics for ductile fracture. *Engineering fracture mechanics*, 27(5):547–558.

Chuan-Zhi, W., Zhen-Hai, G., and Xiu-Qin, Z. (1987). Experimental investigation of biaxial and triaxial compressive concrete strength. *Materials Journal*, 84(2):92–100.

Comi, C. and Perego, U. (2001). Fracture energy based bi-dissipative damage model for concrete. *International Journal of Solids and Structures*, 38(36-37):6427–6454.

Corless, R. M., Gonnet, G. H., Hare, D. E., Jeffrey, D. J., and Knuth, D. E. (1996). On the lambertw function. *Advances in Computational mathematics*, 5(1):329–359.

Dal Maso, G. and Toader, R. (2002). A model for the quasi-static growth of brittle fractures based on local minimization. *Mathematical Models and Methods in Applied Sciences*, 12(12):1773–1799.

Desmorat, R., Gatuingt, F., and Ragueneau, F. (2007a). Nonlocal anisotropic damage model and related computational aspects for quasi-brittle materials. *Engineering Fracture Mechanics*, 74(10):1539–1560.

Desmorat, R., Ragueneau, F., and Pham, H. (2007b). Continuum damage mechanics for hysteresis and fatigue of quasi-brittle materials and structures. *International Journal for Numerical and Analytical Methods in Geomechanics*, 31(2):307–329.

Dias-da Costa, D., Alfaiate, J., Sluys, L., and Júlio, E. (2009a). Towards a generalization of a discrete strong discontinuity approach. *Computer Methods in Applied Mechanics and Engineering*, 198(47-48):3670–3681.

Dias-da Costa, D., Alfaiate, J., Sluys, L. J., and Júlio, E. (2009b). A discrete strong discontinuity approach. *Engineering Fracture Mechanics*, 76(9):1176–1201.

Dias-Da-Costa, D., Alfaiate, J., Sluys, L. J., and Júlio, E. (2010). A comparative study on the modelling of discontinuous fracture by means of enriched nodal and element techniques and interface elements. *International Journal of Fracture*, 161(1):97–119.

Dragon, A. and Mroz, Z. (1979). A continuum model for plastic-brittle behaviour of rock and concrete. *International Journal of Engineering Science*, 17(2):121–137.

Duarte, C. A. and Oden, J. T. (1996). An h-p adaptive method using clouds. Technical Report 1-4.

Dugdale, D. S. (1960). Yielding of steel sheets containing slits. *Journal of the Mechanics and Physics of Solids*, 8(2):100–104.

Dvorkin, E. N. and Assanelli, A. P. (1991). 2d finite elements with displacement interpolated embedded localization lines: the analysis of fracture in frictional materials. *Computer methods in applied mechanics and engineering*, 90(1-3):829–844.

Dvorkin, E. N., Cuitiño, A. M., and Gioia, G. (1990). Finite elements with displacement interpolated embedded localization lines insensitive to mesh size and distortions. *International journal for numerical methods in engineering*, 30(3):541–564.

Elaqra, H., Godin, N., Peix, G., R'Mili, M., and Fantozzi, G. (2007). Damage evolution analysis in mortar, during compressive loading using acoustic emission and x-ray tomography: Effects of the sand/cement ratio. *Cement and Concrete Research*, 37(5):703–713.

Etse, G. and Willam, K. (1994). Fracture energy formulation for inelastic behavior of plain concrete. *Journal of engineering mechanics*, 120(9):1983–2011.

G. A. Francfort and J. J. Marigo (1998). Revisiting Brittle Fracture As an Energy. Technical Report 8.

Gabet, T., Malécot, Y., and Daudeville, L. (2008). Triaxial behaviour of concrete under high stresses: Influence of the loading path on compaction and limit states. *Cement and Concrete Research*, 38(3):403–412.

Gatuingt, F. and Pijaudier-Cabot, G. (2002). Coupled damage and plasticity modelling in transient dynamic analysis of concrete. *International journal for numerical and analytical methods in geomechanics*, 26(1):1–24.

Geuzaine, C. and Remacle, J.-F. (2009). Gmsh: A 3-d finite element mesh generator with built-in pre-and post-processing facilities. *International journal for numerical methods in engineering*, 79(11):1309–1331.

Grassl, P. and Jirásek, M. (2006). Damage-plastic model for concrete failure. *International journal of solids and structures*, 43(22-23):7166–7196.

Grassl, P., Lundgren, K., and Gylltoft, K. (2002). Concrete in compression: a plasticity theory with a novel hardening law. *International Journal of Solids and Structures*, 39(20):5205–5223.

Griffith, A. A. (1921). The Phenomena of Rupture and Flow in Solids. *Philosophical Transactions of the Royal Society A: Mathematical, Physical and Engineering Sciences*, 221(582-593):163–198.

Gullerud, A. S., Gao, X., Dodds Jr, R. H., and Haj-Ali, R. (2000). Simulation of ductile crack growth using computational cells: numerical aspects. *Engineering Fracture Mechanics*, 66(1):65–92.

Hansen, E., Willam, K., and Carol, I. (2001). A two-surface anisotropic damage/plasticity model for plain concrete. *Fracture Mechanics of Concrete Structures. Balkema, Lisse*, pages 549–556.

Hashemi, M. A., Khaddour, G., François, B., Massart, T. J., and Salager, S. (2014). A tomographic imagery segmentation methodology for three-phase geomaterials based on simultaneous region growing. *Acta Geotechnica*, 9(5):831–846.

Hashin, Z. and Shtrikman, S. (1963). A variational approach to the theory of the elastic behaviour of multiphase materials. *Journal of the Mechanics and Physics of Solids*, 11(2):127–140.

Hauseux, P. (2015). *Propagation d'incertitudes paramétriques dans les modèles numériques en mécanique non linéaire: applications à des problèmes d'excavation*. PhD thesis, Lille 1.

Hillerborg, A., Modéer, M., and Petersson, P.-E. (1976). Analysis of crack formation and crack growth in concrete by means of fracture mechanics and finite elements. *Cement and concrete research*, 6(6):773–781.

Hofacker, M. and Miehe, C. (2012). Continuum phase field modeling of dynamic fracture: Variational principles and staggered FE implementation. *International Journal of Fracture*, 178(1-2):113–129.

Hofstetter, G. and Mang, H. (1995). *Computational mechanics of reinforced concrete structures*. Vieweg+ Teubner Verlag.

Ibrahimbegovic, A., Markovic, D., Matthies, H. G., Niekamp, R., and Taylor, R. L. (2005). Multi-scale modelling of heterogeneous structures with inelastic constitutive behavior. In *Complas VIII-8th International Conference on Computational Plasticity*. Citeseer.

Imran, I. and Pantazopoulou, S. (1996). Experimental study of plain concrete under triaxial stress. *ACI Materials Journal-American Concrete Institute*, 93(6):589–601.

Jirasek and Zimmermann, T. (1998a). Analysis of rotating crack model (1998a).

Jirasek and Zimmermann, T. (1998b). Rotating crack model with transition to scalar damage (1998b).

Jirásek, M. (2000). Comparative study on finite elements with embedded discontinuities. Technical Report 1.

Jirásek, M. (2011). Damage and smeared crack models. In *Numerical modeling of concrete cracking*, pages 1–49. Springer.

Kachanov, M. L. (1982a). A microcrack model of rock inelasticity part i: Frictional sliding on microcracks. *Mechanics of Materials*, 1(1):19–27.

Kachanov, M. L. (1982b). A microcrack model of rock inelasticity part ii: propagation of microcracks. *Mechanics of Materials*, 1(1):29–41.

Kamel, K. E. M., Colliat, J.-B., Gerard, P., and Massart, T. J. (2019a). Comparison of advanced discretization techniques for image-based modelling of heterogeneous porous rocks. *Acta Geotechnica*, pages 1–21.

Kamel, K. E. M., Sonon, B., and Massart, T. J. (2019b). An integrated approach for the conformal discretization of complex inclusion-based microstructures. *Computational Mechanics*, pages 1–23.

Kishta, E. (2016). *Anisotropic crack modelling of reinforced concrete structures with an enhanced kinematics: Application to bidimensional elements under cyclic loading*. PhD thesis, Université Paris-Saclay.

Krajcinovic, D. (1985). Continuous damage mechanics revisited: basic concepts and definitions. *Journal of Applied Mechanics*, 52(4):829–834.

Krätzig, W. B. and Pölling, R. (2004). An elasto-plastic damage model for reinforced concrete with minimum number of material parameters. *Computers & structures*, 82(15-16):1201–1215.

Kuhn, C. and Müller, R. (2010). Phase field simulation of thermomechanical fracture. *Pamm*, 9(1):191–192.

Kupfer, H., Hilsdorf, H. K., and Rusch, H. (1969a). Behavior of concrete under biaxial stresses. In *Journal Proceedings*, volume 66, pages 656–666.

Kupfer, H., Hilsdorf, H. K., and Rusch, H. (1969b). Behavior of Concrete Under Biaxial Stresses. *ACI Journal Proceedings*, 66(8):656–666.

Landis, E. N., Nagy, E. N., and Keane, D. T. (2003). Microstructure and fracture in three dimensions. *Engineering Fracture Mechanics*, 70(7-8):911–925.

Larsson, R., Runesson, K., and Sture, S. (1996). Embedded localization band in undrained soil based on regularized strong discontinuity—theory and fe-analysis. *International Journal of Solids and Structures*, 33(20-22):3081–3101.

Lemaitre, J., Chaboche, J.-L., Benallal, A., and Desmorat, R. (2009). *Mécanique des matériaux solides-3eme édition*. Dunod.

Li, T., Marigo, J. J., Guilbaud, D., and Potapov, S. (2016). Numerical investigation of dynamic brittle fracture via gradient damage models. *Advanced Modeling and Simulation in Engineering Sciences*, 3(1):26.

Linhua, J., Dahai, H., and Nianxiang, X. (1991). Behavior of concrete under triaxial compressive-compressive-tensile stresses. *Materials Journal*, 88(2):181–185.

Lotfi, H. R. and Shing, P. B. (1995). Embedded representation of fracture in concrete with mixed finite elements. *International Journal for Numerical Methods in Engineering*, 38(8):1307–1325.

Lu, S., Landis, E., and Keane, D. (2006). X-ray microtomographic studies of pore structure and permeability in portland cement concrete. *Materials and structures*, 39(6):611–620.

Lubliner, J., Oliver, J., Oller, S., and Onate, E. (1989a). A PLASTIC-DAMAGE MODEL FOR CONCRETE. Technical Report 3.

Lubliner, J., Oliver, J., Oller, S., and Oñate, E. (1989b). A plastic-damage model for concrete. *International Journal of solids and structures*, 25(3):299–326.

Malecot, Y., Daudeville, L., Dupray, F., Poinard, C., and Buzaud, E. (2010). Strength and damage of concrete under high triaxial loading. *European Journal of Environmental and Civil Engineering*, 14(6-7):777–803.

Mazars, J. (1984). Application de la mécanique de l'endommagement au comportement non linéaire et à la rupture du béton de structure. *THESE DE DOCTEUR ES SCIENCES PRESENTEE A L'UNIVERSITE PIERRE ET MARIE CURIE-PARIS 6*.

Mazars, J., Berthaud, Y., and Ramtani, S. (1990). The unilateral behaviour of damaged concrete. *Engineering Fracture Mechanics*, 35(4-5):629–635.

Mazars, J. and Lemaitre, J. (1985). Application of continuous damage mechanics to strain and fracture behavior of concrete. In *Application of fracture mechanics to cementitious composites*, pages 507–520. Springer.

Mazars, J. and Pijaudier-Cabot, G. (1989). Continuum damage theory—application to concrete. *Journal of Engineering Mechanics*, 115(2):345–365.

Melenk, J. M. and Babuŝka, I. (1996). The partition of unity finite element method: basic theory and applications. *Computer methods in applied mechanics and engineering*, 139(1-4):289–314.

Menetrey, P. and Willam, K. (1995). Triaxial failure criterion for concrete and its generalization. *Structural Journal*, 92(3):311–318.

Miehe, C., Schaenzel, L.-M., and Ulmer, H. (2015). Phase field modeling of fracture in multi-physics problems. part i. balance of crack surface and failure criteria for brittle crack propagation in thermo-elastic solids. *Computer Methods in Applied Mechanics and Engineering*, 294:449–485.

Miehe, C., Welschinger, F., and Hofacker, M. (2010a). Thermodynamically consistent phase-field models of fracture: Variational principles and multi-field FE implementations. *International Journal for Numerical Methods in Engineering*, 83(10):1273–1311.

Miehe, C., Welschinger, F., and Hofacker, M. (2010b). Thermodynamically consistent phase-field models of fracture: Variational principles and multi-field fe implementations. *International Journal for Numerical Methods in Engineering*, 83(10):1273–1311.

Moës, N., Cloirec, M., Cartraud, P., and Remacle, J.-F. (2003). A computational approach to handle complex microstructure geometries. *Computer methods in applied mechanics and engineering*, 192(28-30):3163–3177.

Moës, N., Dolbow, J., and Belytschko, T. (1999). A finite element method for crack growth without remeshing. *International journal for numerical methods in engineering*, 46(1):131–150.

Needleman, A. and Xu, X. P. (1994). Numerical simulations of fast crack growth in brittle solids. Technical Report 9.

Oliver, J. (1996a). Modelling strong discontinuities in solid mechanics via strain softening constitutive equations. part 1: Fundamentals. *International journal for numerical methods in engineering*, 39(21):3575–3600.

Oliver, J. (1996b). Modelling strong discontinuities in solid mechanics via strain softening constitutive equations. part 2: Numerical simulation. *International journal for numerical methods in engineering*, 39(21):3575–3600.

Oliver, J. (2000). On the discrete constitutive models induced by strong discontinuity kinematics and continuum constitutive equations. *International Journal of Solids and Structures*, 37(48):7207–7229.

Oliver, J., Huespe, A. E., Pulido, M., and Chaves, E. (2002). From continuum mechanics to fracture mechanics: the strong discontinuity approach. *Engineering fracture mechanics*, 69(2):113–136.

Oliver, J., Huespe, A. E., Pulido, M. D. G., and Chaves, E. (2001). From continuum mechanics to fracture mechanics: The strong discontinuity approach. Technical Report 2.

Oliver, J., Huespe, A. E., and Sánchez, P. J. (2006). A comparative study on finite elements for capturing strong discontinuities: E-FEM vs X-FEM. *Computer Methods in Applied Mechanics and Engineering*, 195(37-40):4732–4752.

Ortiz, M. (1985). A constitutive theory for the inelastic behavior of concrete. *Mechanics of materials*, 4(1):67–93.

Ortiz, M., Leroy, Y., and Needleman, A. (1987). A finite element method for localized failure analysis. *Computer methods in applied mechanics and engineering*, 61(2):189–214.

Papa, E. (1996). A unilateral damage model for masonry based on a homogenisation procedure. *Mechanics of Cohesive-frictional Materials: An International Journal on Experiments, Modelling and Computation of Materials and Structures*, 1(4):349–366.

Pijaudier-Cabot, G. and Bazant, Z. P. (1987). Nonlocal damage theory. *Journal of engineering mechanics*, 113(10):1512–1533.

Piotrowska, E. (2013). *Rôle du squelette granulaire dans le comportement du béton sous trés fortes contraintes: analyse expérimentale et numérique.* PhD thesis, Université de Grenoble.

Planas, J., Elices, M., and Guinea, G. V. (1993). Cohesive cracks versus nonlocal models: Closing the gap. Technical report.

Poinard, C., Piotrowska, E., Malecot, Y., Daudeville, L., and Landis, E. N. (2012). Compression triaxial behavior of concrete: the role of the mesostructure by analysis of x-ray tomographic images. *European Journal of Environmental and Civil Engineering*, 16(sup1):s115–s136.

Poinard, C., Piotrowska, E., Marin, P., Malecot, Y., and Daudeville, L. (2011). Mesoscopic scale modeling of concrete under triaxial loading using x-ray tomographic images. In *Particle Based Methods Conference*, pages 117–129.

Pugh, H. L. D. (1973). Mechanical behaviour of materials under pressure.

Qi, M. (2016). *Modélisation micromécanique de l'endommagement et du frottement dans des géomatériaux initialement anisotropes.* PhD thesis, Lille 1.

Ragueneau, F. (2007). *Comportements endommageants des matériaux et des structures en béton armé.* LMT-Cachan.

Ramakrishnan, V. and Malhotra, T. B. V. (1993). Fatigue strength and endurance limit of lightweight concrete. *Special Publication*, 136:397–420.

Ramtani, S. (1990). *Contribution à la modélisation du comportement multiaxial du béton endommagé avec description du caractère unilatéral.* PhD thesis, Paris 6.

Ramtani, S., Berthaud, Y., and Mazars, J. (1992). Orthotropic behavior of concrete with directional aspects: modelling and experiments. *Nuclear Engineering and design*, 133(1):97–111.

Rashid, Y. R. (1968). Ultimate strength analysis of prestressed concrete pressure vessels. *Nuclear Engineering and Design*, 7(4):334–344.

Reinhardt, H. W. (1984). Fracture mechanics of an elastic softening material like concrete. *HERON, 29 (2), 1984.*

Ren, W., Yang, Z., Sharma, R., Zhang, C., and Withers, P. J. (2015). Two-dimensional x-ray ct image based meso-scale fracture modelling of concrete. *Engineering Fracture Mechanics*, 133:24–39.

Richard, B. and Ragueneau, F. (2013). Continuum damage mechanics based model for quasi brittle materials subjected to cyclic loadings: Formulation, numerical implementation and applications. *Engineering Fracture Mechanics*, 98(1):383–406.

Rots, J. G. (1991). Smeared and discrete representations of localized fracture. In *Current Trends in Concrete Fracture Research*, pages 45–59. Springer.

Rots, J. G., Nauta, P., Kuster, G., and Blaauwendraad, J. (1985). Smeared crack approach and fracture localization in concrete. *HERON, 30 (1), 1985.*

Roubin, E. (2013). *Modélisation EF et morphologique de milieu hétérogènes à l'échelle mésoscopique: applications aux matériaux à matrices cimentaire.* PhD thesis, Thèse de doctorat, Ecole Normale Supérieure de Cachan.

Roubin, E., Vallade, A., Benkemoun, N., and Colliat, J.-B. (2015). Multi-scale failure of heterogeneous materials: A double kinematics enhancement for embedded finite element method. *International Journal of Solids and Structures*, 52:180–196.

Salari, M., Saeb, S., Willam, K., Patchet, S., and Carrasco, R. (2004). A coupled elastoplastic damage model for geomaterials. *Computer methods in applied mechanics and engineering*, 193(27-29):2625–2643.

Salençon, J. (2002). *De l'élasto-plasticité au calcul à la rupture.* Editions Ecole Polytechnique.

Sfer, D., Carol, I., Gettu, R., and Etse, G. (2002). Study of the behavior of concrete under triaxial compression. *Journal of engineering mechanics*, 128(2):156–163.

Simo, J. C. and Ju, J. (1987). Strain-and stress-based continuum damage models—i. formulation. *International journal of solids and structures*, 23(7):821–840.

Simo, J. C., Oliver, J., and Armero, F. (1993). An analysis of strong discontinuities induced by strain-softening in rate-independent inelastic solids. *Computational mechanics*, 12(5):277–296.

Simo, J. C. and Rifai, M. (1990). A class of mixed assumed strain methods and the method of incompatible modes. *International journal for numerical methods in engineering*, 29(8):1595–1638.

Sluys, L. and Berends, A. (1998). Discontinuous failure analysis for mode-i and mode-ii localization problems. *International Journal of Solids and Structures*, 35(31-32):4257–4274.

Stamati, O., Roubin, E., Andò, E., and Malecot, Y. (2018a). Phase segmentation of concrete x-ray tomographic images at meso-scale: Validation with neutron tomography. *Cement and Concrete Composites*, 88:8–16.

Stamati, O., Roubin, E., Andò, E., and Malecot, Y. (2018b). Tensile failure of micro-concrete: from mechanical tests to fe meso-model with the help of x-ray tomography. *Meccanica*, pages 1–16.

Suidan, M. and Schnobrich, W. C. (1973). Finite element analysis of reinforced concrete. *Journal of the Structural Division*, 99(st1).

Sukumar, N., Chopp, D. L., Moës, N., and Belytschko, T. (2001). Modeling holes and inclusions by level sets in the extended finite-element method. *Computer methods in applied mechanics and engineering*, 190(46-47):6183–6200.

Taliercio, A., Berraf, M., and Pandolfi, A. (1999). Effect of high-intensity sustained tri-axial stresses on the mechanical properties of plain. *Magazine of Concrete Research*, 51(6):437–447.

T.C. Hsu, T. (1981). Fatigue of plain concrete. *Journal of the American Concrete Institute*, 78:292–305.

Tepfers, R. and Kutti, T. (1979). Fatigue strength of plain, ordinary, and lightweight concrete. In *Journal Proceedings*, volume 76, pages 635–652.

Terrien, M. (1980). Emission acoustique et" comportement mecanique post-critique" d'un beton sollicite en traction. *BULL LIAISON LAB PONTS CHAUSS*, (105).

Tvergaard, V. (1982). On localization in ductile materials containing spherical voids. *International Journal of fracture*, 18(4):237–252.

Vallade, A. (2016). *Modélisation multi-échelles des shales: influence de la microstructure sur les propriétés macroscopiques et le processus de fracturation*. PhD thesis, Lille 1.

Vu, X. H., Malecot, Y., Daudeville, L., and Buzaud, E. (2009). Experimental analysis of concrete behavior under high confinement: Effect of the saturation ratio. *International Journal of Solids and Structures*, 46(5):1105–1120.

Washizu, K. (1968). Variational methods in elasticity and plasticity.

Wells, G. N. (2001). *Discontinuous modelling of strain localisation and failure*. PhD thesis.

Wong, R. and Chau, K. (2005). Estimation of air void and aggregate spatial distributions in concrete under uniaxial compression using computer tomography scanning. *Cement and Concrete Research*, 35(8):1566–1576.

Wu, J. Y. (2011). Unified analysis of enriched finite elements for modeling cohesive cracks. *Computer Methods in Applied Mechanics and Engineering*, 200(45-46):3031–3050.

Wu, J. Y., Li, F. B., and Xu, S. L. (2015). Extended embedded finite elements with continuous displacement jumps for the modeling of localized failure in solids. *Computer Methods in Applied Mechanics and Engineering*, 285:346–378.

Wu, J. Y., Li, J., and Faria, R. (2006). An energy release rate-based plastic-damage model for concrete. *International Journal of Solids and Structures*, 43(3-4):583–612.

Xu, X.-P. and Needleman, A. (1994). Numerical simulations of fast crack growth in brittle solids. *Journal of the Mechanics and Physics of Solids*, 42(9):1397–1434.

Yazdani, S. and Schreyer, H. (1988). An anisotropic damage model with dilatation for concrete. *Mechanics of Materials*, 7(3):231–244.

Zaitsev, Y. V. (1985). Inelastic properties of solids with random cracks. In *Mechanics of geomaterials*, pages 89–128. Wiley Chicester.